

**POLY(METHYL METHACRYLATE-CO-BUTYL
ACRYLATE-CO-ACRYLIC ACID): SYNTHESIS,
CHARACTERIZATION AND TARGETED SOLID STATE-
DYE SENSITIZED SOLAR CELL APPLICATION**

R SHANTI A/P RAJANTHARAN

**FACULTY OF SCIENCE
UNIVERSITY OF MALAYA
KUALA LUMPUR**

2018

**POLY(METHYL METHACRYLATE-*CO*-BUTYL
ACRYLATE-*CO*-ACRYLIC ACID): SYNTHESIS,
CHARACTERIZATION AND TARGETED SOLID
STATE-DYE SENSITIZED SOLAR CELL
APPLICATION**

R SHANTI A/P RAJANTHARAN

**THESIS SUBMITTED IN FULFILMENT OF THE
REQUIREMENTS FOR THE DEGREE OF
DOCTOR OF PHILOSOPHY**

**DEPARTMENT OF PHYSICS
FACULTY OF SCIENCE
UNIVERSITY OF MALAYA
KUALA LUMPUR**

2018

UNIVERSITY OF MALAYA
ORIGINAL LITERARY WORK DECLARATION

Name of Candidate: **R SHANTI A/P RAJANTHARAN**

Matric No : **SHC110087**

Name of Degree : **DOCTOR OF PHILOSOPHY**

Title of Project Paper/Research Report/Dissertation/Thesis (“this Work”):

POLY(METHYL METHACRYLATE-CO-BUTYL AC

**RYLATE-CO-ACRYLIC ACID): SYNTHESIS, CHARACTERIZATION
AND TARGETED SOLID STATE-DYE SENSITIZED SOLAR CELL
APPLICATION**

Field of Study : **EXPERIMENTAL PHYSICS**

I do solemnly and sincerely declare that:

a

- (1) I am the sole author/writer of this Work;
- (2) This Work is original;
- (3) Any use of any work in which copyright exists was done by way of fair dealing and for permitted purposes and any excerpt or extract from, or reference to or reproduction of any copyright work has been disclosed expressly and sufficiently and the title of the Work and its authorship have been acknowledged in this Work;
- (4) I do not have any actual knowledge nor do I ought reasonably to know that the making of this work constitutes an infringement of any copyright work;
- (5) I hereby assign all and every rights in the copyright to this Work to the University of Malaya (“UM”), who henceforth shall be owner of the copyright in this Work and that any reproduction or use in any form or by any means whatsoever is prohibited without the written consent of UM having been first had and obtained;
- (6) I am fully aware that if in the course of making this Work I have infringed any copyright whether intentionally or otherwise, I may be subject to legal action or any other action as may be determined by UM.

Candidate’s Signature

Date:

Subscribed and solemnly declared before,

Witness’s Signature

Date:

Name:

Designation:

**POLY(METHYL METHACRYLATE-CO-BUTYL ACRYLATE-CO-ACRYLIC
ACID): SYNTHESIS, CHARACTERIZATION AND TARGETED SOLID
STATE-DYE SENSITIZED SOLAR CELL APPLICATION**

ABSTRACT

A series of polymeric solid state electrolytes (PSSE) was developed using ultra high molecular weight (UHMW) poly(methyl methacrylate-*co*-butyl acrylate-*co*-acrylic acid) [P(MMA-*co*-BA-*co*-AA)] targeted for solid-state dye-sensitized solar cell (DSSC). The copolymer was synthesized *via* emulsion polymerization and formulated as such that it possessed low glass transition temperature (T_g). For properties optimization, different ratios of MMA to AA were tested. All the analogous copolymers have similar bulk properties but their colloidal stabilities and conversion efficiencies vary. Among these, AA05 formulation [abbreviated as P(MMA-*co*-BA-*co*-AA) with (55 : 40 : 5) wt.%] has the highest monomer conversion and colloidal stability. The combination with other superior properties allows AA05 to be the most suitable matrix for PSSE development. The first PSSE system developed from the host AA05 was formulated by doping different amounts of sodium iodide (NaI, System I) into the matrix containing a fixed ratio of plasticizer mixture [ethylene carbonate (EC): propylene carbonate (PC) at 1:1 ratio] and iodine (I_2). The complexation between NaI and AA05 increases the amorphicity, and causes the ionic conductivity (σ) to rise up to $4.21 \times 10^{-4} \text{ S cm}^{-1}$ in NaI-PSSE containing 20 wt.% NaI (abbreviated as NaI-20) for solid film with thickness of 100 μm . A photovoltaic efficiency, as high as 3.22 % under 1 Sun was recorded for the rubbery-PSSE (above T_g) containing 15 wt.% NaI (NaI-15; $\sigma = 3.85 \times 10^{-4} \text{ S cm}^{-1}$). The utilization of rubbery-PSSE offers a number of appealing properties for device fabrication, such as (i) soft electrolyte film that forms good interfacial contact with dye-sensitized semiconductor such as titanium oxide (TiO_2 ; photoanode) and (ii) high availability of free volume when the cell temperature at 50 °C (cell processing) is

brought to 25 °C (cell working). Although good cell performance was successfully obtained, the ionic conductivity diminution in NaI-15 at increasing temperature near to its $T_g = 50$ °C may have limited the cell performance. In order to eliminate this possibility, two additional PSSE systems (System II and III) were developed using NaI-15 as the control. System II contains higher concentration of EC: PC while System III contains dispersed fumed silica nanoparticles (SiO_2 NPs). Enhancement of ionic conductivity was observed in both EC: PC and SiO_2 NPs systems, with no drop in conductivity near to the T_g of highly conducting PSSE. This arises as the subsequent increase of amorphous content. Unfortunately, the PSSE developed from System II were not suitable for cell fabrication owing to its soft mechanical strength. The cell efficiency of System III ($\eta = 6\%$ under 1 Sun in the presence of 2 wt.% SiO_2) was enhanced by two folds as compared to that of NaI-15. The recorded value is comparable to that of gel polymer electrolyte (GPE) assembly. The fast ion tunneling along the highly conducting interface layer (grain boundary) of SiO_2 NPs and high free volume availability (or amorphous phase) may explain the high photovoltaic performance. All the observations led us to believe that UHMW P(MMA-*co*-BA-*co*-AA) with AA05 formulation can be a good substitute for polymers with molecular weight ranges in hundreds of thousands.

Keywords: P(MMA-*co*-BA-*co*-AA), emulsion polymerization, PSSE, dye-sensitized solar cell

**POLI(METIL METAKRILAT-KO-BUTIL AKRILAT-KO-AKRILIK ASID):
SINTESIS, PENCIRIAN DAN SASARAN APLIKASI PEWARNA SENSITIF
SOLAR SEL DALAM KEADAAN PEPEJAL**

ABSTRAK

Satu siri elektrolit polimer keadaan pepejal (PSSE) telah dibangunkan menggunakan polimer berat molekul ultra tinggi (UHMW) (metil metakrilat-ko-butiril akrilat-ko-akrilik asid) [P(MMA-co-BA-co-AA)]; yang disasarkan untuk aplikasi pencelup sensitif solar sel (DSSC). Kopolimer ini disintesis melalui pempolimeran emulsi dan diformulakan sedemikian sehingga ia mempunyai suhu peralihan kaca (T_g) yang rendah. Bagi pengoptimuman sifat, nisbah MMA kepada AA telah diuji. Semua kopolimer mempunyai sifat pukal yang sama tetapi berbeza dari segi kestabilan koloid dan kecekapan penukarannya. Di antara semua kopolimer yang dikaji, formulasi AA05 [disingkat sebagai P(MMA-ko-BA-ko-AA) dengan (55: 40: 5) wt.%] mempunyai penukaran monomer dan kestabilan koloid tertinggi. Gabungan dengan sifat unggul lain membolehkan AA05 menjadi matriks yang paling sesuai untuk pembangunan PSSE. Sistem PSSE pertama dirumuskan menggunakan formulasi AA05 dengan menambahkan natrium iodida (NaI, Sistem I) ke dalam matriks yang mengandungi nisbah tetap campuran plasticizer [etilena karbonat (EC): propilena karbonat (PC) pada nisbah 1: 1] dan iodin (I_2). Kompleks antara NaI dan AA05 meningkatkan kepekatan amorfus, dan menyebabkan kekonduksian ionik meningkat hingga $4.21 \times 10^{-4} \text{ S cm}^{-1}$ untuk filem pepejal NaI-20 yang mempunyai ketebalan 100 μm . Kecekapan fotovoltai, setakat 3.22 % di bawah 1 Matahari dicatatkan untuk amorfus-PSSE (di atas T_g) yang mengandungi 15 wt.% NaI (disingkat NaI-15; $\sigma = 3.85 \times 10^{-4} \text{ S cm}^{-1}$). Penggunaan amorfus-PSSE menawarkan beberapa sifat menarik untuk fabrikasi peranti, seperti (1) filem elektrolit lembut yang membentuk hubungan interfasial yang baik dengan pewarna sensitif dan (2) tingginya ketersediaan fraksi volume bebas apabila suhu sel

pada 50 °C (pemrosesan sel) dibawa ke 25 °C (berfungsi sel). Walaupun prestasi sel yang baik berjaya diperolehi dalam percubaan ini, penurunan kekonduksian di NaI-15 pada peningkatan suhu berhampiran dengan $T_g = 50$ °C mungkin menghadkan prestasi sel. Untuk menghapuskan kemungkinan ini, dua sistem PSSE tambahan (Sistem II dan III) telah dibangunkan menggunakan NaI-15 sebagai kawalan. Sistem II mengandungi kepekatan EC: PC yang berbeza sementara Sistem III mengandungi fumed nanopartikel silika (SiO_2 NPs). Peningkatan kekonduksian ionik diperhatikan dalam sistem EC: PC dan SiO_2 NPs, tanpa penurunan kekonduksian berhampiran dengan T_g . Ini timbul sebagai peningkatan kandungan amorf yang seterusnya. Malangnya, PSSE yang dibangunkan dari Sistem II tidak sesuai untuk pembuatan sel kerana kekuatan mekanikal yang lembut. Kecekapan sel Sistem III ($\eta = 6\%$ di bawah 1 Matahari di hadapan 2 wt.% SiO_2) telah ditingkatkan sebanyak dua kali ganda berbanding dengan NaI-15. Nilai yang direkodkan adalah sebanding dengan elektrolit polimer gel (GPE). Prestasi fotovoltaiik yang tinggi ini disebabkan oleh ion yang bergerak dengan pantas di sepanjang lapisan antaramuka SiO_2 NPs yang berkonduksi tinggi (sempadan butir). Ianya juga boleh disebabkan oleh kandungan 'free volume' yang tinggi (atau fasa amorf). Kesemua pemerhatian membawa kita percaya bahawa UHMW P(MMA-*ko*-BA-*ko*-AA) dengan formulasi AA05 boleh menjadi pengganti yang baik untuk polimer yang mempunyai ratusan ribuan berat purata molekul.

Kata kunci: P(MMA-*ko*-BA-*ko*-AA), pempolimeran emulsi, PSSE, pewarna sensitif solar sel

ACKNOWLEDGEMENTS

This dissertation is the product of a large measure of serendipity and self-fortuitous encounters. The successful completion was possible with the help of so many kind hearts that have contributed in many ways. My first gratitude is surely towards my family members including cousins, whom have tolerated all the emotional shears that I have showed throughout my studies. Thanks to Prof. Dr. Ramesh Subramaniam and Assoc. Prof. Dr. Ramesh Kasi for being a constant source of motivation. I am hugely indebted to Dr. Sandeep Rai, Dr. Kiran and Dr. Yoga Sugama Salim for finding time to reply to my e-mails subjecting to enormous numbers of doubts on research and being a constant source of motivation. I extended my deepest gratitude to Dr. Federico Bella with whom I had the privilege to collaborate for the electrochemical application studies. Not to forget, the contribution from Dr. Chee Swee Yong is also appreciated. Immeasurable appreciations to all my friends; Ng Mei Yoke, Kuhan, Thulasi, Miss Lau, Tina Vallie and many others who put their faith in me and urged me to do better whenever I am emotionally crushed. Each and everyone had helped me to shape my translation skills in good and bad, words can never be enough to thank those kindnesses. Apart from individual contributions, institutional organizations such as Bright Spark Scholarship and HIR Grant also have helped me financially throughout my years of studies. My gratitude was also expressed to my labmates, suppliers, lab technicians, unnamed individuals that have given me moral support and thoughtful suggestions in my research. Lastly, to those that have created some trouble time in my life. Without those troubles I may not be as who I am now. Thanks to the entire universal including God for the opportunity given and adequate strength to face all the hustles.

TABLE OF CONTENTS

ABSTRACT.....	iii
ABSTRAK.....	v
ACKNOWLEDGEMENTS.....	vii
TABLE OF CONTENTS.....	viii
LIST OF FIGURES.....	xvi
LIST OF TABLES.....	xx
LIST OF SYMBOLS AND ABBREVIATIONS.....	xxi
LIST OF APPENDICES.....	xxiii
CHAPTER 1: INTRODUCTION.....	1
1.1 Overview.....	1
1.2 Problem statement.....	5
1.3 Highlight of research.....	6
1.4 Motivation of study.....	6
1.5 Aim and objectives.....	7
1.6 Scope of thesis.....	7
CHAPTER 2: LITERATURE REVIEW.....	9
2.1 Solid-state DSSC: History and limitation.....	9
2.1.1 Acceleration of ionic conductivity.....	10
2.1.1.1 Liquid plasticization.....	12
2.1.1.2 Composite addition.....	13
2.1.2 Wetting properties.....	17
2.1.2.1 TiO ₂ modification.....	17
2.1.2.2 Liquid oligomers incorporation.....	18
2.1.2.3 In-situ polymerization.....	20

2.2	Solid polymer electrolytes.....	21
2.2.1	Polymer structure: Glass transition phase.....	21
2.2.2	Polymer structure: Molecular weight.....	23
2.3	Ions nature in iodide-based SPE.....	23
2.4	Mode of ion transport in SPE.....	25
2.4.1	Hopping <i>via</i> frozen chain segments.....	26
2.4.2	Ion motion mediated by segmental dynamics.....	27
2.4.3	Self-ion diffusion.....	27
2.4.4	Ion percolation <i>via</i> space charge layer.....	28
2.5	General criteria of PSSE.....	29
2.6	UHMW polymer: History and development.....	30
2.6.1	UHMW polymer in DSSC fabrication: Current state-of-art.....	32
2.6.2	Benefit of UHMW polymer in SPE development.....	33
2.6.3	Synthesis of UHMW polymer.....	34
2.7	Why P(MMA- <i>co</i> -BA- <i>co</i> -AA)?.....	36
2.7.1	Poly(methyl methacrylate).....	37
2.7.2	Poly(butyl acrylate).....	38
2.7.3	Poly(acrylic acid).....	39
2.8	Theoretical background.....	40
2.8.1	Gordon-Taylor equation.....	40
2.8.2	Scattering function.....	40
2.8.3	Jump relaxation model.....	40
2.8.4	Nernst-Einstein equation.....	41
	CHAPTER 3: MATERIALS AND METHOD.....	43
3.1	UHMW P(MMA- <i>co</i> -BA- <i>co</i> -AA).....	43
3.1.1	Materials.....	43

3.1.2	Reactor assembly.....	43
3.1.3	Emulsion polymerization.....	44
3.1.4	Film preparation.....	45
3.1.5	UV irradiation.....	46
3.2	PSSE formulation.....	46
3.2.1	Materials.....	46
3.2.2	PSSE thin film preparation.....	47
3.3	Fabrication of DSSC.....	48
3.3.1	Materials.....	48
3.3.2	Preparation of photoanode and counter electrode.....	48
3.3.2.1	Photoanode.....	48
3.3.2.2	Counter electrode.....	48
3.3.3	Solid-state DSSC assembly.....	49
3.4	Analytical techniques.....	49
3.4.1	P(MMA- <i>co</i> -BA- <i>co</i> -AA).....	49
3.4.1.1	Gravimetry.....	49
3.4.1.2	Light scattering (particle size and zeta potential).....	49
3.4.1.3	Attenuated total reflectance-Fourier transform infrared spectroscopy (ATR-FTIR).....	50
3.4.1.4	Solubility test.....	50
3.4.1.5	Nuclear magnetic resonance spectroscopy (NMR).....	50
3.4.1.6	Thermogravimetry analysis (TGA).....	51
3.4.1.7	Differential scanning calorimetry (DSC).....	51
3.4.1.8	Gel permeation chromatograph (GPC).....	51
3.4.1.9	Four point probe.....	52
3.4.1.10	Tensile test.....	52

3.4.2	UV irradiated P(MMA-co-BA-co-AA).....	52
3.4.2.1	UV-visible-near IR (UV-Vis-NIR).....	52
3.4.2.2	Atomic force microscope (AFM) and other related analyses.....	53
3.4.3	Characterization of PSSE.....	54
3.4.3.1	X-ray diffraction.....	54
3.4.3.2	Impedance spectroscopy.....	54
3.4.3.3	Thermal analysis.....	54
3.4.4	Electrochemical performance of solid-state DSSC.....	54
CHAPTER 4: RESULTS AND DISCUSSION.....		55
<i>Synthesis, Physico-Chemical and Photo-degradation of Random P(MMA-co-BA-co-AA)</i>		
4.1	Synthesis of P(MMA-co-BA-co-AA).....	55
4.1.1	Particle-size distribution.....	55
4.1.2	Zeta potential.....	56
4.1.3	Monomer conversion and TSC.....	56
4.1.4	Solubility test.....	57
4.1.5	ATR-FTIR.....	58
4.1.6	NMR.....	59
4.1.7	GPC.....	62
4.1.8	TGA.....	62
4.1.9	DSC.....	64
4.1.10	Four Point Probe.....	65
4.1.11	Tensile property.....	67
4.2	Summary.....	68
4.3	Photo-degradation of AA05.....	69

4.3.1	FTIR.....	69
4.3.2	UV-Vis-NIR Spectroscopy.....	73
4.3.3	GPC.....	74
4.3.4	Chromaticity analysis.....	76
4.3.5	AFM study.....	77
4.3.6	TGA.....	78
CHAPTER 5: RESULTS AND DISCUSSION.....		80
<i>Characterization of PSSE: System I- NaI variation</i>		
5.1	Chain relaxation time.....	80
5.1.1	Room temperature measurement.....	80
5.1.2	Temperature variation.....	82
5.2	Nyquist plot.....	84
5.2.1	Room temperature measurement.....	84
5.2.2	Temperature variation.....	87
5.3	Ion relaxation time.....	90
5.3.1	Room temperature measurement.....	90
5.3.2	Temperature variation.....	93
5.4	Frequency-dependent ionic conductivity.....	95
5.4.1	Room temperature measurement.....	95
5.4.2	Temperature variation.....	97
5.5	Ionic conductivity at room temperature.....	100
5.6	Conductivity-temperature dependence.....	102
5.7	XRD.....	106
5.8	Thermal properties.....	108
5.8.1	DSC.....	108
5.8.2	TGA.....	110

CHAPTER 6: RESULTS AND DISCUSSION..... 112

Characterization of PSSE: System II- EC: PC variation

6.1	Chain relaxation time.....	112
6.1.1	Room temperature measurement.....	112
6.1.2	Temperature variation.....	113
6.2	Nyquist plot.....	114
6.2.1	Room temperature measurement.....	114
6.2.2	Temperature variation.....	116
6.3	Ion relaxation time.....	117
6.3.1	Room temperature measurement.....	117
6.3.2	Temperature variation.....	119
6.4	Frequency-dependent ionic conductivity.....	120
6.4.1	Room temperature measurement.....	120
6.4.2	Temperature variation.....	122
6.5	Ionic conductivity at room temperature.....	123
6.6	Conductivity-temperature dependence.....	125
6.7	XRD.....	128
6.8	Thermal properties.....	129
6.8.1	DSC.....	129
6.8.2	TGA.....	130

CHAPTER 7: RESULTS AND DISCUSSION..... 132

Characterization of PSSE: System III- SiO₂ variation

7.1	Chain relaxation time.....	132
7.1.1	Room temperature measurement.....	132
7.1.2	Temperature variation.....	133
7.2	Nyquist plot.....	134

7.2.1	Room temperature measurement.....	134
7.2.2	Temperature variation.....	136
7.3	Ion relaxation time.....	138
7.3.1	Room temperature measurement.....	138
7.3.2	Temperature variation.....	140
7.4	Frequency-dependent ionic conductivity.....	141
7.4.1	Room temperature measurement.....	141
7.4.2	Temperature variation.....	143
7.5	Ionic conductivity at room temperature.....	145
7.6	Conductivity-temperature dependence.....	148
7.7	XRD.....	152
7.8	Thermal properties.....	153
7.8.1	DSC.....	153
7.8.2	TGA.....	154
7.9	Summary of PSSE systems.....	156
CHAPTER 8: RESULTS AND DISCUSSION.....		157
<i>Electrochemical analysis of solid-state DSSC</i>		
8.1	NaI-PSSE system.....	157
8.2	SiO ₂ -PSSE system.....	159
8.3	Cell stability.....	161
CHAPTER 9: CONCLUSIONS, CHALLENGES & FUTURE RECOMMENDATIONS.....		162
9.1	Conclusions.....	162
9.2	Challenges.....	163
9.3	Future recommendation.....	164
REFERENCES.....		166

LIST OF PUBLICATIONS AND PAPER PRESENTED.....	182
APPENDIX.....	186

University of Malaya

LIST OF FIGURES

Figure 2.1	: Structure and working principle of a DSSC (O'Regan and Grätzel, 1991).....	9
Figure 2.2	: Lewis acid-base interaction between SiO ₂ NPs with salt and polymer chain (Wang and Alexandridis, 2016).....	14
Figure 2.3	: Hopping of ions <i>via</i> inter- and intra-chain hopping in SPE.....	26
Figure 2.4	: Self-ion diffusion in SPE.....	28
Figure 2.5	: Model representation of percolation pathway through the space charge layer of the neighboring SiO ₂ grains at the boundaries (Ramesh and Liew, 2012).....	29
Figure 2.6	: Chemical structure of MMA, BA and AA.....	37
Figure 3.1	: Experimental set-up for copolymer synthesis.....	43
Figure 3.2	: (a) Emulsion copolymer and (b) cast film.....	45
Figure 3.3	: Final assembly of solid-state DSSC.....	49
Figure 4.1	: Particle size distribution curve of (a) AA05, (b) AA20 and (c) AA30.....	55
Figure 4.2	: FTIR spectra of P(MMA- <i>co</i> -BA- <i>co</i> -AA) thin films and pure MMA.....	58
Figure 4.3	: ¹ H NMR of AA05 thin film measured at room temperature.....	60
Figure 4.4	: Monomer conversion of P(MMA- <i>co</i> -BA- <i>co</i> -AA) calculated from ¹ H NMR.....	61
Figure 4.5	: DTG curves of (a) AA05, (b) AA20, (c) AA30 and (d) AA40. The inset figure shows corresponding thermograms.....	63
Figure 4.6	: Experimental (■) and theoretical (---●---) <i>T</i> _g of P(MMA- <i>co</i> -BA- <i>co</i> -AA) calculated using Gordon-Taylor equation	65
Figure 4.7	: <i>R</i> _{sheet} and <i>R</i> _{volume} of P(MMA- <i>co</i> -BA- <i>co</i> -AA) measured at room temperature.....	66
Figure 4.8	: Tensile measurement of P(MMA- <i>co</i> -BA- <i>co</i> -AA) at room temperature.....	68
Figure 4.9	: FTIR spectra of non-irradiated and irradiated AA05.....	70
Figure 4.10	: Carbonyl index of AA05 at different irradiation time (dashed line is for visual aid).....	72

Figure 4.11	: Decomposed ester unit of AA05 at different irradiation time (dashed line is for visual aid).....	72
Figure 4.12	: UV-Vis-NIR absorption spectra of AA05 before and after UV irradiation.....	73
Figure 4.13	: Molecular weights of P(MMA- <i>co</i> -BA- <i>co</i> -AA) at different UV irradiation time. Symbols representation; ★/★: Non-irradiated sample, ▼ and ●: Irradiated samples (open symbol-crosslink structure and filled symbol-fragmentation). Dense region showed degraded samples.....	75
Figure 4.14	: AFM images of AA05 (a) before and after UV irradiation at (b) 120 min, (c) 240 min, and (d) 480 min.....	78
Figure 4.15	: Thermogram of AA05 before and after UV irradiation.....	79
Figure 5.1	: Chain relaxation time as the function of NaI content in NaI-PSSE.....	81
Figure 5.2	: Plot of $-Z''$ vs. f as the function of temperature for (a) NaI-5 (b) NaI-10, (c) NaI-15, (d), NaI-20, (e) NaI-25 [Note: The filled marker represents data below T_c], and (f) τ_{chain} of selected samples.....	82
Figure 5.3	: Nyquist plot of NaI-PSSE and its representative RC circuits: (a) NaI-5, (b) NaI-25, (c) NaI-10, (d) NaI-15, (e) NaI-20 and (f) NaI-30.....	85
Figure 5.4	: C_{dl} of NaI-PSSE at room temperature.....	86
Figure 5.5	: Nyquist plot of NaI-PSSE as function of temperature: (a) NaI-5, (b) NaI-10, (c) NaI-15, (d) NaI-20, (e) NaI-25; and (f) RC circuit representation [Legend: 30 °C (□), 40 °C (○), 50 °C (△), 60 °C (▽), 70 °C (◇), 80 °C (◁), 90 °C (▷) and 100 °C (⊙); filled marker represents the increasing resistivity trend, open marker represents the decreasing resistivity]	88
Figure 5.6	: Variation of $\tan \delta$ as the function of NaI content (results from selected trial).....	91
Figure 5.7	: Ion relaxation of NaI-PSSE at room temperature.....	91
Figure 5.8	: Loss tangent delta of NaI-PSSE as the function of temperature: (a) NaI-5, (b) NaI-10, (c) NaI-15 (d) NaI-20 and (e) NaI-25.....	93
Figure 5.9	: The frequency-dependent conductivity spectra of NaI-PSSE at room temperature.....	95

Figure 5.10	: The frequency-dependent conductivity spectra of NaI-PSSE at different temperatures: (a) NaI-5, (b) NaI-10, (c) NaI-15, (d) NaI-20 and (e) NaI-25.....	98
Figure 5.11	: Ionic conductivity of NaI-PSSE at room temperature.....	100
Figure 5.12	: Number of ions and ion diffusion coefficient of NaI-PSSE at room temperature.....	101
Figure 5.13	: Arrhenius plot of NaI-PSSE compositions: (a) NaI-5, (b) NaI-10, (c) NaI-15, (d) NaI-20, (e) NaI-25 and (f) NaI-30.....	102
Figure 5.14	: N_{ion} and D_{ion} of NaI-PSSE as the function of temperature: (a) NaI-5, (b) NaI-10, (c) NaI-15, (d) NaI-20 and (e) NaI-25.....	104
Figure 5.15	: XRD pattern of pure AA05 and NaI-PSSE thin films at room temperature.....	107
Figure 5.16	: DSC thermogram of NaI-PSSE with NaI content variation.....	109
Figure 5.17	: (a) DTG curve of pure AA05 and (b) T_d results of NaI-PSSE.....	111
Figure 6.1	: Chain relaxation time of EC: PC-PSSE at room temperature.....	112
Figure 6.2	: Plot of imaginary impedance against frequency for EC: PC-20 at different temperatures.....	113
Figure 6.3	: Nyquist plot of (a) NaI-15 and EC: PC-PSSE: (b) EC: PC-20, (c) EC: PC-30, (d) EC: PC-40 and (e) EC: PC-50.....	114
Figure 6.4	: C_{dl} of EC: PC-PSSE at room temperature.....	115
Figure 6.5	: Nyquist plot of (a) EC: PC-20 and (b) EC: PC-30 as the function of temperature [Legend: 30 °C (□), 40 °C (○), 50 °C (△), 60 °C (▽), 70 °C (◇), 80 °C (◁), 90 °C (▷) and 100 °C (◊)]......	116
Figure 6.6	: Dissipation tangent loss of EC: PC-PSSE as a function of frequency.....	118
Figure 6.7	: Ion relaxation time of EC: PC-PSSE at room temperature.....	118
Figure 6.8	: Plot of $\tan \delta$ vs. frequency of EC: PC-20 at different temperatures.....	120
Figure 6.9	: Frequency-dependent conductivity spectra of EC: PC-PSSE with different EC: PC contents.....	121
Figure 6.10	: Conductance spectra of (a) EC: PC-20 and (b) EC: PC-30 at different temperatures.....	123
Figure 6.11	: Ionic conductivity of EC: PC-PSSE at room temperature.....	124

Figure 6.12	: N_{ion} and D_{ion} of EC: PC-PSSE at room temperature.....	124
Figure 6.13	: Arrhenius plot of (a) NaI-15 (b) EC: PC-20 and (c) EC: PC-30.....	125
Figure 6.14	: N_{ion} and D_{ion} of (a) EC: PC-20 and (b) EC: PC-30 at different temperatures.....	126
Figure 6.15	: XRD pattern of EC: PC-PSSE containing different EC: PC contents.....	128
Figure 6.16	: DSC curves of EC: PC-PSSE at different EC: PC contents.....	129
Figure 6.17	: (a) DTG curve of pure AA05 and (b) T_d variation upon different EC: PC contents doping in NaI-15.....	131
Figure 7.1	: Chain relaxation time of SiO ₂ -PSSE at room temperature.....	132
Figure 7.2	: Changes in the chain relaxation time of SiO ₂ -PSSE: (a) SiO ₂ -2, (b) SiO ₂ -6 and (c) SiO ₂ -8 at temperature variation.....	134
Figure 7.3	: Nyquist plot of (a) NaI-15 and SiO ₂ -PSSE: (b) SiO ₂ -2, (c) SiO ₂ -4, (d) SiO ₂ -6, (e) SiO ₂ -8 and (f) SiO ₂ -10 with its RC circuit representation.....	135
Figure 7.4	: C_{dl} layer formation in SiO ₂ -PSSE at room temperature.....	135
Figure 7.5	: Nyquist plot of SiO ₂ -PSSE as the function of temperature: (a) SiO ₂ -2, (b) SiO ₂ -4, (c) SiO ₂ -6, (d) SiO ₂ -8, (e) SiO ₂ -10 and (f) RC circuit.....	137
Figure 7.6	: Tangent dissipation loss of SiO ₂ -PSSE at room temperature.....	139
Figure 7.7	: Ion relaxation time calculated as the function of SiO ₂ content.....	139
Figure 7.8	: Tangent dissipation loss of SiO ₂ -PSSE: (a) SiO ₂ -2, (b) SiO ₂ -6 and (c) SiO ₂ -8 at different temperatures.....	140
Figure 7.9	: Frequency-dependent ionic conductivity of SiO ₂ -PSSE at room temperature.....	142
Figure 7.10	: Conductance spectra of SiO ₂ -PSSE as the function of temperature: (a) SiO ₂ -2, (b) SiO ₂ -4, (c) SiO ₂ -6, (d) SiO ₂ -8 and (e) SiO ₂ -10.....	143
Figure 7.11	: Ionic conductivity variation as the function of SiO ₂ content.....	146
Figure 7.12	: N_{ion} and D_{ion} for SiO ₂ -PSSE calculated using Nernst-Einstein equation.....	146
Figure 7.13	: Arrhenius plot of (a) NaI-15 and SiO ₂ -PSSE: (b) SiO ₂ -2, (c) SiO ₂ -4, (d) SiO ₂ -6, (e) SiO ₂ -8 and (f) SiO ₂ -10.....	149

Figure 7.14	: N_{ion} and D_{ion} calculated in variation of temperature for SiO ₂ -PSSE: (a) SiO ₂ -2, (b) SiO ₂ -6 and (c) SiO ₂ -8.....	150
Figure 7.15	: XRD diffractogram of NaI-15 with SiO ₂ NPs doping (inset figure shows the XRD pattern of pure SiO ₂ NPs).....	153
Figure 7.16	: DSC thermogram of SiO ₂ -PSSE containing different SiO ₂ NPs.....	154
Figure 7.17	: (a) DTG curve of pure AA05 and (b) TGA data of SiO ₂ -PSSE.....	155
Figure 8.1	: J - V curve of solid-state DSSC fabricated with NaI-15.....	158
Figure 8.2	: J - V curve of solid-state DSSC fabricated with SiO ₂ -2.....	160
Figure 8.3	: Figure 8.3: Normalized light-to-electricity conversion efficiency of the cell versus conservation time under 60 °C.....	161

University of Malaya

LIST OF TABLES

Table 1.1	: Comparison between solid-state DSSC and perovskites.....	4
Table 2.1	: List of UHMW polymers.....	31
Table 3.1	: Monomer compositions for P(MMA- <i>co</i> -BA- <i>co</i> -AA) synthesis.....	44
Table 3.2	: Chemical compositions of three solution mixtures; (1) Initial charge solution, (2) Delayed monomer solution and (3) Catalyst solution.....	44
Table 3.3	: Formulation of PSSE systems.....	46
Table 4.1	: TSC and monomer conversion of P(MMA- <i>co</i> -BA- <i>co</i> -AA) determined using gravimetric method.....	56
Table 4.2	: Solubility test of P(MMA- <i>co</i> -BA- <i>co</i> -AA) in different solvents.....	57
Table 4.3	: FTIR absorption peaks of P(MMA- <i>co</i> -BA- <i>co</i> -AA).....	59
Table 4.4	: ¹ H NMR chemical shifts of AA05.....	60
Table 4.5	: Average molecular weights of synthesized P(MMA- <i>co</i> -BA- <i>co</i> -AA).....	62
Table 4.6	: Chromaticity data for AA05 as the function of irradiation time.....	76
Table 8.1	: Photovoltaic parameters of solid-state DSSCs assembled with NaI-PSSEs.....	158
Table 8.2	: Photovoltaic parameters of solid-state DSSCs assembled with SiO ₂ -PSSEs.....	160

LIST OF SYMBOLS AND ABBREVIATIONS

E_a	activation energy
σ	conductivity
T_c	critical temperature
T_d	decomposition temperature
C_{dl}	double layer capacitance
η	efficiency
R_{Ω}	electrolyte resistance
$T_{enthalpic}$	enthalpic relaxation
f	frequency
f_0	frequency at which stable conducting network forms
T_g	glass transition temperature
R_{ct}	interfacial charge-transfer resistance
D_{ion}	ion diffusion
N_{ion}	number of ion
V_{oc}	open circuit voltage
J_{sc}	photocurrent
n	power law exponent
τ	relaxation time
s	scattering function
\square	square
ζ	zeta potential
C	capacitance
C.I	carbonyl index

DSSC	dye-sensitized solar cell
EP	electrode polarization
FF	fill factor
PSSE	polymeric solid state electrolytes
R	resistance
TSC	total solid content
W	Warburg impedance

University of Malaya

LIST OF APPENDICES

Appendix A	:	Reaction Mechanism of P(MMA-<i>co</i>-BA-<i>co</i>-AA).....	186
Figure A.1	:	Capturing of radicals by a particle in homogeneous nucleation.....	186
Figure A.2	:	Propagation stage of UHMW P(MMA- <i>co</i> -BA- <i>co</i> -AA).....	187
Figure A.3	:	Chemical structure of UHMW P(MMA- <i>co</i> -BA- <i>co</i> -AA).....	188
Appendix B	:	¹H NMR Spectrum of AA20, AA30 and AA40 (In DMSO).....	189
Appendix C	:	¹³C and Dept-135 NMR Spectrum of AA05 Thin Film Measured at Room Temperature.....	190
Table C.1	:	¹³ C and DEPTH-135 NMR data of P(MMA- <i>co</i> -BA- <i>co</i> -AA).....	191
Appendix D	:	Photo-Degradation Mechanism of AA05.....	192
Appendix E	:	Plot of $Z'/-Z''$ against Frequency for (a) NaI-5, (b) NaI-10, (c) NaI-15, (d) NaI-20, (e) NaI-25 and (f) NaI-30.....	193
Appendix F	:	Nyquist Plot of NaI-20 with Labeled Physical Parameters.....	194
Appendix G	:	Plot of $Z'/-Z''$ against Frequency for (a) NaI-15 and EC: PC-PSSE: (b) EC: PC-20, (c) EC: PC-30 and (d) EC: PC-40.....	195
Appendix H	:	Plot of $Z'/-Z''$ against Frequency for (a) NaI-15 and SiO₂-PSSE: (b) SiO₂-2 and (c) SiO₂-8.....	196

CHAPTER 1: INTRODUCTION

1.1 Overview

The conquest for renewable and green energy has led to significant discovery of technologies that are capable of converting natural resources (*e.g.* wind, water and solar) into electricity. Among the many natural resources, solar energy has a huge demand in the worldwide electricity supply owing to its abundance. This has been quantified in the United Nations Development Programme as 1,575-49,837 EJ per annum during 2000 World Energy Assessment. The reported value was several times higher to that in used (559.8 EJ in 2012) (Goldemberg *et al.*, 2000; Millar, 2017). Other benefits such as clean, powerful and high affordability make the solar energy a reliable resource for long term usage.

To make use of solar power, a special technology called photovoltaic (PV) was developed. The development of PV began with a classical silicon (Si) cell (1st generation), *e.g.* semiconductor wafer-based Si PV technologies. This is the most established technology that grants robust innovation. Currently in the industrial scale, this PV module yields efficiency exceeding 24 % (Blakers *et al.*, 2013) and is expected to reach more than 45 % in future development (Grätzel, 2006; Fantechi, 2011). Despite its success story, the high manufacturing cost and complexity of process limit its utilization.

For the PV to be practically useful and commercially reliable, it needs to be affordable, highly efficient and stable. This has led to the development of PV cells based on thin film (2nd generation). The next development is the third generation hybrid cells that are made of either organic (*i.e.* DSSC or quasi-DSSC) or inorganic materials (*i.e.* perovskites). Among the hybrid cells, organic-hybrid is the most appealing innovation due to its simplicity in technology and cost efficient. In the organic-hybrid

cells, solar energy is converted to electricity during photo-electrochemical reaction by a combination process of light absorption by a sensitizer-dye (which behaves similarly to chlorophyll) and charge separation by the thin film oxide semiconductor (Nwanya *et al.*, 2011). The DSSC technology has gained huge acceptance in industry owing to its competent benefits such as (i) low manufacturing cost, (ii) high volume production using roll-to-roll processing, (iii) ability to perform well in diverse light conditions such as high angle of incidence, low intensity and partial shadowing, and (iv) lightweight, flexible and semi-transparent.

During the initial DSSC development, the pioneer focused on cell fabrication using organic solvent-based electrolytes [or liquid electrolytes (LE)]. In the last two decades, the development has progressed with the highest cell efficiency from ~7 % to 14 % (Lee *et al.*, 2017). The use of this cell in practical application, however, is still limited by the poor durability over time and temperature. This is associated to the liquid state of electrolyte that leads to volatilization (which induce to iodine decomposition), leakage and corrosion at the counter electrode (Hsu *et al.*, 2014). Another challenge of LE from the industrial point-of-view is the temperature-sensitivity of the cell (Luk, 2010). At low temperatures, the LE can freeze while at high temperatures the liquid may expand and offsets the sealing of solar panels.

Since the drawbacks of liquid-cell assembly are caused by the free-flowing liquid, polymer can be incorporated to suppress the flowing tendency. Two types of solvent-free membrane, also known as solid polymer electrolytes (SPE), have been developed from this approach such as GPE and PSSE. The utilization of GPE is a promising alternative, especially when the chemically-crosslink GPE is used. This has been experimentally proven based on the comparatively similar cell performance to that of liquid assembly. The good performance could be resulted from the liquid-like ion

transportation in the gel network structure. Nevertheless, the low stability over time and poor electrolyte contact with sensitizer-dye still remains as a challenge. The size difference between the polymer coil and the pore of semiconductor (photoanode) explains the scenario (Song *et al.*, 2014). For GPE with physically-crosslink structure, a better contact with sensitized-dye molecules could be achieved but the occurrence of phase separation at high temperature and long-term storage had further raised the instability issue in DSSC performance (Vasquez, 2007; Wu, 2015).

In search for better solutions, research has been directed towards PSSE development. The difference between GPE and PSSE lies with the liquid content; GPE is formed by polymer entrapping large amounts of plasticizers during its dissolution process, *i.e.* plasticizer is used as polymer solvent, while in PSSE the amount of plasticizer is very low, *i.e.* plasticizers is used as an additive rather than dissolving solvent. This PSSE thin film technology offers flexibility and high safety guard from the absence of mobile liquid. Although PSSE based-DSSC features a number of technical advantages over gel and liquid cells, the photoelectric conversion efficiency of the cell is far too low for commercialization. At present, the cell assembled from PSSE with absence of any low molecular weight substances has never exceeded efficiency above 1 % under 1 Sun. The low cell performance arises from the poor liquid-like ion motion that is caused by the low segmental dynamics. Moreover, this cell assembly also suffers from intense charge recombination effect due to the poor electrolyte wetting with sensitized-dye molecules.

To tackle the above-mentioned limitations, several attempts to improve the performance and stability of solid-state DSSC, particularly for GPE, have been considered, *i.e.* in-situ growing of the polymer chain inside the semi-conductor mesopores (Farrell, 2014) and incorporation of oligomers into SPE (Nagarajan *et al.*, 2013; Chae *et al.*, 2014). Typically, these approaches were adopted to improve the ion

diffusion and electrolyte wetting with photoanode. Although the cell from this assembly exhibits good efficiency, the effect from charge recombination could not be completely suppressed. Bella and his coworkers (2013) claimed that the phenomenon was originated from the poor control of in-situ polymerization of oligomers in the presence of redox couple (e.g. I^-/I_3^-) (Bella *et al.*, 2013). The poor control of polymerization yields limited electrode-electrolyte contact and unwanted secondary reaction. As for that, direct utilization of PSSE film in its original form for solid-state DSSC assembly is much preferred.

For perovskite cells, their performances ($\eta = \sim 22\%$) have overruled the capability of advanced DSSC (Tang *et al.*, 2017). Yet, companies like Sony, Dyesol and SunPower are still actively working on perfecting the work function of solid-state DSSC through optimization of dye molecules, photoanodes and electrolytes. A comparison between solid-state DSSC and perovskites is summarized in Table 1.1.

Table 1.1: Comparison between solid-state DSSC and perovskites

Criteria	Solid-state DSSC	Perovskites
Manufacturing cost	Low	High (e.g. gold is used as electrode material. Cheaper cells have low life span)
Toxicity	No	High toxic (e.g. lead and breakdown products of PbI are carcinogenic)
Production volume	High	-not applicable-
Wavelength of lights	Vary between dyes (e.g. for N-719 ~ 290–700 nm)	Can react to various different wavelengths of light
Flexibility		Yes
Transparency		Semi-transparent
Light-weight		Yes

In general, solid-state DSSC offers greater benefits over perovskites. The perovskites cell with the current technology utilizes small cell, which is great for lab testing but the practical implication for actual solar panel is still far from reality. For this very reason, solid-state DSSC research is still an area of interest that can be pushed forward to overcome the current limitations.

1.2 Problem statement

Solid-state DSSC that is fabricated using PSSE without any inclusion of oligomers usually results in poor cell performance. Typically, the efficiencies may range between 1-5 % under 10 mW cm^{-2} illuminations (Nogueira *et al.*, 2001; Haque *et al.*, 2003; Kim *et al.*, 2005). The issues with this cell assembly are the poor electrolyte wetting with sensitized-oxide semiconductor (substantially with the sensitizer-dye molecules) and restrictive liquid-like ion transport. These are the common issues of PSSE that are developed from conventional polymers with hundreds of thousands of molecular weights. It has been a practice to perform solid-state DSSC assembling at $50 \text{ }^\circ\text{C}$ in order to improve the interfacial contact between electrode and electrolyte. However when the DSSC working temperature is brought down to $25 \text{ }^\circ\text{C}$, the polymer chains lose their dynamics and re-arrange themselves close to their original state (chain repacking). These changes cause reduction in the liquid-like ion transport and consequently lower the device performance. The coupling between ion motion and chain dynamics is the root cause for deterioration of cell performance below the DSSC assembling temperature. The decoupling between these two entities could solve the problem. This approach has been tested on rigid polymers but due to the high resistance in segmental mobility (higher T_g), the alternative was excluded.

1.3 Highlight of research

In this study, the conventional polymers of high molecular weight were substituted with UHMW polymer. Undoubtedly, the polymer loses its chain dynamic when the molecular weight increases, and this is unfavorable to allow disentangling or chain alignment. This characteristic resembles the nature of UHMW polymer with high T_g . Well tuning of the UHMW polymer in such a way that it possesses low T_g can suppress the drawbacks but not entirely. This could be appealing for electrolyte development as frustration in the chain repacking may occur when the temperature of electrolyte that has been heated up above its T_g is cooled. This offers high free volume for better ion transportation.

In this work, the T_g of UHMW polymer is decreased by copolymerizing with butyl acrylate (BA) (Fernández-García *et al.*, 2001), at the same time intended to increase the process-ability of the polymer. As the coil size of UHMW polymer should be greater than that of the conventional polymers, therefore no chain penetration into the semiconductor meso-pores is expected. A better approach to this is by using rubbery-PSSE for cell assembly. The soft-elastic-adhesive characteristic film may give good adherence to the electrode and subsequently achieves good interfacial contact with the dye molecules that are sensitized on the surface of mesoporous layer.

1.4 Motivation of study

This research is an extended study of the intellectual property that had been filed in Ramesh *et al.*, 2013. The claim was based on the existence of mechanical bonding between the soft and adhesive film of salt doped UHMW P(MMA-co-BA-co-AA) and poly(tetrafluoroethylene). A method to remove this soft and sticky film from poly(tetrafluoroethylene) without losing its mechanical integrity was also reported in the patented work. When this PSSE was tested for battery application, the soft and sticky

properties of the film form an intact interfacial contact with the electrode. This depicts good electrolyte wetting. Moreover, the assembly also has illustrated some appealing preliminary test measurements in terms of the battery performance (for PSSE conductivity of 10^{-5} S cm^{-1}), stability and thermal-shut down at 50 °C (reversible process). The good electrolyte wetting (*via* mechanical bonding) perhaps could contribute to the battery performance. Thus, similar host polymer was used to prepare the PSSE for solid-state DSSC that demands for good electrolyte wetting.

1.5 Aim and objectives

The aim of this research was to study the cell conversion efficiency and stability of solid-state DSSC that had been assembled using PSSE containing UHMW P(MMA-*co*-BA-*co*-AA) as the host polymer matrix. In order to accomplish this, a set of objectives was drafted such as:

- 1) To optimize the synthesis of P(MMA-*co*-BA-*co*-AA). This will be done by varying the reacting ratio of MMA: AA. The optimized copolymer will be identified based on its physical, chemical and thermal properties.
- 2) To develop PSSE using the optimized UHMW P(MMA-*co*-BA-*co*-AA) formulation. Additives such as NaI, EC: PC and SiO₂ will be varied and the bulk properties will be characterized in order to understand the structural, ionic conductivity, dielectric and thermal behaviors.
- 3) To evaluate the photovoltaic performance of solid-state DSSC.

1.6 Scope of thesis

A brief introduction on solid-state DSSC, in particular of the SPE development has been discussed in Chapter 1. The details are further elaborated in Chapter 2 with precise literature surveys. Relevant studies on UHMW polymer, polymerization technique and

characteristics of iodide-PSSE (*e.g.* ions nature, structure, ion transport mode, *etc.*) are enclosed. Chapter 3 presents the experimental method for copolymer synthesis and PSSE formulations including their measurement techniques. The experimental design for DSSC assembling and its testing method are also reported in this chapter. The results from the experiments performed are reported from Chapter 4 to Chapter 8. To further elaborate, Chapter 4 includes characterizations of the entire formulated copolymers. The characteristic of well-suited copolymer doped with NaI is discussed in Chapter 5. Further optimization of the best performing NaI-PSSE in variation of EC: PC and SiO₂ NPs are discussed in Chapter 6 and Chapter 7, respectively. The photo-electrochemical performance of solid-state DSSC is presented in Chapter 8. Chapter 9 summarizes our findings and future recommendation.

CHAPTER 2: LITERATURE REVIEW

2.1 Solid-state DSSC: History and limitations

Solid-state DSSC is a photovoltaic cell that uses solvent-free membrane as replacement for liquid electrolyte (LE). The cell assembly and working principle of solid-state DSSC is similar to the liquid cell, as depicted in Figure 2.1 (Rahman *et al.*, 2014). The difference lies in the method of safe guarding the mobile liquid.

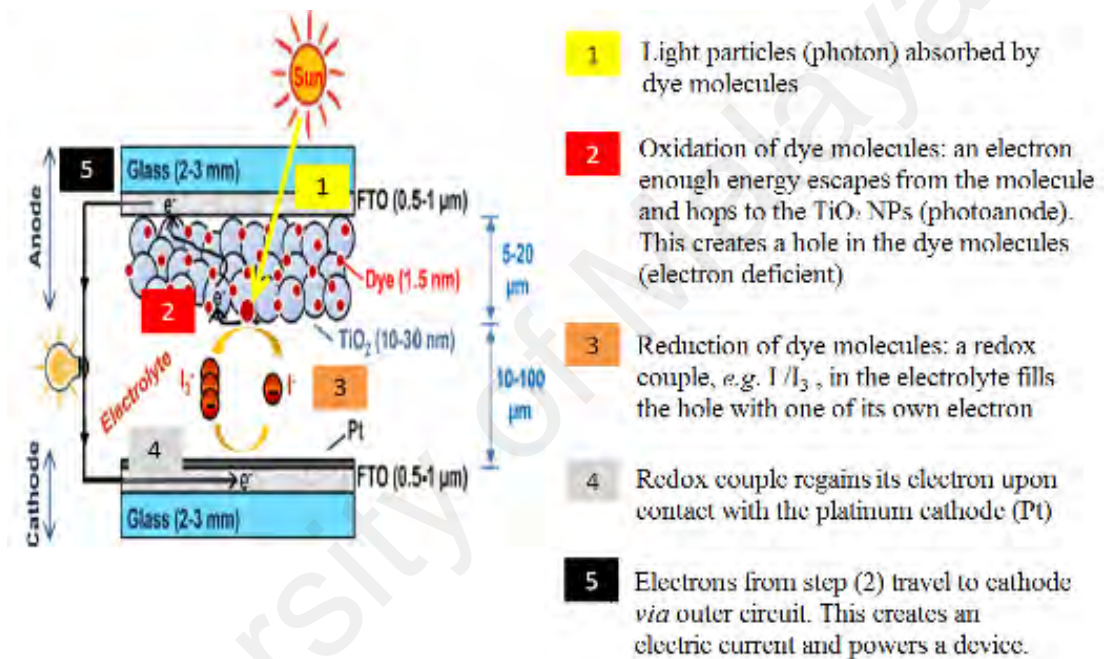


Figure 2.1: Structure and working principle of a DSSC (O'Regan and Grätzel, 1991)

Typically, the SPE is formulated by either re-precipitating the polymer (*i.e.* PPSE) or entrapping LE into polymer (*i.e.* GPE). The choice of polymer determines the physical nature of polymer electrolyte whether it is gel-like or solid (plastic) [also known as PSSE or quasi-solid (plastic) electrolyte]. The difference lies between the liquid compatibility of polymer with LE. Polymers with high compatibility with LE form GPE upon casting (Zhao *et al.*, 2012), while PSSE is formed at partial compatibility between

polymer and LE (Song *et al.*, 1999). In the absence of free-flowing liquid, both phases give better merit to cell safety and stability over liquid assembly.

Despite so, PSSE shows better physical stability over the gel-type. There were cases where liquids were reported to leach out from GPE when the network structure collapsed. This usually occurs in GPE with physically-crosslink gel structure. However, no such consideration needs to be taken into account when PSSE is used. Unfortunately, the poor electrolyte wetting and low ion diffusion in PSSE limit the cell efficiency (Gray and Connor, 1997; Stephan and Nahm, 2006). Poor light-soaking effect is another challenge for this assembly, in which the exhaustion in cell efficiency occurs under intense light. To tackle these limitations, combination techniques that were discussed hereafter are adopted to improve the ionic conductivity and interfacial contact between the electrolyte and electrode of PSSE. The reviews are not only limited to PSSE but also it covers GPE.

2.1.1 Acceleration of ionic conductivity

The basic requirement to obtain high efficient solid-state DSSC is by utilizing SPE with high iodide-ionic conductivity. This is crucial in order to generate high cell photocurrent (Dissanayake *et al.*, 2012). The preferred conductivity range for SPE is from 10^{-4} to 10^{-3} S cm^{-1} ; however SPE with conductivity equivalent to 10^{-5} S cm^{-1} may have good practicability in application development (Fenton *et al.*, 1973). The ionic conductivity (σ) is strongly influenced by two factors such as number of ion (N_{ion}) and ion mobility (μ_{ion}). The mathematical expression is shown below:

$$\sigma = \sum_{\text{ion}} q_{\text{ion}} N_{\text{ion}} \mu_{\text{ion}} \quad (2.1)$$

where, q_{ion} is the charge magnitude

The term “ions” defines dissociated iodide salts (or free ion). The commonly used iodide salts for DSSC application are sodium iodide (NaI), ammonium iodide (NH₄I) and lithium iodide (LiI). Any circumstances that devalue either of the factors mentioned-above in polymer-salt complex may cause a drop in DSSC photocurrent [including the cells open-circuit voltage (V_{oc}) and fill factor (FF)] and cell efficiency.

Polymer-salt complex generally exhibits ionic conductivity in the range of 10^{-6} to 10^{-5} S cm⁻¹ at room temperature. This conductivity range was reported to be low for practical application as the assembly fabricated using this complex matrix recorded cell efficiency lower than 1 % under 1 Sun (Singh *et al.*, 2013). Similar exhaustion of cell performance was reported by Singh and coworkers (2015) for polymer-salt complex with conductivity order ranging from 10^{-3} to 10^{-4} S cm⁻¹ (Singh *et al.*, 2015). The assembly was performed with iodine complex of poly(vinylpyrrolidone) and potassium iodide (KI). Another cell assembly based on carboxymethyl kappa-carrageenan/carboxymethyl cellulose complex with ammonium iodide was also reported (Rudhziah *et al.*, 2015).

The underline cause to the poor cell performance is low chain dynamics, which impede liquid-like ion motion. This may obstruct efficient ion transport to complete the redox cycle and consequently affects the dye-regeneration process. Another limiting factor of polymer-salt complex is the occurrence of ions association, which is best known as salt re-crystallization. This can significantly reduce the number of hopping ions and cause a drop in the cell performance. To overcome these limitations, the polymer-salt complex is generally plasticized either with low molecular weight substances such as liquid plasticizers or with fillers that act as solid plasticizer in order to improve the polymer electrolytes bulk properties.

Plasticization generally improves the ionic conductivity of SPE by increasing ion dissolution (which minimizes the ion association) and its transportation *via* increasing chain dynamics. The incorporation of other substances, *e.g.* oligomers, ionic liquid (IL) and nanotubes can also efficiently improve the ionic conductivity. In the following section, only the details of liquid plasticization and filler incorporation are discussed.

2.1.1.1 Liquid plasticization

Liquid plasticization is the most common adopted method to tailor the polymer chain flexibility in SPE to yield good ionic conductivity. Some examples of low molecular weight liquid plasticizers from the class of cyclic carbonic acid ester and chain-like esters are EC, PC, dimethyl carbonate and diethyl carbonate. Plasticization using the mixture of these is preferred.

There are several models to describe the plasticization behavior of polymer, *e.g.* free volume, lubricity, gel and mechanistic theory (Pandey *et al.*, 2013). To understand the chain dynamics in plasticized-SPE, the free volume theory is of particular importance. In this theory, the penetration of plasticizer molecules into polymer chains suppresses the cohesive bonds or intermolecular attraction (Entwistle and Rowe, 1979; Barenswaard *et al.*, 1999). The reduced cohesive force can be observed from the reduction of T_g . This creates randomness in chain ordering (increase amorphous nature) and further improves the segmental dynamics, chain slippage and free volume between the end-chains. All these improvements allow more interstitial vacant sites to be available to facilitate the ion transport and consequently enhance the photocurrent and efficiency of solid-state DSSC. Nevertheless, the enhancement is still far below the required efficiency for commercialization.

A better cell efficiency could be obtained with addition of additives such as composite and oligomers. Although higher loading of plasticizer molecules may result in a very high ionic conductivity, no better efficiency was ever recorded. This is limited by the deterioration of SPE mechanical stability, which is too soft to form high resilient separator. The typical composition range of plasticizer used is 10-15 wt.%. Anything above this may just halt the SPE performance.

Apart from plasticizer concentration, the choice of plasticizer gives significant effect to the enhancement of SPE bulk properties. The plasticizer shall be chosen based on the physical properties, such as

- 1) high dielectric constant, which may give good suppression to ion association
- 2) low liquid viscosity (high flowing consistency), which allows easier liquid penetration in between the chain-ends
- 3) low melting point, so that it remains in liquid state (no crystallization) at wide temperature range
- 4) high evaporation temperature (or flash point) is crucial to minimize its volatilization from the matrix. For instance, common plasticizers such as EC, PC or their mixtures may dissipate from SPE matrix close to the dehydration temperature (~ 150 °C). Therefore, the assembling and operation temperature of device should be below the flash point of this plasticizers in order to have stable device functioning.

2.1.1.2 Composite addition

Another well-known approach to increase the ionic conductivity of SPE is through incorporation of fillers [*e.g.* nanoparticles (NPs)]. This type of formulation is categorized under composite polymer electrolytes (CPE). The improvement of ionic

conductivity in CPE is attributed to the enlargement of amorphous phase upon suppression of polymer crystallinity (Stergiopoulos *et al.*, 2002 and Zhou *et al.*, 2009). Polymer chains lose their chain ordering as the subsequent weakening of intermolecular polymer bonds when NPs form Lewis acid-base interaction with the polymer chain. Consequently, the free volume between interfaces of NPs and polymer chain enhances; this allows more amorphous phase to be present. Similar interaction can be observed between the NPs and anions of the metal salt. This interaction increases salt dissociation (Knauth and Schoonman, 2007) upon weakening of Coulombic interaction in salt molecules. The graphical representation of Lewis acid-base interaction in CPE is depicted in Figure 2.2.

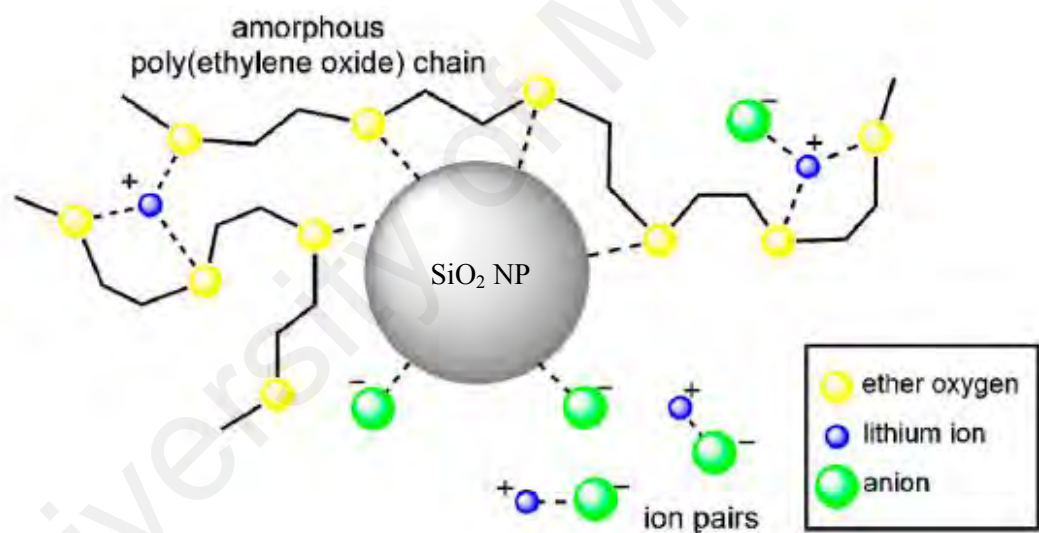


Figure 2.2: Lewis acid-base interaction between SiO₂ NPs with salt and polymer chain (Wang and Alexandridis, 2016)

The Lewis acid-base interaction between NPs and polymer chain may not necessary form at all time. In some cases, the NPs bond with their neighboring particles through oxygen bridge and form non-bonded complex. Yet, improvement in ionic conductivity is still observed in CPE due to the good ion tunneling. This is resulted from the overlapping of space charge in NPs which provides additional pathway for ion transport

as reported by Vrentas and Duda (1977). Similar mode of ion transportation is seen in CPE bonded complex structure where Lewis acid-base interaction forms between NPs and polymer chains. This mode of ion transportation is favorable compared to the ion motion mediated by segmental-assisted motion. Correlating to that, high diffusion of I^-/I_3^- redox couple was detected when NPs were incorporated into PEO-based electrolytes. This synchronically increases the CPE ionic conductivity and enables the solid-state DSSC with high cell performance to be produced.

In Nogueira's pioneering work, a cell performance of 1.6 % under 1 Sun was reported for polymer electrolytes with conductivity of $1.5 \times 10^{-5} \Omega \text{ cm}^{-1}$ at 30 °C (photocurrent, $J_{sc} = 4.2 \text{ mA cm}^{-2}$) (Nogueira *et al.*, 2001). In the following year, Falaras and coworkers (2002) reported two fold enhancement in the cell efficiency ($\eta = 4.2 \%$ under 65 mW cm^{-2} , $J_{sc} = 7.2 \text{ mA cm}^{-2}$) as compared to that of Nogueira's pioneering work. This cell was assembled with poly(ethylene oxide)/TiO₂ and LiI/I₂ as polymer electrolytes (Stergiopoulos *et al.*, 2002). The increase of cell efficiency was reported to be due to the increase of cell photocurrent. In another work by the same group, a lower cell efficiency of 0.97 % ($J_{sc} = 2.05 \text{ mA cm}^{-2}$) was recorded for similar polymer electrolyte assembly (Katsaros *et al.*, 2002). Increment in the cell photocurrent is mainly influenced by ionic conductivity of polymer electrolytes. High ionic conductivity polymer electrolyte may yield high photocurrent (also known as current density) and *vice versa*. The innovation progresses with years and many researchers have incorporated filler NPs in SPE formulations for the purpose of ionic conductivity enhancement.

Common fillers used in CPE for DSSC fabrications are fumed silica (SiO₂), alumina (Al₂O₃), titanium oxide (TiO₂), *etc.* Among the many types of fillers available, only the SiO₂ and TiO₂ NPs are widely used as solid plasticizer. They have shown good prospect

in device performance. Generally, the cells that were developed from CPE matrix shows efficiency ranging from 4-8 % at 100 mW cm^{-2} . Although these CPE have inclusion of either oligomers or chemicals that suppresses the electron recombination (e.g. MPII), or even with different hosting polymer matrix, the good cell performance can arise from the filler incorporation. This conclusion was highlighted in the work published by Stathatos and coworkers (2001), which reported a remarkable improvement in DSSC efficiency up to 4.50 % at 100 mW cm^{-2} by doping PEG200/KI/I₂ mixture with SiO₂ NPs. Similar observation was reported by Stergiopoulos and coworkers (2002), who recorded 4.20 % cell efficiency at 65.6 mW cm^{-2} for the assembly fabricated with CPE containing TiO₂ NPs in PEO/LiI/I₂. All the recorded improvement in cell efficiency corresponds to the increase of ionic conductivity and good interfacial contact between the electrolyte and electrode. Higher cell performance was also reported with the utilization of electrically conducting composite materials such as carbon nanotube, activated carbon and graphene. This alternative is appealing as the architecture of these materials gives fast ion diffusion due to their high surface areas.

Other benefits of incorporating NPs are (i) light scattering effect at utilization of NPs with size over 100 nm (Kang *et al.*, 2008), (ii) chemical effect of NPs in controlling the local concentration of the ionic species (Chae *et al.*, 2014) and (iii) mechanical strength, which is crucial to improve the film forming ability in plasticized matrix. All these combinations allow high efficient and stable DSSC to be developed. Instead of using bare NPs, the functionalization of its surface, which is typically done using IL, was reported to show better cell performance and stability (Hu *et al.*, 2014). The effectiveness can be rationalized by the high compatibility of IL-functionalized NPs with polymer. Other factors to consider when choosing the appropriate NPs are size, shape and composition. These factors may significantly affect the bulk properties of SPE.

2.1.2 Wetting properties

As mentioned before, one of the factors that limit efficient solid-state DSSC fabrication utilizing SPE is the poor interfacial contact between electrolyte and photoanode (specifically refers to dye-molecules). The non-fluidic SPE cannot penetrate into mesoporous TiO₂ layer (photoanode) due to the huge difference between size of polymer chain diameter (or coil size in a given solvent) and TiO₂ pore (Kang *et al.*, 2007). Commonly, two ranges of TiO₂ mesopore sizes are used; one having pore size in nanoscale [*i.e.* 15 to 20 nm depending on the nature of TiO₂ (*e.g.* rutile, anatase, brookite) (Song *et al.*, 2014)] and another exists in microscale. Both the sizes typically have diameter smaller than that of polymer coil size in solution. Hence, the polymer coils are not able to penetrate into the mesopores and this substantially minimizes the SPE contact with sensitizer-dye. As the result, this impedes the dye regeneration process and raises the charge recombination effect and results in a decrease of cell photocurrent (also the V_{oc} and FF). In fluidic system (or LE), such drawback is minimal. This is because the liquid can readily penetrate into the TiO₂ pore and form a good contact with dye molecules. The optimization of interfacial contact between the non-fluidic SPE and dye molecules is summarized in the following sections.

2.1.2.1 TiO₂ modification

The easiest way to improve the electrolyte wetting with TiO₂ layer is by increasing the pore size of TiO₂. Pore size can be enlarged using one-dimensional photoanode structures with high surface area such as nanowire (Law *et al.*, 2005), nanorod (Song *et al.*, 2005), nanofiber (Song *et al.*, 2004) and nanotube (Flores *et al.*, 2007). So far, this alternative had not been focused in cell assembly with SPE. In the case of GPE-cell, the utilization of TiO₂ materials in the form of nanofiber (4.6 % efficiency) (Song *et al.*, 2004) or nanotube (4.03 %) (Flores *et al.*, 2007) has shown enhancement in the cell

performance as compared to the TiO₂ NPs-based assemblies. Ahn and coworkers (2010) reported a better cell design utilizing a well-organized mesopore TiO₂ films (Ahn *et al.*, 2010). The excellent channel connectivity was developed *via* the sol–gel process using an organized poly(vinyl chloride)-*g*-(oxyethylene methacrylate) graft copolymer. The utilization of this material in device fabrication has proved that well-organized TiO₂ is better in efficiency than randomly oriented TiO₂ pore size.

Although the above-mentioned alternatives help in optimizing the electrolyte contact with dye molecules, enlargement of TiO₂ pore size may significantly lower the surface area for dye adsorption and result in photocurrent loss. A hierarchical photoanode formed from aggregation of many small nanoparticles (with sizes of 9.1 nm) becomes very attractive as it offers large pore size for electrolyte penetration as well as large surface area for dye adsorption (Kim *et al.*, 2009). The high concentration of dye molecules on the surface enables the cell to be effective in collecting incident light while the enlarged pores provide additional light scattering effect. Other photoanode structures based on the mixtures of small and large NPs, inverse opal, hollow sphere, scattering spherical void and 3D photoanodes have been developed to improve the pore-filling of SPE into TiO₂ pores.

2.1.2.2 Liquid oligomers incorporation

Apart from TiO₂ modification, the SPE wetting with dye molecules can be improved using “Oligomer Approach”. In this approach, liquid oligomers with coil size less than 3 nm are penetrated into the mesopores of photoanode in order to have contact with the dye molecules. Substantially, the liquid is solidified and form SPE either through formation of multiple hydrogen bonds, NPs incorporation or with polymer matrix. The typically used oligomers in this approach has the molecular weights ranging from 250 to 1000 g mol⁻¹, such as poly(ethylene glycol), oligo-PEG, and poly(propylene glycol),

oligo-PPG. Oligomers in this range of molecular weights have coil size of 1-3 nm depending on the dissolving solvent (Kim *et al.*, 2004; Jeon *et al.*, 2010). As the coil size is smaller than the mesopore size, the oligomers may readily penetrate into the mesopore and forms good contact with dye molecules. This significantly suppresses the charge recombination at the interface of electrode-electrolyte and improves the dye-regeneration process.

The success of this approach was reported by Kim and coworkers (2004). The developed cell exhibited efficiencies of 4.59 % and 3.34 % under the illumination of 42.9 and 100 mW cm⁻², respectively, utilizing oligo-PEG ($M_w=1000$ g mol⁻¹) (Kim *et al.*, 2004). Although the light soaking effect (*i.e.* charge recombination) was observed for this cell assembly, the extent of performance drop is considered low compared to the cell with absence of oligomers. To suppress the charge recombination effect, the authors had performed different oligomer solidification approach. In the former finding, oligo-PEG was solidified *via* quadruple hydrogen bond between TiO₂ mesopores. In the latter work, the oligomer was separately solidified using silica NPs and solid polymer, respectively. This approach increased the cell efficiency up to 4.50 % and 4.42 % under 100 mW cm⁻² using silica NPs and solid polymer, respectively.

Apart from efficient pore-filling, the incorporation of oligomers may also enhance the electrolytes bulk conductivity. As reported by Kang and coworkers (2005), the conductivity enhanced nearly 14-fold higher than that of a pure PEO at room temperature for the complex of PEO-doped oligo-PEG (2.57×10^{-5} S cm⁻¹) (Kang *et al.*, 2005). A good ion transport may effectively occur as the consequent mediation of highly mobile short oligomer chain. The combination of these properties improves the cells photocurrent and stability over time.

2.1.2.3 In-situ polymerization

Another common method to optimize the interfacial contact between electrolyte and dye molecules is through the formation of SPE in mesoporous structure. This can be done by filling the mesopores with monomers (particularly of low viscous monomers) and subsequently polymerize them in-situ either by thermal-activation (Suzuki *et al.*, 2004), chemical-crosslink reaction (Lim *et al.*, 2010) or photo-irradiation (Matsumoto *et al.*, 1996). Several assemblies developed from this alternative have shown considerable enhancement in the cell performance. However there are some inevitable consequences that limit the life span of the cell such as:

- 1) unwanted secondary reaction may occur in the presence of un-reacted liquid monomer when there is poor control of in-situ polymerization,
- 2) generation of radicals during redox reaction and I₂ dissociation hinders the well-control radical polymerization,
- 3) longer polymerization time is required under UV irradiation since TiO₂ film absorbs UV light,
- 4) degradation or detachment of dye molecules may occur on the TiO₂ surface during photo-polymerization, and
- 5) voids may form at the interface of electrolyte and mesopore when polymer volume shrinks during polymerization. This obstructs the dye-regeneration process.

If any of the above-mentioned aspects were present, a significant exhaustion in the cell performance and its stability is accounted.

A better alternative over in-situ polymerization was reported by Nejati and Lau (2011), in which poly(2-hydroxyethyl methacrylate) was directly deposited into TiO₂ pore *via* initiated chemical vapor deposition (iCVD). This is a solvent-free technique

that uses reacting monomer in the gaseous form. iCVD offers physical control at the nanoscale and chemical control over synthesis pathways (including copolymerization and cross-linking) needed for device fabrication. Apart from cell optimization using the techniques discussed above, it is equivalently crucial to understand the bulk properties of SPE to further widen the materials prospect in cell assembly.

2.2 Solid polymer electrolytes

Among the electrolytes that are developed, PSSE is of particular interest over LE and GPE. This is associated to its optimum safety against electrode corrosion, liquid leakage, iodide decomposition and liquid volatilization. These features may extend the safety, performance and stability of the cell. However in practical, this is not the real observation. Since the cell function is highly dependent on the salt dissociation and ion movement in the polymer structure, it is challenging to speculate the real phenomenon occurring in PSSE. This is because the polymer chains are vulnerable towards changes even at small variation in the composition and/or conditions (*e.g.* temperature, pressure, humidity, mechanical change, *etc.*). Consequently, factors such as ions nature, its population, mobility and mechanism of hopping are affected.

In earlier subsection, we have discussed matters about cell optimization through ionic conductivity acceleration by dopants and ways to form good interfacial contact between the electrolyte and electrode. In this section, we focus on the optimization of polymer structure for better cell fabrication. Some factors involving the ions in SPE such as its nature and mobility will also be explained.

2.2.1 Polymer structure: Glass transition phase

Polymer is a multiphase material that consists of partially amorphous and crystalline phases. In order to tune the conductivity property, the polymer chains (sometimes

referred as chains) in amorphous phase need to be tailored; whereas for mechanical alternation, the tailoring is done for the chains in crystalline phase. The changes can be done either by doping with additives or by controlling the temperature (thermal effect). The important parameter to look at in cell assembly is T_g . Polymers become mechanically soft, elastic and adhesive at temperature close to T_g . This characteristic polymer film generally exhibits increased ionic conductivity. In addition to conductivity, it may provide better interfacial contact between electrolyte and electrode due to its soft-rubbery characteristic. The interfacial contact achieved through this alternative is generally better than that of the PSSE at glassy state. Thus, a maximum electrolyte contact with dye molecules, adsorbed onto the semi-conductor surface (e.g. TiO₂ NPs), can be achieved. This benefits the dye regeneration process.

The utilization of PSSE in rubbery state also offers better ion transport as the results of improvement in the chain dynamics, cooperative movements of ions and fractional free volume. Above T_g , labile bonds are cleaved by kinetic energy and this causes independent motion of short-range chain segments (higher number of local ions movement and cooperative). The independent chain movement subsequently changes the conformation of polymer chain and allows ions to exhibit liquid-like motion. In the macroscopic level, the electrolyte still retains its solid characteristic. The liquid-like ions motion (long-range ion diffusion) occurs *via* formation of continuous random redistribution of the vacant space in the polymer structure. This type of ion transport mode is absent in glassy state as the chains are arranged in “frozen” state. Thus, the randomly arranged and static vacancies are unlikely to percolate into continuous tunnels for ion transport. This explains the typical increment of ionic conductivity above T_g .

2.2.2 Polymer structure: Molecular weight

Molecular weight (M_w) is another strong influencing factor of polymer structure as it affects the entangling density and the segmental dynamics of a polymer chain. Polymer acquires faster segmental dynamics when the chains are short (low M_w). This progressively decreases with the increase of M_w and remains constant above certain threshold. The chain dynamics influence the motion of liquid-like ion in polymer electrolytes. Faster ion transport generally occurs in low M_w polymer (e.g. oligomers) and the mobilization is restricted with increasing kinetic chain length. The shortcoming of low M_w polymers is the poor film forming ability. For this reason, high M_w polymers (M_w ranging in hundreds of thousands) are typically used for SPE preparation as it possesses adequate segmental dynamics to permit liquid-like ion motion and capable of forming mechanically stable membrane. UHMW polymer is another class of high molecular weight polymer with least popularity in the SPE development. Some properties such as poor chain repacking and high mechanical strength upon well tuning its rigidity are hypothesized to benefit the PSSE. The discussion on this is further elaborated in latter section.

2.3 Ions nature in iodide-based SPE

In SPE, the polymer acts as a “solid” solvent to dissolve the metal salts. In iodide-based electrolyte systems, dissolution of iodide salt is possible in the presence of iodine and this dissolution yields a set of iodide species. Only those anions of iodide (I^-) and triiodide (I_3^-) are important in DSSC function whilst other polyiodide species such as I_5^- , I_7^- and I_9^- that are formed at high iodine concentration have no practical importance in DSSC operation (Boschloo and Hagfeldt, 2009).

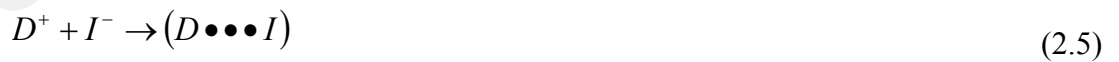
The redox reaction of iodide salt during dissolution in solution is simply explaining by the binding of iodide and iodine forming triiodide. The formation of triiodide however is not a direct transition. The initial dissolution of iodine in organic solvent yields an instable radical of atomic iodine (I^\bullet) and diiodide [I_2^\bullet , upon binding with iodide ion (I^-)]. The empirical representation of the reaction is presented below:



The formation of diiodide radicals has been reported in a number of publications. Those results were obtained using nanosecond-laser spectroscopy (Montanari *et al.*, 2002; Bauer *et al.*, 2002) and pseudo-steady-state photo-induced absorption spectroscopy (Bedja and Hagfeldt, 2011). Reaction between the two diiodides generates triiodide and iodide.



The triiodide is not directly responsible for the regeneration of oxidized dye (D^+). Instead, the oxidized dye is reduced by iodide and forms a complex molecule ($D \bullet \bullet \bullet I$). The complex molecule formation has been successfully demonstrated by Clifford and coworkers (2007) using a sensitizer *cis*-Ru(dcbpy)₂(CN)₂ (Clifford *et al.*, 2007). The pathway for dye-regeneration cycle is shown below (Alebbi *et al.*, 1998; Pelet *et al.*, 2000):



The regeneration of redox cycle maintains high iodide concentration in the electrolyte system while keeping the concentration of free iodine low.

In high concentration of free ions, the ions undergo association and form ion pairs. In most cases, ion pairs start to form near the composition at which the optimum ionic

conductivity is achieved. This characteristic represents a weak electrolyte model. Besides anion, cation also has influence on the SPE bulk properties and cell performance. According to many literatures, the binding of cation on the polymer side chain *via* Lewis acid-base interaction causes structural disorderliness and improves the ionic conductivity of SPE. However, Silva and coworkers (2004) reported a conductivity drop when the cation forms transient crosslink with the polymer chain (Silva *et al.*, 2004). This reduces the segmental-assisted ion motion. Another drawback that can be induced by cation, particularly the cations at interface of TiO₂ layer, is phenomenon that causes interference during the electron transfer process, *i.e.* electron transfer between redox mediator and dye-molecules or between dye-molecules and TiO₂ surface. The interference here is referred to absorption of electrons by the cations during the above-stated processes. As the result, dye-regeneration process is disturbed and this affects the cell performance. In order to suppress the interference of cation in electron transfer process, anion should have higher diffusion as compared to the cation. Anions may have better tunneling owing to its capability to hop *via* many sites such as polar site of polymer (*e.g.* oxygen atom), hydrogen/carbon atom of polymer through halogen bonding, and alternatively *via* ionic clusters and voids.

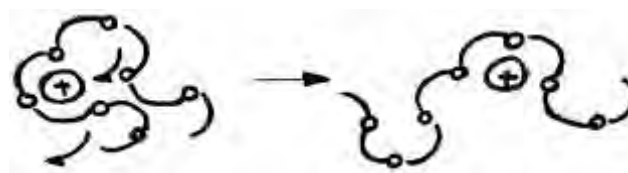
2.4 Mode of ion transport in SPE

The ions in liquid electrolytes move according to random Brownian motion when they collide with neighboring particles (Robinson and Stokes, 2002). When polymer is added, a conducting pathway is required for ions to hop. The cation hops between the mobile coordinating sites by forming and breaking of coordinate bonds; whereas for anion, the hopping occurs between occupied site and void. As the ion transport is highly dependent on the formation of conducting network, the characteristics of polymer chains such as segmental dynamics, number of available polar sites, and free volume

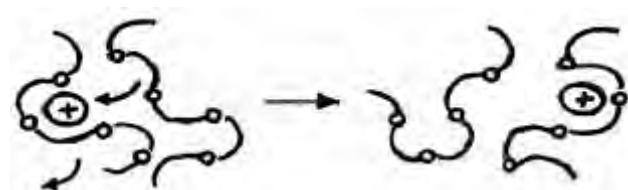
concentration may significantly influence the mode of ion transportation and its mobility. Add on to this, changes in the ion population and its ionic state (e.g. free ion or neutral ion) also may influence to the above scenario. Therefore, it is challenging to understand the “real” mode of ion transport in SPE, particularly in PSSE. The ion transportation in SPE is generally accepted to exhibit more than a single mode of ion transport, which comes in combinations of the transportation routes discussed below.

2.4.1 Hopping *via* frozen chain segments

When polymer is in “frozen” state (below T_g), all the vacancies (or sites of ions hopping) are randomly arranged and static. Therefore, ion hopping occurs primarily through intra-chain hopping. These ions hop *via* neighboring sites of the same polymer chain. Alternatively, inter-chain hopping may also occur at a very low probability. A graphical illustration on these ion transportations is illustrated in Figure 2.3. For successful ion hopping, the ions need to overcome an energy barrier known as activation energy. Typically, the successful ion hopping acquires higher energy and time as the randomly arranged vacant sites may not allow the continuous ion tunneling pathway. The matrix with this type of ion transport generally exhibits poor conductivity due to the constrained ions diffusivity.



Intra-chain hopping



Inter-chain hopping

Figure 2.3: Hopping of ions *via* inter- and intra-chain hopping in SPE

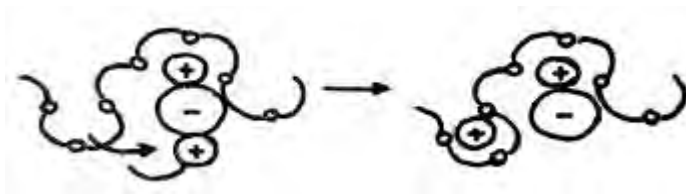
2.4.2 Ion motion mediated by segmental dynamics

This mode of ion transportation is typically observed above the T_g of SPE. The segmental-assisted ion motion occurs through the creation of a continuous and random vacant space in the polymer structure. Subsequently, long-range ion diffusion takes place and exhibits liquid-like ion motion. Simultaneous to that, both intra- and inter-chain ion hopping may also occur easily. In some cases, ions move cooperatively with polymer chains; this usually happens above the T_g . The presence of multiple routes of ion transport above T_g explains the reason for the accompanied ionic conductivity enhancement. As the ion transportation is mediated by polymer segmental dynamics, the relaxation time of ion is usually correlated to chain relaxation. This type of system is known as coupling system, in which the ion transportation is coupled to segmental dynamics. A possible ion motion *via* void or free volume may occur above the T_g .

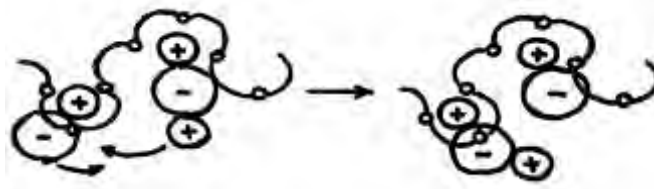
In recent years, there has been report on the increment of ion diffusivity irrespective to the segmental dynamics (Wang *et al.*, 2012). The system shows a decoupling between the motions of ion and chain dynamics. This observation is well established for electrolyte system made from rigid polymers. As the rigid polymers are not the focus of this thesis, the mode of ion transport in rigid polymer is not discussed further.

2.4.3 Self-ion diffusion

Self-ion diffusion occurs as the consequence of oscillating ions pairs. As reported by Kumar and coworkers (2014), this type of ion transportation is generally faster than that of segmental-assisted motion and it is prone to occur in the SPE matrix that contains high concentration of ion pairs (Kumar *et al.*, 2014). This is likely to happen in iodide-based SPE as there is high tendency for triplet ions or higher aggregates to form (Obeidi *et al.*, 2005; Arof *et al.*, 2013). Figure 2.4 shows the mode of ion transportation *via* self-ion diffusion.



Intra-chain hopping via ion cluster



Inter-cluster hopping

Figure 2.4: Self-ion diffusion in SPE

2.4.4 Ion percolation *via* space charge layer

In CPE, a new conducting pathway is formed when there is an efficient overlapping between the space charge layers of NPs. The overlapping efficiency gets stronger with higher packing of NPs. This initiates the formation of grain boundary containing highly disordered chains. Consequently, a sequential manner of ion transportation occurs *via* this long-range ion transfer channel. The percolation *via* space charge layer is favored over the transportation mediated by segmental-assisted motion. Although the ion motions *via* polymer chain and filler surface shares the same potential, ions have faster tunneling along the sites of polymer/filler interface (grain boundary) as they acquire lower activation energy barrier. This finding was reported by Best and coworkers (2001). The authors observed fast Li-ion transportation at the percolating interface regions near filler particles. The schematic diagram of the network formation is illustrated in Figure 2.5.

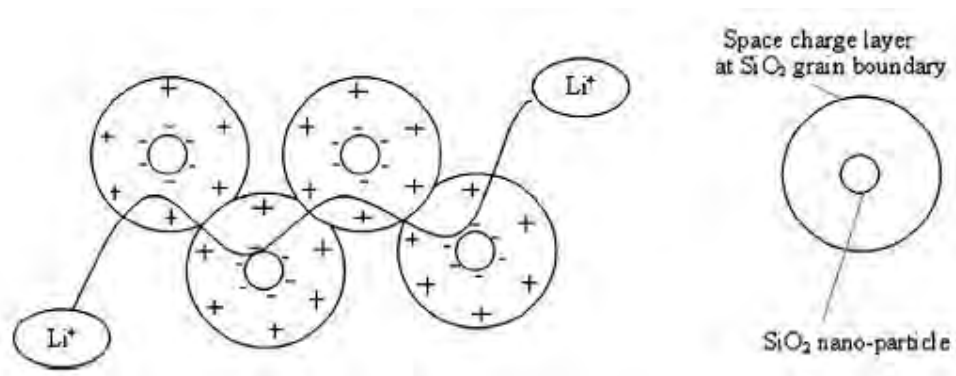


Figure 2.5: Model representation of percolation pathway through the space charge layer of the neighboring SiO₂ grains at the boundaries (Ramesh and Liew, 2012)

2.5 General criteria of PSSE

In order for SPE to be compatible with electrochemical application, certain characteristics need to be met. They need to:

- 1) possess ionic conductivity with minimum of 10^{-5} S cm⁻¹ at room temperature,
- 2) have low T_g for better chain dynamics and ion diffusion,
- 3) be thermally stable above the assembling and operation temperature of device in order to avoid electrolyte from decomposition,
- 4) have wide electrochemical window,
- 5) exhibit elastomeric phase at device operation temperature,
- 6) possess adequate mechanical strength in order to produce a free standing film that is capable of retaining its shape without containment during device assembling process,
- 7) be moisture-resistant in order to avoid from losing its mechanical integrity at ambient condition, and
- 8) be free from ion pairs that could block the conducting pathway and cause the electrolyte to be thermodynamically unstable.

The above-discussed criteria are the general characteristics of SPE that should be complied in order to produce device with good performance. Characteristic (2) is usually the limiting factor, whereby very low liquid-like ion motion can be observed due to the constrained chain movements especially in PSSE. To improve the ion transportation, it is important to increase the free volume fraction by temperature variation in order to create more conducting pathways. When the solid state-DSSC is fabricated at 50 °C (for good electrode-electrolyte contact), free volume expands. At utilization of high molecular weight polymers, the chain has tendency to re-pack to its original state when the cell is brought to 25 °C (cell working temperature). Both chain dynamics and free volume fractions may be reduced, and this subsequently limits the performance. Practically, the improvement cannot be achieved when the high molecular weight polymers in the range of hundreds of thousands are used. To overcome this limitation, polymer with even higher molecular weight, *e.g.* UHMW polymer, needs to be used so that the changes exhibited are negligible. This can benefit the proposed cell assembly method in this work.

2.6 UHMW polymer: History and development

UHMW polymer is a class of macromolecules with molecular weight ranging from $1-6 \times 10^6 \text{ g mol}^{-1}$ (Visjager, 2001). Although UHMW polymer has been actively researched for the past 50 years, the applications are less as compared to other polymers with shorter chain lengths. So far, it has been used in applications where mechanical toughness is of prime concern such as coating, engineering plastic and medical implant material (*e.g.* spine and orthopaedic). An example of a well-established UHMW polymer is poly(ethylene) (PE). This polymer is used either individually or blended with other polymers to create a polymer blend depending on final product requirement.

Examples of other UHMW polymers are summarized in Table 2.1. Most of these inventions had been filed as intellectual properties.

Table 2.1: List of UHMW polymers

Polymer	Molecular weight ($\times 10^6 \text{ g mol}^{-1}$)
Polyethylene	1-6
Polypropylene (isotactic)	1-3
Polyisobutylene	4-6
Poly(acrylamide)	1-21
Polyisoprene	1-5
Poly(ethylene oxide)	1-5
Poly(tetrafluoro ethylene)	5-100
Poly(methyl methacrylate)	1-8
Polystyrene (atactic)	1-50
Poly(vinyl alcohol)	1.5
Poly(acrylic acid)	4-20
Poly(vinyl acetate)	3.2
Nylon-6	1-3.5
Nylon-4	1
Poly(acrylonitrile)	1-2
Poly(l-lactide)	1.5

The superior mechanical strength of UHMW polymer originates from the strong chain entanglement. Due to this entanglement, the polymer chains are more rigid, making the segmental dynamics to be low. This causes the chains to have high resilient and good tolerance towards abrasion and chemical in harsh environment. This characteristic is unlikely seen in low molecular weight polymers, metals or ceramics. Although high entangling density in UHMW polymer offers a number of competitive advantages, it is not favorable during polymer processing. This makes the demand low. For electrochemical applications however, UHMW polymers had shown good prospect in flexible electrode preparation but they are not favorable in SPE development.

2.6.1 UHMW polymer in DSSC fabrication: Current state-of-art

Current DSSC technology utilizes UHMW PE as the substrate to develop flexible metalized electrode. In the work reported by Griep and coworkers (2012), the metalized electrode was prepared by arranging the titanium dioxide nanotube (TiNT) on the substrate in a free-standing array (Griep *et al.*, 2012). This arrangement, which was not possible in a traditional conducting glass (*e.g.* ITO/PET), can now produce a robust cell with high flexibility. In addition to that, the assembly was also reported to show efficient solar harvesting and good suppression of charge recombination effect. Both advantages arise from the organized TiNT structure as it offers barrier-free electron percolation pathway that induces fast electron transfer. This synchronically minimizes the effect of slow electron transport in TiO₂ NPs (that contribute to charge recombination) that is resulted from defects, grain boundaries, surface states and other electron trapping sites.

The positive outcome of the developed metalized electrode was turned down when UHMW polymer was introduced as a host polymer for PSSE formulation. In a recent work by Dzulkurnain and coworkers (2015), low solar-to-light conversion efficiency ($\eta = 0.62\%$ under the illumination of 100 mW cm^{-2}) was recorded for the electrolyte formulated using UHMW poly(methyl methacrylate-*co*-ethyl methacrylate) (Dzulkurnain *et al.*, 2015). The low conversion can plausibly be explained by the low segmental dynamics of UHMW polymer chain that restricts the liquid-like ion transport. Up to date, no other conclusion on the practicability of UHMW polymer in electrolyte formulation can be drawn as there is no further evidence in literature.

2.6.2 Benefit of UHMW polymer in SPE development

There has not been much information concerning the utilization of UHMW polymer as the host material in PSSE development. Some characteristics of UHMW polymer that may benefit the electrolyte development are:

1) *Superior mechanical strength*

Plasticized-SPE exhibits good ionic conductivity at high plasticizer loading. The presence of plasticizer softens the polymer film and makes it to lose its mechanical strength. As the result, it has limited practicability in device fabrication. The effect can be suppressed by substituting the intended polymer with UHMW polymer. Their mechanical superiority over low M_w polymers can further improve the impact strength of plasticized-SPE.

2) *Frustration of chain repacking below T_g*

Long range chain diffusion is generally prohibited above the T_g of polymer (Srinivas, 1999). Since UHMW polymer has low chain dynamics owing to high chain entangling densities, there is a frustration in chain repacking when the temperature is brought from elastomeric phase to glassy. During this time, there is a negligible change in the fraction of available free volume. As the result, ions retain their mobility similar to those experienced in the elastomeric phase. As the consequence, it helps in improving the DSSC performance and extent its stability (due to low segmental chain dynamics) under thermal effect.

3) *High availability of coordination (polar) sites*

In UHMW polymer, huge numbers of repeating units are joined together to form a lengthy single chain. This allows high number of polar sites, if any, to be available in the polymer structure and they potentially increase: (i) salt

dissociation power (Fenton *et al.*, 1973) and (ii) ion-hopping sites. The high salt dissociation allows high number of ions to be available.

The above-discussed characteristics are the general property of UHMW polymers, and these properties vary depending on the choice of monomers and their synthesis techniques. These parameters strongly affect the T_g , and in turn influence the bulk properties of polymer and its processability.

2.6.3 Synthesis of UHMW polymer

In normal practice, UHMW polymers are synthesized *via* free radical polymerization using the techniques of emulsion, suspension, solution and UV photo-initiation. Among these techniques, emulsion polymerization possesses the highest commercial value. This is due to its simplicity in technology and the effect of compartmentalization that can produce high yield of UHMW polymers in a short reaction time (Yamak, 2013). The invariability of emulsion viscosity throughout the synthesis process, *i.e.* polymerization occurs in the micelle interior, is regarded to be another benefit of emulsion polymerization. For other polymerization techniques such as electromagnetic-initiated polymerization, the UHMW polymer will be susceptible to degradation if the experiment were not in a good control. Whereas for the reaction performed *via* solution or suspension polymerization, the occurrence of chain transfer (which induces short chain formation) cannot be completely ruled out due to the high addition of initiator concentration in order to achieve high polymerization rate. For these reasons, emulsion polymerization is still widely employed for the synthesis of UHMW polymer.

The polymer chains are formed when monomeric radicals react with each another in dispersive medium (or solvent) during emulsion polymerization. This reaction occurs at the interior of micelles, which form above the critical micelle concentration. The

initiation of reaction starts when free radicals are generated from the decomposition of initiator either by thermal or redox process (the process is dependent on the type of initiator used). Under an optimized condition (*e.g.* reaction time and temperature), the polymerization yields desirable amount of UHMW polymer with relatively good conversion efficiency. Other reaction ingredients such as stabilizer and catalyst can be used in the synthesis.

The synthesis can be performed in three different ways; *e.g.* bulk, semi-continuous and continuous. Semi-continuous (or semi-batch) process is believed to be the most favorable synthesis method owing to the good control of synthesis method during the propagation stage. For UHMW polymer synthesis, the reaction needs to be carried out at higher rate of propagation with possible low termination rate. A good control in the number of nucleating sites is the prime requirement for UHMW polymer formation. This can only be achieved in semi-batch process.

Apart from the choice of synthesis process, selection of appropriate reaction parameters such as temperature, initiator concentration and synthesis duration are crucial. The temperature shall be slightly above the decomposition temperature of initiator, but it must not be too high as it may cause chain transfer reaction. The chain transfer reaction is known to hamper the formation of long polymer chain (Harrisson *et al.*, 2014). The initiation of reaction with sufficient initiator concentration gives a good control to the number of nucleation sites. The reaction shall also be performed at sufficient time, which typically takes two to three hours to attain high monomer conversion efficiency.

Among the many parameters above-mentioned, selection of monomers and its architecture in polymer have the highest influence to the resulting bulk properties. Different polymer architectures can be synthesized depending on the requirement. To

name the few, they can be either linear (random or non-random), graft, block or branched. Most popular polymer host for electrolyte development are made of ethylene oxide, ethylene, vinyl and acrylics.

2.7 Why P(MMA-co-BA-co-AA)?

GPE based-PMMA and its derivatives are among the most extensively researched polymers after PEO in electrochemical applications, e.g. lithium battery and DSSC, owing to the good room temperature ionic conductivity at $10^{-3} \text{ S cm}^{-1}$. However, its poor chain dynamics in solvent-free condition limit its practicability in the PSSE. Many approaches to increase the PMMA chain flexibility were highlighted in literatures; those common methods are *via* plasticization, polymer blending and copolymerization with monomers of which its homopolymer having low T_g (amorphous polymer).

Among these alternatives, copolymerization of PMMA is preferred as the final polymer possesses better bulk properties suited to the targeted applications. Examples of monomers used to copolymerize with PMMA are BA and ethylene. According to Gigmes (2015), the soft segments of PBA in the copolymer chain alleviates the polymer's T_g and gives better chain flexibility. Apart from the above-mentioned monomers, AA is another preferred combination with PMMA. The incorporation of AA is reported by Grunlan and coworkers (1997) to provide optimal electrostatic colloidal stability for polymer emulsion (Grunlan *et al.*, 1997).

All the three monomers (Figure 2.6) can be polymerized *via* emulsion technique which is initiated by heat, light, peroxides or combination of those. A brief review on the prospect of the three homopolymers (PMMA, PBA and PAA) in DSSC assembly is explained from Section 2.7.1 to Section 2.7.3.

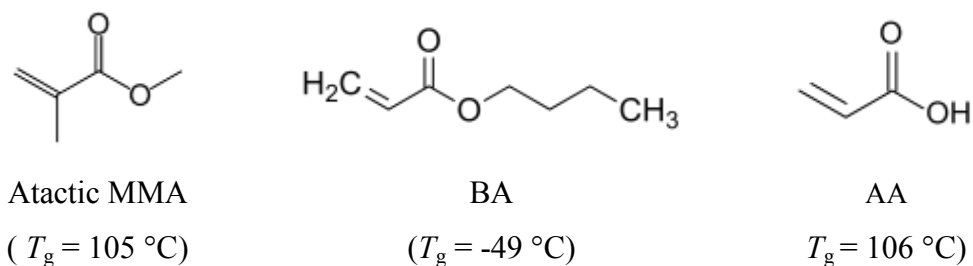


Figure 2.6: Chemical structure of MMA, BA and AA

2.7.1 Poly(methyl methacrylate)

PMMA is another distinguished polymer that has huge demand in SPE development over PEO. Past research focused on the inclusion of ionic liquid in the development of PMMA-based SPE. For more economical approach, Aram and coworkers (2015) used host matrix from physically blended PMMA and PEO to develop the SPE (Aram *et al.*, 2015). This assembly attains cell efficiency of 4.90 % under 100 mW cm^{-2} . In another approach reported by Seidalilir and coworkers (2015), higher cell efficiencies of 6.30 and 8.40 % were recorded under similar light illumination for the gel-type nanotube and NP-based devices, respectively (Seidalilir *et al.*, 2015). In these assemblies, a gelator from the matrix of PMMA copolymerized with ethyl acrylate was used. The recorded cell efficiency is comparable to that of a liquid type-device ($\eta = 6.40$ and 9.10% , respectively, for gel-type nanotube and NP-based devices under 100 mW cm^{-2}). In addition to that, these assemblies exhibit excellent thermal and light-soaking effect which can endure better cell stability compared to its liquid-state counterpart. The utilization of PMMA in combination with other polymers is appealing as the final copolymer shows better suppression to crystallinity and improved in chain flexibility as compared to the homo-PMMA. Therefore, GPE may exhibit high ionic conductivity that enables cell to perform well.

Besides improving the electrolytes conductivity, Kang and Moon (2015) reported on the enhancement of cell performance by optimizing the interfacial contact between the electrolytes and dye-molecules. The in-situ gelation of PMMA/graphene composite gel on the counter electrode yields an efficiency of 8.49 % under 100 mW cm^{-2} . The good cell performance is due to the efficient dye-generation process. Other properties of PMMA that is appealing in the SPE development are high film transparency, retention towards photo-degradation and high mechanical stability.

2.7.2 Poly(butyl acrylate)

PBA is commonly used in paints, sealants, coatings, adhesives, fuel, textiles, plastics, and caulk. The use of PBA as the host matrix in SPE formulations is not of particular interest due to the mechanically soft characteristic (T_g of $-45 \text{ }^\circ\text{C}$). Kim and coworkers (2005) reported a poor cell performance ($\eta = 1.66 \%$ at 10 mW cm^{-2}) in PBA-based GPE assembly, which is due to the low ionic conductivity at $10^{-6} \text{ S cm}^{-1}$ (Kim *et al.*, 2005). When the authors compared PBA-based GPE and PEO-based GPE ($M_w = 1,000,000 \text{ g mol}^{-1}$) with similar ionic conductivity, the exhibited cell efficiency of PBA-based GPE is higher. This can be explained by (i) better penetration of PBA chains into TiO_2 nanoporous layer, which can be ascribed to the lower molecular weight of PBA ($M_w = 99,000 \text{ g mol}^{-1}$) and (ii) soft property of PBA that allows better adherence with photoanode.

Although direct utilization of PBA as the host polymer for GPE does not show any significant importance in the cell performance, its copolymerization with PMMA may plausibly benefit the assembly. This has been shown in the P(MMA-*co*-ethyl acrylate)-based GPE assembly having cell efficiency of 8.4 % (Seidalilir *et al.*, 2015). As the ethylene acrylate has similar basic property to BA, this alleviates chain brittleness and increases the amorphicity of final structure. As the result, there are high chances that

good assembly can be fabricated utilizing the host of P(MMA-*co*-PBA). The incorporation of BA was also reported to provide better thermal stability. Unlike PMMA, PBA is not prone to depolymerization.

2.7.3 Poly(acrylic acid)

Utilization of PAA as a standalone host polymer in SPE has never been reported. Available literatures show that the PAA is generally copolymerized with another polymer such as acrylonitrile (Boonsin *et al.*, 2012), gelatin (Li *et al.*, 2010) and ethylene glycol in combination of electrically conducting polymers such as polyaniline/polypyrrole (Yuan *et al.*, 2014; Liu *et al.*, 2015) for DSSC assembly. In general, all these combinations of PAA matrixes yield high cell efficiency (~6 %) with inclusion of ionic liquids (Sun and Xu, 2016). The matrix with blended conducting polymers such as PANI was also reported to enhance the cell efficiency of PAA/gelatin GPE to 6.94 % under 100 mW cm^{-2} light irradiation (Tang *et al.*, 2012). Another approach with comparative cell performance was recorded by Kelkar and coworkers (2014). A cell performance of 5.75 % under 100 mW cm^{-2} was recorded when the authors substituted egg albumen gelatin ($\eta = 4.60 \%$) with the egg albumen that had been functionalized with ethylenediaminetetraacetic dianhydride. The functionalized egg albumen serves as the gelling agent to form hybrid PAA-PANI GPE. All the above-mentioned combinations yield good cell performance owing to its high generated photocurrent, which is resulted by the good GPE conductivity and high transportation rate of Γ/I_3^- (Kelkar *et al.*, 2014).

2.8 Theoretical background

2.8.1 Gordon-Taylor equation

The theoretical T_g of random copolymers, synthesized using monomers with different aqueous solubility index, is best estimated by Gordon-Taylor equation. This technique can be used to deduce the monomer composition dependence on the T_g of copolymers with relatively weak intermolecular interactions.

$$T_{g\text{ mix}} = \frac{\sum_i \left[w_i \Delta C_{pi} T_{gi} \right]}{\sum_i \left[w_i \Delta C_{pi} \right]} \quad (2.7)$$

where, w_i represents the mass fraction of component i , ΔC_p is the change of the heat capacity and T_g represents the glass transition temperature of component i .

2.8.2 Scattering function

The scattering function (s) (also termed as Debye function) of an incoherent XRD pattern describes the approximate chain distance in polymer. This function is generally used to estimate the chain distance in amorphous polymer. The expression of the scattering function is as follow:

$$s = \frac{2 \sin \theta}{\lambda} \quad (2.8)$$

where, θ is the diffraction angle of the highest intensity peak and λ is the wavelength of X-ray (1.546 Å).

2.8.3 Jump relaxation model

Jump model was first introduced by Funke (1991). This model explains the increase in ionic conductivity at high frequency as the effect of forward and backward ion displacements. Both ions hopping occur simultaneously but may show prominent effect over to the other considering the Coulomb interaction between mobile ions.

Experimentally, this information can be accessed from the slope of dispersive conductivity region in frequency-dependent conductivity spectra ($\log \sigma$ vs. f). The slope represents an exponent factor (n). Quantity n is obtained from the ratio of back hop (b_r) to site relaxation (S_r):

$$n = \left[\frac{b_r}{S_r} \right] \quad (2.9)$$

Back hop is defined as the backward motion of hopping ion to its initial site caused by Coulomb repulsive interaction between mobile ions. This signifies the unsuccessful ion hopping to new site. On another hand, the site relaxation is defined as the shift of site potential from minimum level to the position of hopping ion that is caused by rearrangement of neighboring ions. This causes an increase in the successful ion hopping from one site to the new neighboring site. In the case where backward ion hopping occurs faster than the site relaxation, the parameter n exceeds unity. It displaces to the value less than unity when forward hopping is dominant (due to site relaxation).

2.8.4 Nernst-Einstein equation

As mentioned in Section 2.1.1, the ionic conductivity (σ) of polymer electrolytes is influenced by N_{ion} and D_{ion} , (also known as ion diffusivity coefficient). These influencing factors can be calculated using Equation (2.10) and Equation (2.11) from Nernst-Einstein relationship.

$$D_{ion} = \frac{2\pi f_{max} L^2}{32(\tan \delta_{max})^3} \quad (2.10)$$

where, $\tan \delta_{max}$ is the maximum value of ϵ''/ϵ' in the frequency range of EP, f_{max} represents the frequency at which $\tan \delta$ is maximum and L is sample thickness (cm).

$$N_{ion} = \frac{\sigma k_B T}{Dq^2} \quad (2.11)$$

where, k_B is the Boltzman constant ($1.38 \times 10^{-23} \text{ m}^2 \text{ kg s}^{-2} \text{ K}^{-1}$), T is the temperature in Kelvin and q is the elementary charge ($1.60 \times 10^{-19} \text{ C}$).

D_{ion} can be evaluated from the electrode polarization effect according to Trukhan model (Trukhan, 1963). The calculation is performed by agreeing to the assumption that both the cation and anion share equal diffusion coefficient. Although this may not be true [both ions (*e.g.* cation and anion) are different in size], such difference is typically less than an order of magnitude and is therefore negligible (Stolwijk and Obeidi, 2004). The D_{ion} and N_{ion} values should be considered only as a qualitative analysis without giving too much emphasis on the quantitative analysis.

CHAPTER 3: MATERIALS AND METHOD

3.1 UHMW P(MMA-co-BA-co-AA)

3.1.1 Materials

The starting materials for copolymer synthesis such as MMA, BA, AA, potassium persulfate (KPS, 99 % purity) and sodium dodecyl sulfate (SDS) were procured from Sigma Aldrich (USA). MMA and BA were purified in 10 wt.% NaOH prior to synthesis while other chemicals were used as-received. Fresh distilled water was used to prepare the reaction medium and as dissolving solvent.

3.1.2 Reactor assembly

The synthesis was carried out in a five-neck-glass reactor with each neck connected to thermometer, motorized-mechanical stirrer, distillation condenser and two dropping funnels, respectively. The reactor was immersed in water bath throughout the synthesis by keeping the water level above the meniscus of reaction mixture in the vessel. The experimental set-up for this synthesis is shown in Figure 3.1.



Figure 3.1: Experimental set-up for copolymer synthesis

3.1.3 Emulsion polymerization

The synthesis of P(MMA-*co*-BA-*co*-AA) was carried out following semi-batch process using monomer formulations reported in Table 3.1. Reacting ratios of MMA and AA were varied while BA ratio was kept constant.

Table 3.1: Monomer compositions for P(MMA-*co*-BA-*co*-AA) synthesis

Designation	Composition (wt.%)		
	MMA	BA	AA
AA05	55	40	5
AA20	40	40	20
AA30	30	40	30
AA40	20	40	40

Note: The total weight of monomer compositions for entire formulation was fixed at 100 wt.%

The stages of synthesis were summarized in Table 3.2 along with the chemical compositions used. The synthesis was first performed by growing the polymer “seeds” (oligomer radical chain) in the reaction medium using Mixture (1). The “seeds” were formed *via* in-situ process upon addition of pre-weighted monomer mixtures and KPS solution into the reactor flask containing homogenized emulsion (SDS and water). The emulsion homogenization was carried out under agitation of 600 rpm at 80 °C. This parameter was kept constant throughout the synthesis. The successful “seeds” formation was physically inspected through the color change of reaction medium to slight bluish.

Table 3.2: Chemical compositions of three solution mixtures; (1) Initial charge solution, (2) Delayed monomer solution and (3) Catalyst solution

Emulsion stage	Mixture type	Materials	Quantity (g)
Seeding	Mixture (1):	Distilled water	200.0
		SDS (30 %)	1.0
	Initial charge solution	* Monomer mixtures	12.5
		** KPS	0.35
Feeding	Mixture (2):	Distilled water	140.0
		SDS (30 %)	9.0
	Delayed monomer solution	* Monomer mixtures	87.5

Table 3.2, continued

Emulsion stage	Mixture type	Materials	Quantity (g)
Feeding	Mixture (3):	Distilled water	30.0
		KPS	0.35
Catalyst solution			

Note: * The compositions of each monomer were mixed in the ratio summarized in Table 3.1
**The powder KPS was dissolved in 20.0 g of distilled water

After the seeding process, Mixture (2) and (3) were continuously fed into the reactor for an hour. At the completion of feeding stage, the reaction time was extended for another hour to maximize the monomer conversion. The mechanism of P(MMA-*co*-BA-*co*-AA) formation is enclosed in Appendix A. The final product of synthesis appeared as a milky-white emulsion. This emulsion was filtered once the temperature of reactor dropped to 25 °C and was then safely stored against light in a capped poly(ethylene) bottle.

3.1.4 Film preparation

The filtered emulsion was cast onto Teflon[®] plate and oven-dried at 60 °C until a constant weight was achieved. This yields a mechanically free-standing film with high transparency, as seen in Figure 3.2. The film was kept in a sealed plastic bag and stored in desiccators.

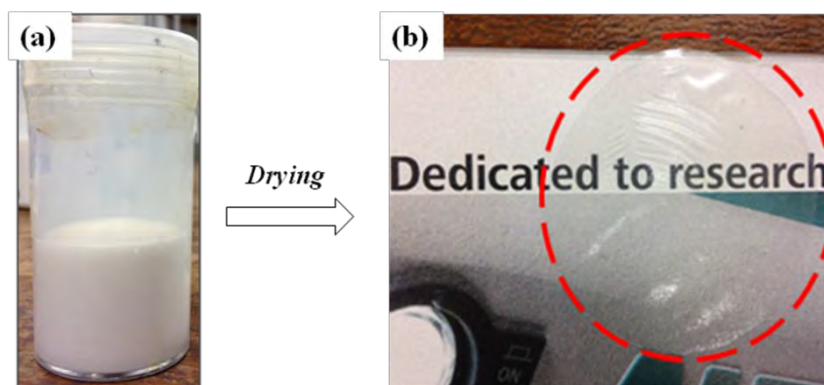


Figure 3.2: (a) Emulsion copolymer and (b) cast film

3.1.5 UV irradiation

The photo-degradation of P(MMA-*co*-BA-*co*-AA) film ($1 \times 1 \text{ cm}^2$ in square shape) was performed in atmospheric and dark conditions. Results were collected after irradiation with 254 nm UV-lamp (UVL-56, Intensity: 1.0 mW cm^{-2}) at different time ranging from 30, 60, 120, 240, 360 to 480 min. The test was performed specifically for copolymer film with formulation AA05 as it had been identified to be the best host polymer for PSSE formulation (*cf.* Chapter 4).

3.2 PSSE formulation

3.2.1 Materials

P(MMA-*co*-BA-*co*-AA) of AA05 formulation was selected for PSSE development. Other dopants such as NaI, I₂, EC, PC and SiO₂ NPs were used as received from Sigma-Aldrich Co. (USA). The chemicals and compositions used to formulate the three systems can be found in Table 3.3(a-c). The three systems were labeled as I, II and III for the PSSE with variation of NaI, EC: PC and SiO₂ NPs, respectively.

Table 3.3: Formulation of PSSE systems

(a): NaI variation (System I)

PSSE	Composition (wt.%)			
	AA05	NaI	I ₂	EC: PC
NaI-5	75	5		
NaI-10	70	10		
NaI-15	65	15		
NaI-20	60	20	10	10
NaI-25	55	25		
NaI-30	50	30		

Note: (i) Total weight of the formulation was fixed at 100 wt.%

(ii) The weight percentage of additives were calculated accordingly; NaI (with respect to AA05 wt.%), I₂ (with respect to NaI wt.%), EC: PC (with respect to AA05 wt.%)

(iii) The optimized PSSE composition (NaI-15) was used as the control for next system

Table 3.3, continued

(b): EC: PC variation (System II)

PSSE	Composition (wt.%)			
	AA05	NaI	I ₂	EC: PC
NaI-15				10
EC: PC-20				20
EC: PC-30	65	15	10	30
EC: PC-40				40
EC: PC-50				50

Note: (i) Total weight of formulation is above 100 wt.%(ii) The weight percentage of additives were calculated accordingly; NaI (with respect to AA05 wt.%), I₂ (with respect to NaI wt.%), EC: PC (with respect to AA05 wt.%)

(iii) The optimized PSSE composition (NaI-15) was used as the control for this system

(c): SiO₂ NPs variation (System III)

PSSE	Composition (wt.%)				
	AA05	NaI	I ₂	EC: PC	SiO ₂
NaI-15					0
SiO ₂ -2					2
SiO ₂ -4	65	15	10	10	4
SiO ₂ -6					6
SiO ₂ -8					8
SiO ₂ -10					10

Note: (i) Total weight of formulation is above 100 wt.%(ii) The weight percentage of additives were calculated accordingly; NaI (with respect to AA05 wt.%), I₂ (with respect to NaI wt.%), EC: PC (with respect to AA05 wt.%) and SiO₂ (with respect to AA05 wt.%)

(iii) The optimized PSSE composition (NaI-15) was used as the control for this system

3.2.2 PSSE thin film preparation

PSSE solutions were prepared by dissolving all the chemicals, in certain proportion, as specified in Table 3.3 into 20 ml of acetone. The solutions were stirred overnight at room temperature. For the system containing SiO₂ NPs, sonication was performed on the homogeneous solution in order to achieve optimum dispersal. The solutions were then poured onto Teflon[®] substrate and dried inside the fume hood. The completion of drying process produced continuous opaque films with light brown appearance. These films were kept in desiccators. The best PSSE composition from System I was selected as a control sample to formulate System II and subsequently the best PSSE composition from System II was used as the control for System III.

3.3 Fabrication of DSSC

3.3.1 Materials

TiO₂ paste (DSL 18NR-AO) and platinum was purchased from Solaronix SA (Switzerland) for electrode preparation. From the same supplier, fluorine doped tin oxide conducting glass (FTO, dimension: 2 × 2 cm², sheet resistance of 7 Ω sq⁻¹) and *cis*-diisothiocyanato-*bis*(2,2'-bipyridyl-4,4'-dicarboxylato) ruthenium(II) *bis*(tetrabutyl ammonium) (N719, Ruthenizer 535 *bis*-TBA) were procured. For the choice of polymer electrolyte (as a separator membrane), the optimized PSSE from Section 3.2 were used.

3.3.2 Preparation of photoanode and counter electrode

3.3.2.1 Photoanode

The FTO glass was rinsed with acetone and ethanol in an ultrasonic bath for 10 min. Consequently, TiO₂ paste (circular shape) was deposited on FTO by doctor-blade technique and dried at 100 °C for 10 min on a hot plate. Then, the coated surface was sintered at 520 °C for 30 min forming a nanoporous TiO₂ film with a mean thickness of 8 μm. This was measured by profilometry (P.10 KLA-Tencor Profiler). Finally, the photoanode was soaked in a mixture of 0.4 mM N719 dye solution and ethanol for 15 hours at room temperature and then rinsed with ethanol to remove the unabsorbed dye.

3.3.2.2 Counter electrode

Platinum thin film (5 nm thickness) was deposited onto the clean FTO surface by thermal evaporation. The FTO surface was cleaned using similar rinsing method as reported in previous section.

3.3.3 Solid-state DSSC assembly

The solid-state DSSC was assembled by sandwiching the optimized PSSE in between the TiO₂-sensitized photoanode and platinum counter electrode (Figure 3.3). The sandwich-type cell was stacked together by sealing with cyanoacrylate blue to avoid from disassembling. Then the cell was placed on a hot plate at 50 °C for 24 hours to favour the formation of adequate interface between the electrolyte and electrode.

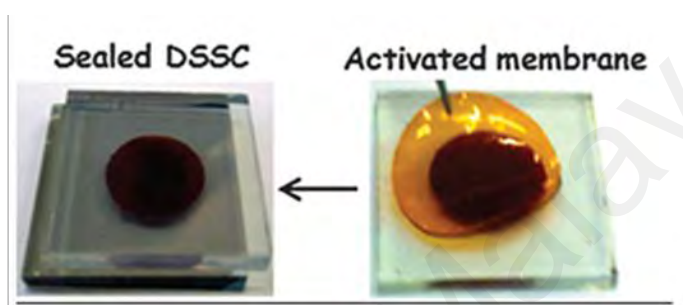


Figure 3.3: Final assembly of solid-state DSSC

3.4 Analytical techniques

3.4.1 P(MMA-co-BA-co-AA)

3.4.1.1 Gravimetry

The total solid content (TSC) in emulsion copolymer was calculated as per ASTM D2834. Three replicates were taken to calculate the average TSC for liquid samples weighted exactly 3.0 g. The drying procedure is similar to the method described in Section 3.1.4. The monomer conversion efficiency was calculated using the method described by Zhang and coworkers (2017).

3.4.1.2 Light scattering (particle size and zeta potential)

The distribution of copolymer particle size and its colloidal stability were determined at 25 °C using *Zetasizer Nano ZS* (Malvern Instruments Ltd., UK). The emulsion was tested without any dilution. The measurement was performed by taking the refractive

index of PMMA (1.49 based on Tanio and Nakanishi, 2006) as the reference. Disposable cuvette was used for the particle size analysis while clear disposable zeta cell was used for zeta potential measurement.

3.4.1.3 Attenuated total reflectance- Fourier transform infrared spectroscopy (ATR-FTIR)

Infrared spectrum was recorded for all the synthesized P(MMA-*co*-BA-*co*-AA) at room temperature using *Nicolet iS10* FTIR (Thermo Fisher Scientific Inc., USA) equipped with ATR Germanium cell. Samples were placed on top of the crystal surface and spectra were recorded at a resolution of 4 cm^{-1} with 16 scans over the range of 4000 to 650 cm^{-1} . All the recorded spectra were normalized against background noise.

3.4.1.4 Solubility test

A broad range of solvents was used to test the solubility of P(MMA-*co*-BA-*co*-AA) such as water, ethanol, dimethyl sulfoxide, tetrahydrofuran, acetone and chloroform. A small piece of copolymer film was placed inside a vial containing the solvent and left overnight. Physical changes of film were observed over time.

3.4.1.5 Nuclear magnetic resonance spectroscopy (NMR)

^1H NMR analysis of P(MMA-*co*-BA-*co*-AA) was carried out on *Avance 500* spectrometer (Bruker Corporation, USA). The spectra were recorded with a 13.2- μs pulse width and 128 scan numbers for copolymer films dissolved in deuterated chloroform (for AA05) and DMSO (for AA20, AA30 and AA40) at $30\text{ }^\circ\text{C}$. The chemical shifts of ^1H NMR were recorded in relative to tetramethylsilane as an internal reference. DEPT-135 and ^{13}C spectra were recorded for AA05 using similar experimental method.

3.4.1.6 Thermogravimetry analysis (TGA)

The thermal decomposition of P(MMA-co-BA-co-AA) was analyzed using *TGA Q5000* (TA Instruments, USA). The measurement was performed by heating 3.0-5.0 mg sample from 30 °C to 500 °C at a rate of 50 °C min⁻¹ under a constant nitrogen purge (20 μL min⁻¹). The reported T_d was obtained from the maximum peak of the derivative weight loss.

3.4.1.7 Differential scanning calorimetry (DSC)

The T_g was analyzed using *DSC Q200* (TA Instruments, USA) equipped with refrigerated cooling system 90-series under nitrogen atmosphere (purity: 99.9995 %; flow rate: 50 mL min⁻¹). Heat-cool-heat cycles were programmed as such from -80 °C to 120 °C at a rate of 100 °C min⁻¹. The T_g value was extracted from the last heating cycle by taking the midpoint of extrapolated tangent between the glassy and rubbery transitions. The DSC was well calibrated using indium and sapphire standards.

3.4.1.8 Gel permeation chromatograph (GPC)

The weight-average (\overline{M}_w) and number-average (\overline{M}_n) molecular weights of P(MMA-co-BA-co-AA) were estimated at 40 °C using *GPC 1200* (Agilent Technologies, USA) coupled with *Waters 2414* refractive index detector, *Waters 717* plus auto sampler and *Waters 600* controller (Waters Corporation, USA). Tetrahydrofuran was used as the solvent to prepare copolymer solutions with concentration of 1.0 mg mL⁻¹ and as eluent at a flow rate of 1.0 mL min⁻¹. Prior to measurement, all the samples were filtered using 0.22 μm PTFE. A total of 100 μL aliquot samples were injected in the system and the analysis proceeded for 55 min. The calibration curve was obtained from polystyrene standard.

3.4.1.9 Four point probe

Four point probe measurement was performed from 50 Hz to 1 MHz at the amplitude of 10 mA using four point probe system (KeithLink Technology Co. Ltd., Taiwan) integrated with *Gamry Interface 1000 potentiostat* (USA). The film sample was cut into 2 cm × 2 cm (length × width) prior to analysis. Five replicates were taken from each copolymer formulations. The sheet resistance (R_{sheet}) of P(MMA-co-BA-co-AA) film was obtained using Van der Pauw method and was corrected to the nearest correcting factor of 4.1712.

3.4.1.10 Tensile test

Tensile test was carried out according to ASTM standard D882-02, using a bench top *Tinius Olsen H10KS* instrument (Tinius Olsen TMC, USA) equipped with an electromechanical extensometer. The test P(MMA-co-BA-co-AA) film was prepared by casting 25 g of the emulsion in a plastic tray (length × width: 17 cm × 10 cm) at 70 °C. Similar tray and consistent liquid weight was used for the casting to form film with the thickness controlled within 0.25 mm. A small strip with dimension of 1.5 cm × 7 cm (width × length) was cut from the cast film and conditioned at 27 °C and 50 ± 5 % relative humidity for 24 hours prior to testing. The parameters for tensile measurement are as summarized: spacing between grips (20 mm), stress range (450 MPa), extension range (1000 %), speed (500 mm min⁻¹), sample length (50 mm) and preload (1 N).

3.4.2 UV irradiated P(MMA-co-BA-co-AA)

3.4.2.1 UV-visible-near IR (UV-Vis-NIR)

Changes of chemical structure in the irradiated film were observed under UV-Vis-NIR spectrometers. UV-Vis-NIR spectra were collected using *AvaSpec-ULS2048 StarLine* UV-Vis-NIR spectrometer (Avantes, The Netherlands). A *Spectroline TVC-*

312A UV light source was attached together in order to perform chromaticity test. All the spectra were collected at room temperature within the range of 1100-180 nm. For chromaticity study, all the parameters of L^* (lightness) and color coordinates (a^* and b^*) were measured. The color coordinates a^* is comprised of the color directions from $+a^*$ (red direction) to $-a^*$ (green direction), whereas for the b^* coordinates, the color direction is from $+b^*$ (yellow direction) to $-b^*$ (blue direction). Parameters of a^* and b^* were used to calculate the metric chroma-color intensity (C^*) and total color difference (ΔE^*):

$$C^* = \sqrt{(a^*)^2 + (b^*)^2} \quad (3.1)$$

$$\Delta E^* = \sqrt{(\Delta L^*)^2 + (\Delta a^*)^2 + (\Delta b^*)^2} \quad (3.2)$$

3.4.2.2 Atomic force microscope (AFM) and other related analyses

ATR-FTIR technique was used to confirm the UV-Vis-NIR results. The experimental procedure for ATR-FTIR measurement was according to Section 3.4.1.3. Changes of molecular weight, thermal stability and morphology at different irradiation time were studied using GPC, TGA and AFM, respectively. The experimental method for TGA and GPC had been discussed in Section 3.4.1.6 and Section 3.4.1.8, respectively. The AFM images of irradiated samples were captured using *Ambios Q-Scope Series AFM* (Accurion GmbH, Germany) at room temperature. Irradiated samples were periodically removed from the exposure cell and analyzed under the scanning probe microscope operated in contact mode. The scanning was performed at frequency of 1.0 mHz. Those surfaces were viewed using scan atomic software. Similar software was used to calculate the surface roughness, which was quantified by the root mean square (rms) value obtained from three measurements.

3.4.3 Characterization of PSSE

3.4.3.1 X-ray diffraction (XRD)

XRD analysis was performed using *Siemens D5000* (Siemens AG, Germany) with Cu-K α radiation ($\lambda=1.54060$ Å) operating at 40 kV and 40 mA at a step size of 0.026°. The samples were scanned at room temperature over the diffraction angle (2θ) of 5° to 80°.

3.4.3.2 Impedance spectroscopy

Impedance analyzer *HIOKI 3532-50 LCR Hi-TESTER* (HIOKI E.E. Corporation, Japan) was used to measure the resistivity of PSSE in the frequency range of 5 Hz to 50 MHz at 10 mV signal level. The measurement was performed by sandwiching the PSSE, with pre-determined thickness, in between the stainless steel blocking electrodes. Experimental data was collected in the temperature range of 25 °C to 100 °C. Three replicates were used to calculate the average results. Other dielectric parameters such as Z impedance and loss tangent were obtained from the impedance data.

3.4.3.3 Thermal analysis

The experimental procedure to determine the T_d and T_g of PSSE samples were carried out according to Section 3.4.1.6 and Section 3.4.1.7, respectively.

3.4.4 Electrochemical performance of solid-state DSSC

The active area of the cells was 0.78 cm² and the photovoltaic measurements were performed with a 0.22 cm² rigid black mask. The current (J)-voltage (V) plot was recorded 5 times at 10 mV s⁻¹ under AM1.5G illumination (1 Sun = 100 mW cm⁻²) using a class A solar simulator (91195A, Newport) and a *Keithley 2440* source measure unit. Three replicates were taken to obtain the average result.

CHAPTER 4: RESULTS AND DISCUSSION

Synthesis, Physico-Chemical and Photo-degradation of Random P(MMA-co-BA-co-AA)

4.1 Synthesis of P(MMA-co-BA-co-AA)

4.1.1 Particle-size distribution

Particle-size distribution of P(MMA-co-BA-co-AA) with AA05, AA20 and AA30 formulations are shown in Figure 4.1. In general, all the results show a broad Gaussian distribution. This exemplifies the formation of irregular chain lengths during polymerization. The average particle size calculated from these irregular chain lengths is as follow: 75 nm (for AA05), 235 nm (for AA20) and 1813 nm (for AA30). The result for AA40 is not presented in this section and the following section due to its high emulsion viscosity that requires dilution during particle-size measurement. For such case, the dilution could trigger ambiguity among the replicates.

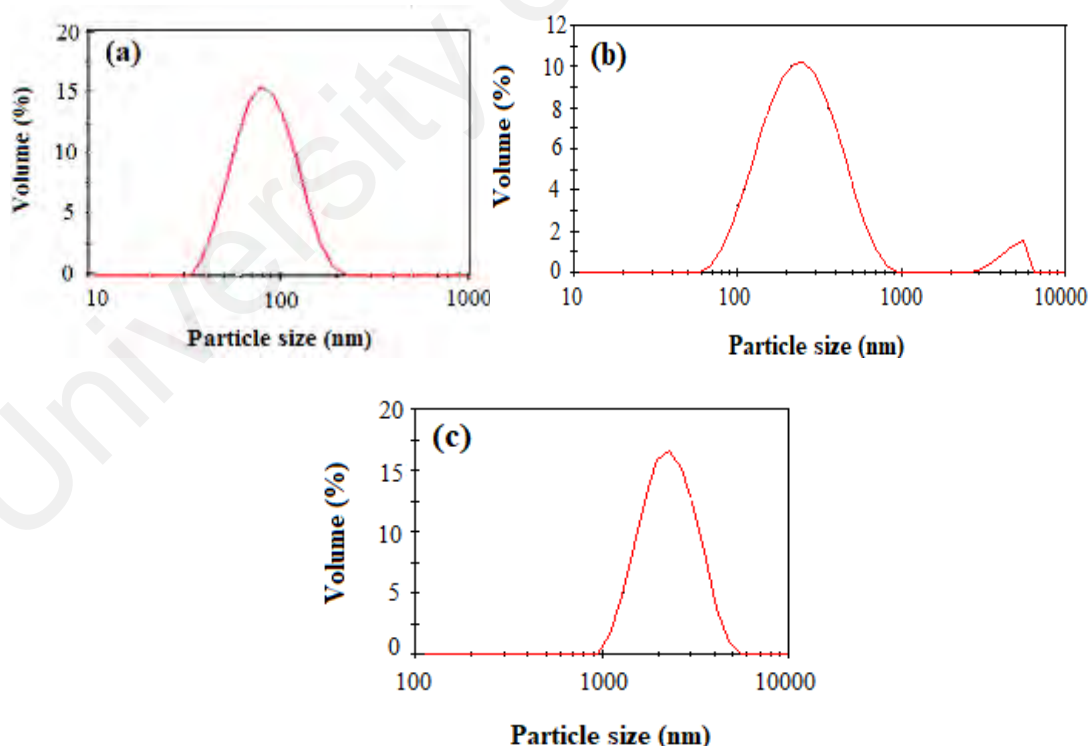


Figure 4.1: Particle-size distribution curve of (a) AA05, (b) AA20 and (c) AA30

4.1.2 Zeta potential

Measurement of zeta potential was taken in order to understand the effect of polymer particle size on the colloidal stability. The following results were obtained for individual formulation such as -48.3 (for AA05), -15.5 (for AA20) and -12.4 (for AA30). Negative values hint the adsorption of negatively charged SDS and persulfate ions (from the initiator) on the particle surface. The developed surface charge however, depletes with increasing particle size. This can be associated to the lowering of SDS molecules for stabilization (reduced in repulsive force). Consequently, this causes the particles to lose their colloidal stability and in some cases, they are prone to flocculation (Polte, 2015). This finding is consistent with the grit formation in aged AA20 and AA30 (*cf.* Table 4.1) that had been stored for a year. A stable emulsion was produced in both AA05 and AA40 formulations.

4.1.3 Monomer conversion and TSC

Table 4.1 shows the calculated TSC and monomer conversion of P(MMA-*co*-BA-*co*-AA) synthesis. High polymer yield with good monomer conversion was obtained in AA05 and AA40 formulations. On another hand, poor monomer conversion with low TSC can be observed in AA20 and AA30 formulations. The TSC results of AA05 and AA40 ($\sim 20\%$ in un-purging systems) are reasonable when compared to that of the emulsion technique performed in purging systems (typically, it does not exceed 30%) reported by Blackley (1997).

Table 4.1: TSC and monomer conversion of P(MMA-*co*-BA-*co*-AA) determined using gravimetric method

Copolymer	TSC (%)	Monomer conversion (%)
AA05	18.4	92
AA20	9.0	45
AA30	13.2	66
AA40	19.0	86



Note: Dashed box represents unstable emulsion (formation of grit)

4.1.4 Solubility test

Table 4.2 summarizes the solubility of P(MMA-*co*-BA-*co*-AA) in different solvents. The presence of hydrophobic and hydrophilic segments in P(MMA-*co*-BA-*co*-AA) gives intermediate polarity; this polarity varies among the formulated copolymers. The tested samples remain insoluble in water over time due to their immiscible hydrophobic chain segments. The hydrophobic segment, regardless of its compositions, can be effectively dissolved in organic solvents such as THF and DMSO due to their broad polarity ranges.

Table 4.2: Solubility test of P(MMA-*co*-BA-*co*-AA) in different solvents

Copolymer	Solvents (arranged in increasing polarity)					
	THF	Chloroform	Acetone	Ethanol	DMSO	Water
AA05	/	/	/	X	/	X
AA20	/	X	P	/	/	X
AA30	/	X	P	/	/	X
AA40	/	X	P	/	/	X

Note: (i) “/” marked the complete solubility of copolymer in solvent and “X” represents insolubility.

(ii) Partially soluble samples are denoted by “P”. The grey color area in “P” represents the intensity of turbid solution [the higher the intensity (which is indicated by darker grey), the higher the turbidity].

Chloroform and acetone are good solvent for AA05 formulation. When more AAs are present in P(MMA-*co*-BA-*co*-AA), the copolymers (AA20, AA30 and AA40) cannot be dissolved in chloroform due to the increase of copolymer polarity. On another hand, the same copolymers are partially insoluble in acetone due to the presence of oxygen atom (higher polarity). The immediate effect of AA present in the copolymers lies on the turbidity intensity in acetone. For instance, at low AA content (AA05), the hydrogen bonding between the copolymer and solvent is high enough to cause the miscibility. With increasing AA content (polarity increases), however, there is a limited hydrogen bond and this suppresses the dissolution of copolymers in acetone and results in higher turbidity.

In contrary to chloroform and acetone, the copolymers with higher polarity (increasing AA content) can be dissolved well in ethanol. The hydrophobic nature of AA05 does not permit enough hydrogen bond to form, therefore it is insoluble. To sum up, the solubility of copolymers with different monomer compositions differs from solvent to solvent depending on polarity change. AA05 has the best chance of solubility in a wide range of solvents as compared to other copolymers.

4.1.5 ATR-FTIR

The overlay FTIR spectra of synthesized P(MMA-*co*-BA-*co*-AA) is shown in Figure 4.2. In the spectra of thin film samples (AA05, AA20, AA30 and AA40), the characteristic peak for C=C unsaturation at 1600-1650 cm^{-1} were not present (Litvinov and De, 2002; Liu *et al.*, 2017). Instead, this peak exists in pure monomer spectrum (e.g. MMA, BA and AA); for justification, only spectrum of pure MMA was enclosed.

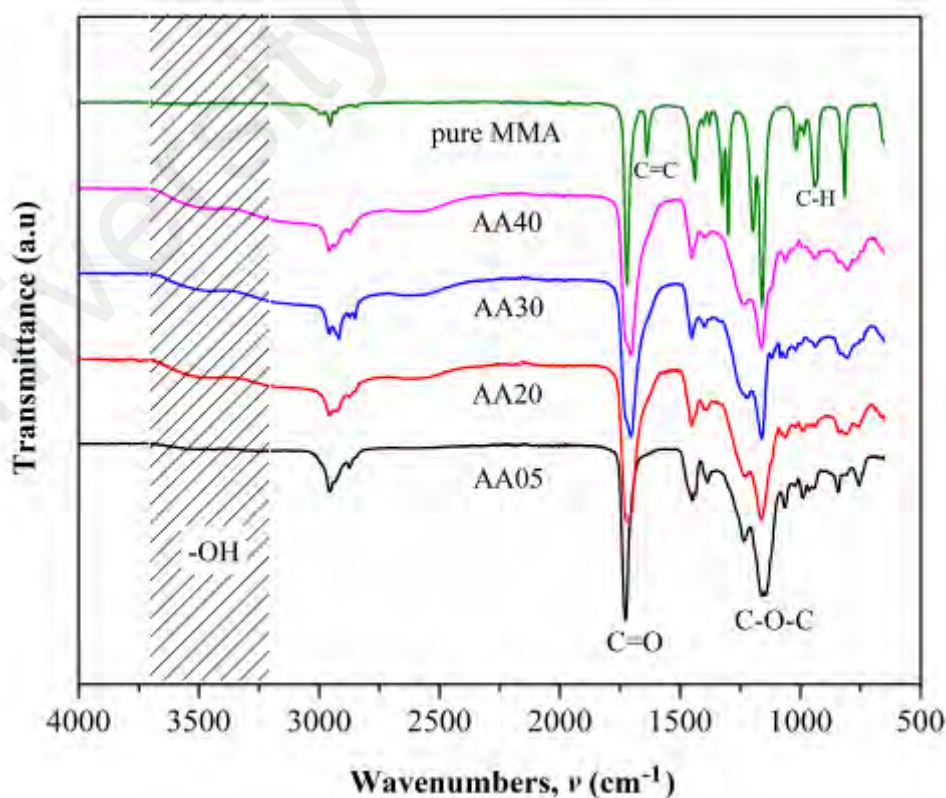


Figure 4.2: FTIR spectra of P(MMA-*co*-BA-*co*-AA) thin films and pure MMA

The absence of unsaturated bond indicates good monomer conversion. As the consequence of bond rupturing, the peak intensity of unsaturated =C–H bond at 900-960 cm^{-1} are affected (the intensity reduces) (Kozanoğlu *et al.*, 2011). The formation of polymer chain that contains all three monomers is obvious from the presence of characteristic peaks such as hydroxyl (–OH), methoxy (C–O–C) and carbonyl (C=O). Other absorption peaks are summarized in Table 4.3 (Chen *et al.*, 2006; Ismayil *et al.*, 2010; Ennis and Kaiser 2010; Wang, 2011; Sayyah *et al.*, 2012; Tiwari *et al.*, 2014). The sharp absorption peak of C=O in AA05 becomes slightly broader with incorporation of more AA segments.

Table 4.3: FTIR absorption peaks of P(MMA-*co*-BA-*co*-AA)

Characteristic peak	Wavenumbers, ν (cm^{-1})			
	AA05	AA20	AA30	AA40
-OH		3200-3700		
C-H	2955- 2874	2825-3000	2719-3025	2780-3020
C=O	1726	1719	1705	1704
*C-H	1350, 1500	1392, 1449	1399, 1451	1398, 1450
C-C-O	1237	1228	1220	1235
C-O-C	1160	1161	1161	1162
skeletal C-C	1064	1063	1060	1062
CH ₃ rocking		842		
CH ₂ skeletal	755	759	N/V	N/V

Note: Asterisk (*) represents the bending mode while the unmarked characteristic peak designation represent the stretching vibrational mode. Those absorption peaks that are not visible in the spectrum are marked as N/V.

4.1.6 NMR

The ^1H NMR spectrum of AA05 is shown in Figure 4.3 and the peak assignments are tabulated in Table 4.4. The ^1H NMR spectra of other copolymers are enclosed in Appendix B. The presence of chemical shifts (δ) at 3.6 ppm (–OCH₃ in PMMA) (Kwon *et al.*, 2002; Hatada *et al.*, 2003; Kitayama and Hatada, 2004), 4.0 ppm (–OC₄H₉ in PBA) (Wang, 2011) and 12 ppm (–OH in PAA) (Chen *et al.*, 2006) confirms the synthesis of P(MMA-*co*-BA-*co*-AA). In AA05 formulation, the signal at 12 ppm is not visible due to the low AA concentration. The success of polymerization is also confirmed using ^{13}C -NMR and DEPT-135 as shown in Appendix C.

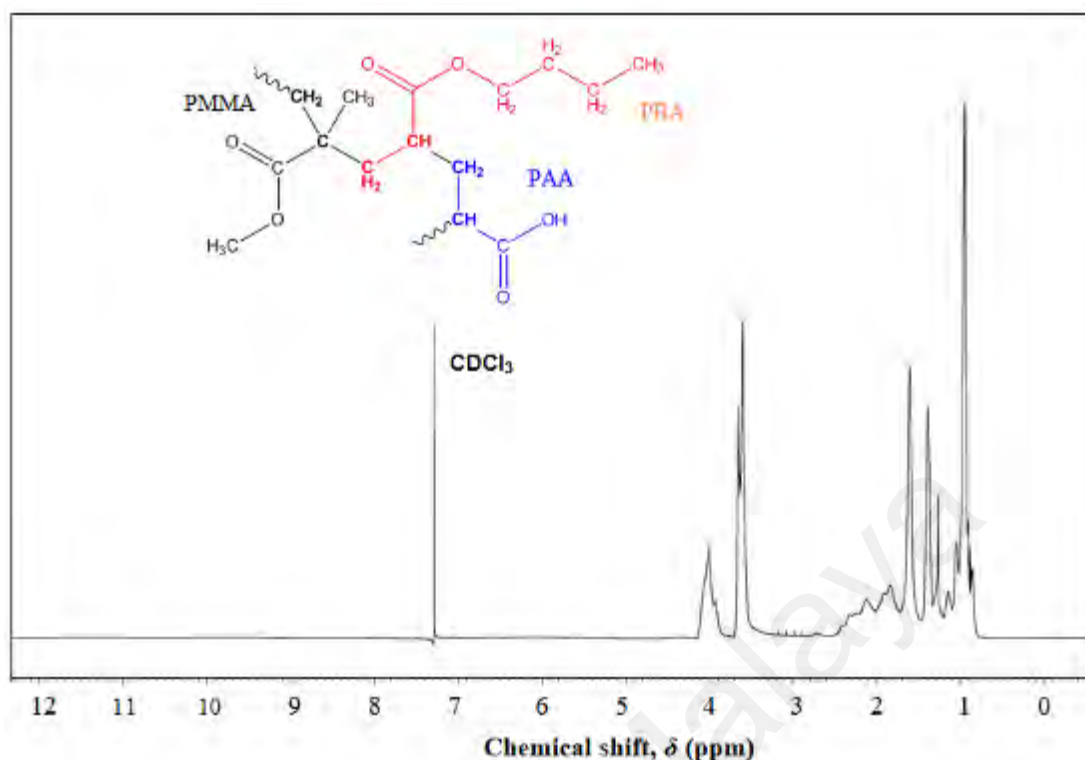


Figure 4.3: ^1H NMR of AA05 thin film measured at room temperature

Table 4.4: ^1H NMR chemical shifts of AA05

Polymer structure	Resonance type	Chemical shift, δ (ppm)
PMMA	-OCH ₃	3.6
	-CH ₂ [#]	1.6
	-CH ₃	< 1.0
PBA	-CH ₂ [#]	1.8
	-CH [#]	2.2 – 2.5 (centered lower than PAA)
	-OCH ₂ CH ₂ CH ₂ CH ₃	4.0 (a)
	(a) (b) (c) (d)	1.4/1.38 (b)
		1.2/1.26 (c)
	< 1.0 (d)	
PAA	-OH	Undetectable
	-CH ₂ [#]	2.1
	-CH [#]	2.2 – 2.5 (centered higher than PBA)

Note: The pound (#) symbol denotes the characteristic peak of proton/carbon backbone. The alphabets (a-d) label the signals.

In addition to qualitative identification, individual monomer conversion can be quantified by using the integration of chemical shifts (or ^1H NMR peak). In the case of MMA and BA, the calculation was performed using peak integration of ester functional group while AA conversion was determined from the $-\text{CH}$ signal. The calculation was performed according to the method reported by Arnold (2012).

$$\text{Monomer conversion (\%)} = \frac{\text{P.I. (polymer)}}{\text{P.I. (polymer)} + \text{P.I. (monomer)}} \quad (4.1)$$

where, P.I.(polymer) and P.I.(monomer) corresponds to integration area of polymer and monomer, respectively.

The conversion of individual monomer is presented in Figure 4.4. The total converted monomer percentage identified from this study is close to the values calculated using gravimetric method (Section 4.1.3).

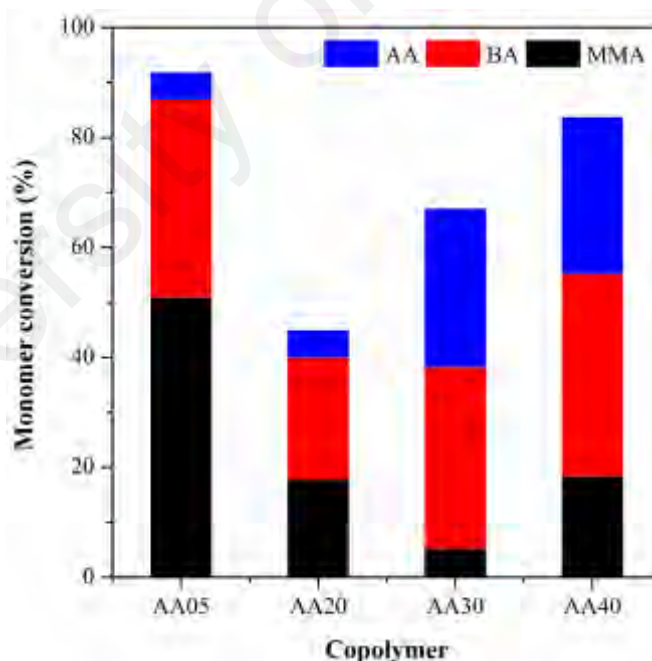


Figure 4.4: Monomer conversion of P(MMA-co-BA-co-AA) calculated from ^1H NMR

4.1.7 GPC

The average molecular weights (\overline{M}_w and \overline{M}_n) of P(MMA-*co*-BA-*co*-AA) are summarized in Table 4.5. All the copolymers have relatively high \overline{M}_w above 2.0×10^6 g mol⁻¹. By referring to the classification of polymer, it can be generally accepted that all the studied copolymers are UHMW polymer (Kitayama and Okubo, 2016; Visjager, 2001). The polydispersity index (PDI) for entire tested formulation varies from 4.3 to 23. Narrow molecular weight distribution (MWD) can be found in AA20 and AA30 formulations, with PDI of 4-5. Whereas broad MWD was observed in AA05 and AA40 samples, with PDI above 13. It appears that the copolymers with broad MWD show good colloidal stability (*e.g.* AA05 and AA40) as compared to that of the narrow MWD. The grit formation is prone to occur in AA20 and AA30 because the uniform chain length can pack easily and efficiently.

Table 4.5: Average molecular weights of synthesized P(MMA-*co*-BA-*co*-AA)

Copolymer	Average molecular weights (g mol ⁻¹)		PDI
	$\overline{M}_n \times 10^5$	$\overline{M}_w \times 10^6$	
AA05	1.29	2.01	15.4
AA20	5.26	2.44	4.3
AA30	4.19	2.05	4.9
AA40	0.92	2.12	23

4.1.8 TGA

The derivative weight loss (DTG) of pure P(MMA-*co*-BA-*co*-AA) with different compositions is shown in Figure 4.5. The thermogram is enclosed in the inset. All the copolymers exhibit continuous weight loss up to 500 °C. The initial weight loss from 30-150 °C can be ascribed to a dehydration process. The magnitude of weight loss during the dehydration process becomes intense with increasing AA content. This is owing to the increase in the -OH group that is susceptible to moisture absorption. Above 150 °C, a continuous weight loss happens with increasing temperature. This weight loss falls on

the decomposition temperature of SDS at 160-380 °C, as reported by Ramimoghadam and his coworkers (2012).

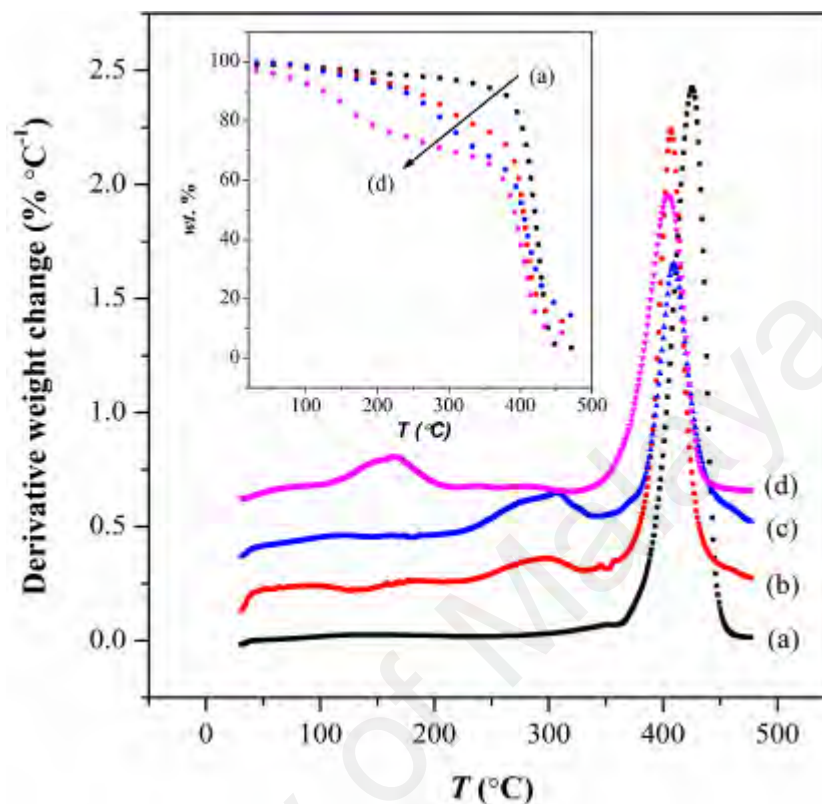


Figure 4.5: DTG curves of (a) AA05, (b) AA20, (c) AA30 and (d) AA40. The inset figure shows corresponding thermograms

Aside from SDS decomposition, the decomposition at 300 °C can be caused by:

- (i) decarboxylation of anhydride rings evolving water and carbon dioxide. The decarboxylation takes place on the six-membered glutaric anhydride rings, which are formed during the intramolecular cyclization of AA involving adjacent monomer units. The structure formation may gradually increase with increasing temperature along with decarboxylation.
- (ii) hemolytic cleavage of C-C bond. The hemolytic cleavage of C-C bond on another hand is catalyzed by the radicals that are formed during the cleavage of
 - (a) weak peroxide/ hydroperoxide linkages (these linkages are formed when monomer reacts with oxygen during the synthesis) and
 - (b) head-to-head (H-H)

linkages (these linkages are formed *via* coupling of the active radicals during termination process) (Gundogdu, 2012). The cleavage of these labile bonds may potentially cause the evaporation of oligomers at low temperature.

The process in (i) and (ii) are not visible in AA05 due to the low occurrence of decomposition. The same observation was seen in AA40, in which the massive weight loss at lower temperature overshadows these processes.

Above 400 °C, a massive weight loss can be observed in all the tested copolymers. Major structural disruption occurs at this stage *via* random chain scission and it forms volatile short chains. At this temperature, the decarboxylation also occurs simultaneously along with random chain cleavage. The T_d of AA05 at 425 °C shifts to lower temperature (~400 °C) with increasing AA segments. This may owe to the substitution of thermally stable MMA with AA chains segments. The recorded T_d values are presumably higher compared to that of P(MMA-*co*-BA), which falls in the range of 313-332 °C (Moldoveanu, 2005). This suggests that incorporation of AA segment in the copolymer chain enhances the thermal stability (Leskovac *et al.*, 1999). The total residual mass for all formulations at 480 °C is around 3 wt.% in AA05, and 10 to 13 wt.% in other three copolymer formulations. The copolymer with high PMMA content (AA05) undergoes quick depolymerization as compared to those of lower in PMMA contents (AA20, AA30 and AA40).

4.1.9 DSC

The T_g of pure P(MMA-*co*-BA-*co*-AA) is plotted in Figure 4.6. All the experimental T_g s fall in the range of 10 to 30 °C [$\Delta C_p = 0.4 \text{ J (g °C)}^{-1}$], which are at the intermediate range between individual homopolymers: PBA ($T_g = -45 \text{ °C}$), PMMA ($T_g = 105 \text{ °C}$) and PAA ($T_g = 106 \text{ °C}$). According to Zhang and coworkers (2017), the appearance of single T_g evidences the successful polymerization of random copolymer (Zhang *et al.*, 2017).

These copolymers belong to the classification of amorphous polymer as there is no visibility of crystallization and melting peak. A good fitting between experimental T_g and theoretical T_g (Gordon-Taylor) was obtained in formulations with high monomer conversion rate (e.g. AA05 and AA40) while those with poor conversion show deviation.

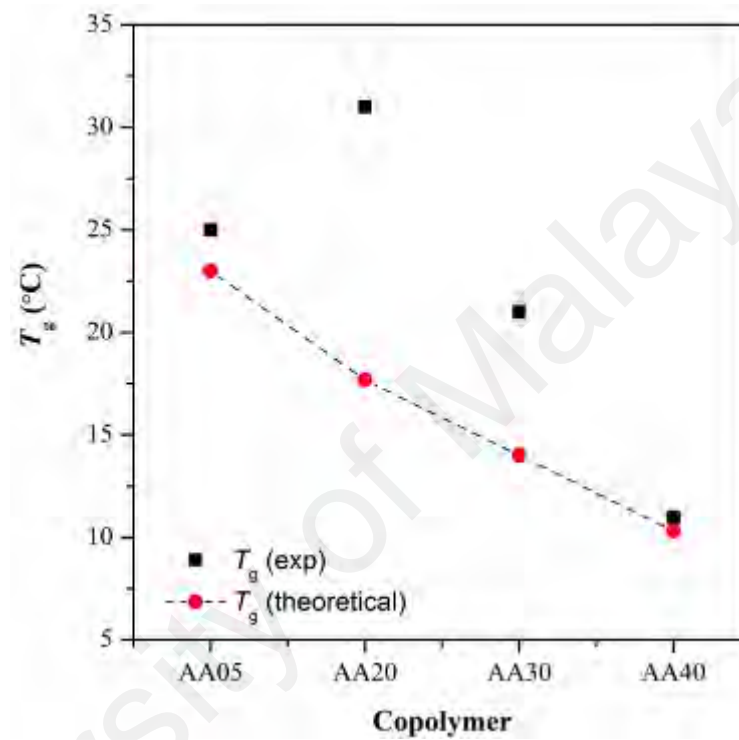


Figure 4.6: Experimental (■) and theoretical (---●---) T_g of P(MMA-*co*-BA-*co*-AA) calculated using Gordon-Taylor equation

4.1.10 Four Point Probe

Figure 4.7 shows the variation of R_{sheet} and R_{volume} of pure P(MMA-*co*-BA-*co*-AA).

The values were respectively calculated using Equations (4.2) and (4.3).

$$\text{Corrected } R_{\text{sheet}} (\Omega \square^{-1}) = \sum R_{\text{sheet}} \times 4.1712 \quad (4.2)$$

$$R_{\text{volume}} (\Omega \cdot \text{cm}) = \text{Corrected } R_{\text{sheet}} \times L \quad (4.3)$$

where, L represents the thickness of sample in cm

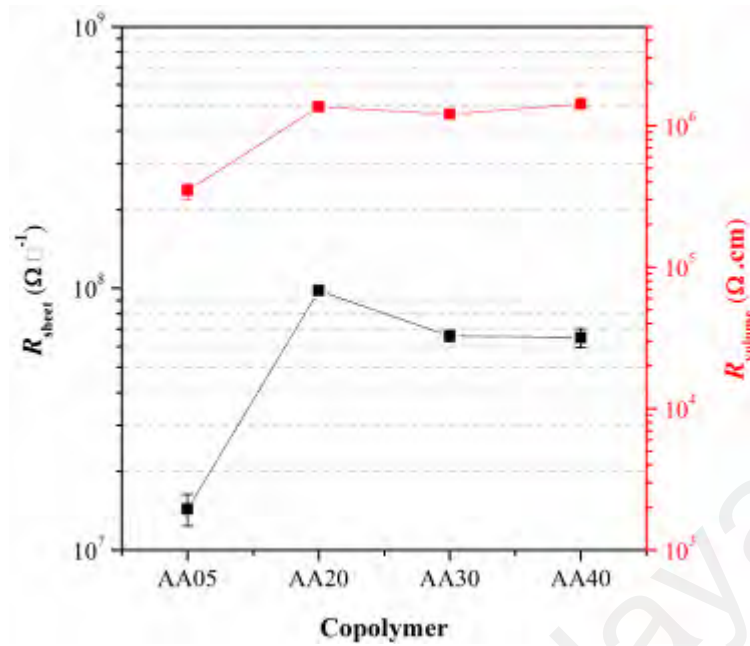


Figure 4.7: R_{sheet} and R_{volume} of P(MMA-co-BA-co-AA) measured at room temperature

A brief inspection from the results shows that the film resistivity of AA05 ($R_{\text{sheet}} = 1.43 \times 10^7 \Omega \square^{-1}$, $R_{\text{volume}} = 3.48 \times 10^5 \Omega \cdot \text{cm}$) increases drastically in AA20 and later decreases progressively in AA30 and AA40. The highest recorded resistivity value in AA20 may be correlated to the poor segmental dynamics (highest M_w) and lowest free volume concentration. Low free volume may be present in AA20 as the chains in this formulation have almost similar chain length (narrow PDI) that allows compact chain packing. All these effects restrict the current flow. The suppression of these effects in AA30 and AA40 results in lower resistivity.

In general, all the R_{sheet} values are higher than the R_{volume} . This exemplifies that the current flow on the film surface is lower than the bulk. Comparing the results with those of other UHMW polymers, the calculated values are considerably lower, *i.e.* UHMW PE recorded R_{sheet} of $10^{13} \Omega \square^{-1}$ and R_{volume} of $10^{18} \Omega \cdot \text{cm}$. Typically, the UHMW polymers (including UHMW PE) possess high resistance due to the poor dynamics of long polymer chain (high chain entanglement). However the effect exhibited in UHMW

P(MMA-*co*-BA-*co*-AA) is lower which is due to the (i) low T_g that gives better dynamics at chain ends, and (ii) high free volume availability at room temperature. High free volume may be available when films that had been dried at 60 °C are cooled to room temperature. This process causes frustration in the chain packing. Both effects (*e.g.* chain dynamics and free volume) are prominent in AA05 as compared to other formulations based on the lowest recorded resistivity value.

4.1.11 Tensile property

The tensile property of P(MMA-*co*-BA-*co*-AA) is shown in Figure 4.8. AA05 has a tensile strength (TS) of (19.3 ± 3.5) MPa with elongation-at-break (ϵ) of (30 ± 13) %. The low elongation-at-break in this sample is due to the adjacent pendant groups that eliminates slip between polymer chains. This causes PMMA to be rigid and brittle. With further increase of AA content to AA20, the TS reduces with a compromised increase in the ϵ . The reduction of TS is attributed to the low presence of PMMA chain segments. However, the AA20 chains have better reconfiguration due to the increased in the intermolecular hydrogen bonding (Park *et al.*, 2013). The subsequent increment of AA (AA30 and AA40) however does not show significant improvement to their ϵ . Instead, they possess similar TS to that of AA05. The consistent increment of ϵ with AA content (AA20, AA30 and AA40) can be ascribed to the presence of more carboxylic groups that form intermolecular hydrogen bonding between the polymer chains.

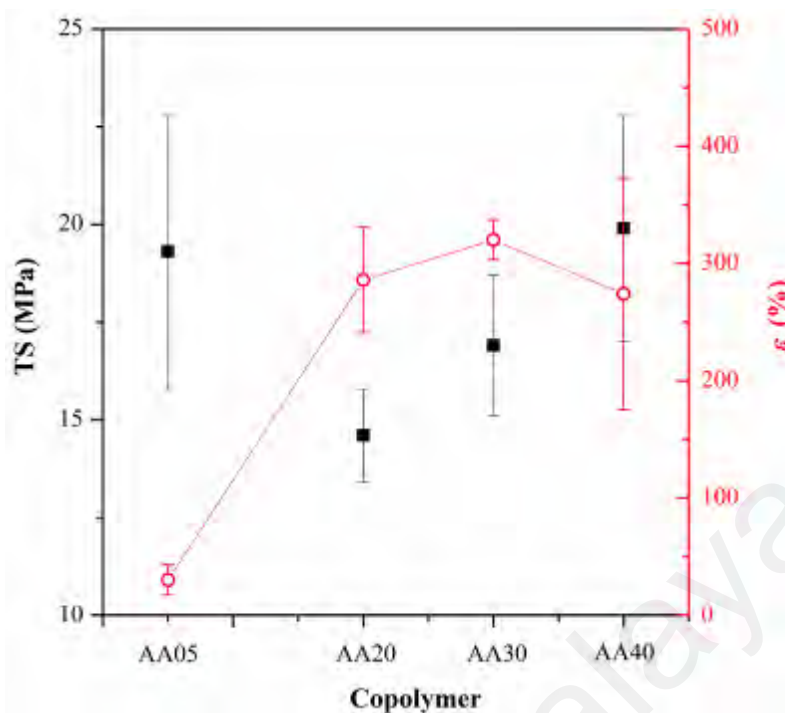


Figure 4.8: Tensile measurement of P(MMA-*co*-BA-*co*-AA) at room temperature

4.2 Summary

Random P(MMA-*co*-BA-*co*-AA) was synthesized in this study *via* emulsion polymerization upon initiation with persulfate radicals. The successful synthesis was confirmed from FTIR analysis through the disappearance of C=C absorption peak, and from assignment peaks in ^1H NMR. By using the preset experimental conditions, UHMW copolymer was obtained. This copolymer offers a number of competitive advantages as the host polymer for PSSE formulation over the conventional polymers (M_w ranges in hundreds of thousands). To name a few, (i) high availability of polar sites in long chain polymer provides good salt dissociation and (ii) low chain dynamics allow the polymer chains to be loosely packed at temperature below its T_g . Despite having large M_w , the copolymer exhibits low T_g (< 40 °C). This value is lower than what would have been expected for UHMW polymer. Low T_g is beneficial in the processing of UHMW polymer, and shall be kept to minimum as there would be a rise in T_g of PSSE upon doping with salt/plasticizer/NPs.

All the properties of formulated copolymers in this work show good suitability as the host polymers for PSSE. Nevertheless, the choice can be narrowed down to AA05 and AA40 due to the high monomer conversion efficiency. Between these two formulations, AA05 was selected owing to its low emulsion viscosity. Lower viscosity offers better flexibility during processing (drying time, temperature, *etc.*) especially when it involves bulk production during commercialization. Other appealing characteristics of AA05 includes good solubility in a wide range of solvents, high colloidal stability at prolonged storing in emulsion, low surface resistivity and high thermal stability. Another point to add on the suitability of AA05 is the amorphous nature (*cf.* Section 5.7) that grants better prospect in high conducting electrolytes development. All the characteristics of AA05 film were found to comply closely with the general properties of base polymer that had been discussed earlier in Chapter 2.5. In addition, this copolymer has low moisture uptake owing to the low –OH group from low AA content (result not shown). Thus, the AA05 film has good dimensional stability upon casting.

4.3 Photo-degradation of AA05

4.3.1 FTIR

Changes to the chemical structure (bond scission/forming) of AA05 before and after UV-irradiation were monitored using the FTIR spectra in Figure 4.9. No peak shift was observed in the UV-irradiated samples in reference to the non-irradiated sample. However, a small change in the peak intensities can be observed upon UV-irradiation. This evidences the chemical change. The bands that undergo prominent changes are the functionalities of hydroxyl (O–H at $\nu = 3225 \text{ cm}^{-1}$), carbonyl (C=O at $\nu = 1726 \text{ cm}^{-1}$) and ester (C–O–C at $\nu = 1160$ and 1142 cm^{-1}) moieties. The FTIR characteristic peaks of the afore-mentioned functionalities are alphabetically labeled in the FTIR figure as; (a) O–H, (b) C=O and (c) C–O–C. The O–H characteristic peak, which represents AA segments within the copolymer

chain, decreases in peak intensity upon irradiation [cf. Figure 4.9 (inset)]. This is due to the photo-oxidation reaction of O–H group, which results in the formation of oxidized products containing C=O chromophores (Andrady *et al.*, 1996; Wang *et al.*, 2005; Sionkowska, 2006; Prasad *et al.*, 2011).

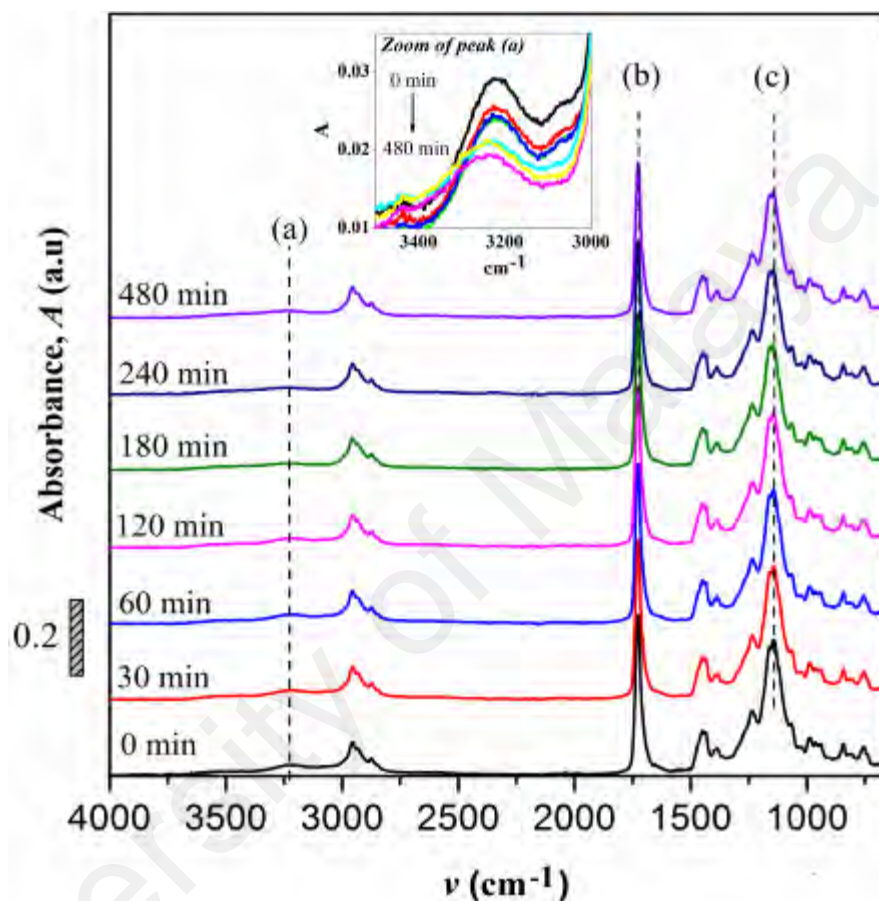


Figure 4.9: FTIR spectra of non-irradiated and irradiated AA05

For the functionalities of carbonyl and ester moieties, the changes are conversed based on the plotted carbonyl index ($C.I.$) and ester decomposition (D_{ester}) shown in Figure 4.10 and 4.11, respectively. The $C.I.$ value was obtained by normalizing the characteristic absorbance peak of C=O with respect to the absorbance of $\nu(\text{C}-\text{C})$ peak at 752 cm^{-1} , shown in Equation (4.4) (Wang *et al.*, 2005):

$$C.I. = \frac{A_{1726\text{cm}^{-1}}}{A_{752\text{cm}^{-1}}} \quad (4.4)$$

where A represents the absorbance of peak. To calculate the ester decomposition value, Equation (4.5) was employed:

$$D_{ester}(\%) = \left(\frac{A_o - A_t}{A_t} \right) \times 100\% \quad (4.5)$$

where A_o and A_t represent the absorbance value of C=O band at 1726 cm^{-1} before and after irradiation, respectively.

Based on the *C.I.* plot, it is understood that the C=O concentration reduces during the initial irradiation and the concentration increases gradually with increase in irradiation time. The initial drop in chromophore concentration is associated to photo-destruction of π bond in C=O. The degraded C=O later reacts with another radically active C-O• site that adjacent in coordination and forms crosslinked structure rather than chain scission. The absence of chain scission at short irradiation time is well supported by the unchanged number of ester decomposition unit, as seen at 30 min of irradiation in Figure 4.11. At prolong irradiation, an exponential increase in C=O concentration was observed as subsequent of the cleavage of crosslink bonds. Therefore, increase in ester decomposition units is accounted. The ester cleavage is more intense above 240 min of irradiation time, indicating an abrupt increase in the decomposed ester unit. The photo-products that may form upon degradation cannot be detected in this measurement since most of the characteristic absorption bands of the products overlap in the same region. The mechanism of bond destruction and bond forming in C=O chromophore during UV-irradiation is further discussed in UV-Vis-NIR spectroscopy.

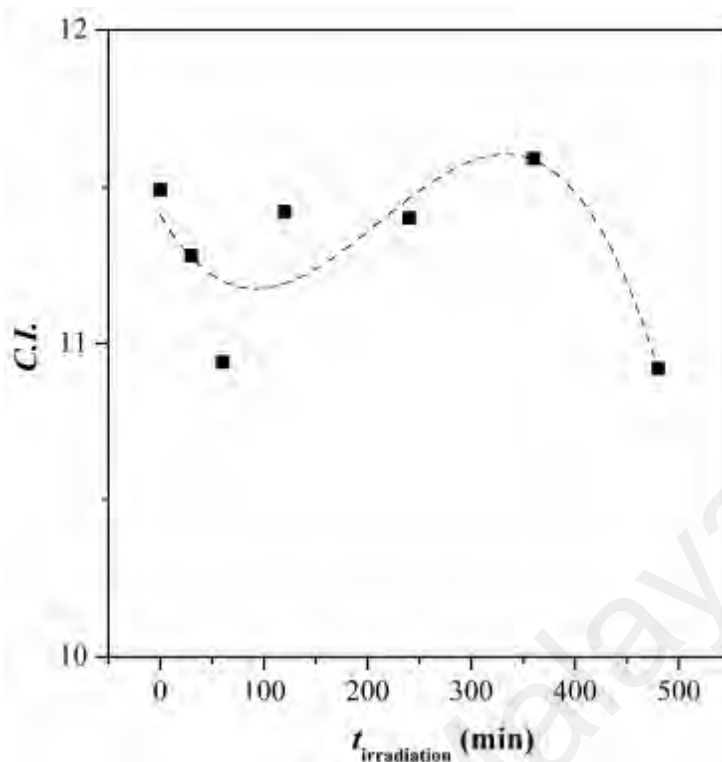


Figure 4.10: Carbonyl index of AA05 at different irradiation time (dashed line is for visual aid)

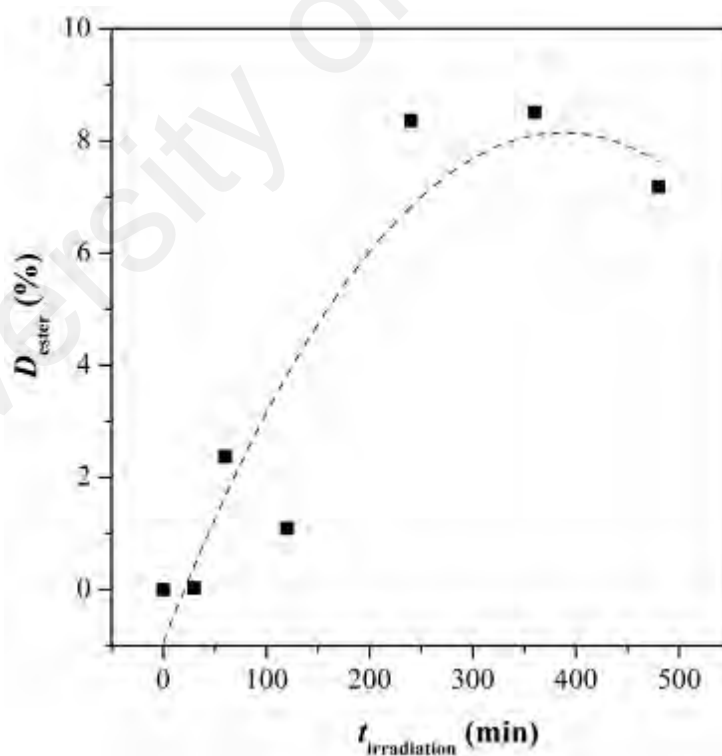


Figure 4.11: Decomposed ester unit of AA05 at different irradiation time (dashed line is for visual aid)

4.3.2 UV-Vis-NIR Spectroscopy

UV-Vis-NIR spectroscopy is used as a supplementary tool to support the observed changes in C=O concentration during irradiation. The overlay UV-Vis-NIR spectra measured for both non-irradiated and irradiated samples are presented in Figure 4.12. All the test samples show an appearance of two absorption bands in the UV region: one peak below 250 nm and another within 250 to 350 nm. These peaks correspond to the characteristic bands of conjugated unsaturation and carbonyl chromophores, respectively. There is no appearance of new absorption band after UV-irradiation. This implies the absence of new chromophore structure formation. The changes in the C=O characteristic peak as function of UV irradiation time is the only focus of the discussion.

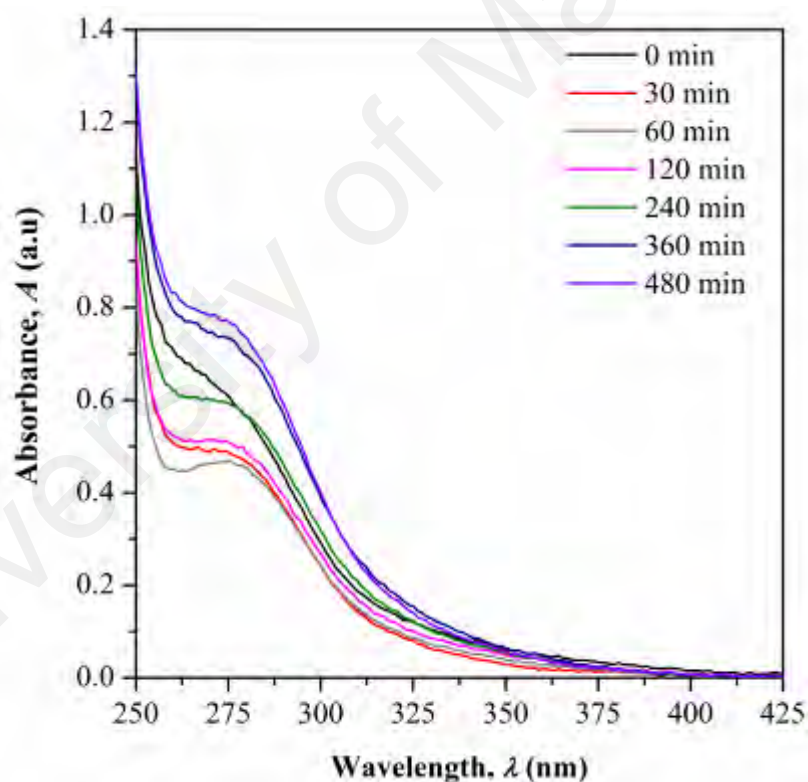


Figure 4.12: UV-Vis-NIR absorption spectra of AA05 before and after UV irradiation

In the spectrum of non-irradiated sample, a shoulder-like curve appears within the studied wavelength as the copolymer contains the C=O functional group in its structure. When the sample was irradiated to 60 min, a more defined peak with reduced intensity can be

observed. With further increase of irradiation time, a broader shoulder with increasing intensities can be observed. The initial decrease of peak intensity is associated to the reduced C=O concentration as effect of photochemical disruption of π bond in C=O. Electron in the π bond undergoes photo-excitation from ground to higher energy state ($\pi \rightarrow \pi^*$ transition) and cleaves the bond (Calcagno *et al.*, 1992; Kumar *et al.*, 2011; Kushwaha *et al.*, 2014). This consequently generates active radicals at the C–O•, which then reacts further with the side chain of the adjacent monomer units forming crosslink structure *via* oxygen bridge. Crosslink reaction is prone to occur at low irradiation time due to ‘cage’ recombination of the primary radicals (Wochnowski *et al.*, 2005).

With increased irradiation time, the C=O peak becomes broader and increases in intensity. This may arise from the cleavage of the initially formed crosslink bond during photo-excitation of sigma (σ) electron in C–O. As the consequence, free radicals are generated at the cleaved sites and rearrange themselves to form stable structure. This gives high chances for the regeneration of C=O group. The increment in C=O concentration with irradiation time well supports the occurrence of photo-degradation on the surface of AA05. Photo-oxidation process is also possible to take place simultaneously with the degradation as the irradiation was performed in air. The proposed mechanism of AA05 photo-degradation is summarized in Appendix D.

4.3.3 GPC

GPC was employed to study the changes in the copolymer chain length upon photolytic and/or crosslink reaction at different UV-irradiation time. Variation of \overline{M}_n and \overline{M}_w is presented in Figure 4.13. Result shows that there is an increase of average-molecular weights with increase irradiation up to 60 min. The increase of molecular weights can be linked to the crosslink process. At longer exposure, these values drop rapidly implying random chain scission. During the chain scission, the copolymer chains cleave and cause a reduction in the

kinetic length (decrease in \overline{M}_n values). As the result, the degradation rate increases progressively and P(MMA-*co*-BA-*co*-AA) loses its chemical/mechanical integrity over time. These changes then affect the ability of the materials to perform adequately in some applications and give rise to safety concern. There are two photolysis mechanisms occur during irradiation of UV such as chain scission or unzipping. These mechanisms may occur simultaneously. In finding for the most favorable mechanism that takes place during irradiation, theoretical discussion by Wochnowski and coworkers (2005) was considered. It was reported that the decrease in the molecular weight associated to unzipping process is slower than those observed for photo-degradation (Wochnowski *et al.*, 2005). Referring to this theoretical view, we propose that the immense reduction of \overline{M}_w during initial irradiation is associated to random chain scission. This effect prevails at prolong irradiation time.

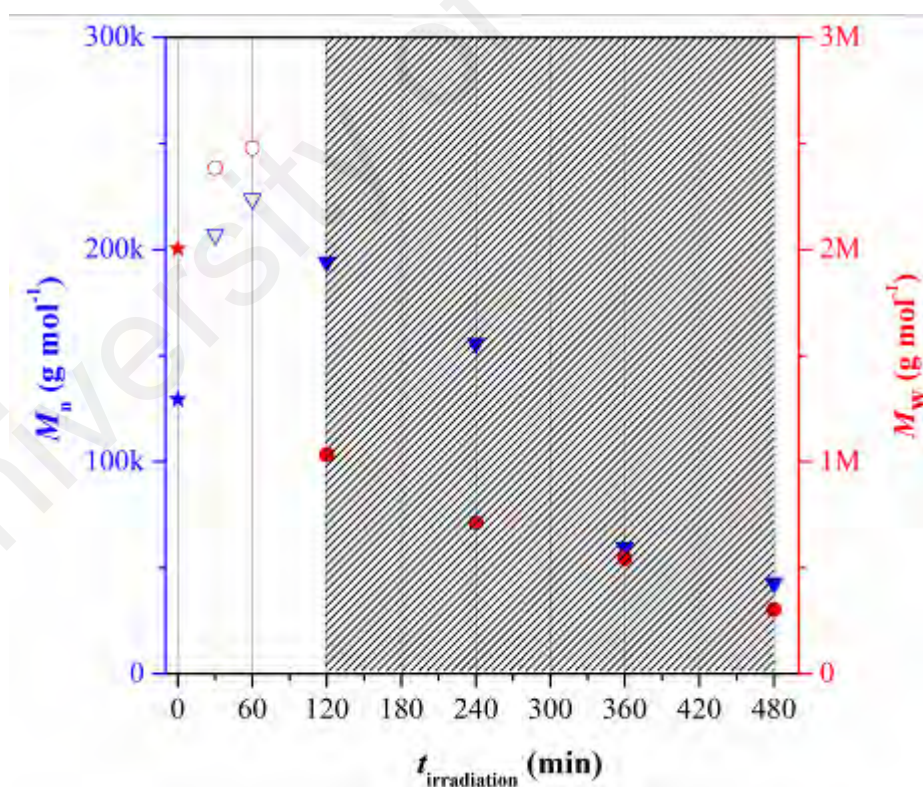


Figure 4.13: Molecular weights of P(MMA-*co*-BA-*co*-AA) at different UV irradiation time. Symbols representation; ★/★: Non-irradiated sample, ▼ and ●: Irradiated samples (open symbol-crosslink structure and filled symbol-fragmentation). Dense region showed degraded samples.

4.3.4 Chromaticity analysis

Chromaticity analysis was performed to study the color changes in copolymer upon UV-irradiation. The color data (L^* , a^* , b^* , C^* and ΔE^*) is presented in Table 4.6. For the non-irradiated sample, it is slightly yellowish due to the presence of C=O functional group. As the copolymer film is irradiated, the sample experiences a quick lightening and shifts towards blue coordination. The shift is caused by a loss of yellowness (b^*) and redness (a^*) on the surface. The decrease of a^* and b^* values is consistent with the reduction of C=O concentration (yellow color reflecting chromophore) (Domb *et al.*, 1998). The reduction dictates formation of crosslink structure at low irradiation time. Upon 60 min of irradiation, the bluish color gradually intensifies and the C^* and ΔE^* values increase. Improvement in the lightness (or brightness) of non-irradiated sample at shorter UV irradiation time implies the materials applicability in optical- and packaging-based development.

At 120 min of irradiation, the color shifts towards yellow coordination as the effect of increasing C=O concentration. The accompanied reduction in L^* value dictates the former observation to be caused by chain scission. With prolong irradiation time, non-linear changes in L^* , a^* and b^* values were observed. The color change at each irradiation time is not noticeable owing to the low color intensity.

Table 4.6: Chromaticity data for AA05 as the function of irradiation time

Irradiation time (min)	L^*	a^*	b^*	C^*	ΔE^*
0	98.30	0.01	0.26	0.2602	0
30	100.54	-0.18	-1.93	1.9384	3.1384
60	105.06	-0.15	-3.54	3.5430	7.7565
120	99.52	-0.10	-0.52	0.5295	1.4522
240	102.52	-0.13	-0.89	0.8994	4.4842
360	99.37	-0.23	-1.51	1.5274	2.0822
480	99.65	-0.08	-1.56	1.5620	2.2678

4.3.5 AFM study

The surface morphology of copolymer upon UV-irradiation can be visualized from 2D-AFM images shown in Figure 4.14. Only the images of degraded samples at 120 min, 240 min and 480 min of UV-irradiation were reported. The changes of morphology are understood using the non-irradiated copolymer as the reference. In the non-irradiated copolymer [Figure 4.14(a)], the surface exhibits a compact chain arrangement with uniform heights. This arrangement is more diffusive upon UV-irradiation above 120 min, as shown in Figure 4.14(b) and (c). The changes on surface architecture are caused by the scission of crosslink bond (oxygen bridge) and ester/hydroxyl bond. This subsequently causes separation between the compactly joined copolymer chains, and the fraction of free volume increases.

As the irradiation time prolongs to 480 min, significant amount of copolymer chains are cleaved. The short segment chains are loosely bound on surface (due to massive free volume surrounded) and may possibly be etched. This results in major irregularities in the structure shown in Figure 4.14(d). The increase irregularities on the surface structure are quantitatively validated by the increase of arithmetic mean roughness (R_a). The values increase from 8.4 nm (in reference sample) to 17.1 nm, 31.0 nm and 32.7 nm upon irradiation at 120, 240 and 480 min, respectively. Chain scission is the most probable cause for the increase in morphology irregularities at prolonged irradiation (Azevedo *et al.*, 2013).

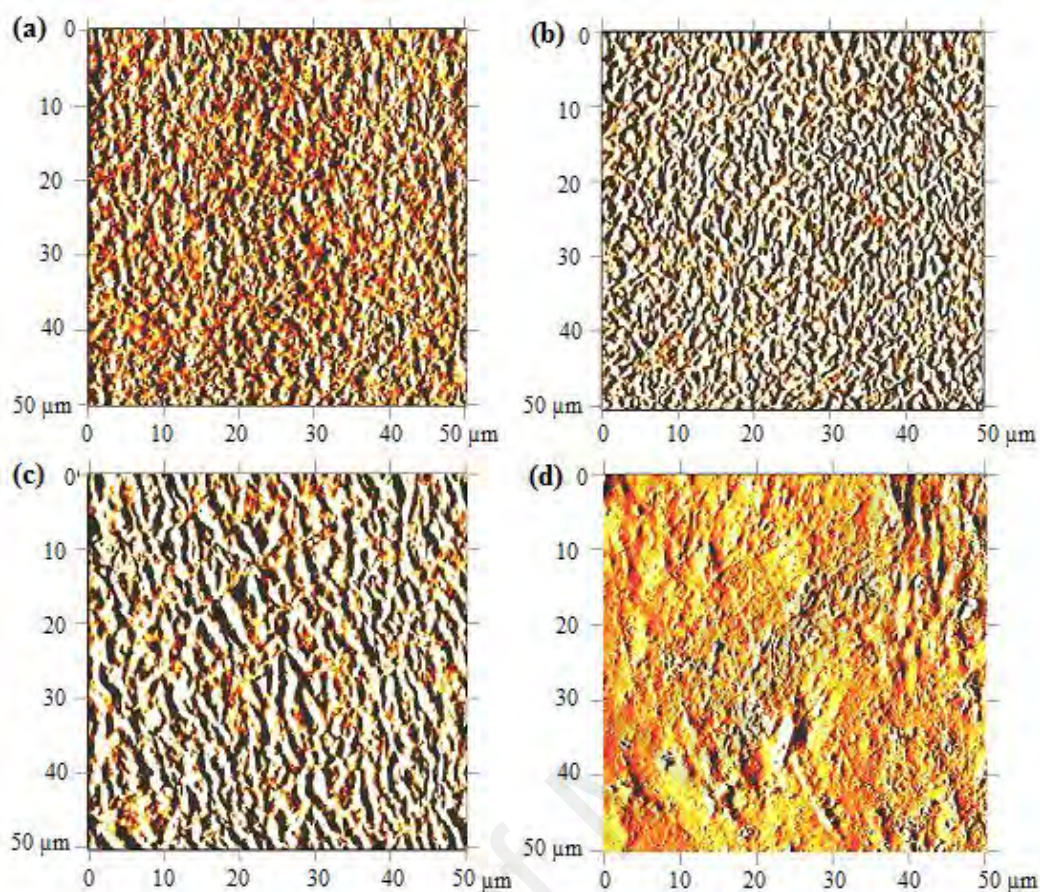


Figure 4.14: AFM images of AA05 (a) before and after UV irradiation at (b) 120 min, (c) 240 min, and (d) 480 min

4.3.6 TGA

Figure 4.15 depicts the TGA curves of non-irradiated and photo-irradiated AA05. All the weight loss curves of irradiated samples exhibit similar shape as the non-irradiated sample. The difference can be seen from the shift of T_d and weight loss. UV-irradiated samples were found to have low affinity towards water based on the reduction in the weight loss during dehydration process (<150 °C). The weight lost decreases with increasing irradiation time. This happens as the subsequent of photo-oxidation of O–H bond. This observation is supported by the reduced FTIR peak intensity at 3100 to 3400 cm^{-1} .

Other obvious changes in UV-irradiated sample is the occurrence of weight loss in between 150 and 250 °C accompanied with shift of T_d from 425 (non-irradiated sample) to

409 °C. Both observations exemplify a reduction of thermal stability in AA05 upon UV-irradiation. The loss of thermal stability is associated to the increase of weak linkages that are formed during photolytic reaction. Therefore, degradation occurs at low temperature, *i.e.* T_d reduces. The average residual mass in all tested samples is lower than 5 wt.% at 650 °C.

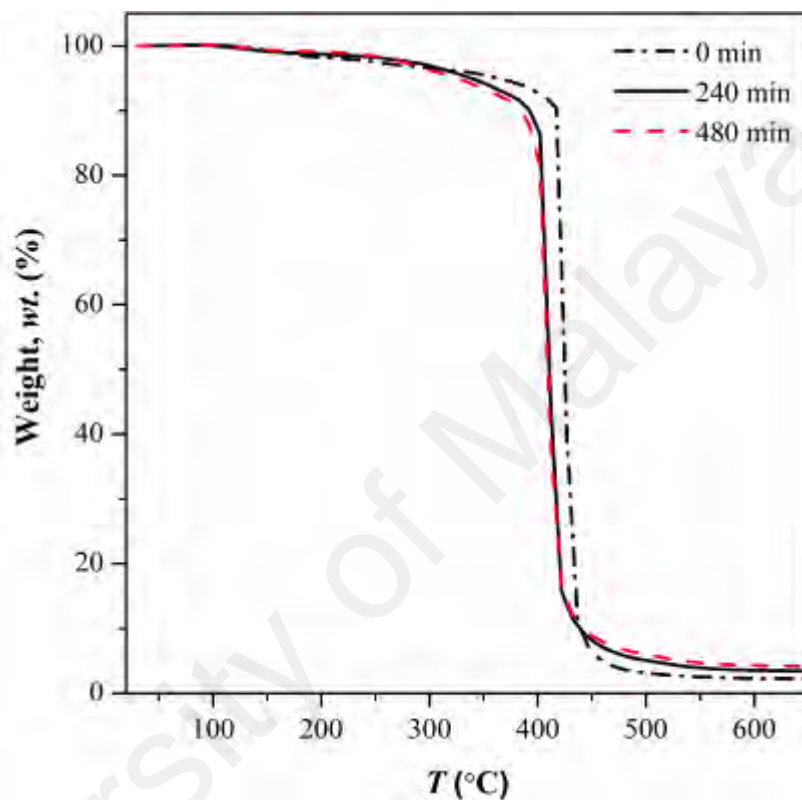


Figure 4.15: Thermogram of AA05 before and after UV irradiation

CHAPTER 5: RESULTS AND DISCUSSION

Characterization of PSSE: System I- NaI variation

Note: The following terms are used concurrently from Chapter 5 to 7

1. ‘Ion’ represents Na^+ and I^-/I_3^- (redox mediator)
2. ‘Ion population’ is also referred to ‘number of ions’
3. ‘Ion pairing’ occurs due to ion association and this is also represented by “ion pair” and ‘multiplets’
4. ‘Ion transport’ refers to ions hopping. The word ‘transport’ is represented by ‘mobilization’, ‘hopping’ and ‘motion’

5.1 Chain relaxation time

5.1.1 Room temperature measurement

Figure 5.1 depicts the chain relaxation time (τ_{chain}) of NaI-PSSE. The values were calculated by substituting $Z''_{\text{max}}(f)$, obtained from Lorentzian peaks in $Z'/-Z''$ vs. frequency plot, into Equation (5.1). The Z''_{max} , in here, represents the value at Lorentzian peak maxima (*i.e.* Appendix E).

$$\frac{1}{\tau_{\text{chain}}} = 2\pi f_0 \quad (5.1)$$

where, f_0 is the frequency at Z''_{max} .

The calculated τ_{chain} shows non-continuous variation with increasing NaI doping as the result of difference formation of temporary coordination between Na^+ and polymer chain. At low NaI content (in NaI-5), the chain shows a tendency of relaxation (or be in static motion) at 10^{-5} s. The value drops by one order in NaI-10 and consistently reduces with minor change until NaI-20. The drop in τ_{chain} exemplifies the increase in chain dynamics. Obvious drop can be seen in NaI-10, which could arise from the strongest

suppression in the polymer crystallinity. This is associated to the increased Na^+ complexation that causes bulky-side chains to form and create more free volume. Above this composition (till NaI-20), the bulky side-chain structure grows in the least favorable way even with increasing ion population. In NaI-25, the formation of bulky-side chains is completely halted and this further induces the ions, in particular of Na^+ , to form a crosslink with polymer chains (Na^+ acts as a transient crosslink). As the result, chains are more localized. This phenomenon is rationalized from the increased in the τ_{chain} value.

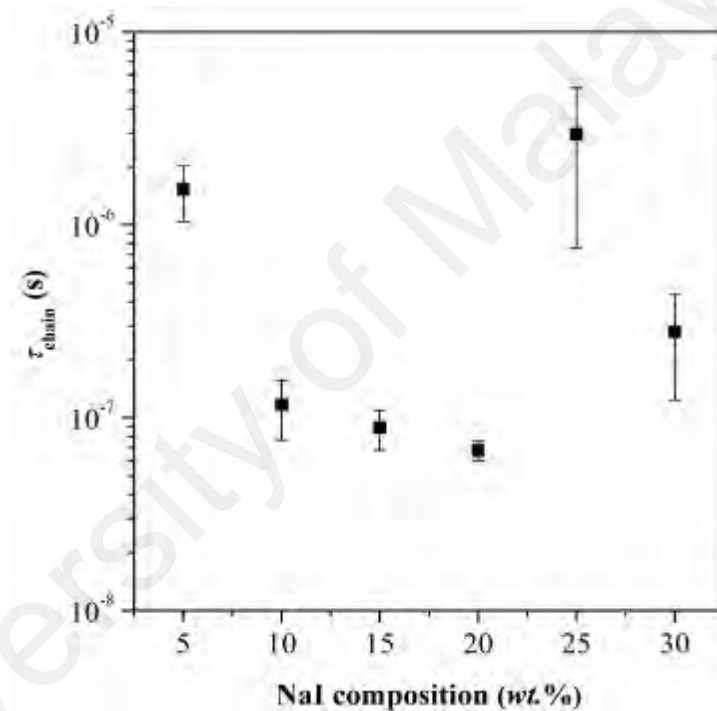


Figure 5.1: Chain relaxation time as the function of NaI content in NaI-PSSE

In NaI-30, the chain dynamics slightly improve based on the decrease of τ_{chain} . The improvement of chain dynamics after a drastic drop is typically resulted from the disruption of crosslink structure, making more ions to be freed. The freeing of ion may then associate to form ion pairs. The presence of ion pairs in this case is confirmed through the non-Debye characteristic of $Z'/-Z''$ vs. frequency plot (non-crossing of Z' and Z'' at Z''_{max}). The presence of contacting ions can also be observed in other NaI-

PSSE compositions such as NaI-10, NaI-15 and NaI-20. The above claim is confirmed in Section 5.5 using Nernst-Einstein equation.

5.1.2 Temperature variation

The effect of temperature on the chain dynamics of NaI-PSSE can be understood based on the shift of $Z''_{\max}(f)$ in Figure 5.2 (a-d). The τ_{chain} was calculated for NaI-PSSE results presented in Figure 5.2(a), (d) and (e); the calculation was excluded in remaining samples since the shift of $Z''_{\max}(f)$ between temperatures is minimal. All the calculated data is plotted in Figure 5.2(f).

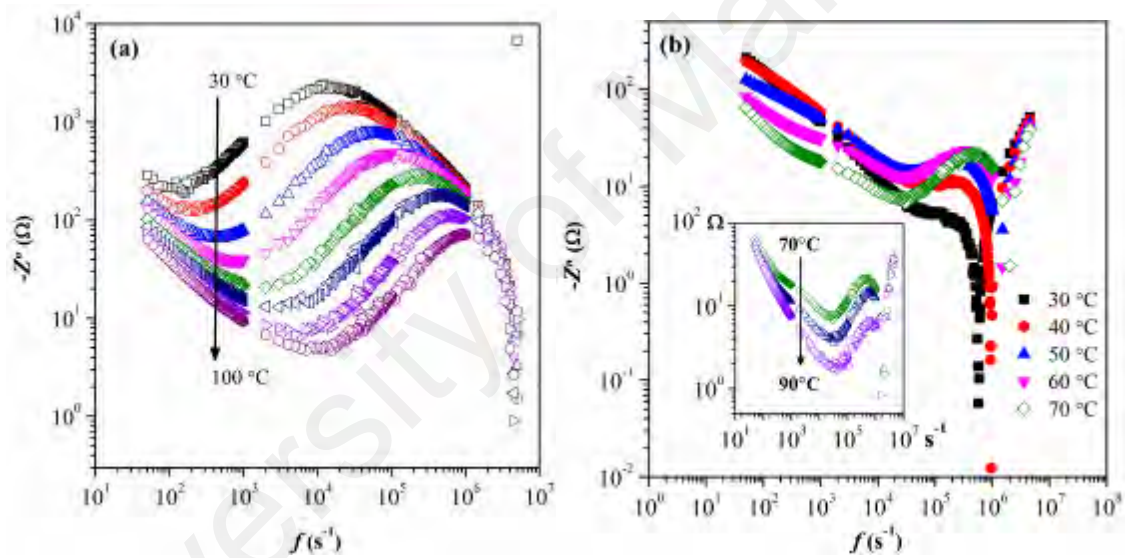


Figure 5.2: Plot of $-Z''$ vs. f as the function of temperature for (a) NaI-5 (b) NaI-10, (c) NaI-15, (d), NaI-20, (e) NaI-25 [Note: The filled marker represents data below T_c], and (f) τ_{chain} of selected samples

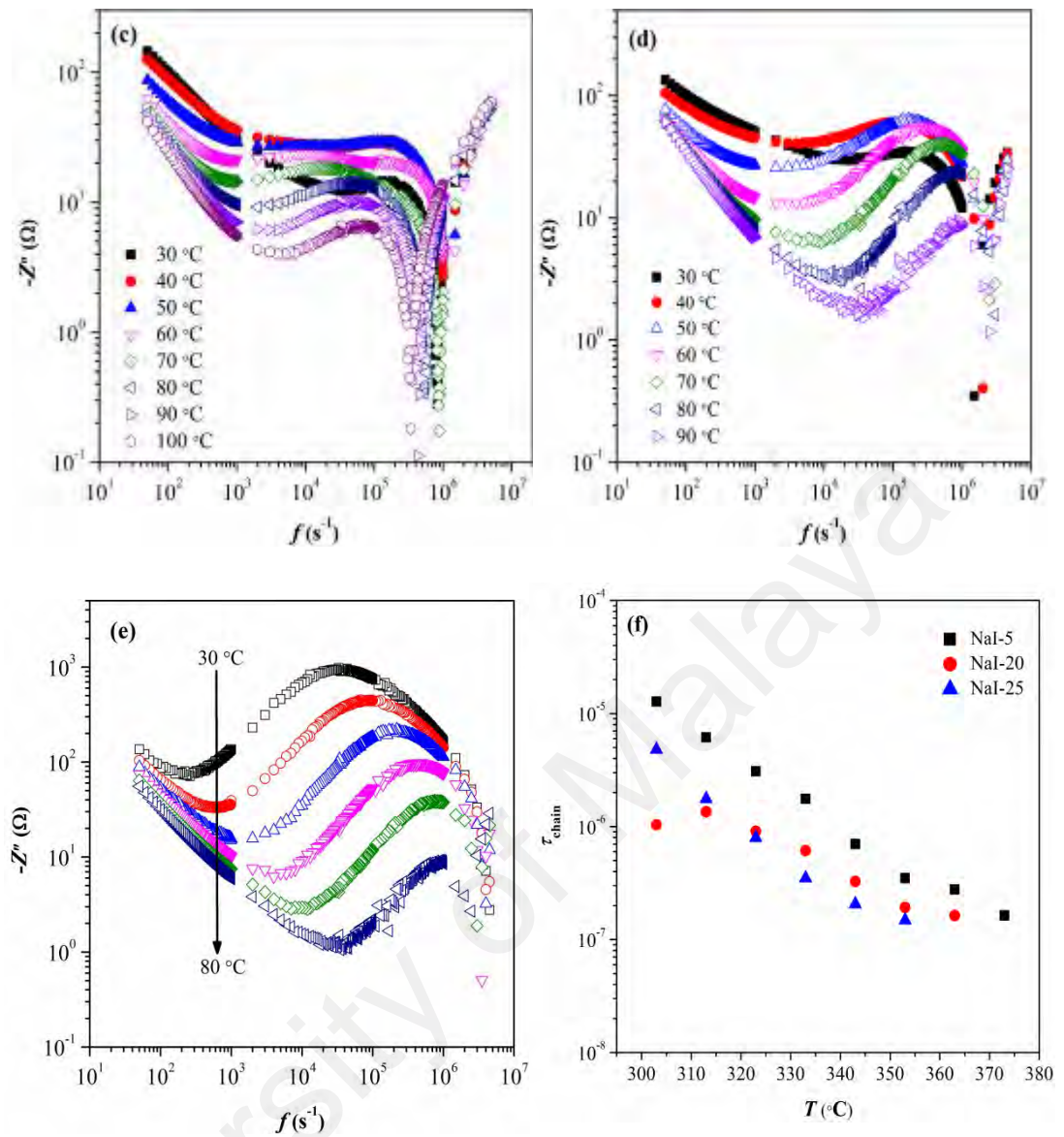


Figure 5.2, continued

Briefly from the illustrated results, a minor shift of $Z''_{max}(f)$ to higher frequency was seen in NaI-5 and NaI-25 over the entire tested temperatures. However in NaI-10, NaI-15 and NaI-20, the $Z''_{max}(f)$ remains constant approaching a critical temperature (T_c): 60 °C (in NaI-10), 50 °C (in NaI-15) and 40 °C (in NaI-20). Surpassing this temperature, $Z''_{max}(f)$ shifts slightly to higher frequency with temperature increment and the change turns insignificant at high temperature. The displacement of $Z''_{max}(f)$ to either higher or lower frequency depicts a rise and lowering in chain dynamics, respectively. Both phenomena are influenced by the increased of ion population. In some instant, the

chain dynamics increase when more ions (that are formed during thermally-activated process) form complexes with the polymer chain. The complexation causes chain-chain separation (through bulky side-chain structure formation) and gives better chain flexibility. The increase in chain flexibility is seen from the reduced τ_{chain} as a function of temperature [*cf.* Figure 5.2(f)]. However when the ions act as the transient crosslinker, the polymer chains become more localized. The $Z''_{\text{max}}(f)$ may stay constant when there is no further complexation with increasing ions population.

Nearly all the $-Z''$ curves are similar, except to that of NaI-15. In NaI-15, a flattening of $-Z''$ curve occurs between the frequency of 10^4 and 10^5 s^{-1} at $40 \text{ }^\circ\text{C}$ and $50 \text{ }^\circ\text{C}$. Approaching $60 \text{ }^\circ\text{C}$ and $70 \text{ }^\circ\text{C}$, a new broad peak is visible within the frequency region, and it disappears at higher temperature. The appearance of new $Z''_{\text{max}}(f)$ peak suggests that there is additional phase with different chain relaxation time. The detail of this new phase is further discussed in Section 5.8.1. The result for NaI-30 was excluded as the Z''_{max} peak could not be assigned. The presence of contacting ions is visible through the non-crossing behavior of Z' and $-Z''$ at $Z''_{\text{max}}(f)$ (the results are not presented here). The tendency grows stronger with temperature. This is reasonable considering that more ions are formed during thermal activated process.

5.2 Nyquist plot

5.2.1 Room temperature measurement

Nyquist plots for the entire formulated NaI-PSSE compositions are shown in Figure 5.3. They are enclosed with the equivalent Randles circuit (RC). The physical parameters obtained from Nyquist plot (*e.g.* f_0 , R_Ω , R_{CT} and R_b) were labeled in one of the representative curves and the figure can be found in Appendix F.

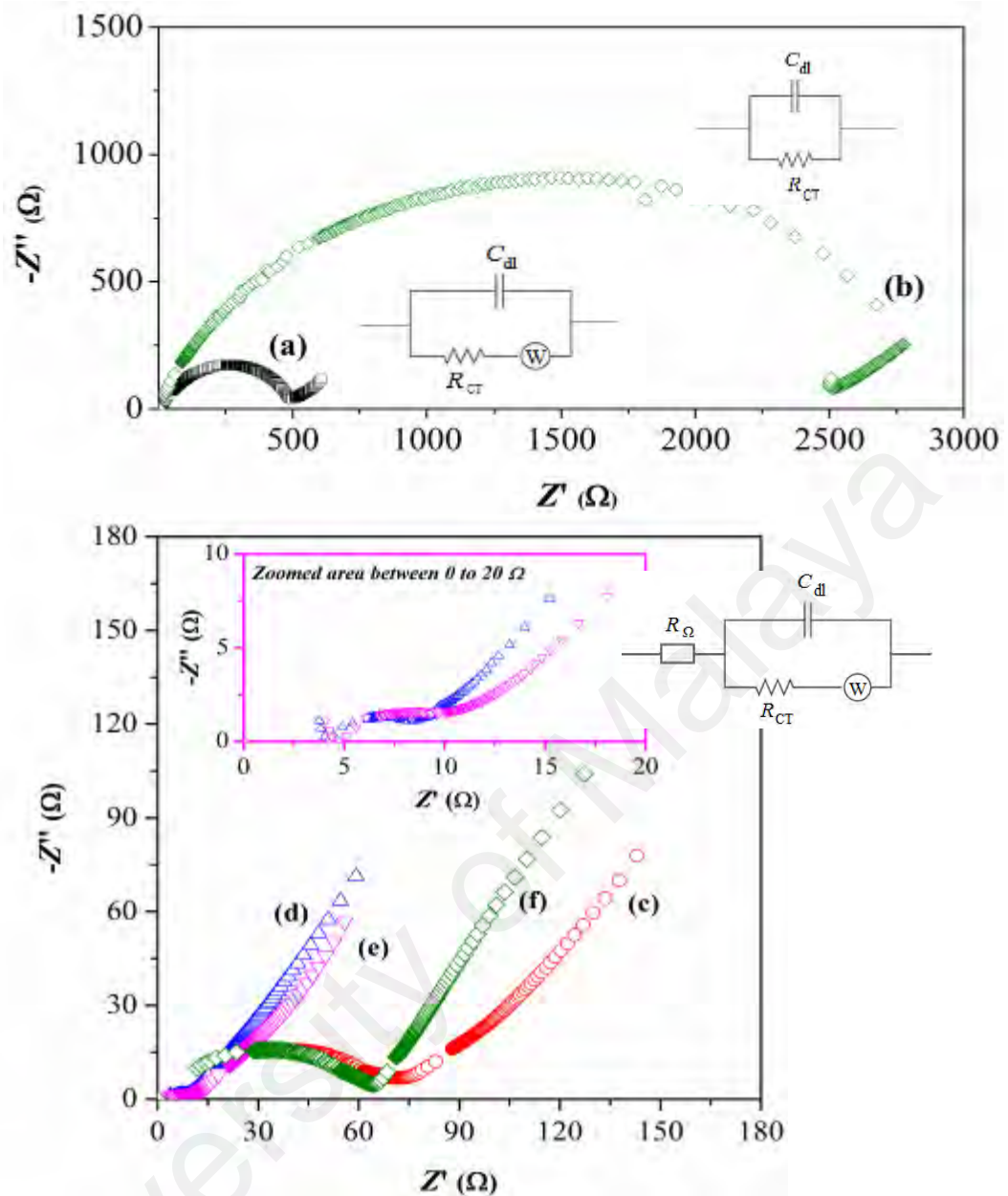


Figure 5.3: Nyquist plot of NaI-PSSE and its representative RC circuits: (a) NaI-5, (b) NaI-25, (c) NaI-10, (d) NaI-15, (e) NaI-20 and (f) NaI-30

All the Nyquist plots except NaI-25 show a semicircle at high frequency and a spike at approximately 45° gradient at low frequency. In NaI-25, the spike is not visible. The appearance of semicircle shows the parallel combination of charge-transfer resistance (R_{CT} ; is the resistance to ions mobility) and double layer capacitance (C_{dl}), whereas the spike represents the Warburg impedance (W). Additional spike at high frequency in NaI-15 and NaI-20 is characterized by ohmic resistance (R_{Ω}). This characteristic is also

present in NaI-10 and NaI-30 as the semicircle cuts through non-zero x -axis. The C_{dl} value (or the thickness of double layer at the electrode-electrolyte interface) was determined using Equation (5.2) and the result is shown in Figure 5.4. This parameter is discussed later in Section 5.4.

$$\omega = \frac{1}{R_{CT}C_{dl}} \quad (5.2)$$

where, ω represents the angular frequency ($\omega = 2\pi f_0$)

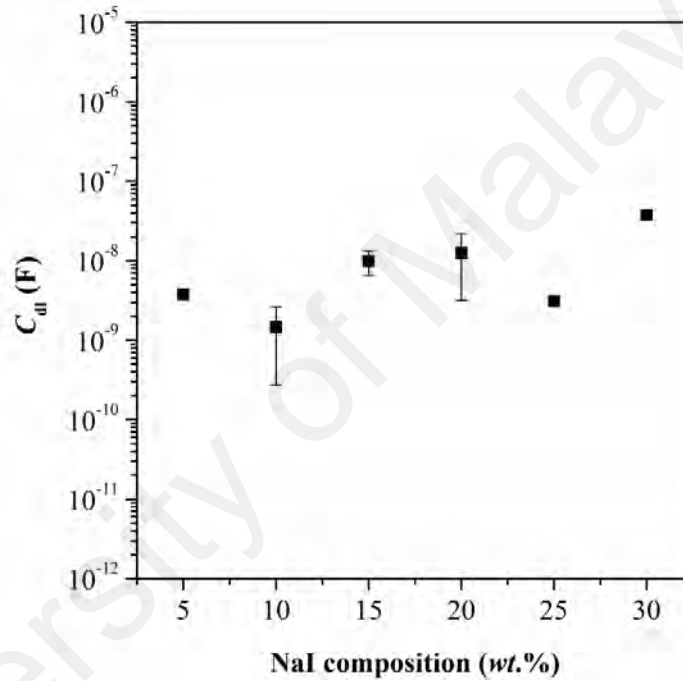


Figure 5.4: C_{dl} of NaI-PSSE at room temperature

In NaI-5, the impedance semicircle starts from zero. At higher NaI loading (e.g. NaI-10 and NaI-15), the semicircle depresses and there is a shift of x -axis intersection away from zero (existence of R_{Ω}). The depressed semicircle decreases R_b (substantially the R_{CT}). This suggests an increase in the ion transport, which could arise as the consequence of fast formation of fully stabilized network (f_0 reduces). The faster formation of stabilized network is attributed to the increase of chain dynamics, as manifested by the shift of $Z''_{max}(f)$ to higher frequency in Section 5.1.1. The progressive

decrease in the resistance toward ion diffusion from NaI-5 to NaI-15 allows higher ions to diffuse at the electrode-electrolyte interface and forms thicker C_{dl} layer. The change however turns insignificant in NaI-20 as the consequence of minor change in the physical parameters of Nyquist plot. This suggests that NaI-20 has achieved saturation point. The appearance of R_{Ω} ($\sim 4 \Omega$) in these samples exemplifies restriction in the ions mobility at high frequency. According to Cesiulis and coworkers (2016) and Zhang and coworkers (2015), the impediment is caused by the high presence of ion.

A major increase in resistivity can however be observed in NaI-25. The poor ion transport (reduced in R_{CT}) is resulted by poor chain dynamics, and this gives rise to lower C_{dl} thickness. At further NaI doping (NaI-30), a lower resistivity was recorded. The ions have increased mobility ascribing to the increased segmental dynamics and allows thicker C_{dl} layer to form. This happens when Na^+ is freed from interacting with polymer chain. The increase of segmental dynamics however does not lower the restriction in ion transport at high frequency (based from the appearance of $R_{\Omega} \neq 0$).

Among the assigned RC circuits, only those of NaI-5 and NaI-25 follow ideal capacitor while others deviate from ideality due to the presence of contacting ions (ion pairs). The presence of contacting ions can be seen from the non-Debye characteristic of $Z'/-Z''$ vs. frequency plot (non-crossing of Z' and Z'' at Z''_{max}). Examples of the plot can be found in Appendix E. According to Kumar and coworkers (2014), formations of contacting ions are very likely to happen in iodide-based electrolytes as the iodine have high tendencies to form multiplet (Kumar *et al.*, 2014).

5.2.2 Temperature variation

The Nyquist curves of NaI-PSSE as the function of temperature are shown in Figure 5.5(a-e). Based on the plot representation of NaI-5 and NaI-25, the resistance towards

ion transport is suppressed with increasing temperature (R_b and R_{CT} decrease). This occurs as the consequence of increasing segmental dynamics [increase in $Z''_{max}(f)$, cf. Figure 5.2], which allows faster formation of fully stabilized network (f_o shifts to higher frequency). As the formation of ions is a thermally-assisted process, the overcrowding of ions during initial temperature increment (30 °C) causes slight impediment to their mobility ($R_\Omega \neq 0$). This effect reduces with further increase of temperature as visualized from the reduction of R_Ω . General RC circuits for these NaI-PSSE compositions are shown in Figure 5.5(f). The RC does not follow ideal capacitor owing to the presence of ion pairs (non-Debye curves are not presented here).

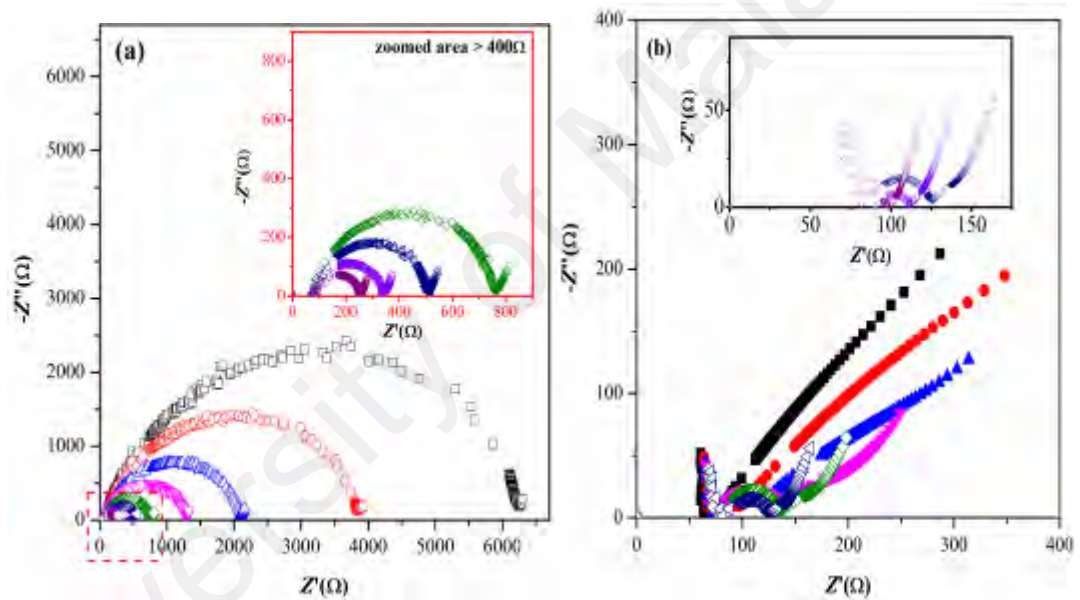


Figure 5.5: Nyquist plot of NaI-PSSE as function of temperature: (a) NaI-5, (b) NaI-10, (c) NaI-15, (d) NaI-20, (e) NaI-25; and (f) RC circuit representation [Legend: 30 °C (\square), 40 °C (\circ), 50 °C (\triangle), 60 °C (∇), 70 °C (\diamond), 80 °C (\triangleleft), 90 °C (\triangleright) and 100 °C (\circ); filled marker represents the increasing resistivity trend, open marker represents the decreasing resistivity]

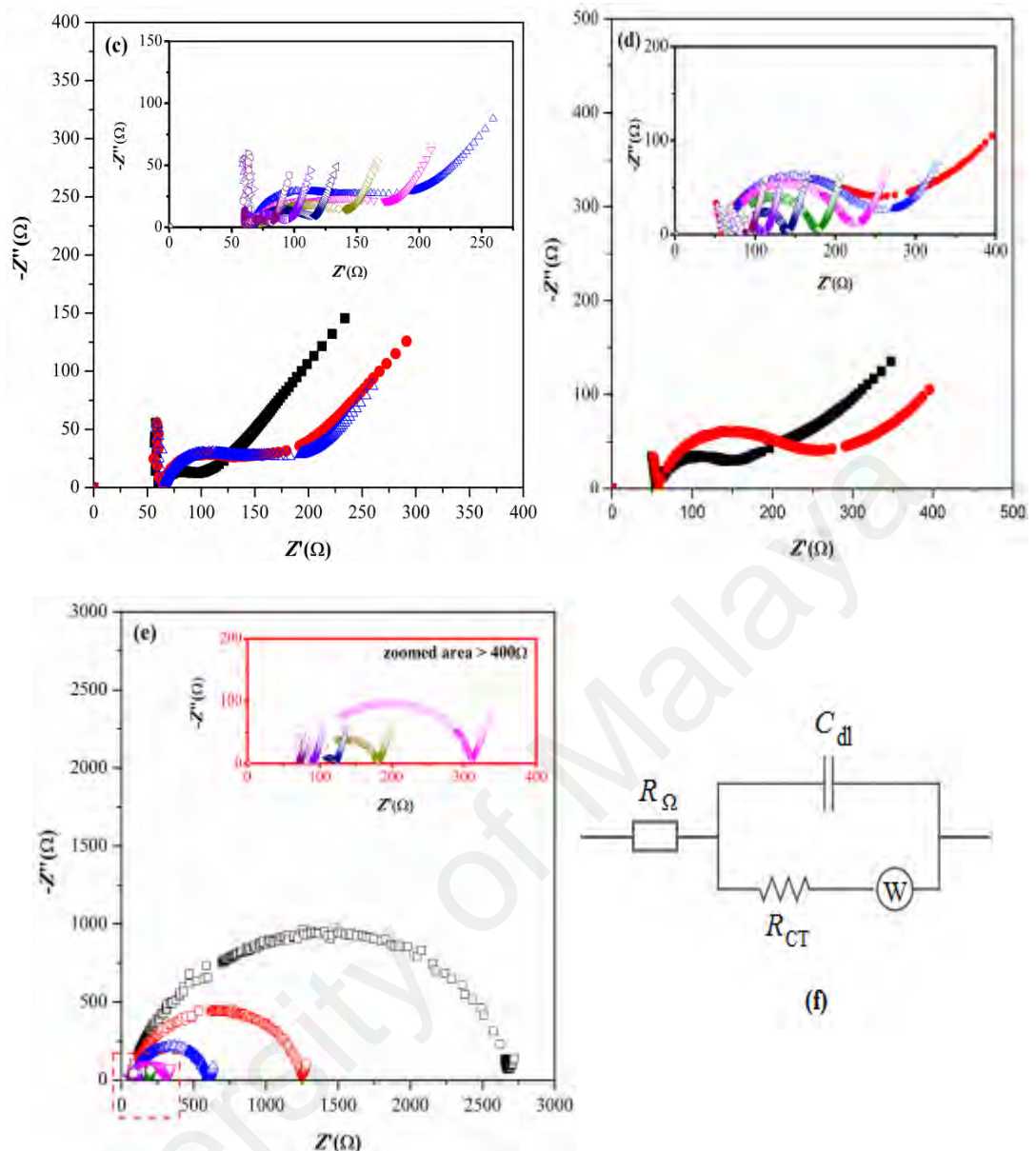


Figure 5.5, continued

From NaI-10 to NaI-20, impediment of ion transport can be seen from the increased R_{CT} up to T_c . The reduced ion mobility is substantial caused by the reduced segmental dynamics, which delays the formation of fully stabilized network. Surpassing the T_c : 60 °C (in NaI-10), 50 °C (in NaI-15) and 40 °C (in NaI-20), a depression in semicircle was observed. Quantity f_0 shifts to higher frequency with increasing temperature. This illustrates the quicker formation of stable network for ions hopping with increased NaI content. The extended semicircles in NaI-10 (60 to 70 °C) and NaI-15 (40 °C to 80 °C) coincide with the overlapping of semicircles, which progressively transforms into single

semicircle at higher temperature. At the temperature with overlapping semicircles, more than a single mode of ion transport with different mobility speed can be observed. The restriction of ions mobility at high frequency can be seen from the appearance of R_{Ω} . This value remains constant throughout the studied temperatures.

The data for NaI-30 was set aside as there was irregularity in the R_b and f_o trends with increasing temperature. This characteristic PSSE closely resembles the thermodynamically instable ion pairs. The C_{dl} component in RC circuit was not quantified here because the value fluctuates with increasing temperature.

5.3 Ion relaxation time

5.3.1 Room temperature measurement

Figure 5.6 shows the overlay loss tangent ($\tan \delta$) curves of NaI-PSSE measured at room temperature. A broad relaxation peak with single peak maxima (f_{max}) was observed in all the test results. This broad peak represents the segmental mode relaxation (Kumar *et al.*, 2014). The inverse of f_{max} [angular frequency (ω)] corresponds to the relaxation time of segmental-assisted ion motion (τ_{ion}), which is presented in Figure 5.7. The τ_{ion} is treated as a distribution value rather than a single time constant owing to the appearance of broad relaxation peak.

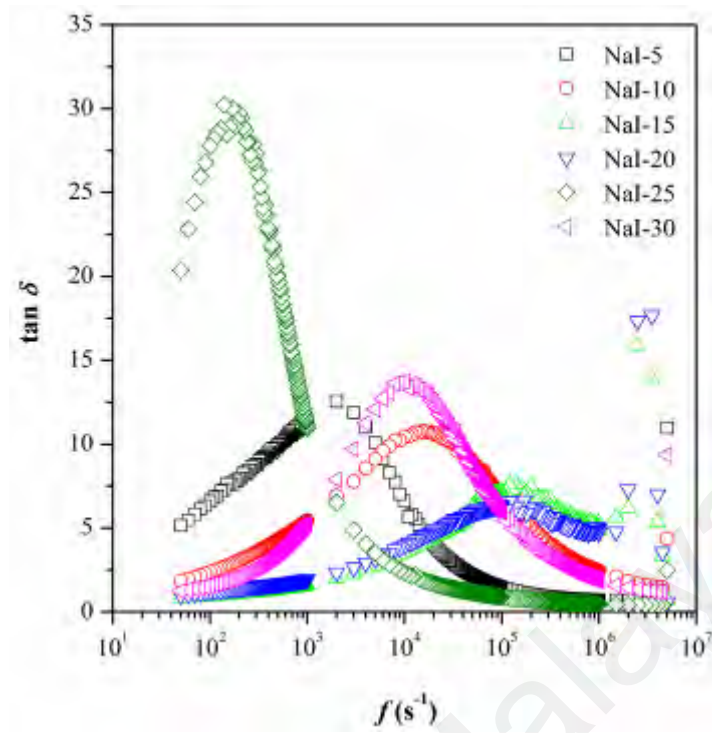


Figure 5.6: Variation of $\tan \delta$ as the function of NaI content (results from selected trial)

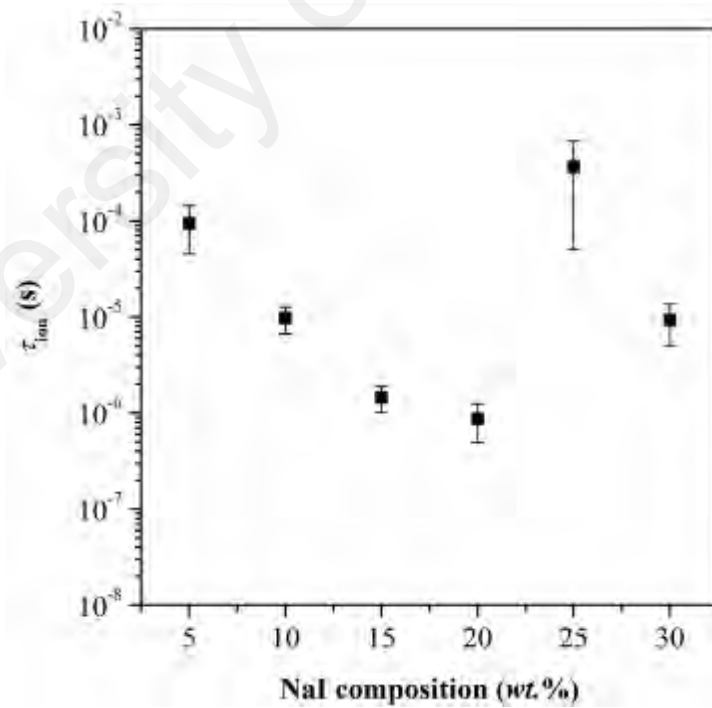


Figure 5.7: Ion relaxation of NaI-PSSE at room temperature

In Figure 5.6, the broad relaxation peak shifts to higher frequency with increasing NaI content from 5 to 15 wt.%, and the change results in a reduction of τ_{ion} . This exemplifies increase in segmental-assisted ion motion. Ions may have better mobilization as consequence to the reported increase of segmental dynamics in Section 5.1.1. This signifies that the ion transport is coupled with polymer chain dynamics. The ion transport is facilitated by relaxation process. In addition to this mode of ion transport, the occurrence of self-ion diffusion (hop *via* oscillating ion pairs) was also detected in these compositions based on the reduced $\tan \delta_{\text{max}}$ (Kumar *et al.*, 2014).

In NaI-20, an insignificant improvement in the segmental-assisted ion motion was observed as the f_{max} is merely unchanged. This could arise when optimum complexation between NaI and copolymer chains was attained, causing no increase in structural disorderliness. When more NaI is doped (in NaI-25), the overcrowding of ions gives rise to transient crosslink structure formation, as evident by the shift of f_{max} to lower frequency. This structure thereby impedes the chain dynamics and subsequently restricts the segmental-assisted ion motion (increased in τ_{ion}). The absence of self-ion diffusion, as indicated by the increase of $\tan \delta_{\text{max}}$, further proves the higher ion interaction with polymer chain.

The stronger occurrence of self-ion diffusion in NaI-30 illustrates the freeing of Na^+ from interacting with polymer chain and forms ion pairs. This gives better chain dynamics and further improves the segmental-assisted ion motion (τ_{ion} increases). Aside from segmental-assisted ion motion and self-ion diffusion, a localized motion of ions ('ion mode' relaxation) is possible. This phenomenon is dominant in NaI-5 and NaI-25. According to Fu and coworkers (1991), the frequency of 'ion mode' relaxation is at least two orders of magnitude below the frequency of segmental mode relaxation (Fu *et al.*, 1991). Similar observation was reported by Furukawa and coworkers (2002). In our

case, the relaxation peak is out of the studied frequency range. The initial data that starts above zero energy lost in Figure 5.6 supports the observation of ‘ion mode’ relaxation.

5.3.2 Temperature variation

Figure 5.8 shows the variation of $\tan \delta$ vs. f plot with temperature for NaI-PSSE. Stronger segmental-assisted ion motion can be seen above 25 °C. This is evident from the increase of $\tan \delta_{\max}$ with temperature. The τ_{ion} values were not determined; instead the trend was estimated from the inverse of f_{\max} . Based on the increasing trend of f_{\max} with temperature in NaI-5 and NaI-25, it can be deduced that ion relaxes at the coordination site with increasingly shorter time and consequently lead to faster segmental-assisted ion motion. This occurs simultaneously with increasing chain dynamics. Whereas in NaI-PSSE containing 10 to 20 wt.% of NaI, the ion transport that is mediated *via* segmental-assisted motion is increasingly restricted when temperature increases close to T_c (f_{\max} decreases). The ions have tendency to self-diffuse. Above the T_c , ions have better segmental-assisted ion motion accompanied by higher suppression of self-ion diffusion (increased of $\tan \delta_{\max}$).

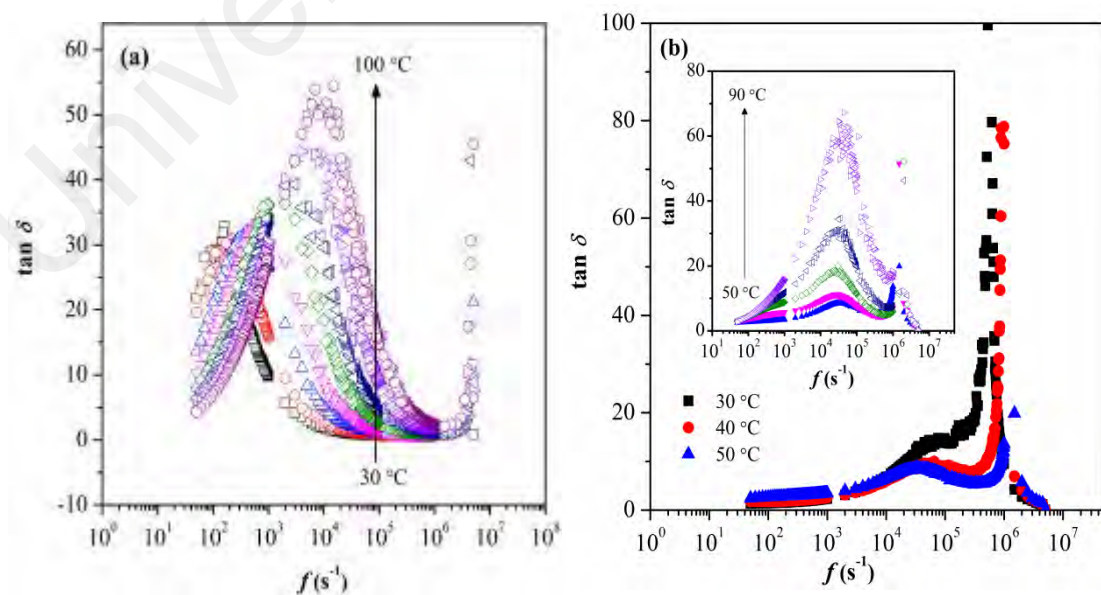


Figure 5.8: Loss tangent delta of NaI-PSSE as the function of temperature: (a) NaI-5, (b) NaI-10, (c) NaI-15 (d) NaI-20 and (e) NaI-25

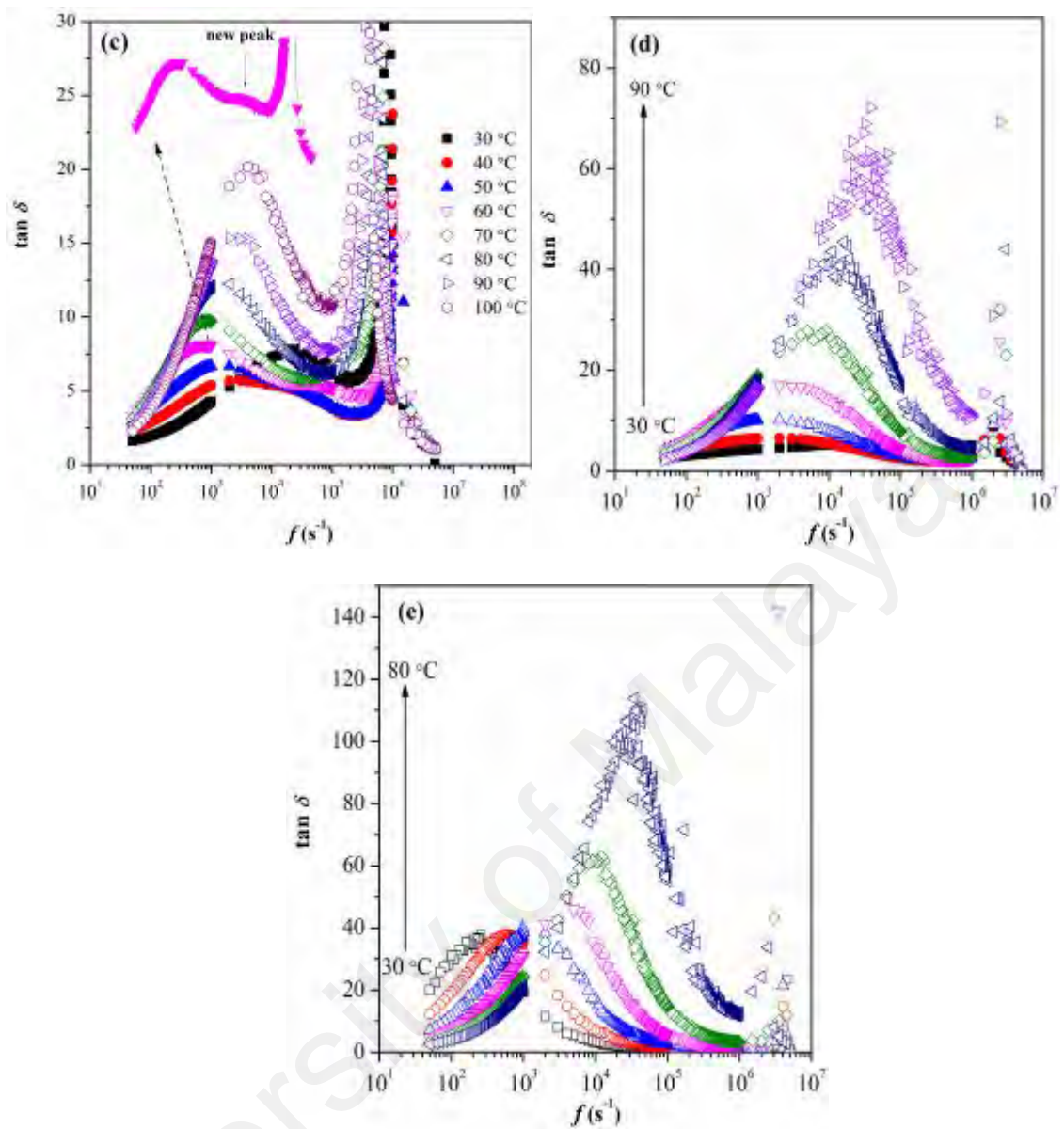


Figure 5.8, continued

All the test results show single relaxation peak with increasing temperature, except for NaI-15 (two relaxation peaks). During the initial increment of temperature, the width of relaxation peak increases. At 60 °C, a small new peak appears at high frequency (10^4 - $3 \times 10^5 \text{ s}^{-1}$) and later diminishes above 70 °C. This additional peak can only appear when there is a formation of new chain structure. It is further elaborated in Section 5.8.1.

5.4 Frequency-dependent ionic conductivity

5.4.1 Room temperature measurement

Figure 5.9 shows the frequency-dependent conductivity spectra of NaI-PSSE at room temperature. The spectra depict continuous increase in the ac conductivity (σ_{ac}) with increasing frequency for the entire NaI compositions. Three frequency regions can be assigned such as: (i) low frequency dispersive region (Region I), (ii) mid frequency saturation region (Region II) and (iii) high frequency dispersive region (Region III) (Shukla *et al.*, 2014), over the studied frequency range except for NaI-25. This particular sample exhibits Region II and Region III. The Region I is out of frequency range.

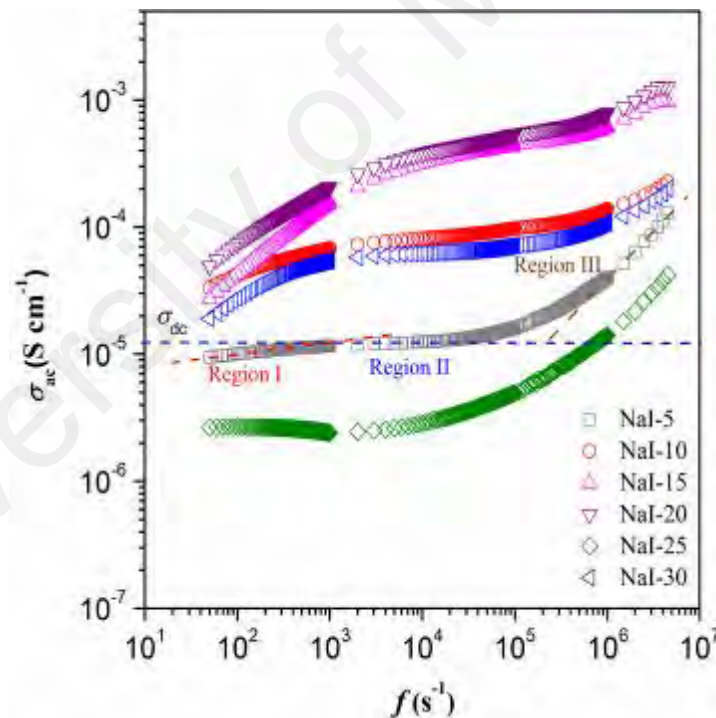


Figure 5.9: The frequency-dependent conductivity spectra of NaI-PSSE at room temperature

In Region I, the conductivity increment can be ascribed to electrode polarization (EP). This effect is also known as space charge polarization. The conductivity in this region increases with increasing number of ions that diffuse into electrode-electrolyte

interface layer, forming ion accumulation. The extent of ion accumulation can be learned from the steepness of EP region. A steeper region signifies higher ion accumulation and *vice versa*. This accumulation allows the formation of double-layer capacitance (C_{dl}) (Mishra and Rao, 1998). Correlation between the charge accumulation (based on the steepness) and the formation of C_{dl} layer in NaI-PSSE can be validated from the thickness of C_{dl} layer summarized in Figure 5.4. The steepness of EP region gradually increases with increasing NaI from NaI-5 to NaI-15. This means that there is an increase in the ion accumulation, resulting in a larger C_{dl} value. With further NaI doping, the steepness decreases to a minimum in NaI-25, depicting disruption in the C_{dl} layer formation. The effect is however suppressed in NaI-30 leading to better C_{dl} formation.

Above the EP region, a plateau can be observed (Region II). In this region, the conductivity stays constant, and this conductivity represents the dc conductivity (σ_{dc}). According to Jonscher model, the frequency-independent conductivity is resulted by the successful ion hopping from one site to another vacant site (Funke, 2011). The hopping is possible due to the long ion relaxation time, and such jumps often results in a long-range ion transportation (Shukla *et al.*, 2014; El Bachiri *et al.*, 2016). The close approximation between the estimated σ_{dc} and those values calculated from impedance isotherm illustrates the dependence of ionic conductivity on salt complexation and ionic interaction.

At higher frequency (Region III), the conductivity starts to be dispersive. The dispersed conductivity originates from a localized orientation hopping (Funke, 1993) and therefore, long-range ion transport is halted at high frequency. Two competing ion mode transports occur in Region III according to the Jump model: (i) hopping of ions back to its initial site (which is correlated to forward-backward-forward), *i.e.*

unsuccessful hopping and (ii) site relaxation (the neighboring ions become relaxed and stays at the site), *i.e.* successful hopping.

The ion transportation mode that occurs prominently at high frequency [whether it is (i) or (ii) in the Jump model] can be identified from the fractional exponent (n) obtained from the slope of dispersive region. All the n values are in the range of 0.4 (NaI-10, NaI-15, NaI-20) to 0.8 (in NaI-5 and NaI-25). The decrease of n value with increasing NaI contents up to NaI-20 illustrates the dominance of site relaxation. The relaxation allows formation of free vacant sites for ions hopping. There is no occurrence of backward ion motion stipulated in the entire NaI-PSSE compositions as the n values do not exceed 1.

5.4.2 Temperature variation

Figure 5.10 shows the frequency-dependent conductivity spectra of NaI-PSSE as the function of temperature. Quantity σ_{ac} increases with increasing frequency and temperature. All the presented spectra exhibits three frequency regions discussed earlier. In NaI-5 and NaI-25, the EP which is not present at low temperature gradually increases with temperature. The EP effect enhances in conjunction to the increasing formation of ions (thermal-activated process). Thus, more ion accumulates at the interface of electrode-electrolyte layer and this leads to thicker C_{dl} layer formation. In here, the C_{dl} layer formation was estimated from the steepness of EP region, and not supported by the quantitative measurement from Nyquist plot. Restriction of ion accumulation in NaI-10 to NaI-20 is obvious above 30 °C based on the decreased steepness of EP region.

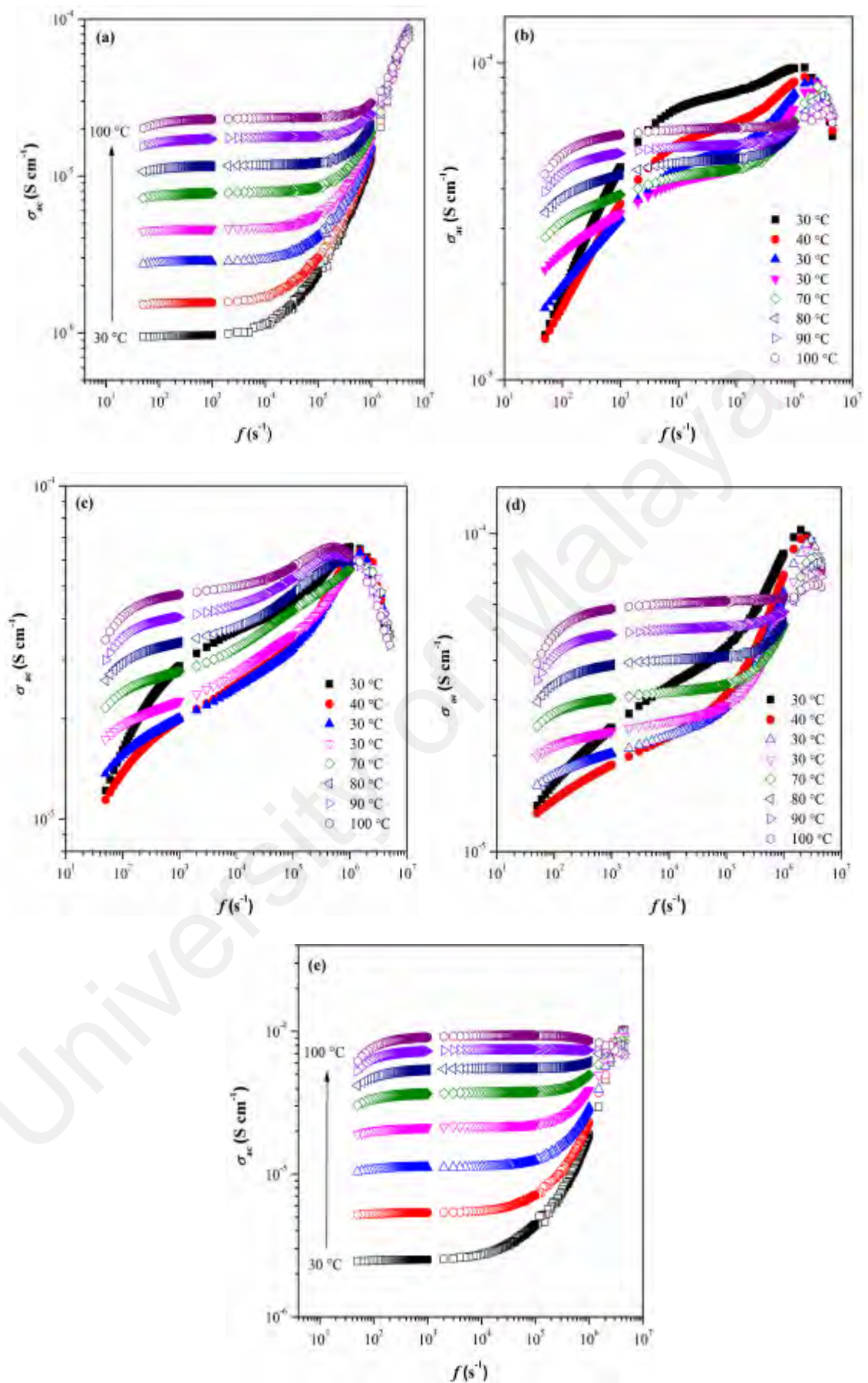


Figure 5.10: The frequency-dependent conductivity spectra of NaI-PSSE at different temperatures: (a) NaI-5, (b) NaI-10, (c) NaI-15 (d) NaI-20 and (e) NaI-25

Above the EP region, conductivity remains constant throughout the frequency increment in Region II. The corresponding plateau region is obvious in NaI-5 and NaI-25, while in other NaI-PSSE compositions this region is only obvious above the T_c . The successful ion hopping in this region occurs due to ion relaxation process. Those NaI-PSSE compositions that permits ion to have adequate relaxation time displays obvious plateau region. For those samples with short ion relaxation time, this region is not obvious.

From the plateau region, one could extract σ_{dc} value. In this case, the σ_{dc} increases with temperature as the consequence increase in the formation of ions that improves the NaI complexation and ionic interaction. The ion formation with temperature (in the case of thermally-activated process that obeys Arrhenius law in NaI-5, NaI-25 and remaining PSSE compositions above T_c) can be clearly seen from the well-separated plateau region. Below T_c , the decrease of σ_{dc} with temperature implies the poor complexation between the polymer and increasing ion population (ion formation remains as a thermally activated process). The poor complexation hinders ion hopping.

In the dispersive region (Region III), all the temperature-dependence curves merged. This happens because the processes in this region are thermally inactive. There are two regions that could be assigned such as: (i) nearly constant loss region (NCL) and/or (ii) super linear power law region (SLPL). The ion dynamics of both NCL and SLPL originate from the caged ion movements. According to Funke (1993), localized ions such as neighboring mobile ion or polyion have slight movement in PSSE as these matrices do not have complete rigid environment. This confirms the proposal discussed earlier in Section 5.3.2, which dictates the possible presence of 'ion mode' relaxation.

The occurrence of backward ion hopping to the initial hopping site is obvious in NaI-5, where the n value exceeds 1 (at 30 °C). The value subsequently reduces with

temperature rise. Similar phenomenon can be observed in NaI-25. The suppression gives better ion transport *via* site relaxation, which further results in successful ion hopping. The n value was not determined for other NaI-PSSE compositions as there was drop in the conductivity at high frequency. The drop in dispersive conductivity could be caused by the non-favorable caged ion movements at high frequency. The spectra representation of NaI-30 was not included in this discussion as the sample is thermodynamic unstable. This type of NaI-PSSE does not benefit electrolyte material.

5.5 Ionic conductivity at room temperature

Ionic conductivity (σ) of NaI-PSSE containing different NaI compositions is presented in Figure 5.11. The values were calculated using Equation (5.3).

$$\sigma = \frac{L}{R_b A} \quad (5.3)$$

where, L is the thickness in cm, A is the area of electrode in cm^2 and R_b represents the bulk resistivity in Ω (obtained from the Nyquist plot).

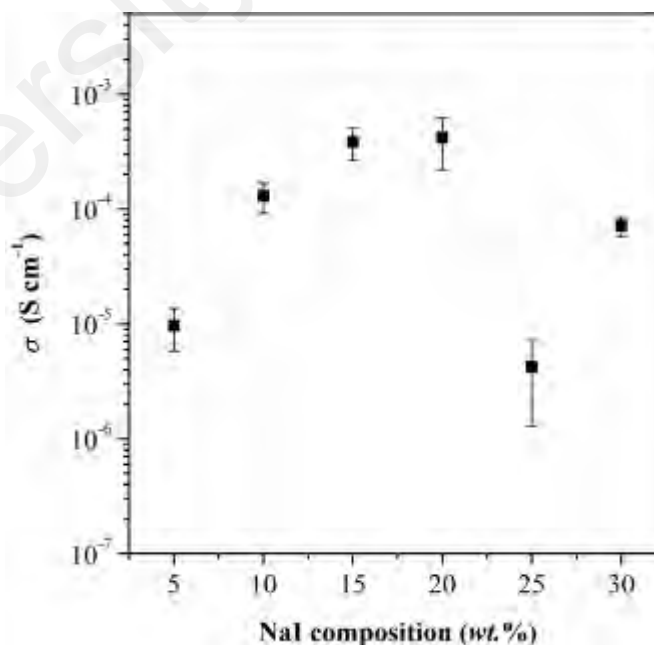


Figure 5.11: Ionic conductivity of NaI-PSSE at room temperature

The variation of ionic conductivity could be understood from the N_{ion} and D_{ion} values in Figure 5.12. Based from the plotted data in Figure 5.11, a good enhancement in ionic conductivity of NaI-PSSE was recorded from 5 to 15 wt.% of NaI doping, and the change turns insignificant in NaI-20. The ionic conductivity increases by two-orders of magnitude to the highest of $4.21 \times 10^{-4} \text{ S cm}^{-1}$ in NaI-20. The increment is caused by freeing of more Na^+ from the crosslink structure, which in turn increases the segmental-assisted ion motion (D_{ion} increases). The freeing of the ions consequently results to ion association forming ion pairs or ion aggregates. This is apparent from the drop in N_{ion} values. The result is consistent with the observed self-ion diffusion in Section 5.3.1 for these samples. The insignificant change of ionic conductivity in NaI-20 as compared to that of NaI-15 suggests that an optimum NaI complexation could have occurred in NaI-15. The saturation point happens at NaI-20.

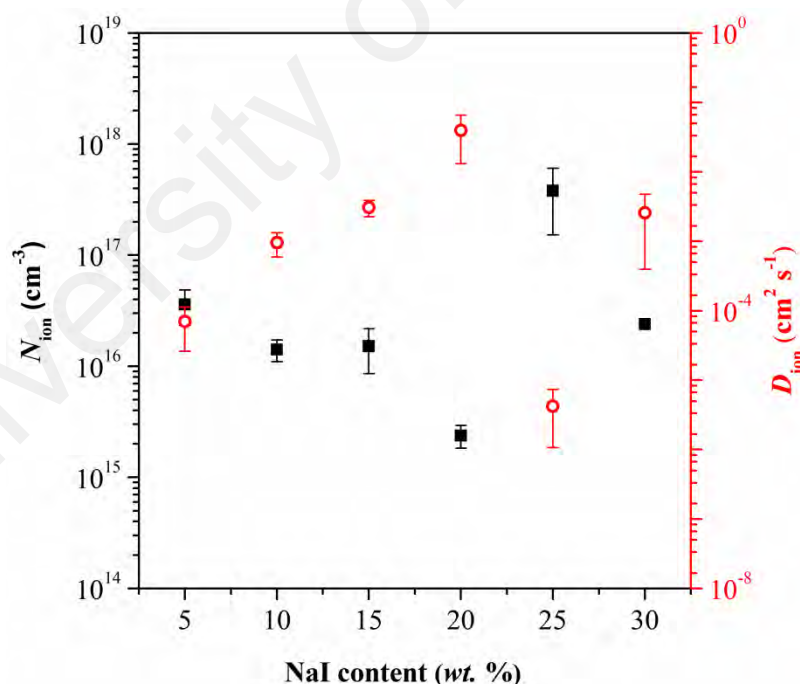


Figure 5.12: Number of ions and ion diffusion coefficient of NaI-PSSE at room temperature

Above the saturated composition (e.g. NaI-25), excess NaI causes an abrupt increase in the number of ions. These ions form transient crosslink and restrict the mobility of

polymer chains. Subsequently, the conducting pathway for continuous ion tunneling is blocked and ionic conductivity decreases. With further NaI doping (e.g. NaI-30), the ionic conductivity slightly improves which can be corresponded to the enhancement in ion transportation. In this case, ion association reoccurs (N_{ion} reduces) and gives rise to self-ion diffusion. In general, the ions that hop *via* oscillating ion pairs are faster than that of mediated by segmental-assisted motion.

5.6 Conductivity-temperature dependence

Arrhenius plot of NaI-PSSE with different NaI contents is shown in Figure 5.13. The results were discussed with reference to N_{ion} and D_{ion} [Figure 5.14, calculated using Equations (2.10) and (2.11)].

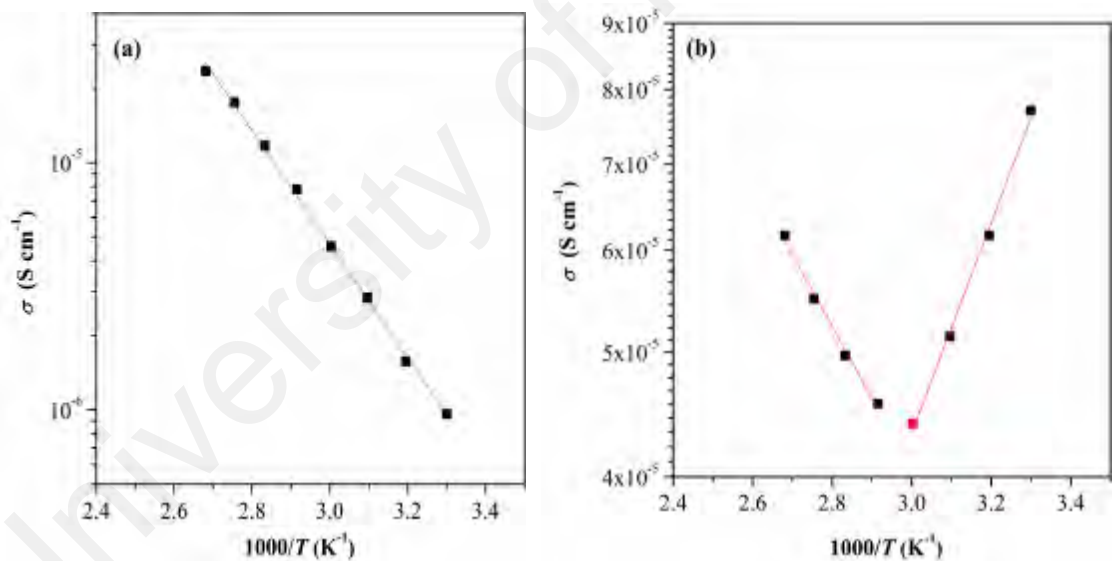


Figure 5.13: Arrhenius plot of NaI-PSSE compositions: (a) NaI-5, (b) NaI-10, (c) NaI-15, (d) NaI-20, (e) NaI-25 and (f) NaI-30

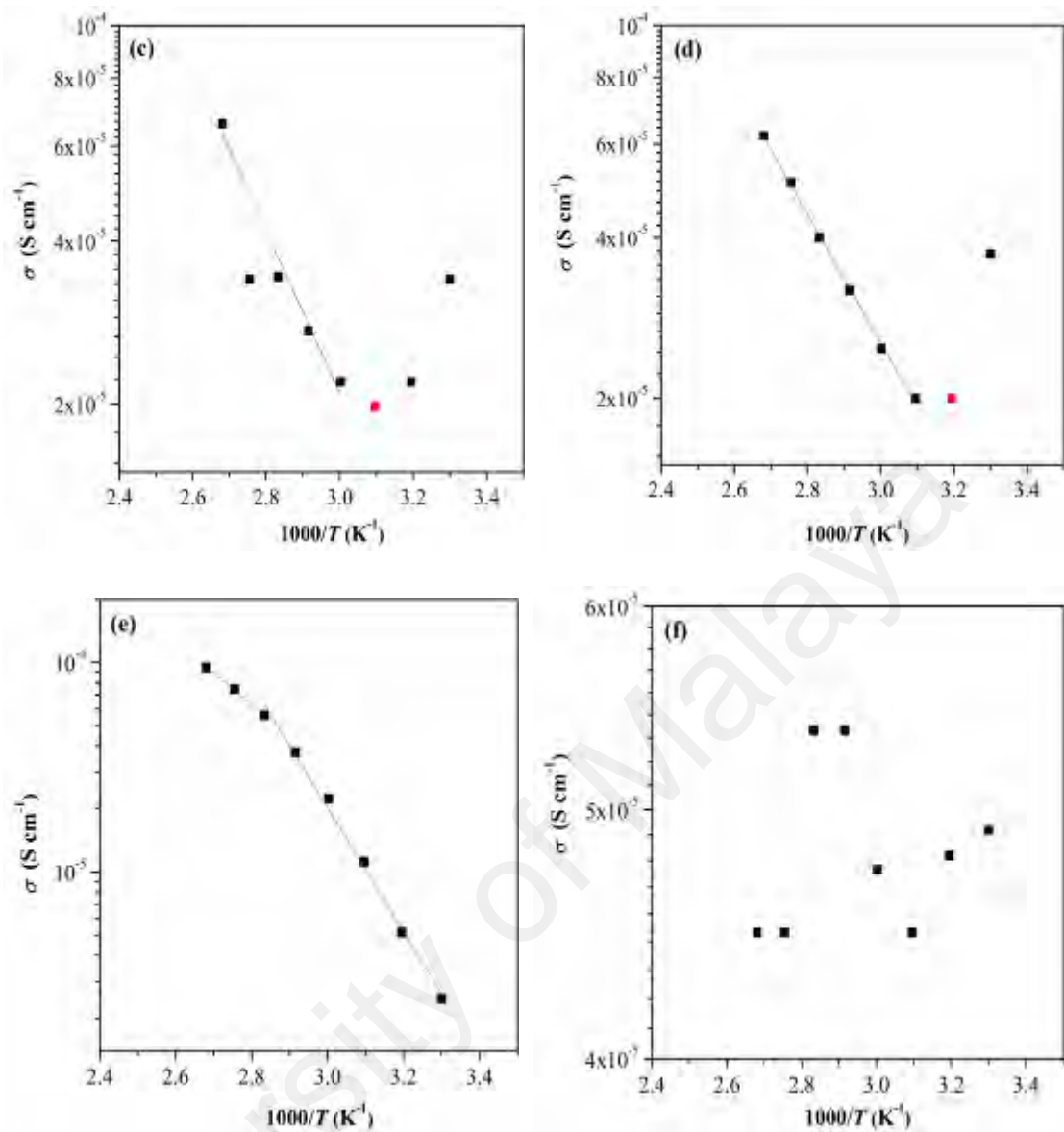


Figure 5.13, continued

Nearly all NaI-PSSE (except NaI-30) shows good Arrhenius fitting over a certain temperature range. This elucidates the ionic conductivity enhancement as the effect of increasing ion population and kinetic energies during thermal-activated process. The increase of these parameters can only be seen in NaI-5 and NaI-25 based on the increase of both N_{ion} (ion pair dissociates) and D_{ion} values with increasing temperature. For the remaining samples (*e.g.* NaI-10, NaI-15 and NaI-20) however, the N_{ion} value increases accompanied with a reduction in D_{ion} .

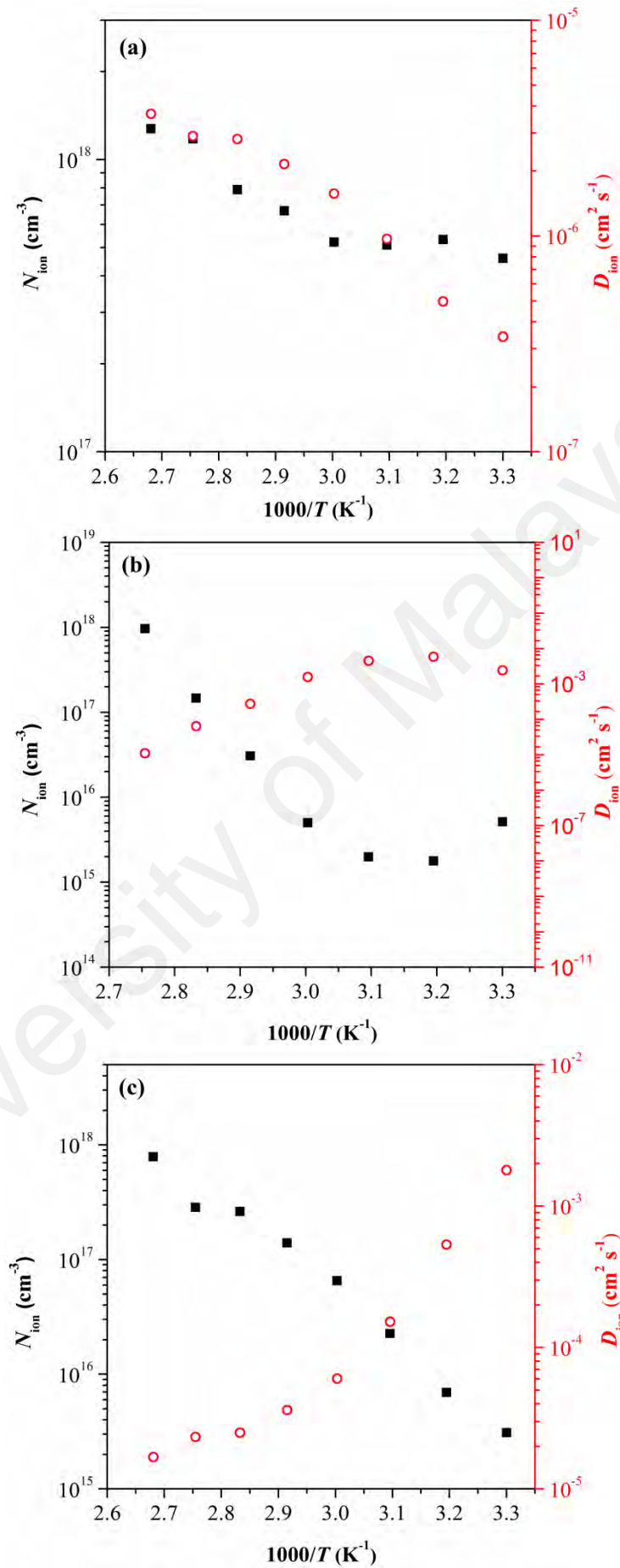


Figure 5.14: N_{ion} and D_{ion} of NaI-PSSE as the function of temperature: (a) NaI-5, (b) NaI-10, (c) NaI-15, (d) NaI-20 and (e) NaI-25

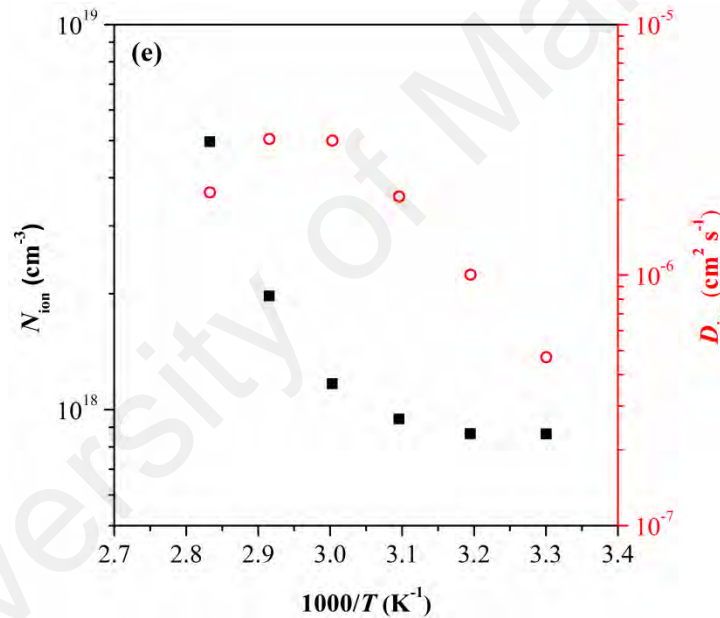
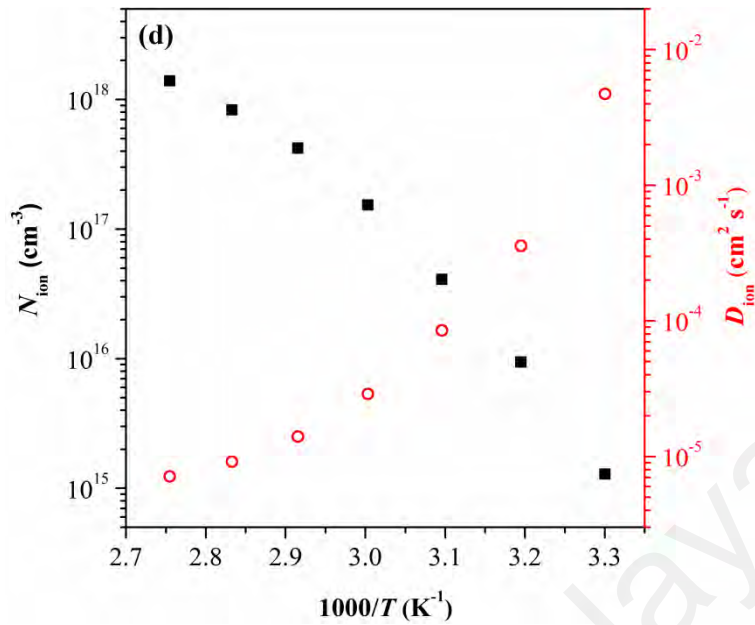


Figure 5.14, continued

In NaI-10, NaI-15 and NaI-20, two ionic conductivity trends were observed within the studied temperature range. The change of trend happens at T_c [as indicated by red color data points in Figure 5.13(b-d)], and this could be observed as consequence to the phase change. This phase change has been identified as glass transition in Section 5.8.1. At low temperature, the ionic conductivity decreases to a minimum value with increasing temperature up to T_c . Surpassing this temperature, the ionic conductivity

increases. The initial decrement is due to the contraction of specific free volume. More Na^+ is formed during the thermal-activated process (N_{ion} increases, Arrhenius behavior) and they participate in transient crosslink formation by interacting with polymer chains. This makes the chains to lose its flexibility and therefore, delays the stable network to form for continuous ions tunneling. Accordingly, the ion diffusivity is restricted (D_{ion} decreases). The effect becomes dominant with increasing temperature to T_c .

The T_c value reduces by *ca.* 10 °C from 60 to 50 °C, and from 50 to 40 °C with increasing NaI doping from 10 to 15 wt.% and 15 to 20 wt.%, respectively. Above T_c , the ionic conductivity gradually increases with temperature. Since the increase is accompanied by the increase of ions population, the occurrence of phase transition at T_c may have halted the formation of transient crosslink. The Na^+ that has been initially crosslinked to polymer structure is now free. This is possible when there are higher formations of free volume. Nevertheless, ion diffusivity is still hampered above T_c . This may be associated to the ion overcrowding effect.

A contradicting trend can be observed in the ionic conductivity of NaI-30 [Figure 5.13(f)], which exhibits a rapid discontinuity with increasing temperature. The fluctuation may arise from the presence of grain boundaries (considered as quasi-two-dimensional phases) that shows phase-like behavior under thermal effect. This phase-like behavior causes the structure, chemistry and properties of the said polymer to vary in discontinuity (Cantwell *et al.*, 2014). As the result, there is an irregular change in the D_{ion} and N_{ion} with increasing temperature.

5.7 XRD

Figure 5.15 shows the incoherent XRD pattern of pure AA05 and NaI-PSSE. The appearance of broad hump at low diffraction angle ($2\theta < 40^\circ$) in AA05 reveals that the

copolymer is an amorphous polymer. The polymer chains in AA05 are arranged with an average chain distance of 0.38 \AA^{-1} . The value was determined using scattering function (cf. Section 2.8.2) by referencing to the peak at $2\theta = 17^\circ$.

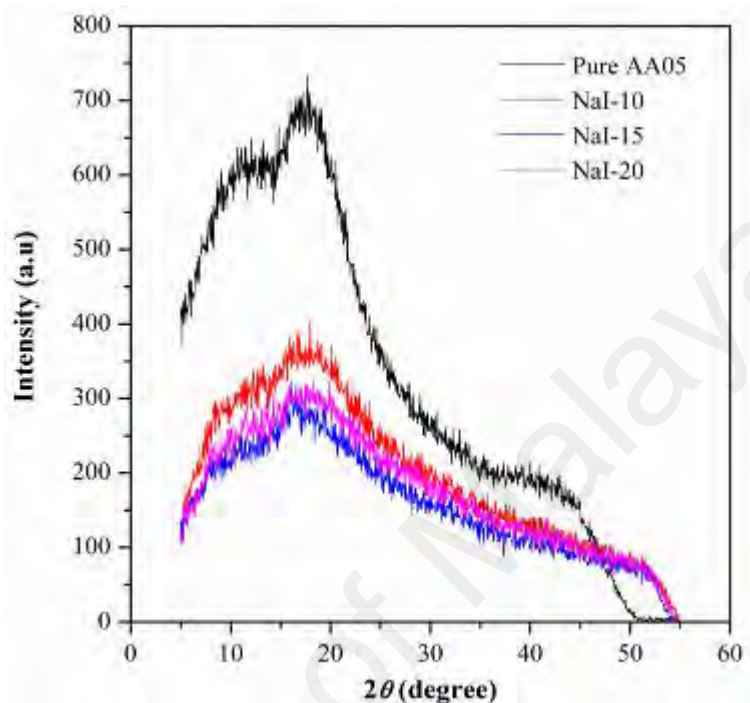


Figure 5.15: XRD pattern of pure AA05 and NaI-PSSE thin films at room temperature

A major randomness in the chain ordering (increase in amorphousness) occurs when AA05 is doped. This is characterized by the increased broadness in the amorphous hump upon overlapping of the peak at $2\theta = 12^\circ$ and 17° in AA05, accompanied by the reduced peaks intensity (two folds) in the entire tested NaI-PSSE. Chain randomness increases as the consequence of complexation in NaI-AA05; whereby bulky-side chain structure forms when Na^+ coordinates with polar oxygen of polymer chain. This subsequently causes chain-chain separation and weakens the intermolecular forces between chains. Add on to this, the presence of plasticizer molecules may also contribute to the intermolecular chain weakening.

In this work, the structural randomness improves with increasing NaI doping from 10 wt.% to 15 wt.% (reduction in intensity). This can be correlated to the increasing inter-cation interaction between increasing Na⁺ and oxygen atom of copolymer side chain (*e.g.* carbonyl or hydroxyl group). Consequently, more bulky side chain structures are formed and they cause chain-chain separation. In NaI-20, the intensity of amorphous hump increases above NaI-15 in a small extent. This implies the decrease of chain disorderliness.

5.8 Thermal properties

5.8.1 DSC

Figure 5.16 shows the DSC thermogram of AA05 and NaI-PSSE. All the T_g s of tested NaI-PSSE fall in the range of 40 to 60 °C, which are higher than the pure AA05 ($T_g = 25$ °C). The higher shift of T_g , for instance in NaI-10, depicts the increase in chain rigidity that can be associated to the presence of transient crosslink. This structure is disrupted with increasing NaI doping as visualized from the gradual decrease of T_g by almost 10 °C. The disruption could be resulted from the reduced Na⁺ participation as transient crosslinker. The ion perhaps favors the formation of bulky-side chain structure that increases the main chain-chain separation (Shukla *et al.*, 2014). This increases the structural amorphous nature and consequently gives better flexibility to chain dynamics.

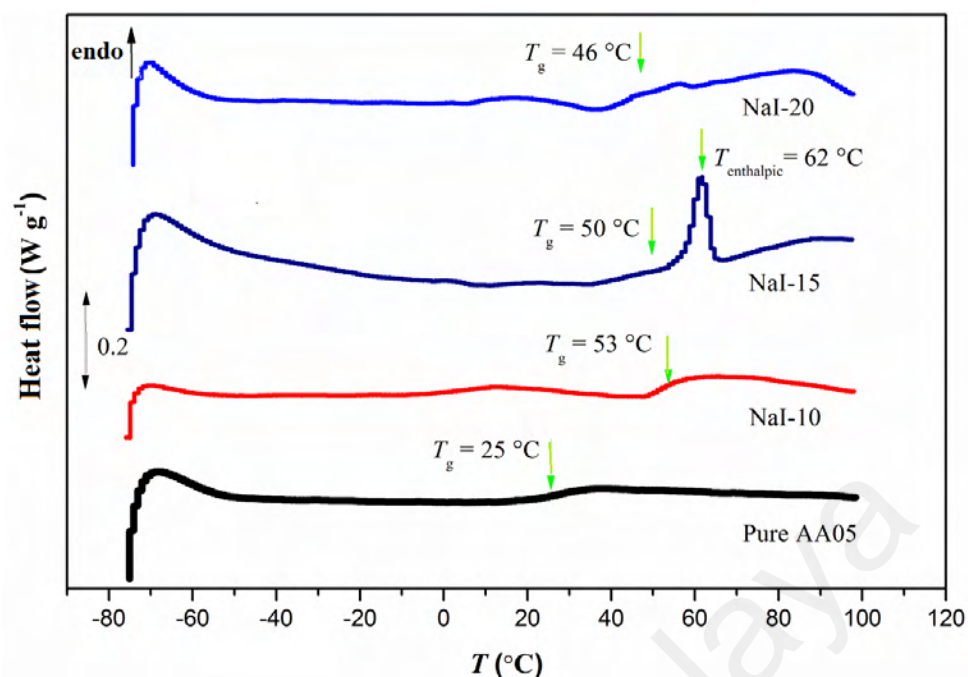


Figure 5.16: DSC thermogram of NaI-PSSE with NaI content variation

The highest chain flexibility was observed in NaI-15 through the appearance of enthalpic relaxation at T_g . Typically, this relaxation occurs in high amorphous structure that contains multiple amorphous segments. In our case, the existence of multiple amorphous segments benefits the ion transport in NaI-15 (highest calculated D_{ion}). The occurrence of enthalpic relaxation at 60 °C forms a new conducting phase with reduced free volume, which may exhibit different ion relaxation processes. This explains the appearance of two relaxation peaks in loss tangent plot representation of NaI-15 at 60 °C (*cf.* Figure 5.8). As the new peak appears at higher frequency, therefore faster ion transport is expected to occur in the new phase. The T_c values mentioned in earlier subsections fit well with the T_g of NaI-10, NaI-15 and NaI-20. Hence the increase of ionic conductivity above T_c could be resulted from the increase of free volume upon phase transition.

5.8.2 TGA

Figure 5.17 presents the T_d s of NaI-PSSE as the function of NaI content. The DTG curve of pure AA05 is enclosed in Figure 5.17(a). Only selected temperature range was labeled with color marker in order to show changes in the thermal behavior of AA05. Based on the results, the first decomposition temperature (green color marker) is obvious only in NaI-PSSE as compared to that of AA05. There are two reasons that could lead to this observation; (i) evaporation of EC: PC at 146-149 °C (flash point) and (ii) hygroscopic nature of NaI-PSSE (upon NaI addition).

The same intense weight loss happens in the second decomposition stage (red color marker). Since the disorderliness (weakening of intermolecular forces) gives high presence of labile bonds, more C-C hemolytic cleavage may occur. The hemolytic cleavage results to a higher formation and dissipation of oligomers from the matrix. As this cleavage continues to progress with increasing temperature, it generates more free radicals. Above 400 °C (third decomposition stage, blue color marker), the radicals actively cleave the polymer chains in a random manner. This induces a massive weight loss (or structural disruption) in all the tested samples including pure AA05. The shift of T_d for pure AA05 (425 °C) to ~400 °C in NaI-PSSE strongly indicates the lowering of thermal stability. This is the consequence effect from the weak intermolecular attractions between the chains upon complexation of NaI with AA05. There is no significant variation in the T_d s of NaI-PSSE as the function of NaI content, as well as the residual mass at 480 °C (5-8 %).

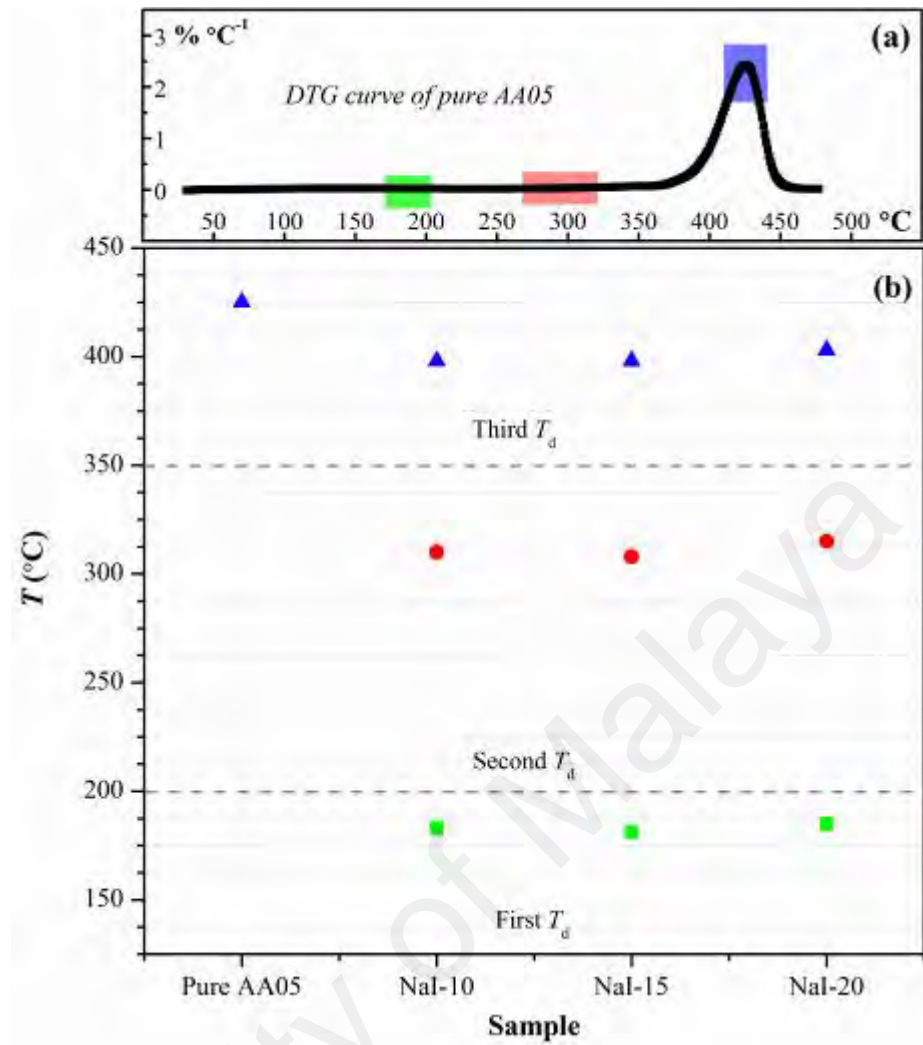


Figure 5.17: (a) DTG curve of pure AA05 and (b) T_d results of NaI-PSSE

CHAPTER 6: RESULTS AND DISCUSSION

Characterization of PSSE: System II- EC: PC variation

6.1 Chain relaxation time

6.1.1 Room temperature measurement

Figure 6.1 depicts the calculated τ_{chain} for NaI-15 (as the reference-PSSE) and EC: PC-PSSE. The raw data for this plot is enclosed in Appendix G (*cf.* Z'' - Z''' vs. f). Results were presented for EC: PC-PSSE with maximum EC: PC compositions of 40 wt.% as the composition thereafter exhibit no obvious Z''_{max} peak.

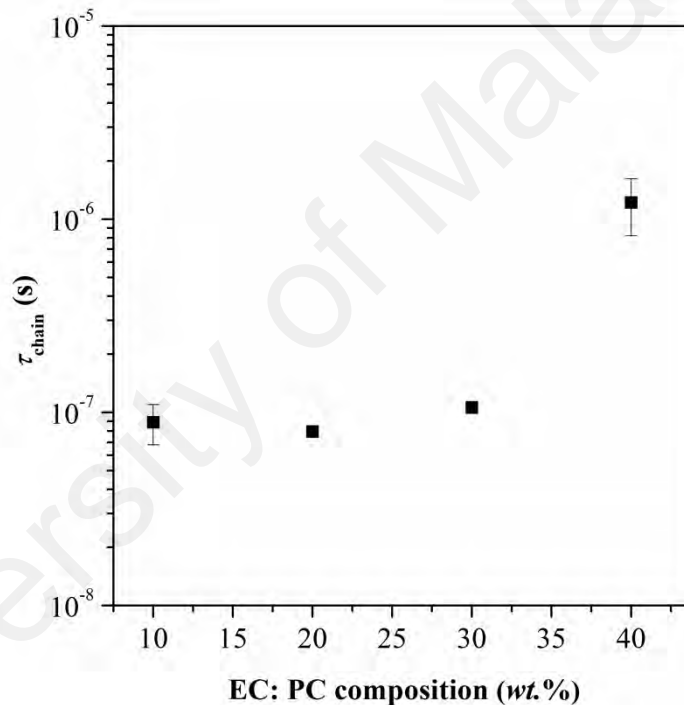


Figure 6.1: Chain relaxation time of EC: PC-PSSE at room temperature

From the plotted data, there is no significant change in the τ_{chain} of NaI-15 when more EC: PC is doped into the matrix (*e.g.* EC: PC-20). This suggests that the chain retains its dynamics with no favorable structural disorderliness upon increasing charge dilution. Formation of transient crosslink structure could have happened. The chain dynamics improves with further plasticization, which can be seen from the reduction of τ_{chain} . Formation of contacting ions or higher aggregates becomes dominant with increasing

dilution based on the appearance of non-Debye characteristic plot of $Z'/-Z''$ vs. f . With this information, the improvement of chain dynamics can be correlated to the rupturing of transient crosslink structure in EC: PC-30 and above.

6.1.2 Temperature variation

Figure 6.2 shows temperature-dependence $-Z''$ vs. f plot for EC: PC-20. A shift of $Z''_{\max}(f)$ illustrates variation in the chain dynamics. Based on the plot, the constant $Z''_{\max}(f)$ with increasing temperature denotes an insignificant change in the segmental dynamics of polymer chains. There is no concomitant increase in the structural disorderliness with increasing formation of ion (Na^+) during thermal-activated process. This may be caused by poor NaI complexation accompanied with ion association. The presence of contacting ions (or ion pairs) is seen from the non-Debye behavior of impedance plot (results are not shown here). Similar results were obtained for EC: PC-30 (results were not shown). Both compositions show reduction in the resistivity with increasing temperature (decrease of $-Z''$).

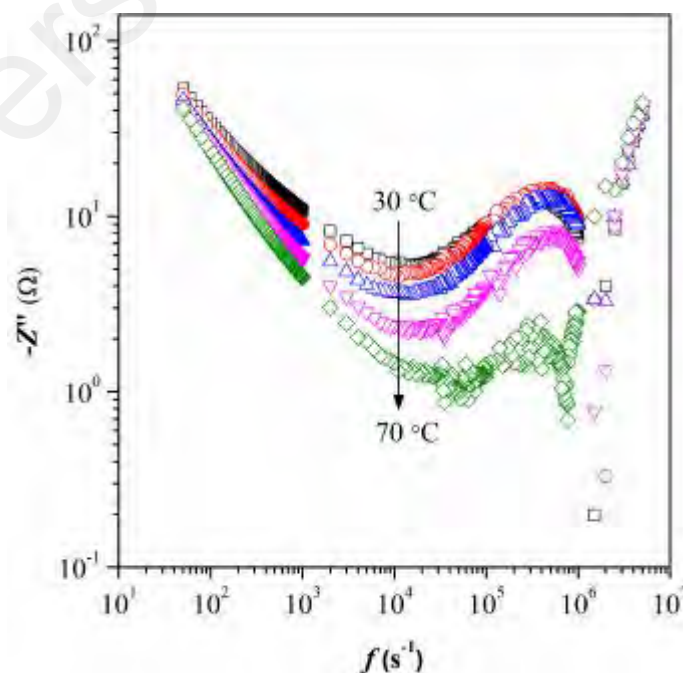


Figure 6.2: Plot of imaginary impedance against frequency for EC: PC-20 at different temperatures

6.2 Nyquist plot

6.2.1 Room temperature measurement

The Nyquist plots of the entire tested EC: PC-PSSE compositions are illustrated in Figure 6.3. All the plots show appearance of spike (45° slope) at low frequency and semicircle at high frequency. The RC circuits are shown in the inset of Figure 6.3. Similarly to NaI-15, the RC circuit does not follow ideal capacitor due to the presence of contacting ions.

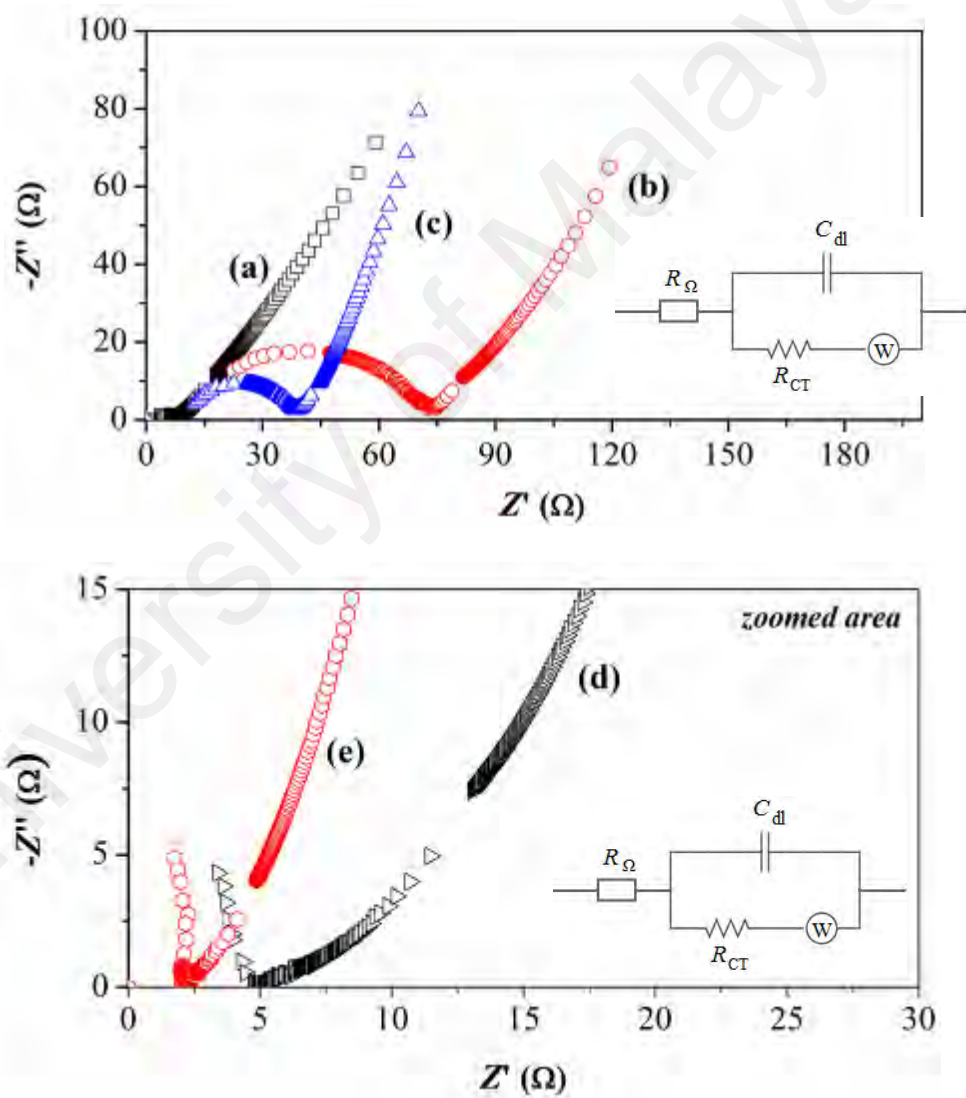


Figure 6.3: Nyquist plot of (a) NaI-15 and EC: PC-PSSE; (b) EC: PC-20, (c) EC: PC-30, (d) EC: PC-40 and (e) EC: PC-50

In reference to the characteristic plot of NaI-15, a broader semicircle forms in EC: PC-20 (R_b and R_{CT} shift to higher value; determination of these values was as per Appendix F). The increase of area under the semicircle signals an increase in the distance of hopping site. Vacant hopping sites are arranged at further distance due to the high occupancy of ions in neighboring sites at higher dilution. This scenario delays the formation of stable network (f_0 shifts to lower frequency) for continuous ion tunneling, and impedes ion transport. The impediment is greater at higher frequency as supported by the increase of R_Ω . In overall, the ion transportation is lower as compared to NaI-15. As the consequence to this, poor C_{dl} layer is formed (*cf.* Figure 6.4).

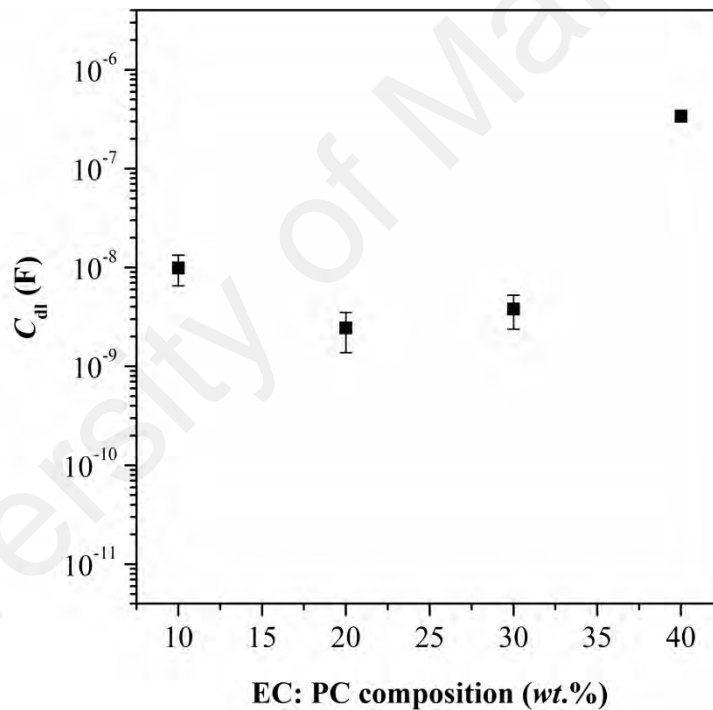


Figure 6.4: C_{dl} of EC: PC-PSSE at room temperature

At higher EC: PC doping, the R_b and R_{CT} reduce with increasing dilution. This reduction shows diminution in the resistance of ion transport. Moreover, the changes are accompanied with the delay in the formation of stable network. With these observations, it can be deduced that the ion transport is not controlled by the formation of stable network structure; instead, other secondary pathways may be favorable. This will be

further discussed in Section 6.3.1. The existence of secondary pathway also allows ions to have better diffusivity at high frequency, especially at increasing EC: PC doping. Evidence to this can be sought through the reduction of R_{Ω} . This causes thicker formation of C_{dl} layer.

6.2.2 Temperature variation

Similar measurement was conducted on EC: PC-20 and EC: PC-30 with variation in temperature. The results are plotted in Figure 6.5(a-b).

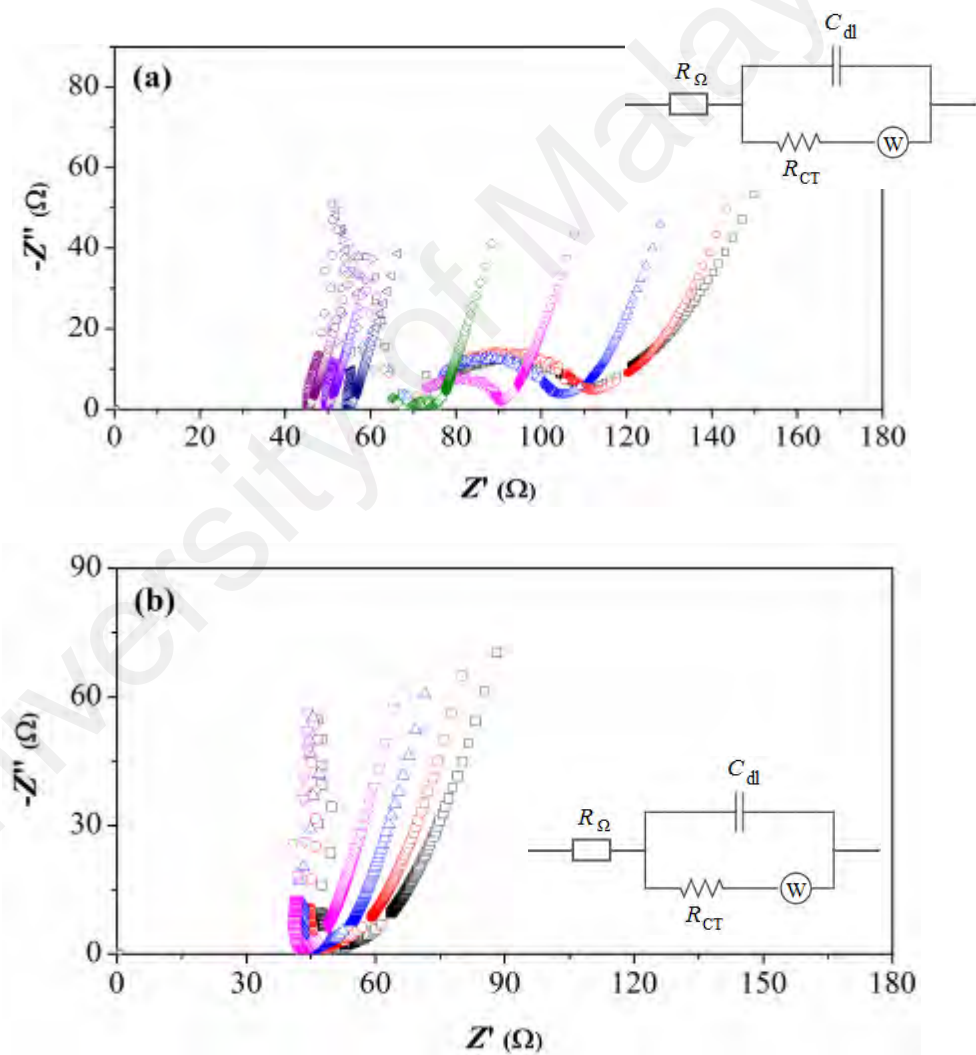


Figure 6.5: Nyquist plot of (a) EC: PC-20 and (b) EC: PC-30 as the function of temperature [Legend: 30 °C (□), 40 °C (○), 50 °C (△), 60 °C (▽), 70 °C (◇), 80 °C (◁), 90 °C (▷) and 100 °C (◊)]

In EC: PC-20, the depressed semicircle shifts towards higher frequency when temperature increases. Above 70 °C, the semicircle characteristic plot changes to a thick-like plot. All the exhibited R_b shifts to lower values with increasing temperature, while the f_0 shifts to higher frequency. This means that the resistance towards ions mobility is reduced as the consequence formation of fully stable network in a shorter time. Similar trends of R_b and f_0 were obtained for EC: PC-30 as the function of temperature. A perpendicular line appears at high frequency in both these samples. This plot resembles the characteristic of pure resistor (R_Ω) that depicts the restriction of ion transport in the presence of high ion population. All the RC circuits are shown in the inset figure of Nyquist plot. The RC does not follow ideal capacitor. The C_{dl} component was not quantified as there is no significant change in the f_0 values at different temperatures.

6.3 Ion relaxation time

6.3.1 Room temperature measurement

The $\tan \delta$ vs. f plot of NaI-15 and EC: PC-PSSE containing 20 to 40 wt.% EC: PC is shown in Figure 6.6. A relaxation peak similar to NaI-15 (segmental mode relaxation) was observed in the EC: PC-PSSE. In EC: PC-20, this peak shifts to frequency lower than that of NaI-15. This indicates restriction of segmental-assisted ion motion. The ions are poorly mediated *via* segments when high transient crosslink structure is formed; this structure causes the chains to be more localized. Consequently, ions have higher relaxation time (Figure 6.7). The accompanied increase of $\tan \delta_{max}$ depicts the absence of self-ion diffusion in this particular EC: PC-PSSE composition.

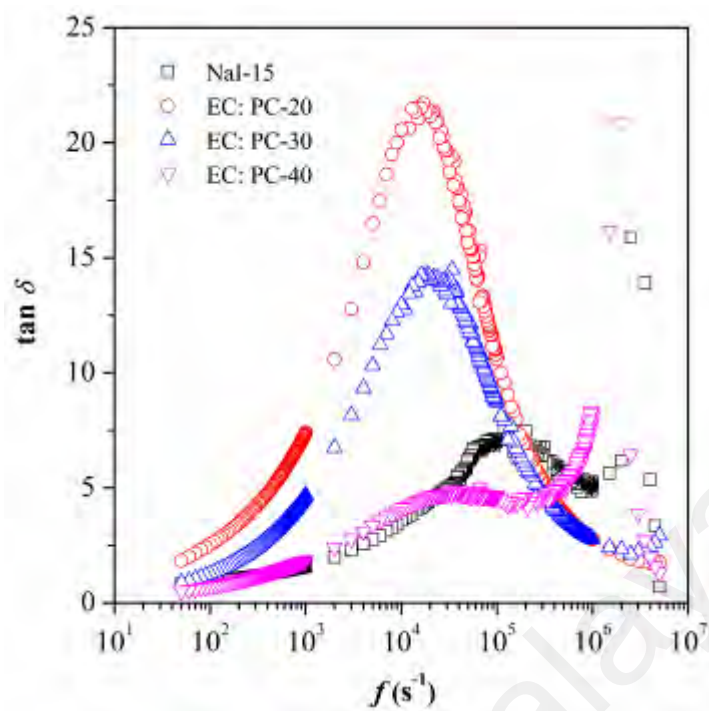


Figure 6.6: Dissipation tangent loss of EC: PC-PSSE as a function of frequency

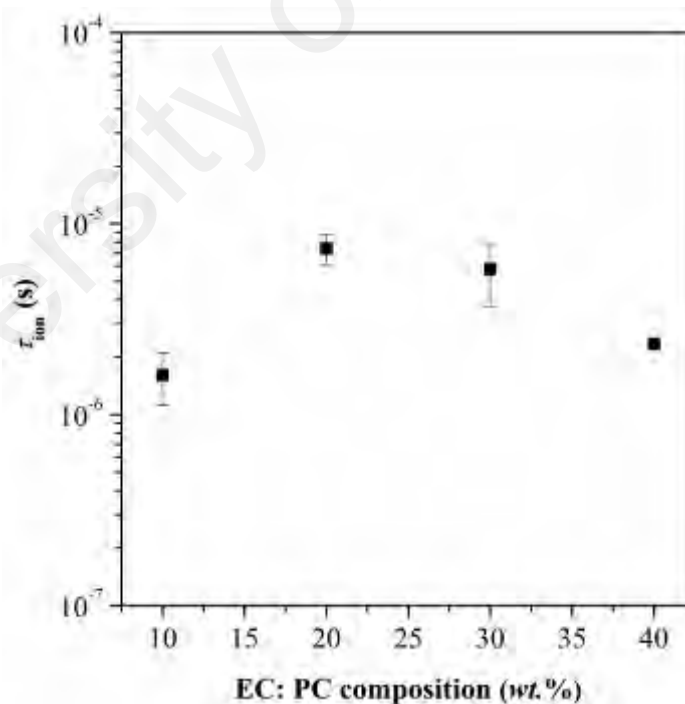


Figure 6.7: Ion relaxation time of EC: PC-PSSE at room temperature

At higher EC: PC loading (e.g. EC: PC-30 and EC: PC-40), the increase in segmental-assisted ion motion becomes insignificant based on the near constant value of f_{\max} in Figure 6.6. The ion movement is primarily controlled by self-ion diffusion (reduction in the $\tan \delta_{\max}$). This shows that high ion association may occur at higher plasticization. Results for EC: PC-50 was excluded from this study as there was no well-defined peak for relaxation process. Besides the segmental mode relaxation, 'ion mode' relaxation may be present in all the tested samples at low frequency.

6.3.2 Temperature variation

The $\tan \delta$ vs. f plot of EC: PC-20 is presented in Figure 6.8. Only the results in between 30 and 70 °C were presented as the relaxation peaks were undefined at higher temperatures. From the collected results, it can be seen that the peak maxima (or f_{\max}) remains unchanged at increasing temperature. The hopping ions move at similar speed corresponding to the insignificant change in chain dynamics (cf. Section 6.1.2). The accompanied increase of $\tan \delta_{\max}$ with temperature strongly dictates the ion transport *via* segments-assisted motion. The dependency of ion transport on polymer chain dynamics explains the coupling behavior. Similar observation as EC: PC-20 is noted in EC: PC-30 up to the maximum temperature of 60 °C. At higher temperature the peaks turn undefined (results are not presented).

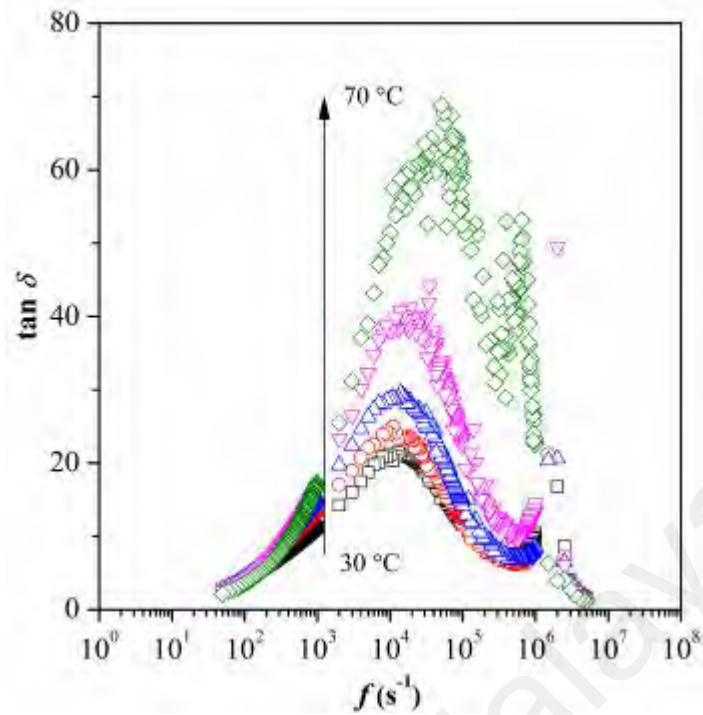


Figure 6.8: Plot of $\tan \delta$ vs. frequency of EC: PC-20 at different temperatures

6.4 Frequency-dependent ionic conductivity

6.4.1 Room temperature measurement

The frequency-dependent conductivity spectra of EC: PC-PSSE with different EC: PC contents are plotted in Figure 6.9. Three frequency regions such as EP (Region I), plateau (Region II) and dispersive conductivity (Region III) exist within the stipulated frequency range over the entire EC: PC composition. All the test results comply with the conductivity behavior that follows Jonscher's universal power law, *i.e.* σ_{ac} increases with frequency.

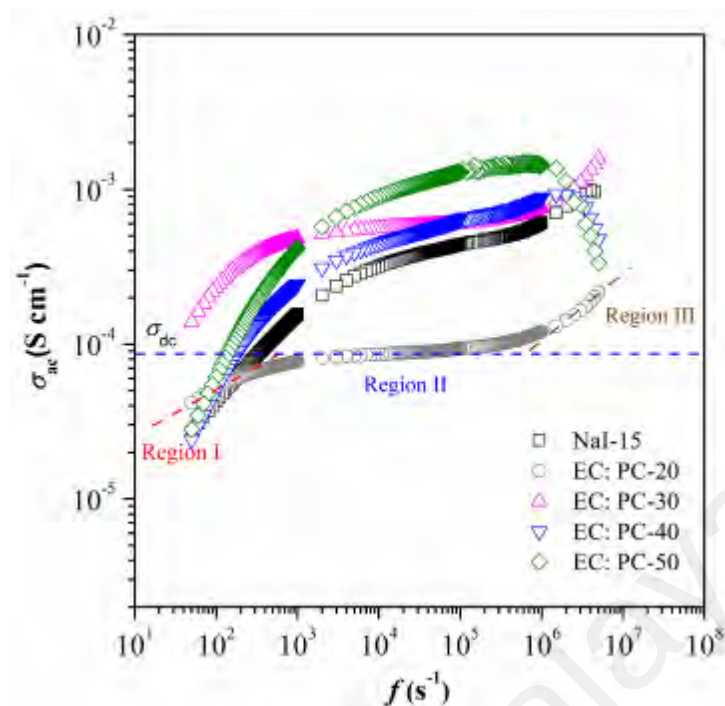


Figure 6.9: Frequency-dependent conductivity spectra of EC: PC-PSSE with different EC: PC contents

The increase of σ_{ac} in the EP region has been discussed in earlier chapter. By comparing the steepness of EP region among samples, which initially drops in EC: PC-20 (compared to NaI-15) and later progressively increases, one could see low ion accumulation at electrode-electrolyte interface in former observation and later improves with increasing plasticization. This is in agreement with the reported thickness of C_{dl} layer in Figure 6.4, in which the thinning of C_{dl} layer occurs in EC: PC-20. At higher EC: PC contents, this layer grows thicker as the result of higher ion accumulation.

The σ_{dc} exhibits similar trend to the reported C_{dl} thickness as the function of EC: PC content. Both parameters are dependent of ions concentration. The decrease of σ_{dc} in EC: PC-20 shows a lowering in the hopping ion concentration and *vice versa* for the compositions that contain higher plasticizations. Higher ion hopping between the neighboring sites occurs in EC: PC-PSSE containing 30 wt.% EC: PC and above.

The hopping of ions to neighboring site (in Region II) creates mismatch. According to Akgöl and coworkers (2007), this mismatch could be suppressed either by ions undergoing backward hopping (ion returns to its initial site) or forward hopping upon rearrangement of its neighboring ions (site relaxation) (Akgöl *et al.*, 2007). This phenomenon occurs in Region III. For the PSSE up to EC: PC-30 composition, ions overcome the mismatch by forward hopping. This is quantitatively exemplified by the calculated n value that falls below 1, for instance $n = 0.4$ (in NaI-15), $n = 0.45$ (in EC: PC-20) and $n = 0.57$ (in EC: PC-30). The successful ion hopping to new sites are the basis for long-range ion transportation. A minor suppression in the site relaxation, however, is visible with increasing plasticization. This may be caused by the interference of ion pairs localization. Reduction in the dispersive conductivity is visible in EC: PC-PSSE containing 40 wt.% of EC: PC and above. This could arise from the increased restriction of caged ion movements that lowers the conductivity.

6.4.2 Temperature variation

Figure 6.10 shows the frequency-dependent conductivity spectra of EC: PC-20 and EC: PC-30 as the function of temperature. Similar conductance pattern to that of the room temperature was observed except for the dispersive region where conductivity decreases with increasing frequency. For this characteristic plot, the n value could not be determined as the trend deviates from the theoretical law. The only speculation that can be drawn from this observation is the non-favorable caged ion movements at high frequency. This could happen due to ions overcrowding, in which the ions population increases from the effect of thermal activation. The increment could be rationalized from the increase of σ_{dc} and EP effect (high ion accumulation). A good thermal-activated process (or Arrhenius behavior) can be seen in EC: PC-20 based on the obvious separated plateau region as compared to that of EC: PC-30.

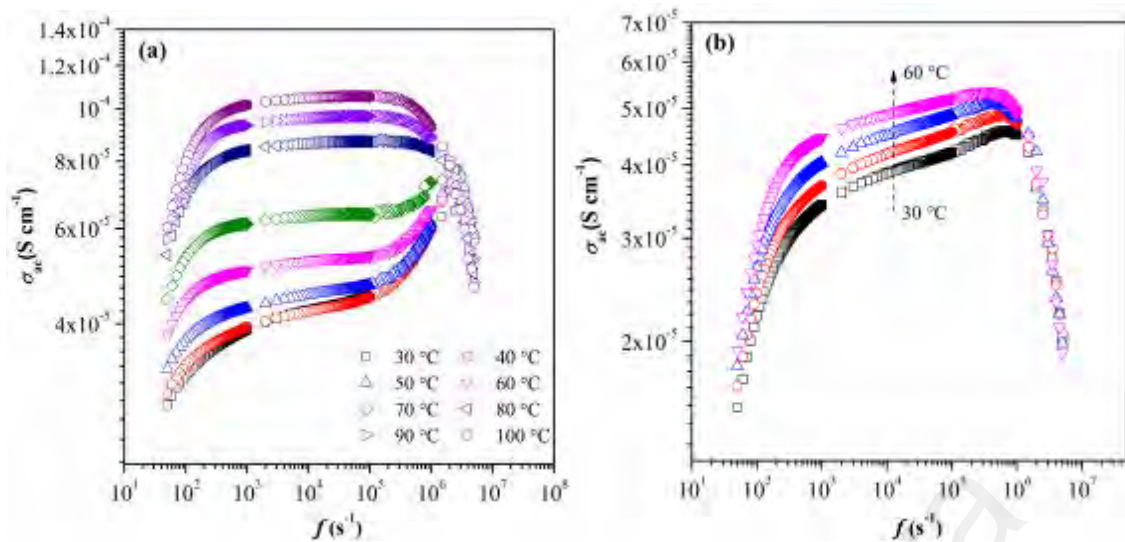


Figure 6.10: Conductance spectra of (a) EC: PC-20 and (b) EC: PC-30 at different temperatures

6.5 Ionic conductivity at room temperature

Figure 6.11 shows the ionic conductivity of plasticizer-PSSE as the function of EC: PC. The variation is discussed with reference to the N_{ion} and D_{ion} values, as shown in Figure 6.12. A drop in ionic conductivity is accounted when additional 10 wt.% of EC: PC is incorporated into NaI-15. Generally, the incorporation of EC: PC causes charge dilution and gives rise to ion formation. Similar phenomenon can be detected in EC: PC-20 based on the increase of N_{ion} . The increase, particularly in the number of Na^+ , dictates possible formation of transient crosslink, which may bridge nearby chains and reduce the chain flexibility. As the result, formation of continuous coordinating sites for ion hopping is restricted and ions move at slower pace. The outcome is depicted by the reduced D_{ion} .

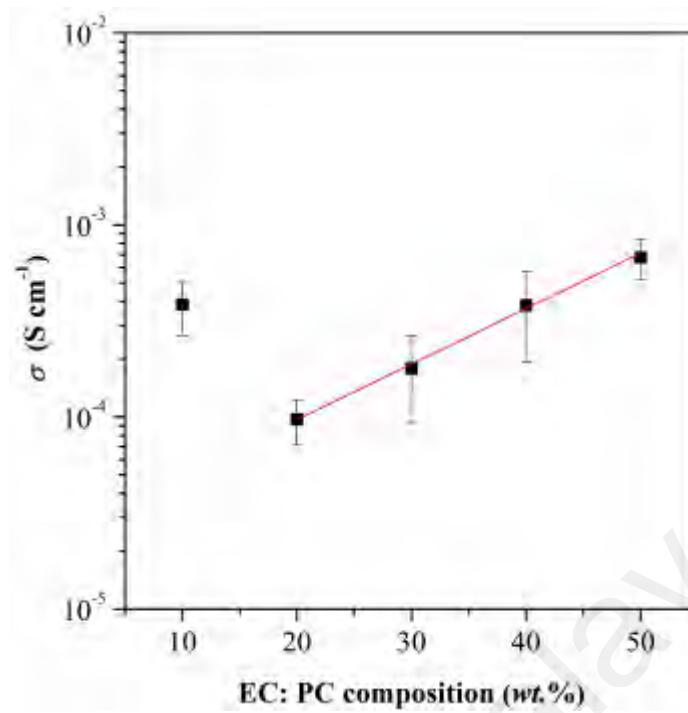


Figure 6.11: Ionic conductivity of EC: PC-PSSE at room temperature

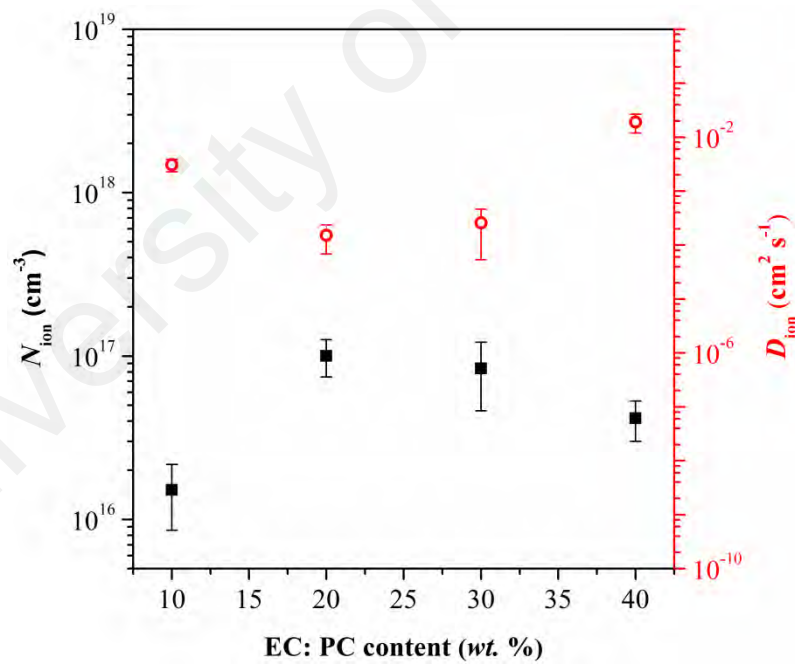


Figure 6.12: N_{ion} and D_{ion} of EC: PC-PSSE at room temperature

With further increase of EC: PC content (above 30 wt.%), the ionic conductivity increases linearly to the highest of 6.77×10^{-4} S cm⁻¹ (in EC: PC-50). The increment is caused by the increase in ion diffusivity. Ions preserve considerably good diffusivity at

higher dilution due to the rupturing of transient crosslink structure. As the effect of the structural rupturing, more number of ions is freed and the ion overcrowding leads to ion-ion interactions (ion association). Consequently, ion pairs or higher aggregates (multiplets) are formed. This is evident from the decrease of N_{ion} .

6.6 Conductivity-temperature dependence

Figure 6.13 elucidates the ionic conductivity of NaI-15 and EC: PC-PSSE as the function of inverse temperature. Only the results of EC: PC-20 and EC: PC-30 was enclosed.

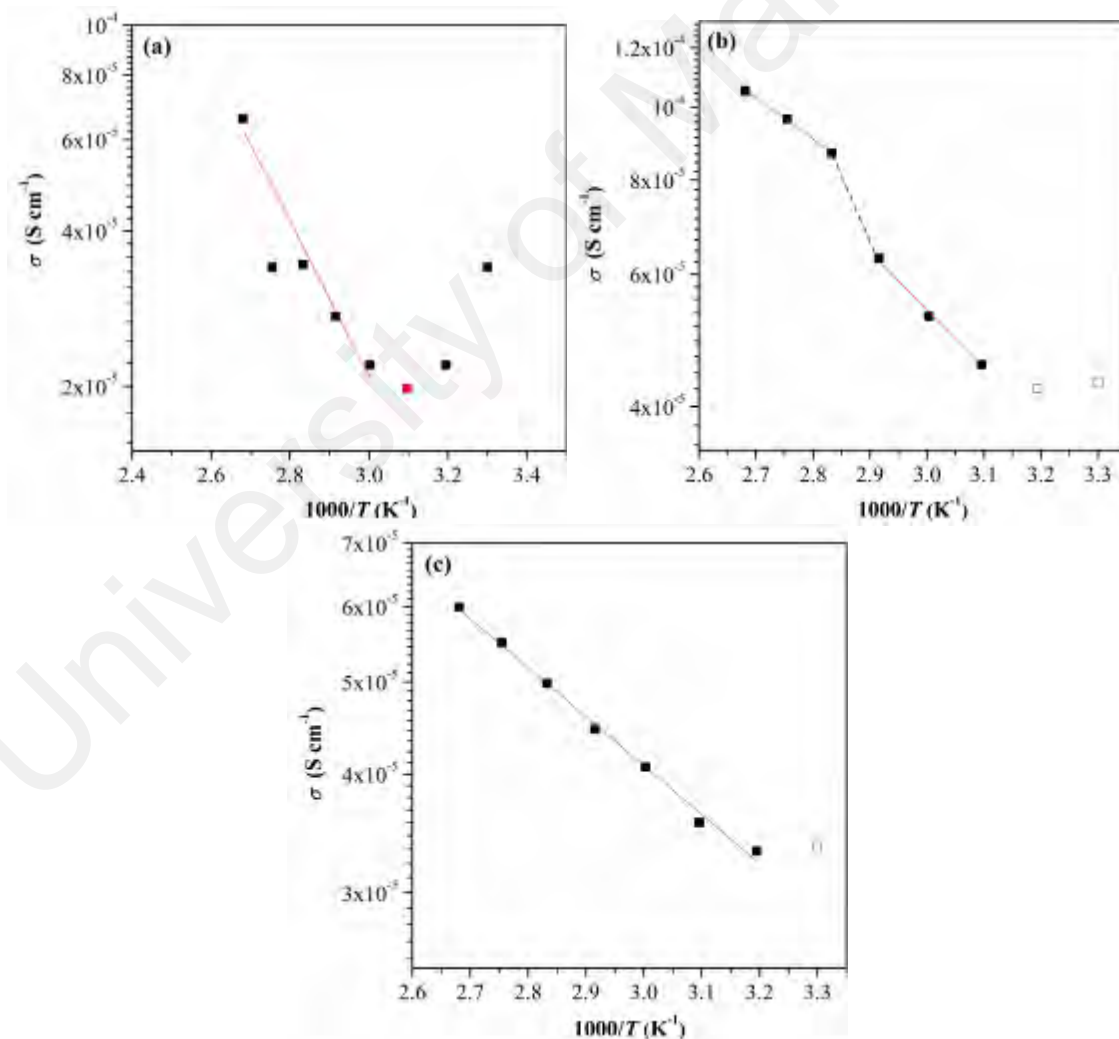


Figure 6.13: Arrhenius plot of (a) NaI-15 (b) EC: PC-20 and (c) EC: PC-30

Ionic conductivity readings for EC: PC-PSSE with higher plasticization could not be obtained owing to the loss of interfacial contact between the electrode and electrolyte. The loss of interfacial contact could be attributed to the excessive ion pair formation with increasing temperature, which causes surface inhomogeneity. Similar effect can be observed in EC: PC-30 above a threshold temperature. The threshold temperature is dependent on film thickness. All the ionic conductivity data was studied in reference to D_{ion} and N_{ion} plot (Figure 6.14) as the function of temperature.

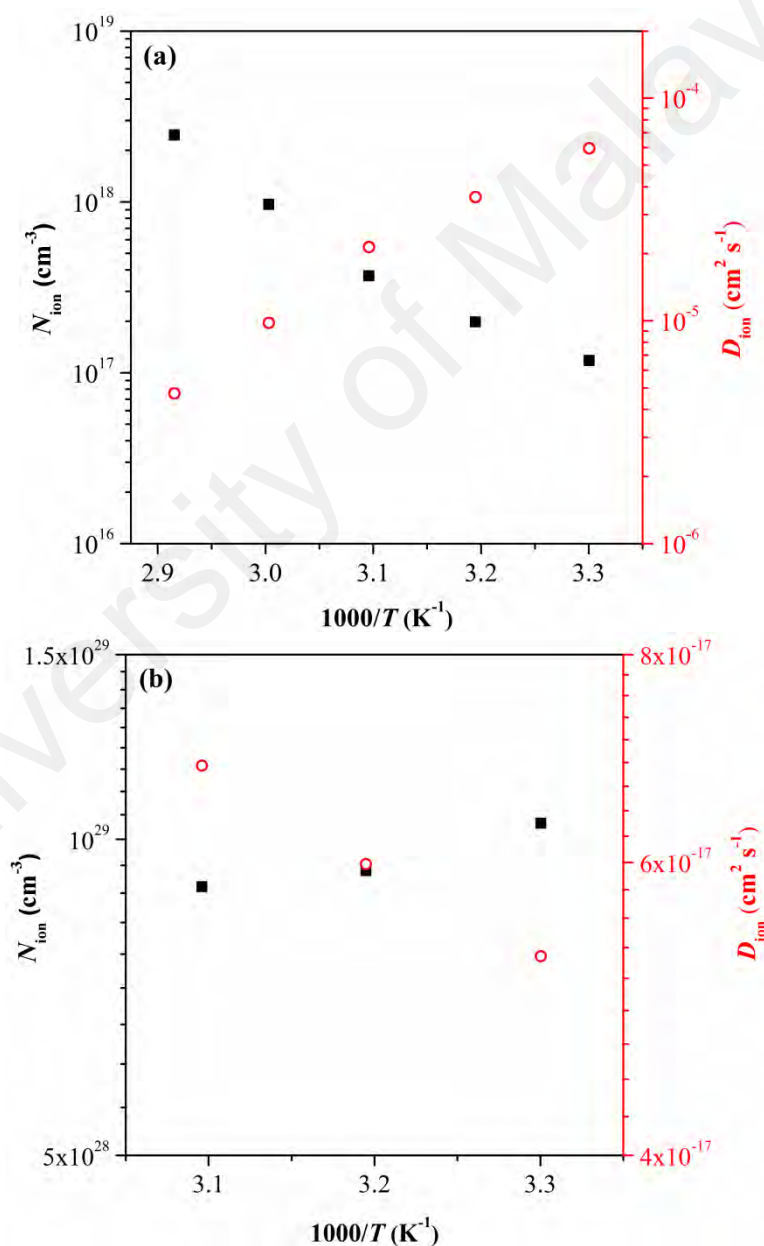


Figure 6.14: N_{ion} and D_{ion} of (a) EC: PC-20 and (b) EC: PC-30 at different temperatures

In NaI-15, the ionic conductivity decreases with increasing temperature up to 50 °C due to the contraction effect of free volume. Whilst at higher loading of EC: PC, this was not observed. Instead, the ionic conductivity increases in the whole temperature range, as confirmed from Figure 6.13(b-c). The conductivity mechanism complies with Arrhenius behavior. In EC: PC-20, the ionic conductivity increases linearly above 50 °C. Approaching 70 °C, the ionic conductivity enhances by nearly one order of magnitude with a distinct transition. This transition temperature is close to the T_g of EC: PC-20 (DSC thermogram is not shown). Typically, phase transition creates more amorphous phase that favors the inter-chain and intra-chain movements of polymer matrix. As the result, there is an improvement to the ion mobility. But in this composition, reduction of D_{ion} was observed with increasing temperature. This could be the effect of increasing ions population (N_{ion} increases) that restricts the segmental dynamics when higher Na^+ forms transient crosslink. Thus, the ionic conductivity enhancement in this sample composition could be correlated to the increased in the ions population rather than its mobility.

Nevertheless in EC: PC-30, the enhancement of ionic conductivity with increasing temperature is resulted from higher ion diffusivity (D_{ion} increases). This may arise from the better chain dynamics when more Na^+ is freed from the crosslink structure. Consequently, higher aggregates (or ion pairs) are formed in EC: PC-30 as evident from the reduced N_{ion} value. Besides, ion associations are prone to occur in EC: PC-30 due to the massive increase in ions population, from $2 \times 10^{17} \text{ cm}^{-3}$ at room temperature to $1 \times 10^{29} \text{ cm}^{-3}$ at 30 °C.

6.7 XRD

Figure 6.15 shows the XRD patterns of NaI-15 doped with different EC: PC contents. An obvious increase in the chain ordering was seen in EC: PC-20 based on the increase of peak intensity at $2\theta = 17^\circ$. The ordered structure forms as the consequence formation of excessive ions by two-order of magnitudes (*cf.* Figure 6.12). This increases the transient crosslink density and the polymer chain loses its flexibility.

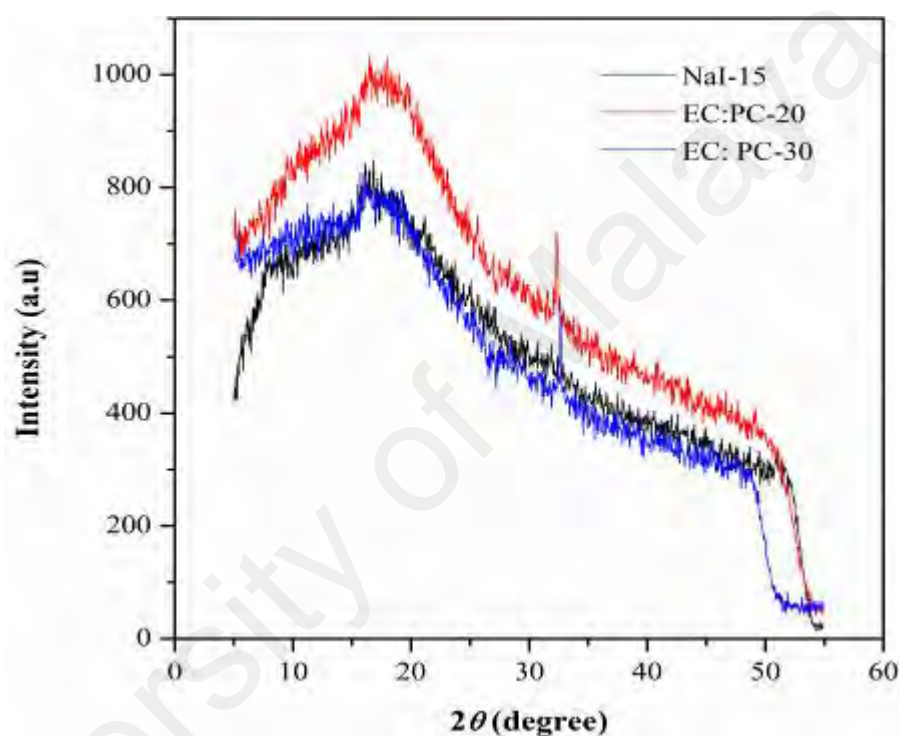


Figure 6.15: XRD pattern of EC: PC-PSSE containing different EC: PC contents

With addition of more EC: PC (*e.g.* 30 wt.%), the amorphous hump decreases to the extent that it looks similar to that of NaI-15. The polymer chain becomes more randomly arranged in the presence of higher EC: PC. This could happen when Na^+ is freed from transient crosslink structure. Subsequently, ion associations happen. The presence of contacting ions is obvious in EC: PC-20 and EC: PC-30 samples based on the appearance of sharp representative NaI peak at $2\theta = 32^\circ$ (Rani *et al.*, 2014).

6.8 Thermal properties

6.8.1 DSC

Changes in the phase transition of NaI-15 with higher EC: PC doping (*i.e.* 30 and 40 wt.%) are illustrated in Figure 6.16. Dramatic drop in the T_g of NaI-15 from 50 °C to -5 °C (ΔC_p of 0.34 J g⁻¹ °C⁻¹) in both tested EC: PC-PSSE compositions depict the weakening of intermolecular attractions between polymer chains. This happens because of the (i) lowering of inter-cation interaction between NaI and polymer chain, and (ii) sliding effect imposed by EC: PC. As there is no difference in the T_g between EC: PC-30 and EC: PC-40, it can be hypothesized that there is no significant difference in their segmental mobilities. It was also noted that both the samples do not exhibit any relaxation process similarly as in NaI-15. Thus, content of amorphocity could be slightly lower in both EC: PC-30 and EC: PC-40.

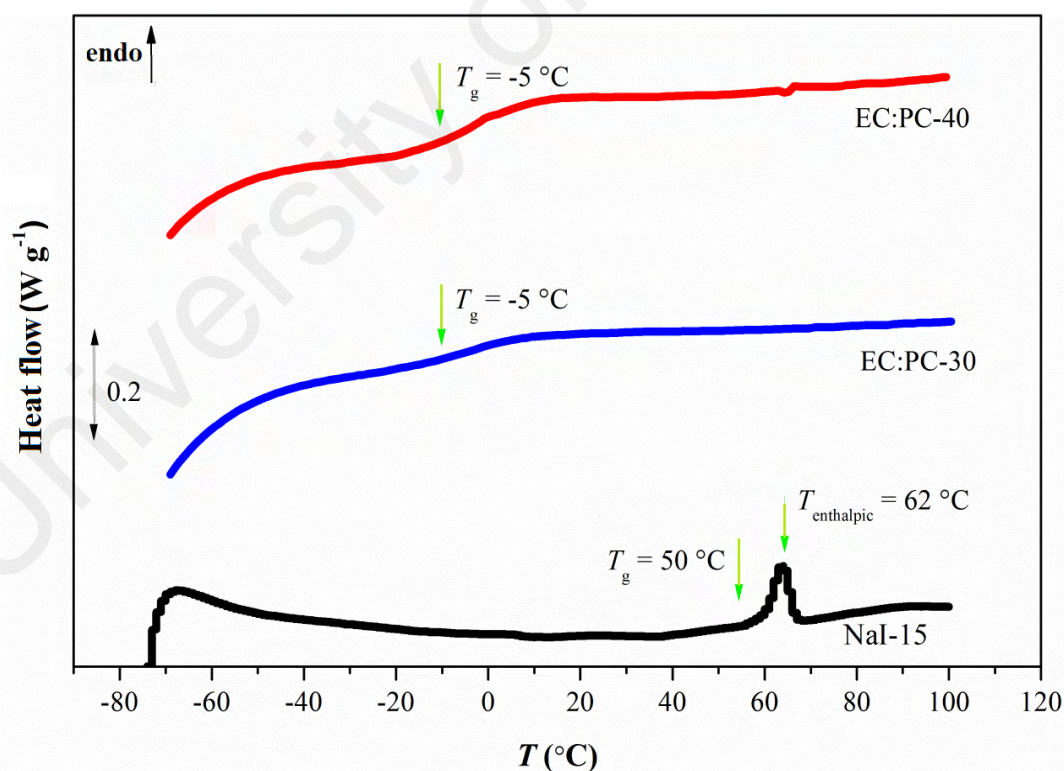


Figure 6.16: DSC curves of EC: PC-PSSE at different EC: PC contents

6.8.2 TGA

Figure 6.17 summarizes all the T_d s recorded in NaI-15, EC: PC-30 and EC: PC-40. The DTG curve of NaI-15 is enclosed in Figure 6.17(a) and the three decomposition stages were labeled accordingly with different color markers. The higher doping of EC: PC causes the first T_d to shift to lower temperature, accompanied by higher weight loss. This may be ascribed to further weakening of chain structure (intermolecular forces) which causes significant amount of EC: PC and other thermo-products such as oligomers to volatilize. Similar effect can be observed in the second T_d . The second T_d in EC: PC-PSSE is given in range value as it was difficult to assign the peak maxima on the broad irregular derivative curve. The peak increasingly broadens with increasing EC: PC content. A reverse trend was observed for the third decomposition stage. The T_d of EC: PC-PSSE shifts slightly to higher temperature as compared to that of NaI-15. The slight increment could be resulted from the reduction of amorphocity in the EC: PC-PSSE. All the recorded final residual mass falls in the range of 6-8 wt.% at 480 °C.

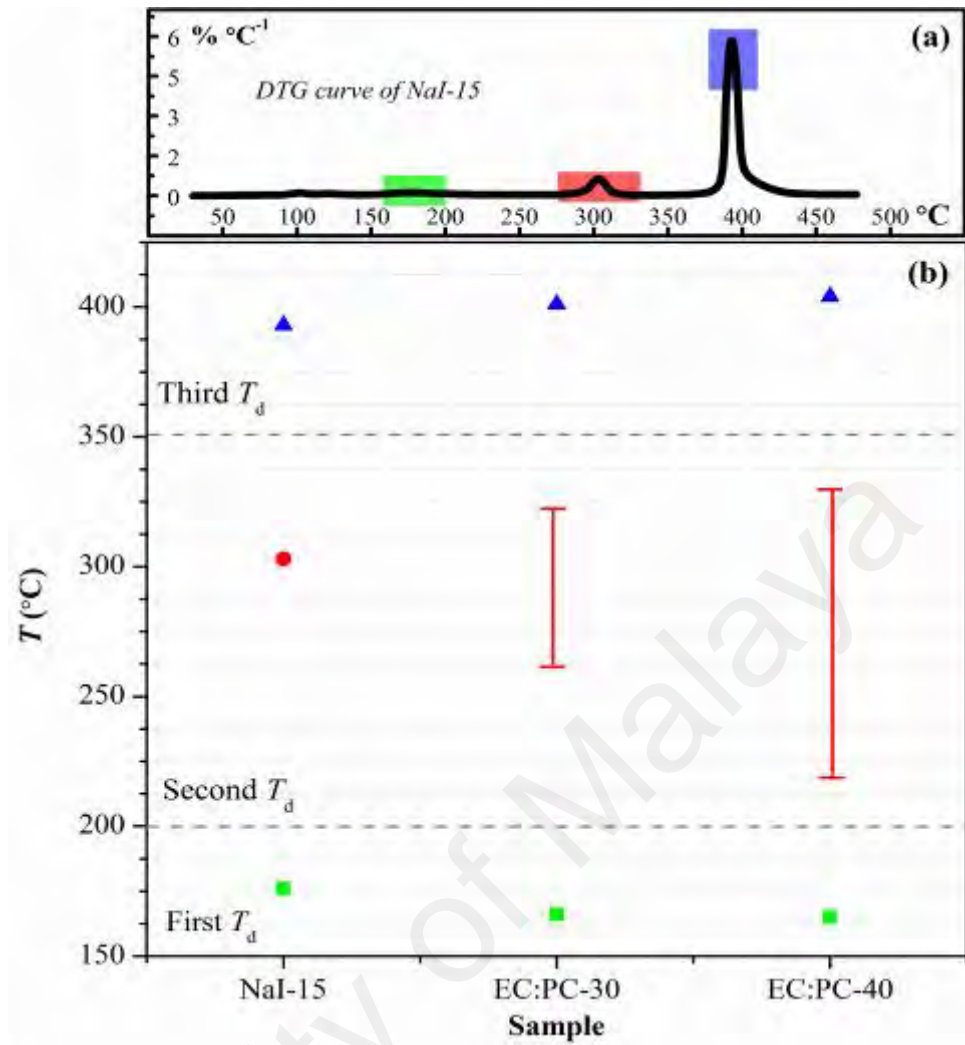


Figure 6.17: (a) DTG curve of pure AA05 and (b) T_d variation upon different EC:PC contents doping in NaI-15

CHAPTER 7: RESULTS AND DISCUSSION

Characterization of PSSE: System III- SiO₂ variation

7.1 Chain relaxation time

7.1.1 Room temperature measurement

Figure 7.1 depicts the variation of τ_{chain} for NaI-15 (reference-PSSE) doped with different SiO₂ NPs contents. Quantity τ_{chain} was determined using similar method reported previously [from Z'/Z'' vs. f plot (Appendix H)]. Results for SiO₂-PSSE containing 4 and 10 wt.% of SiO₂ NPs were excluded as the $Z''_{\text{max}}(f)$ could not be assigned due to the distortion in the Lorentzian shapes.

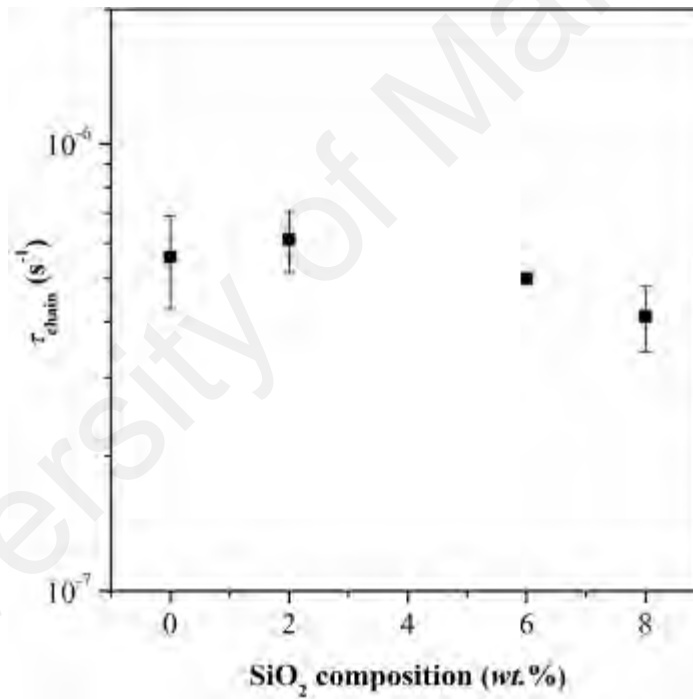


Figure 7.1: Chain relaxation time of SiO₂-PSSE at room temperature

Based on the plotted data, similar τ_{chain} was recorded for SiO₂-2 as compared to NaI-15. This shows insignificant change in the chain dynamics upon initial incorporation of SiO₂ NPs. According to literatures, incorporation of SiO₂ NPs that forms Lewis acid-base interaction with polymer chain typically yields structural disorderliness and increases the chain dynamics. Unfortunately in this case, no such interaction between

SiO₂ NPs and polymer chain is favored. Insignificant change of the chain dynamics is possible when each silicate group is bonded to each other through an oxygen bridge in the silica phase (non-bonded complex structure). This observation is confirmed and shown in Section 7.8.1. The formation of non-bonded complex structure restricts the mobility of polymer domains adjacent to silica clusters. At higher SiO₂ NPs contents (such as SiO₂-6 and SiO₂-8), there is an increase in the chain dynamics (decreased τ_{chain}) which indicates that the formation of Lewis acid-base interaction is more favorable.

7.1.2 Temperature variation

Figure 7.2 depicts the plot of $-Z''$ vs. f for SiO₂-PSSE across different temperatures. In general, the curves exhibit Lorentzian shape. Results for SiO₂-4 and SiO₂-10 was excluded in this study as no Z'' peak maxima can be assigned. In SiO₂-2 and SiO₂-6, the $Z''_{\text{max}}(f)$ progressively shifts to higher frequency with increasing temperature. This implies improvement in the segmental chain dynamics. The difference between each temperature in SiO₂-6 is not as prominent as that of SiO₂-2. This may be associated to the increase restriction of chain dynamics in SiO₂-6 as the consequence formation of Lewis acid-base interaction. This interaction is absent in SiO₂-2. Another non-prominent shift of $Z''_{\text{max}}(f)$ can be seen in SiO₂-8. Below T_c (50 to 60 °C), the chains have reduced dynamics with increasing temperature. This is seen from the increase of impedance resistance (*i.e.* increase in Z''_{max} peak height). Above T_c , the characteristic plot is similar to other samples.

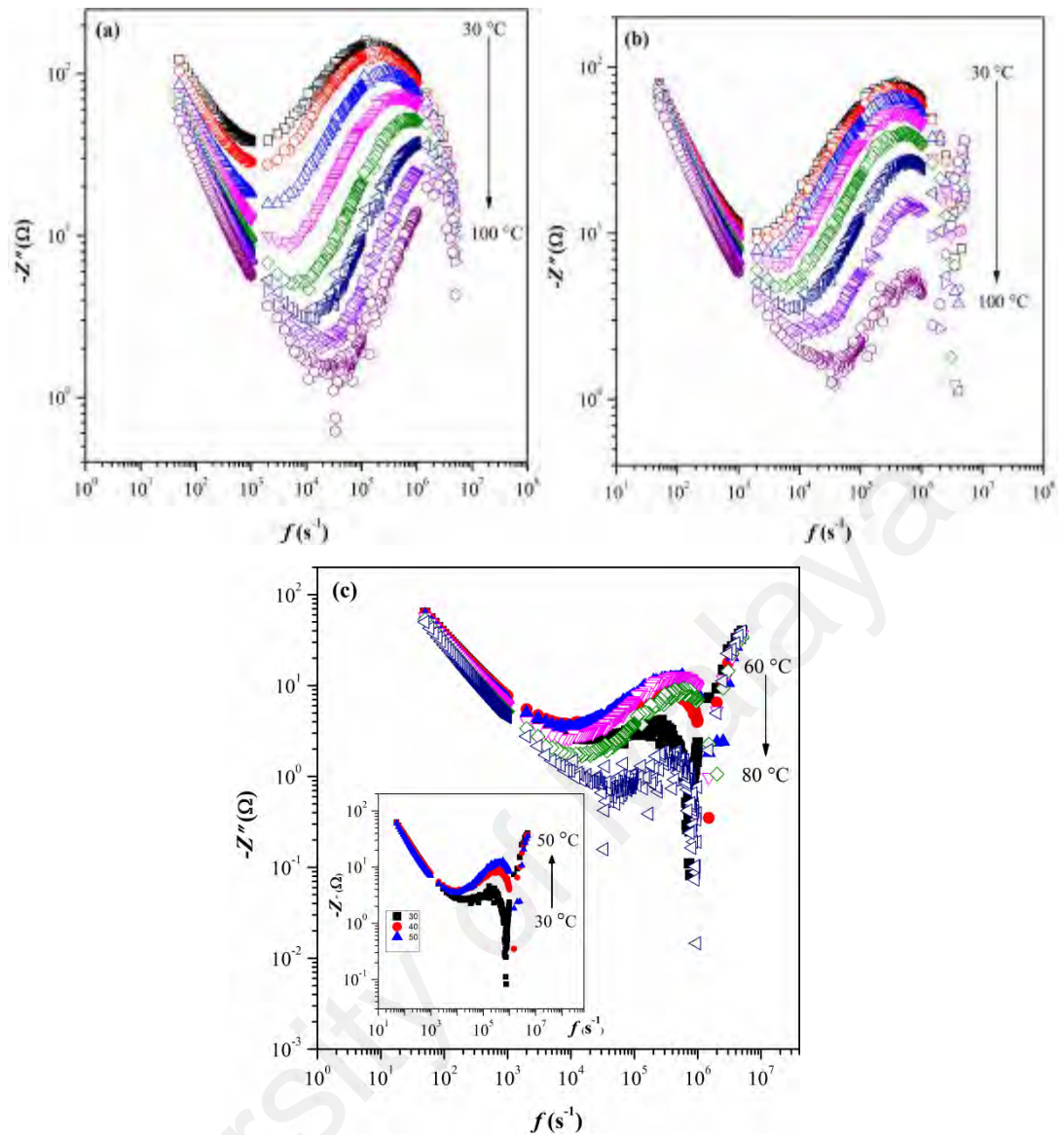


Figure 7.2: Changes in the chain relaxation time of SiO₂-PSSE: (a) SiO₂-2, (b) SiO₂-6 and (c) SiO₂-8 at temperature variation

7.2 Nyquist plot

7.2.1 Room temperature measurement

Figure 7.3 shows the Nyquist plot of SiO₂-PSSE and the assigned RC circuit. The RC circuit does not follow ideal capacitor as seen from the non-Debye characteristic plot of $Z'/-Z''$ vs. f . Initial incorporation of SiO₂ NPs (in SiO₂-2) into NaI-15 results in a broader semicircle (R_b increases). The change is accompanied by delay in the formation of fully stabilized network based on the shift of f_0 to lower frequency. The delay is caused by the increase of chain localization in non-bonded complex structure, as

reported earlier. Consequently, this increases the resistance towards ion transport (R_{CT} increases) and results in thinner C_{dl} layer formation (*cf.* Figure 7.4). The impediment of ion transport however grows stronger at high frequency as depicted by the increase of R_{Ω} .

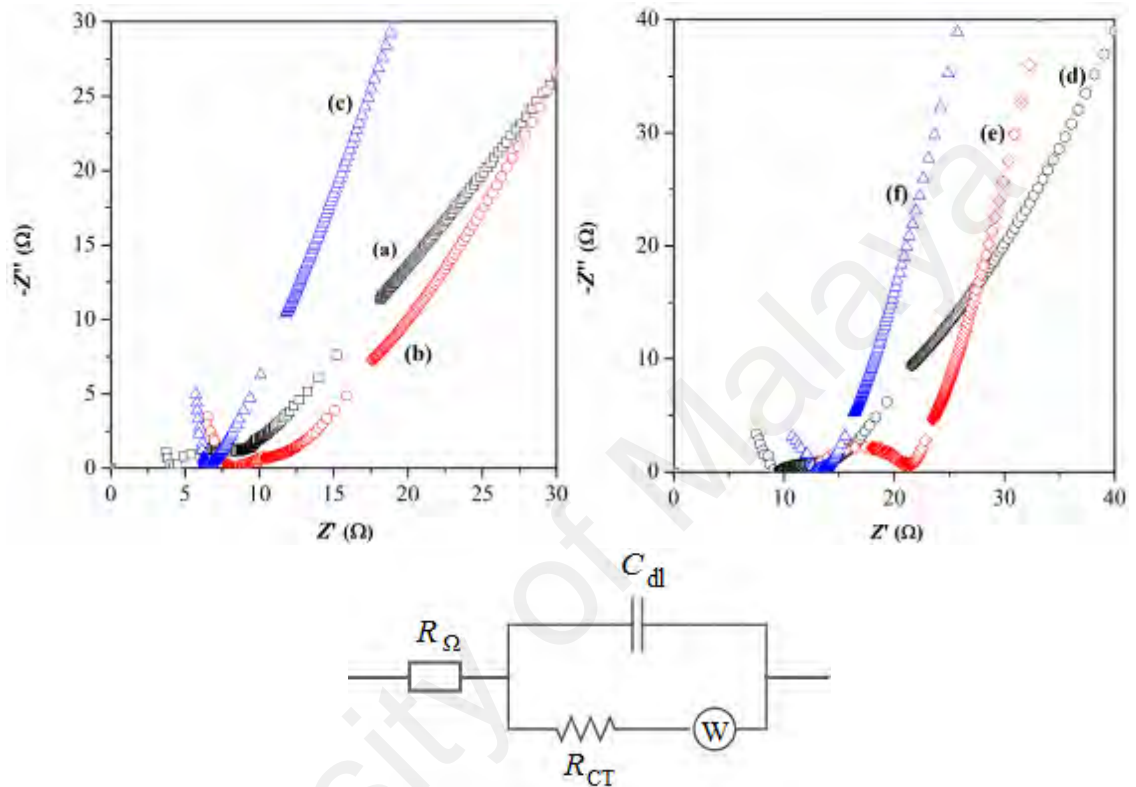


Figure 7.3: Nyquist plot of (a) NaI-15 and SiO₂-PSSE: (b) SiO₂-2, (c) SiO₂-4, (d) SiO₂-6, (e) SiO₂-8 and (f) SiO₂-10 with its RC circuit representation

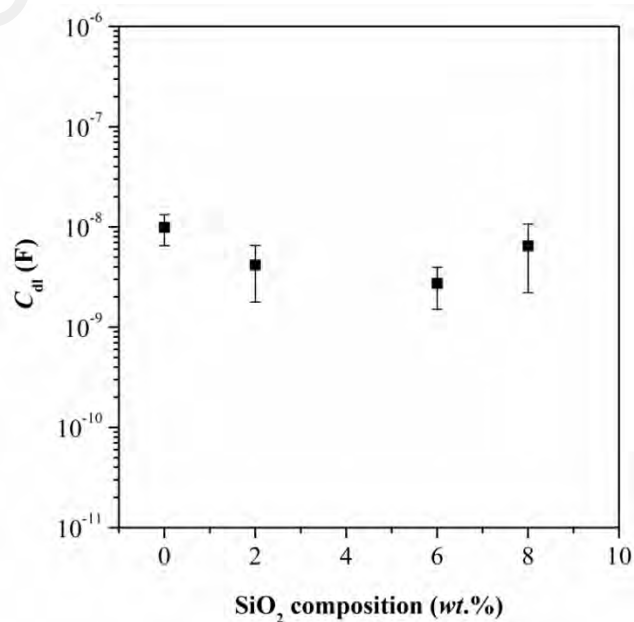


Figure 7.4: C_{dl} layer formation in SiO₂-PSSE at room temperature

In the presence of higher SiO₂ NPs (*e.g.* SiO₂-4), a “thick-like” plot with lower R_b value was observed. The absence of semicircle illustrates good charge-transfer. At higher doping of SiO₂ NPs (*e.g.* SiO₂-6 and SiO₂-8), the plot returns to its semicircle characteristic and displays higher R_b . This demonstrates an increase in the resistance towards charge-transfer. The effect intensifies at higher SiO₂ NPs doping (in SiO₂-8) and further restricts the ion transport at both low and high frequency (which is confirmed from the increase of R_Ω). Whereas in SiO₂-10, the depressed semicircle depicts a slight improvement in the charge-transfer at low and high frequency (R_Ω decreases). There seems to have no difference between the C_{dl} values from SiO₂-2 to SiO₂-8.

7.2.2 Temperature variation

The Nyquist plots of SiO₂-PSSE at different temperatures are shown in Figure 7.5(a-e). There are four different characteristic plots that can be observed with increasing temperature such as (i) depressed semicircle (in SiO₂-2, SiO₂-4 and SiO₂-6), (ii) transition from semicircle to “thick-like” plot at high temperature (in SiO₂-8), (iii) semicircle with increased radius at low temperature that progressively increases with temperature and subsequently depresses above T_c (50-60 °C in SiO₂-8) and (iv) “thick-like” plot throughout the temperature increment (in SiO₂-10). A common RC circuit can be assigned for all the above-mentioned Nyquist characteristic plots, as shown in Figure 7.5(f). The RC circuit does not follow an ideal capacitor based on the strong non-Debye characteristic of $Z'/-Z''$ vs. f plot.

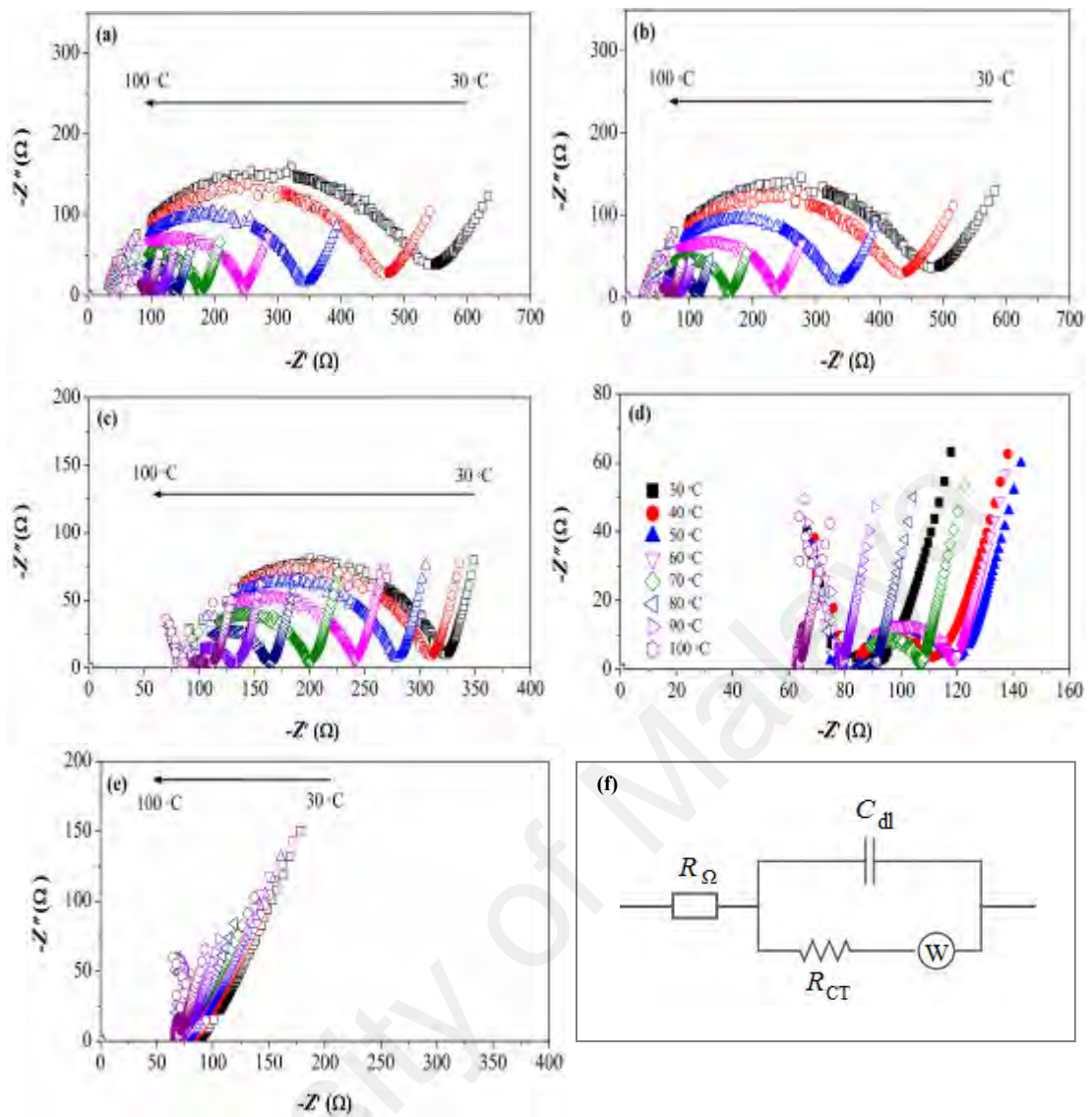


Figure 7.5: Nyquist plot of SiO₂-PSSE as the function of temperature: (a) SiO₂-2, (b) SiO₂-4, (c) SiO₂-6, (d) SiO₂-8, (e) SiO₂-10 and (f) RC circuit

Based on Figure 7.5(a-c), a continuous depression in the radius of semicircle (R_b decreases) can be seen with increasing temperature. This signifies faster ion transportation. The shift of thick-like plot towards the origin in Figure 7.5(e) also indicates the same. The ions acquire faster mobilization as the consequence of increased segmental dynamics, which enable the stable conducting network to form in shorter time (higher shift of f_0).

In contrary to the earlier compositions (*e.g.* SiO₂-2, SiO₂-4 and SiO₂-6), SiO₂-8 shows an increase in the resistivity during the initial temperature increment and subsequently drops above certain temperature. The former observation corresponds to poor segmental dynamics. This causes the vacant sites to be distributed in a longer distance, and subsequently hinders continuous ion hopping. The restriction proceeds with temperature increment up to T_c , and drops thereafter. In general, all the tested SiO₂-PSSE shows restriction in the ion transport at high frequency ($R_\Omega \neq 0$). The highest restriction can be seen in the compositions above 4 *wt.*% of SiO₂ NPs.

7.3 Ion relaxation time

7.3.1 Room temperature measurement

The $\tan \delta$ vs. f curves of NaI-15 and SiO₂-PSSE are depicted in Figure 7.6. All the SiO₂-PSSE exhibits a broad relaxation peak (segmental mode relaxation) similar to NaI-15 except for SiO₂-4 and SiO₂-10. These samples show undefined relaxation peak. The peak maxima in all tested SiO₂-PSSE falls at frequency lower than that of NaI-15. This shows reduction in the segmental-assisted ion motion. The restriction increases with increased doping of SiO₂ NPs based on the rise of τ_{ion} (Figure 7.7). Since the change in f_{max} with increasing SiO₂ content is accompanied by the increase of $\tan \delta_{\text{max}}$, therefore the slowing of segmental-assisted ion motion can be explained by the reduced chain dynamics (*cf.* Section 7.1.1). The accompanied increase in $\tan \delta_{\text{max}}$ also gives insight on the negligible occurrence of self-ion diffusion in the entire presented results.

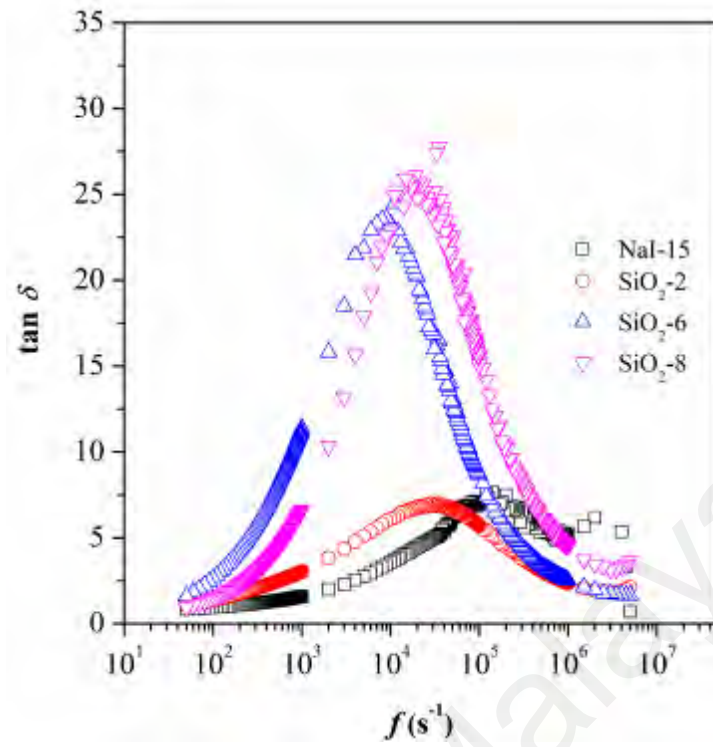


Figure 7.6: Tangent dissipation loss of SiO₂-PSSE at room temperature

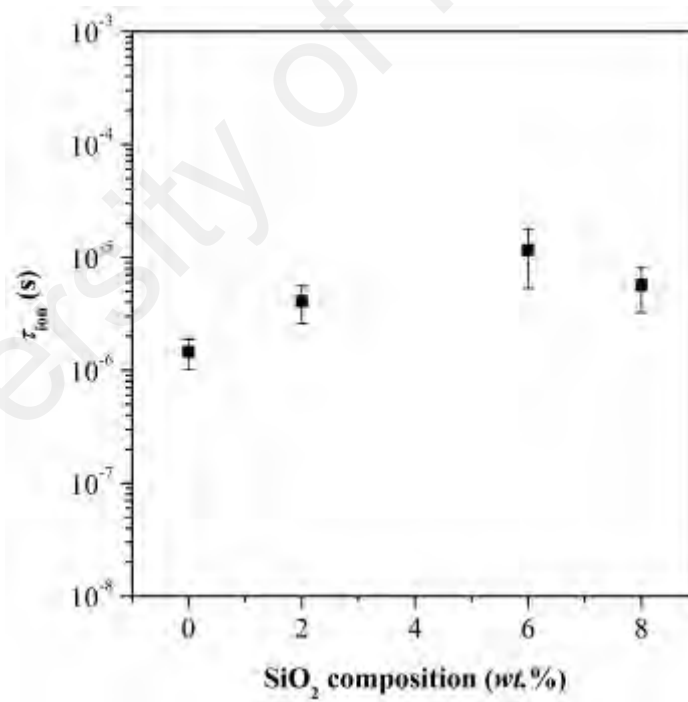


Figure 7.7: Ion relaxation time calculated as the function of SiO₂ content

7.3.2 Temperature variation

Figure 7.8(a-c) shows the overlay $\tan \delta$ vs. f curves of selected SiO₂-PSSE measured at temperature variation. Based on the results of SiO₂-2 and SiO₂-6, the segmental-assisted ion motion is seen to increase with increasing temperature. This is evident from the shift of f_{\max} to higher frequency accompanied by the increase of $\tan \delta_{\max}$. As the result, ion relaxation time is increasingly shortened from 1.09×10^{-4} s (at 30 °C) to 5.5×10^{-6} s (at 100 °C) in SiO₂-2 and from 8.03×10^{-5} s (at 30 °C) to 4.62×10^{-6} s (at 100 °C) in SiO₂-6. This yields good ion transport. The increase in ion hopping occurs as the consequence to the increase in segmental chain dynamics. Different observation can be seen in SiO₂-8, which shows a reduction in the segmental-assisted ion motion (f_{\max} decreases) at temperature increasing to 50 °C (T_c). The ion transportation slightly improves at higher temperature above the T_c , which could be correlated to the increase of chain dynamics.

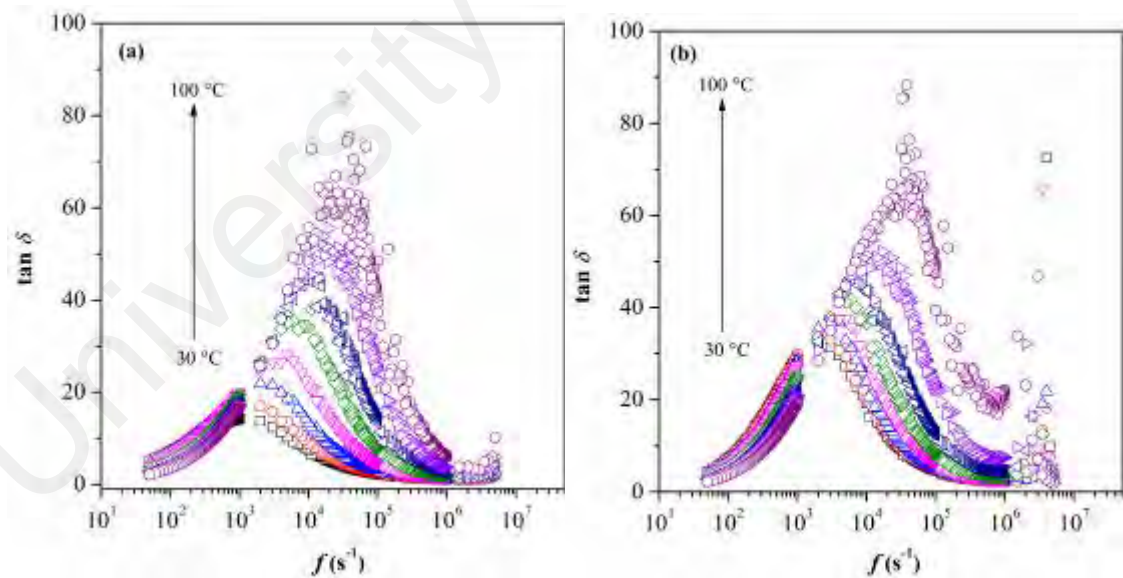


Figure 7.8: Tangent dissipation loss of SiO₂-PSSE: (a) SiO₂-2, (b) SiO₂-6 and (c) SiO₂-8 at different temperatures

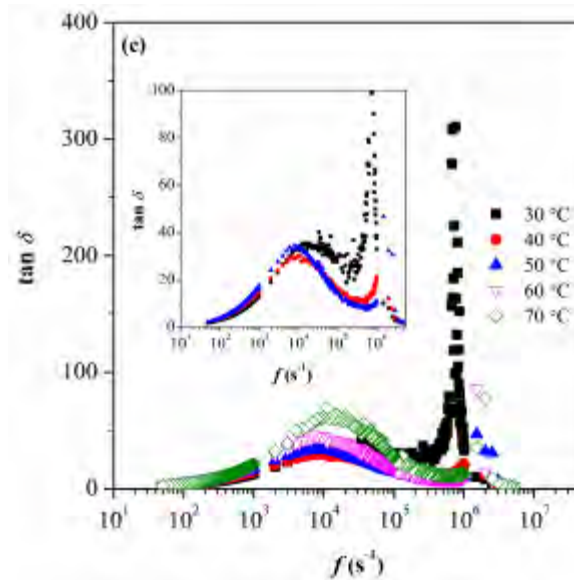


Figure 7.8, continued

7.4 Frequency-dependent ionic conductivity

7.4.1 Room temperature measurement

The frequency-dependent conductivity spectra of NaI-15 and composite-PSSE with different SiO₂ doping at room temperature are presented in Figure 7.9. All the composite-PSSE exhibits three frequency regions similarly as NaI-15. These regions are labeled as Region I, II and III accordingly. There is a progressive increase in σ_{ac} with increasing frequency except for Region II, which shows frequency-independent conductivity (σ_{dc}). The dispersive conductivity (Region III) increases with frequency in all the composite-PSSE except for SiO₂-4.

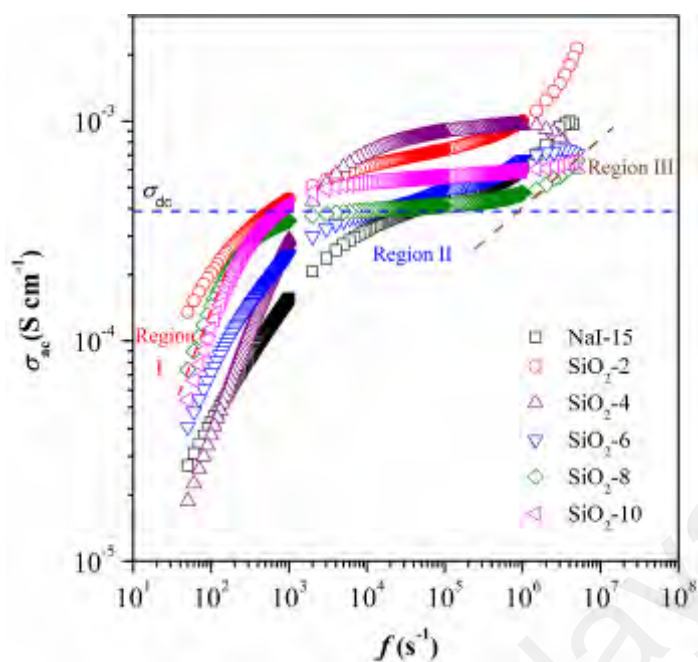


Figure 7.9: Frequency-dependent ionic conductivity of SiO₂-PSSE at room temperature

Other obvious difference between the curve of NaI-15 and composite-PSSE is the appearance of more visible and longer plateau region (except in SiO₂-6). This could be observed associated to the localization of polymer chains in the presence of SiO₂ NPs that provides defined conducting pathways. The plateau region displaces to higher magnitude, causing increase in σ_{dc} with increasing SiO₂ NPs from 2 to 4 wt.%. As the magnitude of σ_{dc} is influenced by the number of ions, thereby the observed increase in σ_{dc} may be correlated to the increasing ions complexation. With further doping of SiO₂ NPs (up to 8 wt.%), the σ_{dc} progressively reduces (which illustrates poor ion complexation) and increase thereafter (in SiO₂-10).

At frequency lower than the plateau region (in EP region), the ionic conductivity gradually drops with decreasing frequency. There is no significant change in the ion accumulation at the electrode-electrolyte interface occurs in SiO₂-2 based on the exhibited similar EP region steepness with NaI-15. This result is in good agreement with the calculated C_{dl} (Figure 7.4) that showed insignificant reduction in the value. The

change in the EP region steepness however gets obvious at higher SiO₂ NPs addition (e.g. SiO₂-4), depicting on higher charge accumulation at low frequency. At further SiO₂ doping, there is a minor decrease in the steepness which illustrates the possible thinning of C_{dl} layer (e.g. SiO₂-6). Thicker C_{dl} layer forms in SiO₂-8 and stays constant at higher SiO₂ NPs composition as the steepness change turns insignificant. Meanwhile in Region III, the σ_{ac} increases with frequency corresponding to site relaxation. This was evident from the n values of composite-PSSE that are below 1.

7.4.2 Temperature variation

Figure 7.10 shows the conductance spectra of composite-PSSE as the function of temperature. The representative regions of EP, dc conductivity and dispersive conductivity are visible within the stipulated frequency range for the entire presented curves.

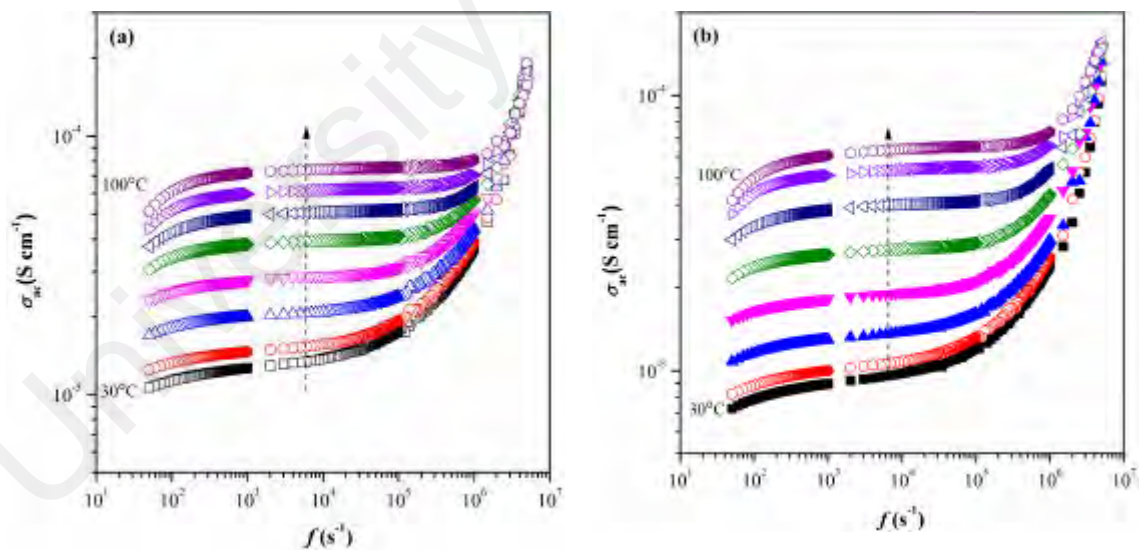


Figure 7.10: Conductance spectra of SiO₂-PSSE as the function of temperature: (a) SiO₂-2, (b) SiO₂-4, (c) SiO₂-6, (d) SiO₂-8 and (e) SiO₂-10

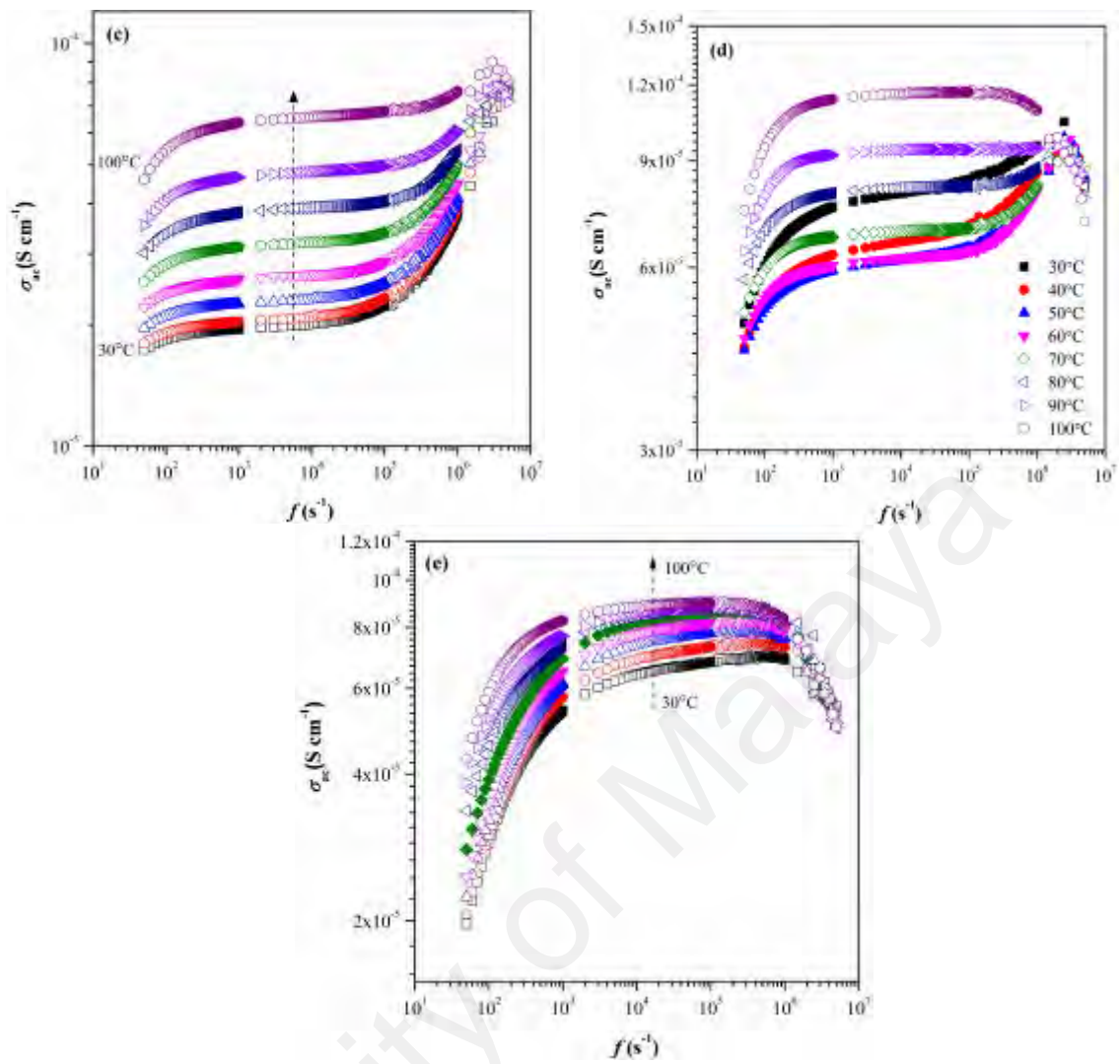


Figure 7.10, continued

All the SiO₂-PSSE exhibits conductivity trend that follows Jonscher power law except in SiO₂-8 and SiO₂-10, which shows opposing conductivity trend at high frequency (Region III). The deviation happens as the consequence of cage ion mode suppression. The dispersive conductivity however rises with temperature in remaining SiO₂-PSSE without any containment, correlating to the increase of NCL and SLPL types of ion dynamics (caged ion movements). These are the temperature-independent processes that occur at high frequency.

Whereas in Region I and II, a stronger thermal influence on the ion transport was observed from the well-separated curves. The effect was least pronounced in SiO₂-10, illustrating on the poor Arrhenius behavior. The strong thermal effect could be caused by the great increase in ions population with temperature increment. This could be further supported by the increase steepness of EP region with temperature, which illustrates the increased ion accumulation at the electrode-electrolyte interface. Flattening in the plateau region becomes obvious with increasing temperature as the ions move to their new neighboring site after an adequate relaxation time. Consequently, shifted the ω_p , which denotes the frequency where transition from dc conductivity to dispersive conductivity occurs, to higher frequency. This was accompanied by the shift of plateau region to higher magnitude with increasing temperature (σ_{dc} increased). Contrary was observed in SiO₂-8 below the T_c , whereby both the factors of σ_{dc} and ω_p decreased with temperature.

The hopping of ions to the new neighboring site, in Region II, creates mismatch. At low temperature, in SiO₂-2 and SiO₂-4, this mismatch was suppressed by the correlated backward ion hopping. This was evident from the calculated n value that falls above 1. Whereas in SiO₂-6 the mismatch was overcome by the forward ion hopping ($n < 0.5$). With increasing temperature, the ion hopping *via* site relaxations gets dominant upon decrease of the n value down to the minimum of ~ 0.6 (in SiO₂-2 and SiO₂-4 at 100 °C) and ~ 0.2 (in SiO₂-6 at 100 °C). The successful ion hopping to a new site are the basis for long-range ion transportation.

7.5 Ionic conductivity at room temperature

Variation in the ionic conductivity of NaI-15 with SiO₂ doping is illustrated in Figure 7.11. The variation is evaluated by referencing the N_{ion} and D_{ion} values shown in Figure

7.12. Results for SiO₂-4 and SiO₂-10 are not presented in Figure 7.12 as the tan δ peak could not be assigned.

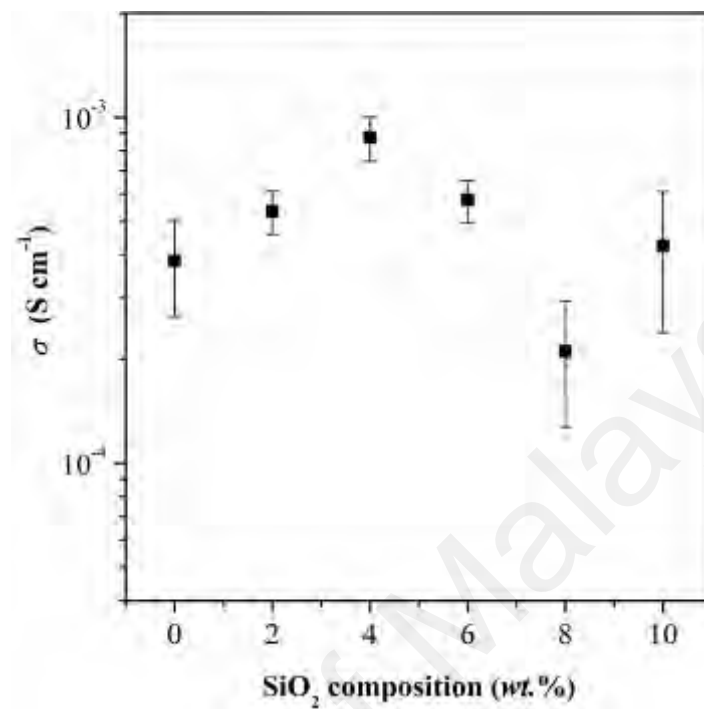


Figure 7.11: Ionic conductivity variation as the function of SiO₂ content

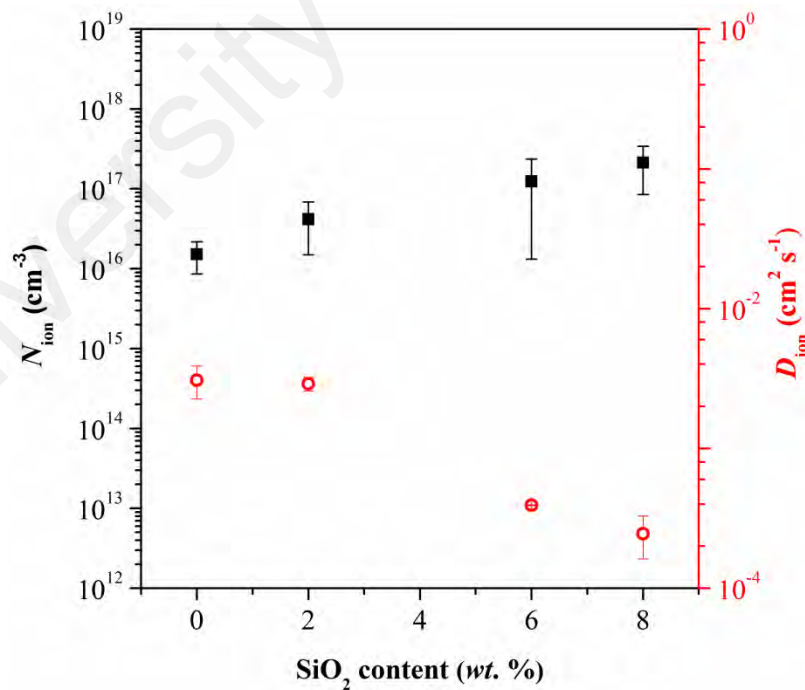


Figure 7.12: N_{ion} and D_{ion} for SiO₂-PSSE calculated using Nernst-Einstein equation

A good enhancement in the ionic conductivity of NaI-15 from $3.85 \times 10^{-4} \text{ S cm}^{-1}$ to the maximum of $8.74 \times 10^{-4} \text{ S cm}^{-1}$ was obtained with SiO₂ doping. The optimum increase was recorded for SiO₂-4. The underline cause for the ionic conductivity increment is listed below:

- Increase of ion population. The formation of Lewis acid-base interaction between SiO₂ NPs and iodide weakens the Coulombic force in NaI. This increases the NaI dissociation and consequently leads to higher free ions formation. Experimentally, this is evident from the increase of N_{ion} value (Lim *et al.*, 2012; Wang and Alexandridis, 2016).
- Enhancement of amorphous structure. In non-bonded complex structure, a strong repulsive force may exist between SiO₂ NPs and polymer chains. This creates free volume.
- Localized polymer chain conformation. The outcome of repulsive force is chain localization (or reduced chain mobility). The localized influence provides more defined pathway for ions hopping (Stephan and Nahm, 2006).
- Favors additional transient sites. The formation of highly conducting interface layer (grain boundary) may provide an extended ion tunneling pathway for long-range ion hopping.

In these SiO₂-PSSE (*e.g.* SiO₂-2 and SiO₂-4), the ion transport occurs prominently *via* the conducting interface layer rather than mediated by segmental-assisted motion. This is inferred by the drop in D_{ion} value. The additional conducting pathway is formed upon overlapping of the interfacial layers of neighboring SiO₂ NPs. This effect intensifies with increasing SiO₂ NPs as the distance between the particles is reduced (Liu *et al.*, 2017). This consequently assists the formation of continuous ion tunneling network structure. The new pathway shares the same potential as the polymer hopping sites but fast and favorable ion hopping may take place *via* grain boundaries. This is

caused by the high sites of defect (flexible local chains) in the grain boundaries, which gives lower activation energy barrier as compared to polymer hopping sites.

At higher SiO₂ NPs contents (*e.g.* SiO₂-6 and SiO₂-8), the ionic conductivity drops with increasing SiO₂. Based on the increase of T_g in these SiO₂-PSSE, formation of Lewis acid-base interaction between SiO₂ NPs and polymer chains could be deduced. According to Wang and Alexandridis (2016), this interaction could hinder the polymer chain motion and reduce the ions mobility (D_{ion} decreases). This has been successfully verified from the earlier subsections. In addition to that, the insignificant change of N_{ion} could also give insight on the formation of ion-ion interactions. This may interrupt the continuous ion hopping. As the consequence of all these effects, the ionic conductivity drops with increasing addition of SiO₂ NPs. At further SiO₂ NPs doping (SiO₂-10), a slight improvement in the ionic conductivity can be observed, which could arise from the improved charge-transfer effect (based from Nyquist characteristic plot).

7.6 Conductivity-temperature dependence

The temperature-dependence ionic conductivity of SiO₂-PSSE is presented in Figure 7.13. Using the plot of D_{ion} and N_{ion} (*cf.* Figure 7.14), the exhibited conductivity trend can be explained. The D_{ion} and N_{ion} were calculated for selected SiO₂-PSSE that contain 2, 6 and 8 wt.% of SiO₂ NPs as the relaxation peak was not visible in other compositions. All the SiO₂-PSSE exhibits ionic conductivity enhancement that follows Arrhenius behavior. This depicts that the conductivity mechanism does not change upon incorporation of SiO₂ NPs.

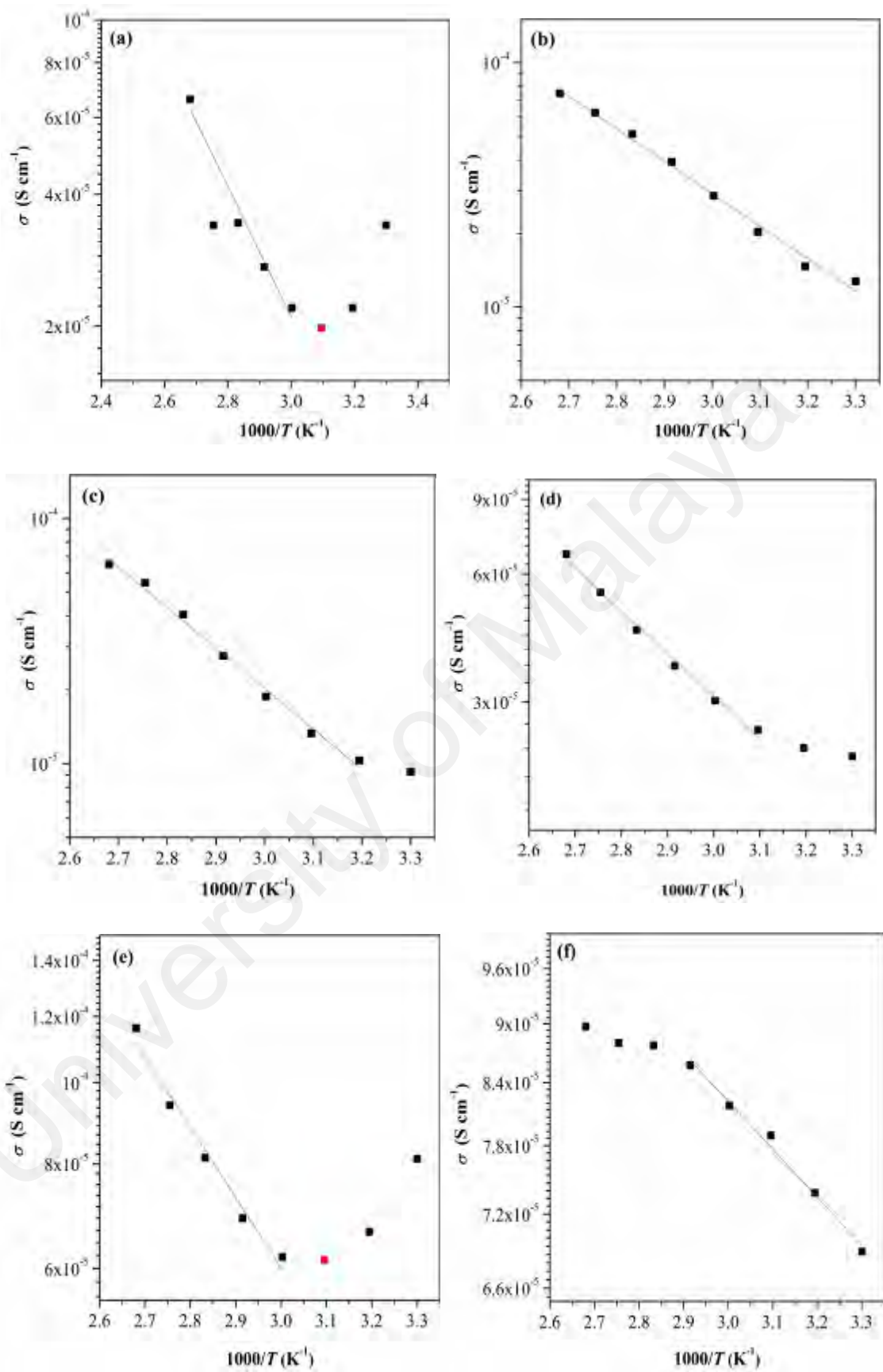


Figure 7.13: Arrhenius plot of (a) NaI-15 and SiO₂-PSSE: (b) SiO₂-2, (c) SiO₂-4, (d) SiO₂-6, (e) SiO₂-8 and (f) SiO₂-10

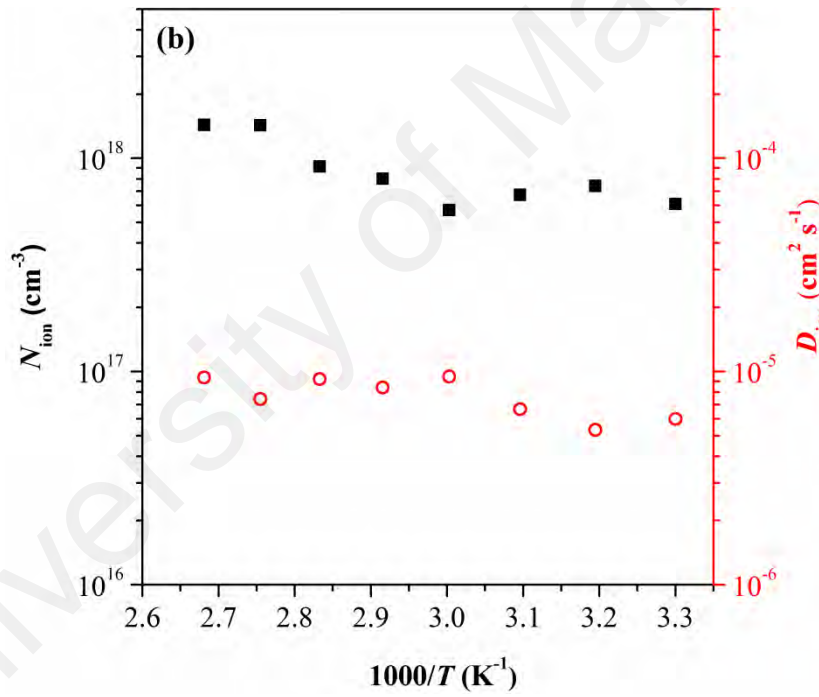
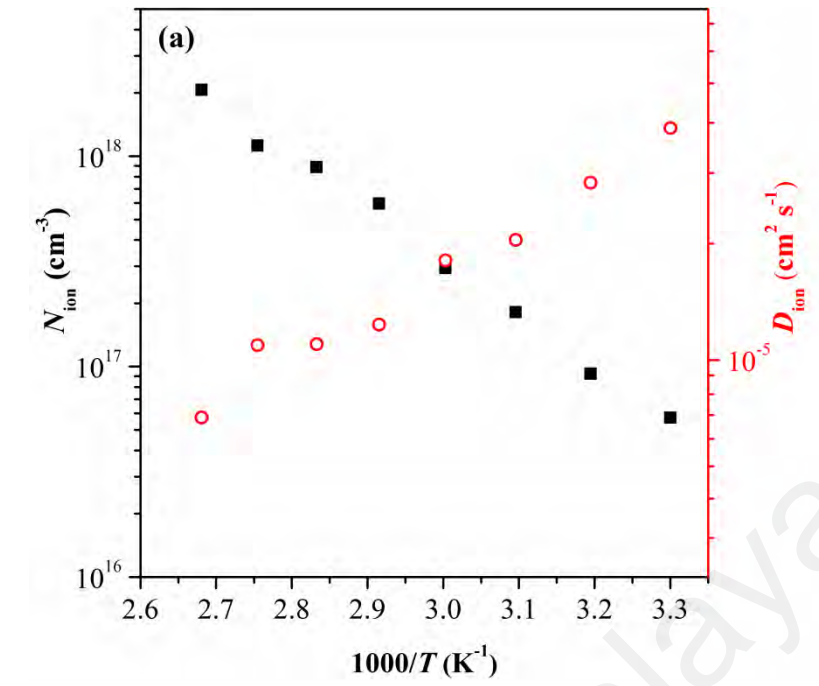


Figure 7.14: N_{ion} and D_{ion} calculated in variation of temperature for SiO_2 -PSSE: (a) SiO_2 -2, (b) SiO_2 -6 and (c) SiO_2 -8

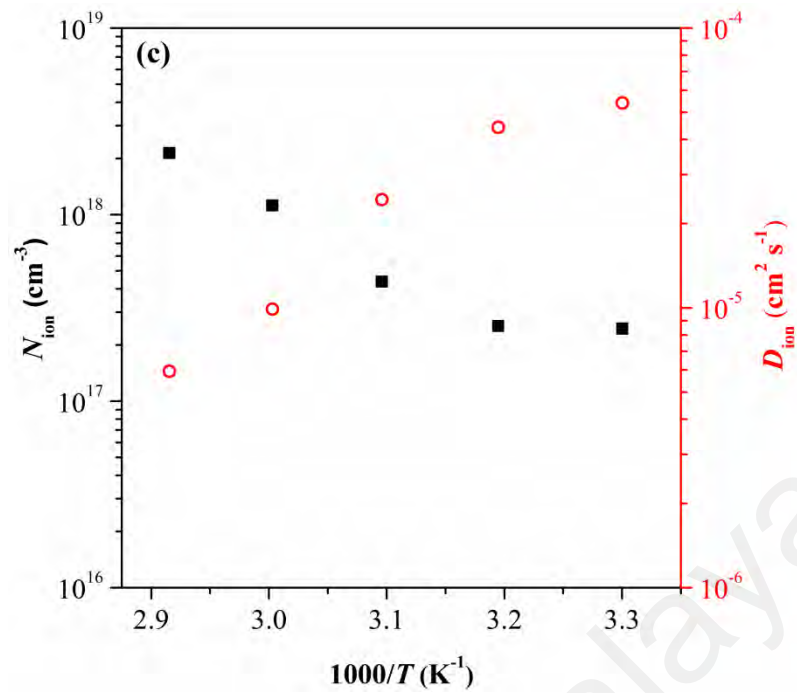


Figure 7.14, continued

The increase of ionic conductivity was postulated to arise from the linear increase in the number of ions during thermal-activated process. This change is accompanied by the decrease of ion diffusivity in SiO₂-2 and SiO₂-8 (*i.e.* D_{ion} reduces) as well as an insignificant increase in SiO₂-6. The poor enhancement in ion diffusion with increasing temperature may arise from the blocking of conducting pathways due to ion overcrowding and ion pairing. The presence of ion pairs could also be the reason for the poor experiment data fitting in SiO₂-4 and SiO₂-6 at low temperatures. The deviation at low temperature shifts to higher temperature with increasing SiO₂ doping (in SiO₂-4 and SiO₂-6). In SiO₂-10, the deviation occurs at high temperature.

In SiO₂-PSSE containing 6 wt.% of SiO₂ NPs and below, free volume diminution is unlikely to happen. This is reasonable as the presence of SiO₂ NPs in between the chains may obstruct the transient crosslink formation. In addition to this, the enlargement of amorphous phase in SiO₂-PSSE could also hinder the free volume diminution. Whilst in SiO₂-8, the effect of transient crosslink formation can be observed

through the drop of ionic conductivity with increasing temperature to T_c . When the SiO_2 NPs agglomerates, the formation of crosslink structure could not be stopped.

7.7 XRD

Changes in the amorphous structure of SiO_2 -PSSE with different SiO_2 additions are observed from XRD diffractograms in Figure 7.15. The initial addition of SiO_2 NPs (2 wt.%) into NaI-15 slightly increases the chain ordering (increased in the peak intensity) and the effect becomes obvious at higher doping. This observation may support the earlier proposal on the chain localization in SiO_2 -PSSE compositions of SiO_2 -2 and SiO_2 -4. The polymer chains may have better localization following to the presence of non-bonded SiO_2 NPs, which reduces the chain dynamics. In addition to that, enhancement of amorphous phase can be also observed. There is a broadening of amorphous hump with SiO_2 NPs addition. A good NaI complexation (or salt dissociation) can be seen in SiO_2 -2 based on the smooth amorphous hump. Whilst at higher SiO_2 NPs content (SiO_2 -4), ion-ion interaction was seen through the appearance of sharp NaI peaks at $2\theta = 23$ - 30° .

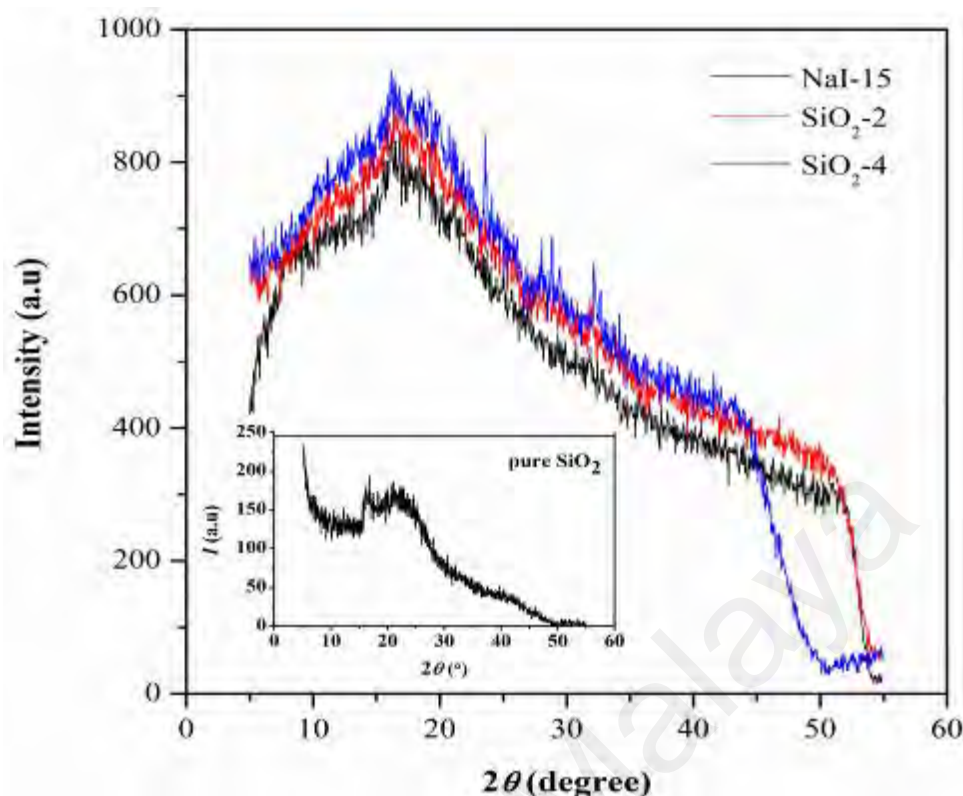


Figure 7.15: XRD diffractogram of NaI-15 with SiO₂ NPs doping (inset figure shows the XRD pattern of pure SiO₂ NPs)

7.8 Thermal properties

7.8.1 DSC

The effect of SiO₂ NPs (2, 4 and 6 wt.%) to the thermal properties of NaI-15 is shown in Figure 7.16. In general, all the T_g s of SiO₂-PSSE fall approximately 30 °C below the T_g of NaI-15, with ΔC_p of 0.30-0.35 J g⁻¹ °C⁻¹. This shows that the intermolecular attraction between chains in SiO₂-PSSE is weaker compared to NaI-15. The depression of T_g in SiO₂-2 suggests the existence of repulsive force between SiO₂ NPs and the interfacial polymer layer (Hanemann and Szabó, 2010). This force may be present in SiO₂-PSSE that has non-bonded complex structure. Each silicate group is bound to each another through an oxygen bridge in the silicate phase (Wieczorek *et al.*, 1995; Mello *et al.*, 2000). The repulsion yields plasticization effect that gives rise to softening of the polymer backbone. Consequently, high fraction of amorphous phase is

available and T_g decreases (Subban and Arof, 2003). The effect gets stronger when more SiO_2 NPs (2 to 4 wt.%) are present.

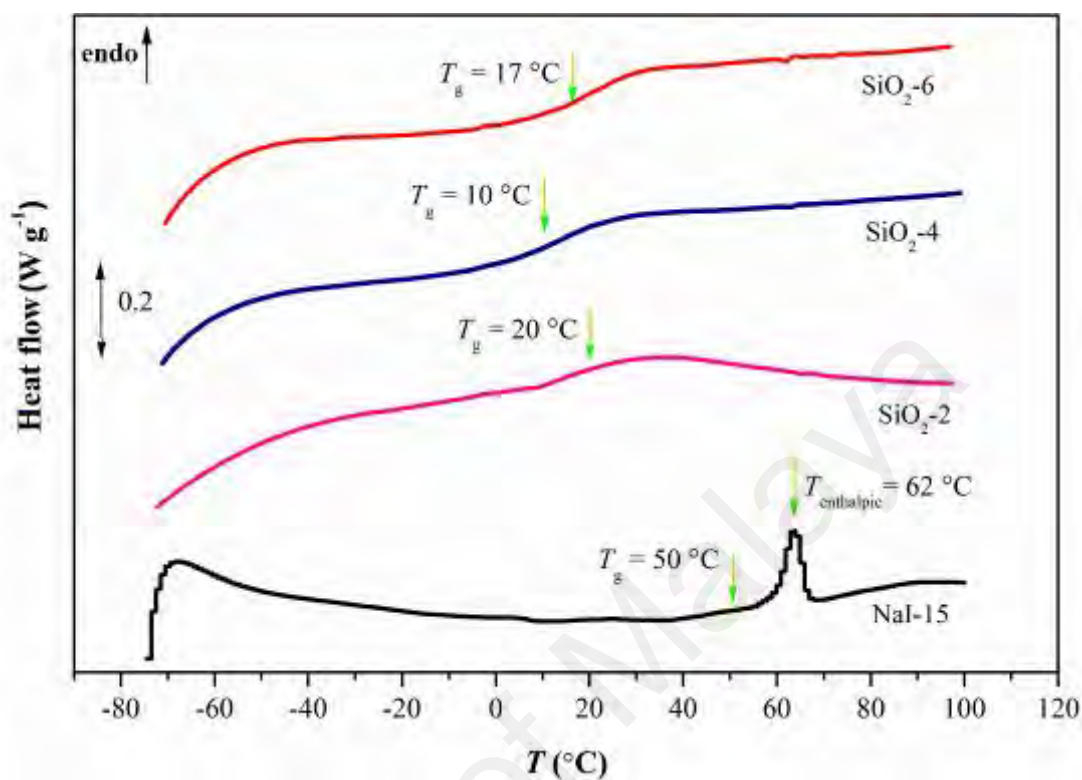


Figure 7.16: DSC thermogram of SiO_2 -PSSE containing different SiO_2 NPs

At further SiO_2 NPs addition (e.g. SiO_2 -6), the T_g shifts to higher temperature. This illustrates the presence of attractive force between SiO_2 NPs and the interfacial polymer layer that could hint the formation of Lewis acid-base interaction (or covalent bonding). The interacting SiO_2 NPs hinders the polymer chain motion and makes the T_g higher.

7.8.2 TGA

Effect of SiO_2 NPs to the thermal stability of NaI-15 is shown in Figure 7.17. The DTG curve of NaI-15 is also enclosed in the same figure and the decomposition stages were labeled by color markers. The incorporation of SiO_2 NPs into NaI-15 reduces the hygroscopic nature of film as evident from the lowering of weight loss during

dehydration process (<150 °C). Above this temperature, all SiO₂-PSSE exhibits three stages of thermal decompositions similar to that of the reference.

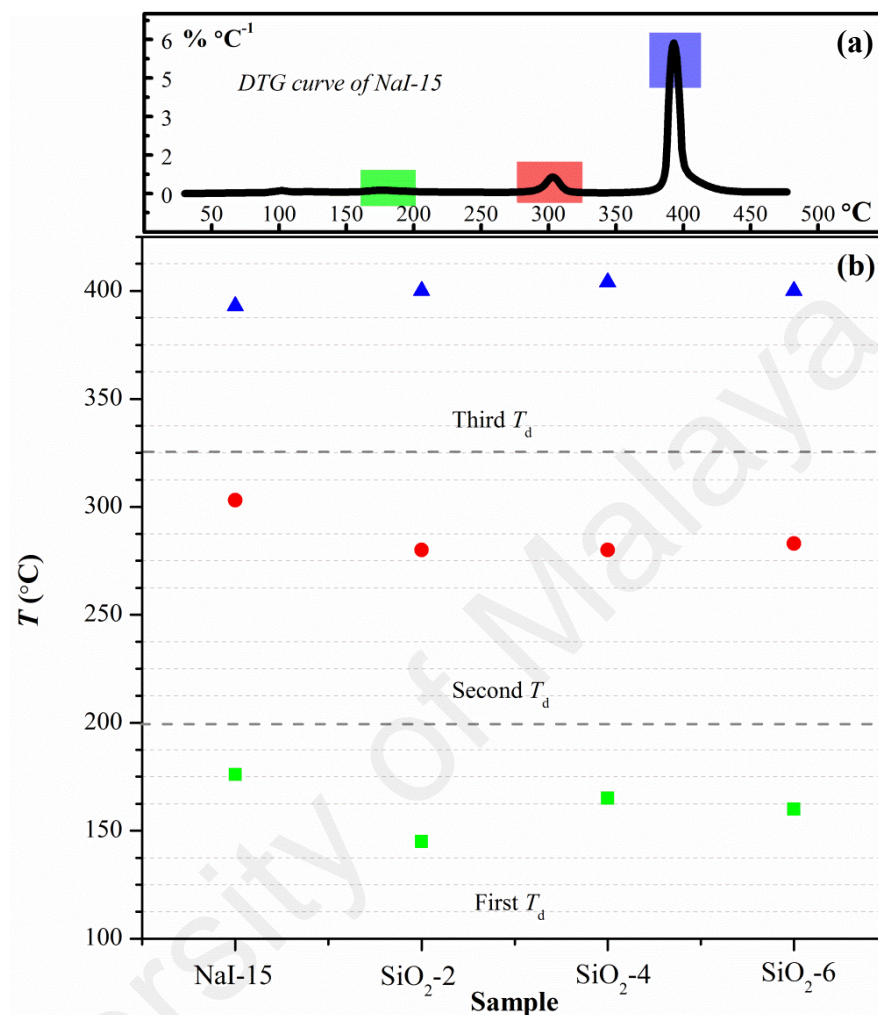


Figure 7.17: (a) DTG curve of pure AA05 and (b) TGA data of SiO₂-PSSE

Based on the plotted figure, all the T_ds of SiO₂-PSSE are lower as compared to that of NaI-15. Obvious change in the T_d of NaI-15 was observed during the initial addition of SiO₂ NPs (*i.e.* SiO₂-2), prominently at the first and second T_ds. The change however becomes insignificant at higher doping except for the first T_d (which shifts to higher temperature). The lowering of T_d suggests a reduction of thermal stability. This could be caused by the plasticization effect from SiO₂ NPs incorporation, which weakens the intermolecular interaction between polymer chains. As the result, higher bond cleavage occurs and releases more volatile compounds during both decomposition stages. Whilst

for the T_d that takes place at 400 °C (third decomposition stage), the temperature is not affected by SiO₂ NPs contents. Apparently, the SiO₂ NPs affect the final residual mass. Higher residual mass at 480 °C was obtained for SiO₂-PSSE (13 wt.%) as compared to NaI-15 (7 wt.%). This suggests that the presence of SiO₂ NPs inhibit the depolymerization process.

7.9 Summary of PSSE systems

Free-standing PSSE films were obtained for the entire formulated compositions using solution casting technique at room temperature. In System I (NaI) and System II (EC: PC), the ion hopping is mediated by segmental dynamics. Unlike in the PSSE with SiO₂ addition (System III), the ions are favorably tunneled *via* conducting interface layer (or grain boundary). Based on the formulated PSSE system, the compositions that yield good ionic conductivity are summarized as follow: NaI-10 to NaI-20 ($\sigma = 1.69\text{-}5.22 \times 10^{-4} \text{ S cm}^{-1}$), EC: PC-40 to EC: PC-50 ($\sigma = 4.97\text{-}14.3 \times 10^{-4} \text{ S cm}^{-1}$) and SiO₂-2 to SiO₂-4 ($\sigma = 6.95\text{-}9.69 \times 10^{-4} \text{ S cm}^{-1}$). Only the PSSE compositions from System I and III were chosen for DSSC fabrication. Despite good ionic conductivity in System II, the increasing plasticization in NaI-15 weakens the film mechanical integrity. The surface in-homogeneity at high temperature also proves that none of the EC: PC-PSSE fits the solid-state DSSC assembling condition at 50 °C.

CHAPTER 8: RESULTS AND DISCUSSION

Electrochemical analysis of solid-state DSSC

This chapter covers the preliminary test of solid-state DSSC that was fabricated using optimized-PSSEs from NaI and SiO₂ systems. Generally, the cells exhibit good performance owing to PSSE characteristic, which stores high number of I⁻/I₃⁻ redox couple and permits fast ion mobility. According to literatures, the recorded D_{ion} values ($\sim 10^{-2}$ - 10^{-5} cm²s⁻¹) are higher than that of the I⁻/I₃⁻ redox couple diffusion reported in GPE and ionic liquid assemblies ($\sim 10^{-7}$ cm²s⁻¹) (Yusof and Yahya, 2016; Buraidah *et al.*, 2017). In addition to this, the rubbery state of PSSEs during cell assembly at 50 °C grants a good interfacial contact between the electrode and electrolyte.

8.1 NaI-PSSE system

Figure 8.1 shows the current-voltage (J - V) characteristic of solid-state DSSC that was fabricated using NaI-15 at direct sunlight irradiation of 100 mW cm⁻². The J - V curve shows a short circuit current density (J_{sc}) of 12.3 mA cm⁻² and an open-circuit voltage (V_{oc}) of 0.48 V. The fill factor (FF) and overall energy conversion efficiency (η) of this cell is 0.55 and 3.22 %, respectively. These values were calculated using Equation (8.1) and Equation (8.2), respectively.

$$FF = \frac{J_{MP} V_{MP}}{J_{SC} V_{OC}} \quad (8.1)$$

where J_{MP} and V_{MP} represents current and voltage at maximum power point, respectively.

$$\eta = FF \times J_{SC} \times V_{OC} \quad (8.2)$$

The photovoltaic parameters of other two assemblies fabricated with NaI-10 and NaI-20 are summarized in Table 8.1.

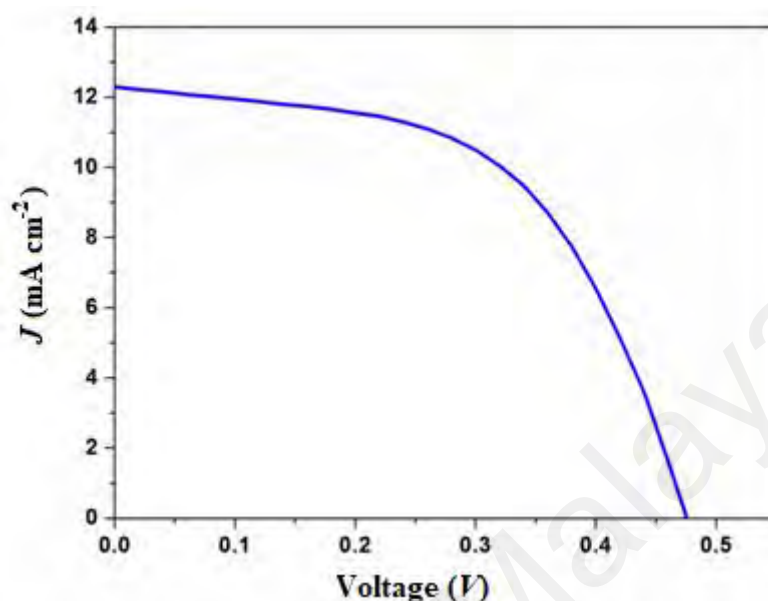


Figure 8.1: J - V curve of solid-state DSSC fabricated with NaI-15

Table 8.1: Photovoltaic parameters of solid-state DSSCs assembled with NaI-PSSes

NaI content (%)	J_{sc} (mA cm ⁻²)	V_{oc} (V)	FF	η (%)
10	9.27	0.50	0.56	2.60
15	12.3	0.48	0.55	3.22
20	13.0	0.46	0.52	3.13

The recorded cell performance for all the three assemblies are among the highest reported in the literature for cell assembled with UHMW polymer electrolytes. This is owing to the high generated cells J_{sc} . The recorded J_{sc} is comparable to those assemblies reported for GPE and oligomer-SPE with similar conductivity order. The cells J_{sc} increases with increasing NaI doping from 10 to 20 wt.% NaI. This increment can be correlated to the increasing ionic conductivity as the consequence of increasing I^-/I_3^- redox couple diffusion rate (D_{ion} increases at room temperature) (de Freitas *et al.*, 2009). This subsequently benefits the dye-regeneration process and allows high numbers of electrons to be transported to the TiO₂ surface in order to complete the

circuit. As the result, the conversion efficiency increases to the highest for cell assembled with NaI-15. Whereas for the cell fabricated with NaI-20, a slight reduction in cell efficiency was recorded. The drop could be caused by a massive ion-ion interaction that reduces the number of I^-/I_3^- redox couple to the lowest. This impedes an efficient solar conversion and results in the lowest FF value. All the recorded FF values fall in the typical range of 0.5 to 0.82 (National Instruments, 2012). Since V_{oc} is affected by the number of I^-/I_3^- redox couple, the reduction of I^-/I_3^- redox couple as subsequent to ion-ion interaction with increasing NaI content causes V_{oc} to reduce (Komiya *et al.*, 2004).

8.2 SiO₂-PSSE system

Figure 8.2 shows the J - V characteristic plot of solid-state DSSC fabricated using SiO₂-2 at direct sunlight irradiation of 100 mW cm⁻². Photovoltaic parameters for cell fabricated using SiO₂-2 and SiO₂-4 are summarized in Table 8.2. Based on these results, a significant enhancement by almost 72 % and 107 % was recorded when 4 and 2 wt.% SiO₂ NPs were incorporated into NaI-15, respectively. This is caused by the increase in the number of I^-/I_3^- redox couple as compared to those in NaI-15 (de Freitas *et al.*, 2009). The increase in the number of I^-/I_3^- redox couple allows the cells to generate high J_{sc} and V_{oc} . Besides this factor, the performance may be enhanced by the increase of I^-/I_3^- redox couple mobility according to Li and co-workers (2007) (Li *et al.* 2007). I^-/I_3^- redox couple may have good diffusion due to the increase of amorphous concentration and existence of new percolation pathway that favours faster ion tunnelling.

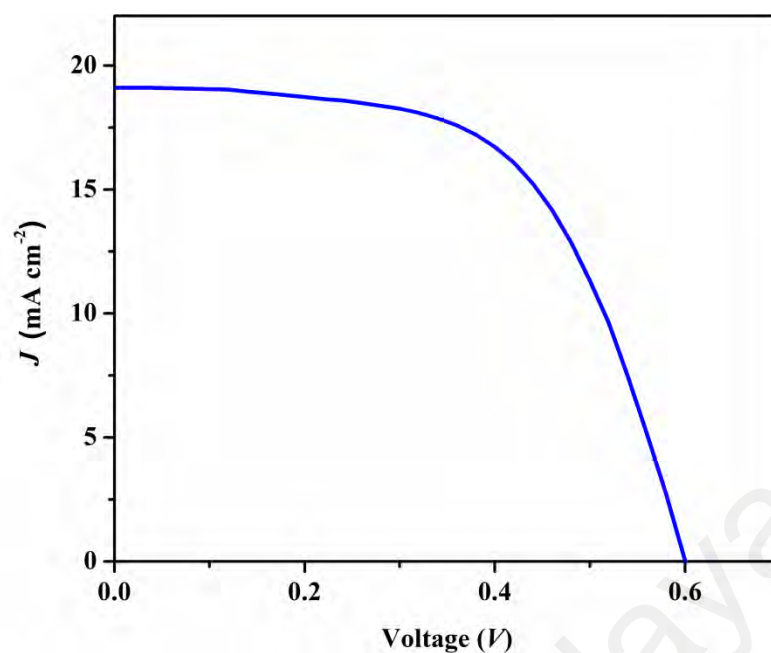


Figure 8.2: J - V curve of solid-state DSSC fabricated with SiO_2 -2

Table 8.2: Photovoltaic parameters of solid-state DSSCs assembled with SiO_2 -PSSEs

SiO_2 NPs content (%)	J_{sc} (mA cm^{-2})	V_{oc} (V)	FF	η (%)
0	12.3	0.48	0.55	3.22
2	19.0	0.6	0.59	6.68
4	17.37	0.56	0.57	5.54

Nevertheless, a slight reduction in the cell efficiency was reported for the cell fabricated with SiO_2 -4 as compared to that of SiO_2 -2 assembly, which is attributed to the formation of ion-ion interaction. As mentioned in sub-section 8.1, this can cause reduction in the number of I^-/I_3^- redox couple and its mobility. As the consequence, the dye regeneration process is hampered. The reduction in the number of I^-/I_3^- redox couple causes FF to drop. In general, the quality (referred to FF) of the NaI-15 cell improves with SiO_2 NPs addition. The recorded cell efficiency is comparable to the cells developed using GPE but it is the highest among the quasi-solid systems (e.g. oligomer- or ionic liquid-SPE polymer electrolytes).

8.3 Cell stability

Figure 8.3 depicts the stability results for the most efficient solid-state DSSC (*e.g.* cells fabricated with NaI-15 and SiO₂-2). In overall, both fabrications possess good cell stability at 60 °C. For the cell assembled using NaI-15, a depletion of 8 % from its initial photo-conversion efficiency was recorded after 250 h. The low depletion may be caused by:

- i) low chances of iodine decomposition due to the absence of liquid volatilization,
- ii) minor loss in the I^-/I_3^- redox couple mobility due to polymer chain that remains almost unchanged attributed to the huge polymer molecular weight,
- iii) good electrolyte wetting with the sensitized-dye molecules and
- iv) low charge recombination.

The stability of NaI-15 cell further improves to 3 % of depletion when SiO₂ NPs were incorporated (*e.g.* SiO₂-2 cell). The higher stability was attained plausibly due to the lowering of charge recombination when more I^-/I_3^- redox couple with good diffusion were present.

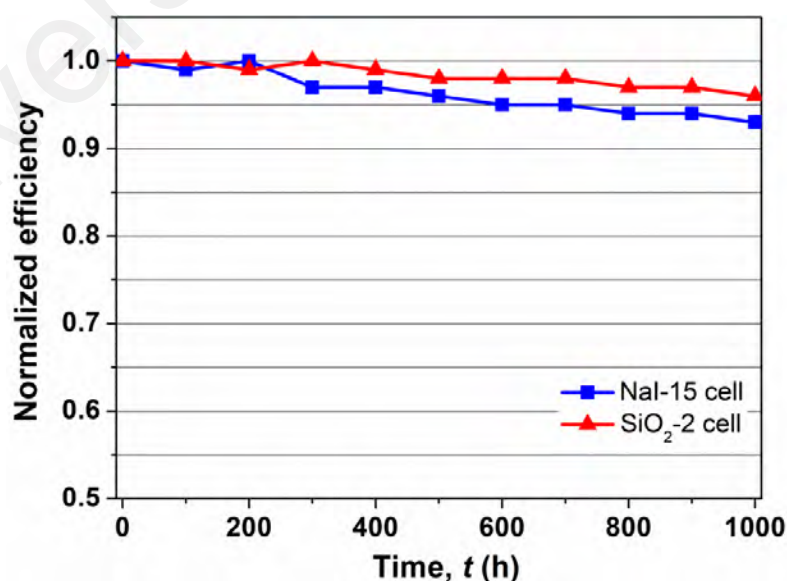


Figure 8.3: Normalized light-to-electricity conversion efficiency of the cell versus conservation time under 60 °C

CHAPTER 9: CONCLUSIONS, CHALLENGES AND FUTURE RECOMMENDATIONS

9.1 Conclusions

This work reports the practical usage of UHMW P(MMA-*co*-BA-*co*-AA) as the host polymer for electrolyte. The main challenge in handling UHMW polymer is the processability due to low chain dynamics. This limitation was overcome in this work by synthesizing a low T_g UHMW copolymer upon polymerizing with PBA. For commercial benefit, the copolymer was synthesized *via* emulsion polymerization at atmospheric environment (non-purging system). Among the tested UHMW P(MMA-*co*-BA-*co*-AA) formulations, AA05 has the highest commercial value due to high conversion efficiency, colloidal stability and bulk properties.

By utilizing AA05, three PSSE systems were developed. Each system was optimized according to the contents of NaI (System I), EC: PC (System II) and SiO₂ NPs (System III). The NaI-15 from System I was used as a control for another two systems. This particular sample was chosen since its matrix contains the highest amorphous concentration that allows high diffusion of I^-/I_3^- redox couple and good electrolyte ionic conductivity. As the consequence, NaI-15 yields a considerably good cell performance with high stability. Results are summarized as follow: $J_{sc} = 12.3 \text{ mA cm}^{-2}$, $V_{oc} = 0.48 \text{ V}$, $FF = 0.55$ and $\eta = 3.22 \%$ under 100 mW cm^{-2} illumination. Higher cell efficiency cannot be obtained when more EC: PC is doped into NaI-15. At higher liquid plasticization, the formation of crosslink and/or ion-ion bonding reduces the ion diffusivity and ion population. This characteristic of PSSE obstructs the dye-regeneration process.

Opposite observation was seen with addition of solid plasticizer such as SiO₂ NPs. Generally, all the afore-mentioned properties of NaI-15 including ion population

increase. Among the tested SiO₂ NPs compositions, matrix SiO₂-2 shows good DSSC performance. The cell characteristics are as follow: $J_{sc} = 19.0 \text{ mA cm}^{-2}$, $V_{oc} = 0.6 \text{ V}$, $FF = 0.59$ and $\eta = 6.68 \%$ and under 100 mW cm^{-2} illumination. Although SiO₂-4 yields better ionic conductivity as compared to that of SiO₂-2, the ion-ion interaction in SiO₂-4 obstructs the dye-regeneration process.

To our best knowledge, the reported cell efficiencies are the highest among the PSSE systems ever reported for UHMW polymer. Moreover, the values are comparable to those cells of GPE and poly(ionic liquid)-based PSSE. The good cell performance may also be due to the rubbery (soft-sticky) characteristic of PSSE that gives combination features of good electrode-electrolyte wetting and negligible chain repacking (high free volume is available) when cooled down to 25 °C (cell working temperature). Generally, these features were not observed in PSSE prepared from conventional polymers ($M_w \leq 10^5 \text{ g mol}^{-1}$). With all the benefits discussed above, it can be generously accepted that this material can be taken as another alternative base polymer for electrolyte development. Apart from PSSE development, the good optical transparency of AA05 may extend its utilization in coating application.

9.2 Challenges

There are several aspects in this research that requires serious consideration in order to meet the targeted proposal and reproducibility. One of those is polymerization temperature. The polymerization shall be carried out above the thermal decomposition of the initiator. This temperature shall not be too high as it may lead to chain transfer reaction and inhibits the UHMW polymer formation. Moreover, a low amount of initiator (or low concentration) is preferred in UHMW polymer synthesis to limit the number of particle nucleation (or nucleation sites).

The assembling temperature of solid-state DSSC is another important aspect to consider. The challenge to this procedure is the requirement of T_g of PSSE that has to be in close approximation to the typically used cell assembling temperature (50 °C). For this reason, the T_g of copolymer shall be lower than 50 °C. Therefore, the Gordon-Taylor equation was used to calculate the theoretical T_g of final copolymer. Using the individual T_g of the co-monomer and the final desired T_g , the monomer composition can be fine-tuned during the synthesis.

9.3 Future recommendation

The PSSE systems that had been developed using UHMW copolymer showed a good performance in solid-state DSSC fabrication. Nevertheless, further improvisation is required in order to boost the commercial benefit of the solid-state DSSC. The following recommendations are suggested for future study.

1. Suppression of charge recombination effect at the interface of electrode and electrolyte. Traditionally, this issue was solved by incorporating either 4-*tert*-butylpyridine (TBP) or *N*-methylbenzimidazole (NMBI) into the electrolytes formulation. The incorporation of these chemicals had been reported to increase the device open-circuit potential (V_{oc}) (Stergiopoulos *et al.*, 2011).
2. Smearing of 400 nm TiO₂ particles onto the conducting glass. This layer allows more light to be diffused into the DSSC and thus increases the cell performance.
3. Optimization of cell assembly by using “screen printing technique” to smear the TiO₂ particles instead of “Dr. Blade”. This optimization also plays a crucial role to obtain high device efficiency. The adoption of this method may give good control of the thickness of electrode, and subsequently good reproducible.
4. The study on the surface profile of the electrode in terms of its roughness and effective surface area is also crucial. Generally, this study can be performed using

microscopy technique for the reason of optimization of the mesoporous titania structure to have better dye sensitization.

Some other least pronounced methods like making use of anti-reflective coating and low sheet resistance substrates may also benefit the solid-state DSSC performance. Effect of cells in the dark also needs to be studied in order to further address the limiting factors. The afore-mentioned points may or may not yield better device efficiency, but to authors' knowledge, these points shall be considered for better understanding of the final device assembly.

University of Malaya

REFERENCES

- Ahn, S. H., Koh, J. H., Seo, J. A., & Kim, J. H. (2010). Structure control of organized mesoporous TiO₂ films template by graft copolymers for dye-sensitized solar cells. *Chemical Communications*, 46(11), 1935-1937.
- Akgöl, Y., Hofmann, C., Karatas, Y., Cramer, C., Wiemhöfer, H.-D., & Schönhoff, M. (2007). Conductivity spectra of polyphosphazene-based polyelectrolyte multilayers. *The Journal of Physical Chemistry B*, 111(29), 8532-8539.
- Alebbi, M., Bignozzi, C. A., Heimer, T. A., Hasselmann, G. M., & Meyer, G. J. (1998). The limiting role of iodide oxidation in *cis*-Os(dcb)₂(CN)₂/TiO₂ photoelectrochemical cells. *The Journal of Physical Chemistry B*, 102(39), 7577-7581.
- Andrady, A. L., Torikai, A., & Kobatake, T. (1996). Spectral sensitivity of chitosan photodegradation. *Journal of Applied Polymer Science*, 62(9), 1465-1471.
- Aram, E., Ehsani, M., & Khonakdar, H. A. (2015). Improvement of ionic conductivity and performance of quasi-solid-state dye sensitized solar cell using PEO/PMMA gel electrolyte. *Thermochimica Acta*, 615, 61-67.
- Arnold, D. (2012). *Synthesis and ¹H-NMR characterization of amphiphilic acrylate block copolymers to investigate the effect of chain rigidity on micelle formation in solution* (Master's Theses and Doctoral Dissertations, Paper 403). Retrieved from <http://commons.emich.edu/> on 12th February 2018.
- Arof, A. K., Aziz, M. F., Noor, M. M., Careem, M. A., Bandara, L. R. A. K., Thotawatthage, C. A., Rupasinghe, W. N. S., & Dissanayake, M. A. K. L. (2013). Efficiency enhancement by mixed cation effect in dye-sensitized solar cells with a PVdF based gel polymer electrolyte. *International Journal of Hydrogen Energy*, 39(6), 2929-2935.
- Azevedo, E. C., Nascimento, E. M., Chierice, G. O., Neto, S. C., & Lepienski, C. M. (2013). UV and gamma irradiation effects on surface properties of polyurethane derivate from castor oil. *Polimeros*, 23(3), 305-311.
- Barenswaard, W., Litvinov, V. M., Socren, F., Scherreenberg, R. L., Gondard, C., & Colemonts, C. (1999). Crystallinity and microstructure of plasticized poly(vinyl chloride). A ¹³C and ¹H solid state NMR study. *Macromolecules*, 32(1), 167-180.

- Bauer, C., Boschloo, G., Mukhtar, E., & Hagfeldt, A. (2002). Interfacial electron-transfer dynamics in Ru(tcterpy)(NCS)₃-sensitized TiO₂ nanocrystalline solar cells. *The Journal of Physical Chemistry B*, 106(49), 12693-12704.
- Bedja, I., & Hagfeldt, A. (2011). Comparative study between dye-sensitized and CdS quantum-dots-sensitized TiO₂ solar cells using photoinduced absorption spectroscopy. *Advances in OptoElectronics*, 2011, Article ID 424071.
- Bella, F., Sacco, A., Salvador, G. P., Bianco, S., Tresso, E., Pirri, C. F., & Bongiovanni, R. (2013). First pseudohalogen polymer electrolyte for dye-sensitized solar cells promising for *in situ* photopolymerization. *The Journal of Physical Chemistry C*, 117(40), 20421-20430.
- Best, A. S., Adebahr, J., Jacobsson, P., MacFarlane, D. R., & Forsyth, M. (2001). Microscopic interactions in nanocomposite electrolytes. *Macromolecules*, 34(13), 4549-4555.
- Blackley, D. C. (1997). *Polymer lattices: Science and technology – Second edition, Volume 2: Types of lattices*. London, UK: Chapman & Hall.
- Blakers, A., Zin, N., McIntosh, K. R., & Fong, K. (2013). High efficiency silicon solar cells. *Energy Procedia*, 33, 1-10.
- Boonsin, R., Sudchanham, J., Panusophon, N., Sae-Heng, P., Sae-Kung, C., & Pakawatpanurut, P. (2012). Dye-sensitized solar cell with poly(acrylic acid-co-acrylonitrile)-based gel polymer electrolyte. *Materials Chemistry and Physics*, 132(2-3), 993-998.
- Boschloo, G., & Hagfeldt, A. (2009). Characteristic of the iodide/triiodide redox mediator in dye-sensitized solar cell. *Accounts of Chemical Research*, 42(11), 1819-1825.
- Buraidah, M. H., Shahan Shah, Teo, L. P., Chowdhury, F. I., Careem, M. A., Albinsson, I., Mellander, B.-E., & Arof, A. K. (2017). High efficient dye sensitized solar cells using phthaloylchitosan based gel polymer electrolytes. *Electrochimica Acta*, 245(0), 846-853.
- Calcagno, L., Compagnini, G., & Foti, G. (1992). Structural modification of polymer films by ion irradiation. *Nuclear Instruments Methods in Physics Research Section B: Beam interactions with materials and atoms*, 65(1-4), 413-422.

- Cantwell, P. R., Tang, M., Dillon, S. J., Luo, J., Rohrer, G. S., & Harmer, M. P. (2014). Grain boundary complexion. *Acta Materialia*, 62, 1-48.
- Cesiulis, H., Tsyntsar, N., Ramanavicius, A., & Ragoisha, G. (2016). The study of thin films by electrochemical impedance spectroscopy. In I. Tiginyanu, P. Topala, & V. Ursaki (Eds.), *Nanostructures and thin films for multifunctional applications* (pp. 3-42). Switzerland: Springer International Publishing
- Chae, H., Song, D., Lee, Y.-G., Son, T., Cho, W., Pyun, Y. B., Kim, T.-Y., Lee, J. H., Fabregat-Santiago, F., & Kang, Y. S. (2014). Chemical effects of tin oxide nanoparticles in polymer electrolytes-based dye-sensitized solar cells. *The Journal of Physical Chemistry C*, 118(30), 16510-16517.
- Chen, S., Wu, G., Liu, Y., & Long, D. (2006). Preparation of poly(acrylic acid) grafted multiwalled carbon nanotubes by a two-step irradiation technique. *Macromolecules*, 39(1), 330-334.
- Clifford, J. N., Palomares, E., Nazeeruddin, Md. K., Grätzel, M., & Durrant, J. R. (2007). Dye dependent regeneration dynamics in dye sensitized nanocrystalline solar cells: Evidence for the formation of a ruthenium bipyridyl cation/iodide intermediate. *The Journal of Physical Chemistry C*, 111(17), 6561-6567.
- de Freitas, J. N., Nogueira, A. F., & de Paoli, M.-A. (2009). New insights into dye-sensitized solar cells with polymer electrolytes. *Journal of Materials Chemistry*, 19(0), 5279-5294.
- Dissanayake, M. A. K. L., Thotawatthage, C. A., Senadeera, G. K. R., Bandara, T. M. W. J., Jayasundera, W. J. M. J. S. R., & Mellander, B.-E. (2012). Efficiency enhancement by mixed cation effect in dye sensitized solar cells with PAN based gel polymer electrolyte. *Journal of Photochemistry and Photobiology A: Chemistry*, 246, 29-35.
- Domb, A. J., Kost, J., & Wiseman, S. (1998). *Handbook of Biodegradable Polymers*. A. J. Domb, J. Kost, D. M. Wiseman (Eds.). The Netherlands, NL: Harwood Academic Publishers.
- Dzulkurnain, N. A., Ahmad, A., & Mohamed, N. S. (2015). P(MMA-EMA) random copolymer electrolytes incorporating sodium iodide for potential application in a dye-sensitized solar cell. *Polymers*, 7(2), 266-280.
- El Bachiri, A., Bennani, F., & Bousselamti, M. (2016). Dielectric and electrical properties of LiNbO₃ ceramics. *Journal of Asian Ceramic Societies*, 4(1), 46-54.

- Ennis, C. P., & Kaiser, R. I. (2010). Mechanical studies on the electron induced degradation of polymethyl methacrylate and Kapton. *Physical Chemistry Chemical Physics*, 12(45), 14902-14915.
- Entwistle, C. A., & Rowe, R. C. (1979). Plasticization of cellulose ethers used in the film coating of tablets. *Journal of Pharmacy and Pharmacology*, 31(5), 269-272.
- Fantechi, S. (2011). *Photovoltaics and nanotechnology: From innovation to industry*. Brussels, BE: European Commission.
- Farrell, S. L. (2014). *Fabrication and characterization of poly(4-vinylpyridine)-based all solid state dye-sensitized solar cells by initiated chemical vapor deposition*. (Master of Science).
- Fenton, D. E., Parker, J. M., & Wright, P. V. (1973). Complexes of alkali metal ions with poly(ethylene oxide). *Polymer*, 14(11), 589.
- Fernández-García, M., de la Fuente, J. L., Fernández-Sanz, M., & Madruga, E. L. (2001). Glass transition temperatures of poly[(methyl methacrylate)-*co*-(butyl acrylate)]s synthesized by atom-transfer radical polymerization. *Macromolecular Rapid Communications*, 22(13), 1046-1052.
- Flores, I. C., de Freitas, J. N., Longo, C., De Paoli, M.-A., Winnischofer, H., & Nogueira, A. F. (2007). Dye-sensitized solar cells based on TiO₂ nanotubes and a solid-state electrolyte. *Journal of Photochemistry and Photobiology A: Chemistry*, 189(2-3), 153-160.
- Fu, Y., Pathmanathan, K., & Stevens, J. R. (1991). Dielectric and conductivity relaxation in poly(propylene glycol)–lithium triflate complexes. *Journal of Chemical Physics*, 94(9), 6323-6329.
- Funke, K. (1991). Solid electrolytes: Jump relaxation and “universal” dynamic response. *Radiation Effects and Defects in Solids: Incorporating Plasma Science and Plasma Technology*, 119-121(2), 463-468.
- Funke, K. (1993). Jump relaxation in solid electrolytes. *Progress in Solid State Chemistry*, 22(2), 111-195.
- Funke, K. (2011). *Progress in Physical Chemistry Volume 4: Ionic motion in materials with disordered structures – from elementary steps to macroscopic transport*, (pp. 526). Muchen, DE: Oldenbourg Wissenschaftsverlag GmbH.

- Furukawa, T., Mukasa, Y., Suzuki, T., & Kano, K. (2002) Microphase separation and ion-conduction mechanisms in polypropylene oxide/lithium perchlorate (LiClO₄) complexes. *Journal of Polymer Science: Part B: Polymer Physics*, 40(7), 613-622.
- Gigmes, D. (2015). Nitroxide mediated polymerization: From fundamentals to applications in materials science. *RSC Polymer Chemistry Series*, 0(19), 512.
- Goldemberg, J., & other members of Editorial Board (2000). *World Energy Assessment: Energy and the challenge of sustainability*. New York, NY: United Nations Development Programme. Retrieved from <http://www.undp.org/> on 5th March 2018.
- Grätzel, M. (2006). The advent of mesoscopic injection solar cells. *Progress in Photovoltaics*, 14(5), 429-442.
- Gray, F. M., & Connor, J. A. (1997). *Polymer Electrolytes (RSC Materials Monographs)*. Cambridge, UK: Royal Society of Chemistry.
- Griep, M. H., Martin, J., Cramer, H., Goodall, M., & Karna, S. P. (2012). *Damage tolerant bio-sensitized solar cells*. Presented in 12th IEEE International Conference on Nanotechnology (IEEE-NANO), 20-23 August 2012, Birmingham, United Kingdom.
- Grunlan, M. A., Xing, L.-L., & Glass, J. E. (1997). Waterborne coatings with an emphasis on synthetic aspects: An overview. In J. E. Glass (Ed), *Technology for Waterborne Coatings* (pp. 1-26), *ACS Symposium Series 663*.
- Gundogdu, S. Ö. (2012). *The characterization of some methacrylate and acrylate homopolymers, copolymers and fibers via direct pyrolysis mass spectroscopy*. (Doctoral dissertation). Retrieved from <http://etd.lib.metu.edu.tr/> on 5th February 2018.
- Hanemann, T., & Szabó, D. V. (2010). Polymer-nanoparticle composites: From synthesis to modern applications. *Materials*, 3(6), 3468-3517.
- Harrisson, S., Liu, X., Ollagnier, J.-N., Coutelier, O., Marty, J.-D., & Destarac, M. (2014). RAFT polymerization of vinyl esters: Synthesis and applications. *Polymers*, 6(5), 1437-1488.

- Hatada, L., Kitayama, T., Terawaki, Y., Sato, H., Hor, F., & members of research group on NMR, SPSJ (2003). NMR measurement of identical polymer samples by round robin method V. Determination of degree of polymerization for isotactic poly(methyl methacrylate) having a *t*-butyl end group. *Polymer Journal*, 35(4), 393-398.
- Haque, S. A., Palomares, E., Upadhyaya, H. M., Otley, L., Potter, R. J., Holmes, A. B., & Durrant, J. R. (2003). Flexible dye sensitised nanocrystalline semiconductor solar cells. *Chemical Communications*, 0(24), 3008-3009.
- Hsu, H.-L., Tien, C.-F., & Leu, J. (2014). Effect of pore size/distribution in TiO₂ films on agarose gel electrolyte-based dye-sensitized solar cells. *Journal of Solid State Electrochemistry*, 18(6), 1665-1671.
- Hu, M., Sun, J., Rong, Y., Yang, Y., Liu, L., Li, X., Forsyth, M., MacFarlane, D. R., & Han, H. (2014). Enhancement of monobasal solid-state dye-sensitized solar cells with polymer electrolyte assembling imidazolium iodide-functionalized silica nanoparticles. *Journal of Power Sources*, 248, 283-288.
- Ismayil, Ravindrachary, V., Bhajantri, R. F., Praveena, S. D., Poojary, B., Dutta, D., & Pujari, P. K. (2010). Optical and microstructural studies on electron irradiated PMMA: A positron annihilation study. *Polymer Degradation and Stability*, 95(6), 1083-1091.
- Jeon, L. S., Kim, S.-Y., Kim, S. J., Lee, Y.-G., Kang, M.-S., & Kang, Y. S. (2010). Supramolecular electrolytes with multiple hydrogen bonds for solid state dye-sensitized solar cells. *Journal of Photochemistry and Photobiology A: Chemistry*, 212(2-3), 88-93.
- Kang, M.-S., Ahn, K.-S., & Lee, J.-W. (2008). Quasi-solid-state dye-sensitized solar cells employing ternary component polymer-gel electrolytes. *Journal of Power Sources*, 180(2), 896-901.
- Kang, M.-S., Kim, J. H., Kim, Y. J., Won, J., Park, N.-G., & Kang, Y. S. (2005). Dye-sensitized solar cells based on composite solid polymer electrolytes. *Chemical Communications*, 0(7), 889-891.
- Kang, M.-S., Kim, J. H., Won, J., & Kang, Y. S. (2007). Oligomer approaches for solid-state dye-sensitized solar cells employing polymer electrolytes. *The Journal of Physical Chemistry C*, 111(13), 5222-5228.

- Kang, Y. I., & Moon, J. H. (2015). In situ poly(methyl methacrylate)/graphene composite gel electrolytes for highly stable dye-sensitized solar cells. *ChemSusChem*, 8(22), 3799-3804.
- Katsaros, G., Stergiopoulos, T., Arabatzis, I. M., Papadokostaki, K. G., & Falaras, P. (2002). A solvent-free composite polymer/inorganic oxide electrolyte for high efficiency solid-state dye-sensitized solar cells. *Journal of Photochemistry and Photobiology A: Chemistry*, 149(1-3), 191-198.
- Kelkar, S., Pandey, K., Agarkar, S., Saikhedkar, N., Tathavadekar, M., Agarwal, I., Gundloori, R. V. N., & Ogale, S. B. (2014). Functionally engineered egg-albumen gel for quasi-solid dye sensitized solar cells. *ACS Sustainable Chemistry & Engineering*, 2(12), 2707-2714.
- Kim, J. H., Kang, M.-S., Kim, Y. J., Won, J., & Kang, Y. S. (2005). Poly(butyl acrylate)/NaI/I₂ electrolytes for dye-sensitized nanocrystalline TiO₂ solar cells. *Solid State Ionics*, 176(5-6), 579-584.
- Kim, Y. J., Kim, J. H., Kang, M.-S., Lee, M. J., Won, J., Lee, J. C., & Kang, Y. S. (2004). Supramolecular electrolytes for use in highly efficient dye-sensitized solar cells. *Advanced Materials*, 16(19), 1753-1757.
- Kim, Y. J., Lee, M. H., Kim, H. J., Lim, G., Choi, Y. S., Park, N.-G., Kim, K., & Lee, W. I. (2009). Formation of highly efficient dye-sensitized solar cells by hierarchical pore generation with nanoporous TiO₂ spheres. *Advanced Materials*, 21(36), 3668-3673.
- Kitayama, T., & Hatada, K. (2004). *NMR spectroscopy of polymers*. Berlin, DE: Springer-Verlag Berlin Heidelberg
- Kitayama, Y., & Okubo, M. (2016). A synthetic route to ultra-high molecular weight polystyrene (>10⁶) with narrow molecular weight distribution by emulsifier-free, emulsion organotellurium-mediated living radical polymerization (emulsion TERP). *Polymer Chemistry*, 7(14), 2573-2580.
- Knauth, P., & Schoonman, J. (2007). *Nanocomposites: Ionic conducting materials and structural spectroscopies*. New York, NY: Springer Science.
- Komiya, R., Han, L., Yamanaka, R., Islam, A., & Mitate, T. (2004). Highly efficient quasi-solid state dye-sensitized solar cell with ionic conducting polymer electrolyte. *Journal of Photochemistry and Photobiology A: Chemistry*, 164(0), 123-127.

- Kozanoğlu, S., Özdemir, T., & Usanmaz, A. (2011). Polymerization of *N*-vinylcaprolactam and characterization of poly(*N*-vinylcaprolactam). *Journal of Macromolecular Science, Part A: Pure and Applied Chemistry*, 48(6), 467-477.
- Kumar, M., Tiwari, T., Chauhan, J. K., & Srivastava, N. (2014). Understanding the ion dynamics and relaxation behavior from impedance spectroscopy of NaI doped Zwitterionic polymer system. *Materials Research Express*, 1, 045003.
- Kumar, V., Sonkawade, R. G., Ali, Y., & Dhaliwal, A. S. (2011). Study of chemical, optical and structural properties of 120 MeV Ni¹¹⁺ ions beam irradiated poly(ethylene terephthalate) film. *International Journal of Applied Engineering Research*, 2(2), 419-430.
- Kushwaha, O. S., Avadhani, C. V., & Singh, R. P. (2014). Effect of UV rays on degradation and stability of high performance polymer membranes. *Advanced Materials Letters*, 5(5), 272-279.
- Kwon, S. S., Nam, Y. S., Lee, J. S., Ku, B. S., Han, S. H., Lee, J. Y., & Chang, I. S. (2002). Preparation and characterization of coenzyme Q10-loaded PMMA nanoparticles by a new emulsification process based on microfluidization. *Colloids and Surfaces A: Physicochemical and Engineering Aspects*, 210, 95-104.
- Law, M., Greene, L. E., Johnson, J. C., Saykally, R., & Yang, P. (2005). Nanowire dye-sensitized solar cells. *Nature Materials*, 4, 455-459.
- Lee, C.-P., Li, C.-T., & Ho, K.-C. (2017). Use of organic materials in dye-sensitized solar cells. *Materials Today*, 20(5), 267-283.
- Leskovac, M., Kovacevic, V., Fles, D., & Hace, D. (1999). Thermal stability of poly(methyl methacrylate-*co*-butyl acrylate) and poly(styrene-*co*-butyl acrylate) polymers. *Polymer Engineering & Science*, 39(3), 600-608.
- Li, P. J., Wu, J. H., Huang, M. L., Hao, S. C., Lan, Z., Li, Q., & Kang, S. (2007). The application of P(MMA-*co*-MAA)/PEG polyblend gel electrolyte in quasi-solid state dye-sensitized solar cell at higher temperature. *Electrochimica Acta*, 53(2), 903-908.
- Li, Q., Wu, J., Tang, Z., Xiao, Y., Huang, M., & Lin, J. (2010). Application of poly(acrylic acid-*g*-gelatin)/polypyrrole gel electrolyte in flexible quasi-solid-state dye-sensitized solar cell. *Electrochimica Acta*, 55(8), 2777-2781.

- Lim, S. J., Kang, Y. S., & Kim, D.-W. (2010). Photovoltaic performance of dye-sensitized solar cells assembled by in-situ chemical cross-linking. *Electrochemical Communications*, 12(8), 1037-1040.
- Lim, Y.-J., An, Y.-H., & Jo, N.J. (2012). Polystyrene-Al₂O₃ composite solid polymer electrolyte for lithium secondary battery. *Nanoscale Research Letters*, 7(1), 19.
- Litvinov, V. M., & De, P. P. (2002). *Spectroscopy of rubbers and rubbery materials*. Exeter, UK: iSmithers Rapra Publishing.
- Liu, H., Bian, J., Wang, Z., & Hou, C.-J. (2017). Synthesis and characterization of waterborne fluoropolymers prepared by the one-step semi-continuous emulsion polymerization of chlorotrifluoroethylene, vinyl acetate, butyl acrylate, Veova 10 and acrylic acid. *Molecules*, 22(1), 184.
- Liu, Q., Wu, J., Lan, Z., Zheng, M., Yue, G., Lin, J., & Huang, M. (2015). Preparation of PAA-g-PEG/PANI polymer gel electrolyte and its application in quasi solid state dye-sensitized solar cells. *Polymer Engineering & Science*, 55(2), 322-326.
- Luk, B. (2010). *Dye-sensitized solar cells* [Coursework for Physics 240]. Retrieved from <http://large.stanford.edu/> on 3th February 2018.
- Matsumoto, M., Miyazaki, H., Matsuhira, K., Kumashiro, Y., & Takaoka, Y. (1996). A dye sensitized TiO₂ photoelectrochemical cell constructed with polymer solid electrolyte. *Solid State Ionics*, 89(3-4), 263-267.
- Mello, N. C., Bonagamba, T. J., Panepucci, H., Dahmouche, K., Judeinstein, P., & Aegerter, M. A. (2000). NMR study of ion-conducting organic-inorganic nanocomposites poly(ethylene glycol)-Silica-LiClO₄. *Macromolecules*, 33(4), 1280-1288.
- Millard, D. (2017). *Key world energy statistics 2017*. Paris, FR: International Energy Agency. Retrieved from <http://www.iea.org/> on 15th March 2018.
- Mishra, R., & Rao, K. J. (1998). Electrical-conductivity studies of poly(ethylene oxide)-poly(vinyl alcohol) blends. *Solid State Ionics*, 106(1-2), 113-127.
- Moldoveanu, S. C. (2005). *Analytical pyrolysis of synthetic organic polymer*. Amsterdam: Elsevier B. V.

- Montanari, I., Nelson, J., & Durrant, J. R. (2002). Iodide electron transfer kinetics in dye-sensitized nanocrystalline TiO₂ films. *The Journal of Physical Chemistry B*, *106*(47), 12203-12210.
- Nagarajan, S., Sudhagar, P., Raman, V., Cho, W., Dhathathreyan, K. S., & Kang, Y. S. (2013). A PEDOT-reinforced exfoliated graphite composite as a pt- and tco-free flexible counter electrode for polymer electrolyte dye-sensitized solar cells. *Journal of Materials Chemistry A*, *1*(4), 1048-1054.
- National Instruments, 2012. Part II–Photovoltaic cell I-V characterization theory and labview analysis code. Retrieved from <http://www.ni.com/> on 15th March 2018.
- Nejati, S., & Lau, K. K. S. (2011). Pore filling of nanostructured electrodes in dye sensitized solar cells by initiated chemical vapor deposition. *Nano Letters*, *11*(2), 419-423.
- Nogueira, A. F., Durrant, J. R., & De Paoli, M. A. (2001). Dye-sensitized nanocrystalline solar cells employing a polymer electrolyte. *Advanced Materials*, *13*(11), 826-830.
- Nwanya, A. C., Ezema, F. I., & Ejikeme, P. M. (2011). Dyed sensitized solar cells: A technically and economically alternative concept to p-n junction photovoltaic devices. *International Journal of the Physical Sciences*, *6*(22), 5190-5201.
- O'regan, B., & Grätzel, M. (1991). A low-cost, high-efficiency solar cell based on dye-sensitized colloidal TiO₂ films. *Nature*, *353*, 737-740.
- Obeidi, S., Stolwijk, N. A., & Pas, S. J. (2005). Mass and charge transport in a cross-linked polyether-based electrolyte. The role of ion pairs. *Macromolecules*, *38*(26), 10750-10756.
- Pandey, K., Asthana, N., Dwivedi, M. M., & Chaturvedi, S. K. (2013). Effect of plasticizers on structural and dielectric behaviour of [PEO + (NH₄)₂C₄H₈(COO)₂] polymer electrolyte. *Journal of Polymers*, 2013, Article ID 752596.
- Park, D. H., Oh, J. K., Kim, S. B., & Kim, W. N. (2013). Synthesis and characterization of sulfonated polyol-based waterborne polyurethane-polyacrylate hybrid emulsions. *Macromolecular Research*, *21*(11), 1247-1253.

- Pelet, S., Moser, J.-E., & Grätzel, M. (2000). Cooperative effect of adsorbed cations and iodide on the interception of back electron transfer in the dye sensitization of nanocrystalline TiO₂. *The Journal of Physical Chemistry B*, 104(8), 1791-1795.
- Polte, J. (2015). Fundamental growth principles of colloidal metal nanoparticles – a new perspective. *CrystEngComm*, 17, 6809-6830.
- Prasad, S. G., De, A., & De, Yu. (2011). Structural and optical investigations of radiation damage in transparent PET polymer films. *International Journal of Spectroscopy*, 2011, Article 810936.
- Rahman, M. Y. A., Ahmad, A., Umar, A. A., Taslim, R., Su'ait, M. S., & Salleh, M. M. (2014). Polymer electrolyte for photoelectrochemical cell and dye-sensitized solar cell: A brief review. *Ionics*, 20(9), 1201-1205.
- Ramesh S., Shanti R., Ramesh K., Arof A.K., Ezra Morris, & Chee S.Y. (2013). A method of producing a polytetrafluoroethylene adhesive polymer membrane. WO2014137207, Malaysia.
- Ramesh, S., & Liew, C.-W. (2012). Exploration on nano-composite fumed silica-based composite polymer electrolytes with doping of ionic liquid. *Journal of Non-Crystalline Solids*, 358, 931-940.
- Ramimoghadam, D., Hussein, M. Z., & Taufiq-Yap, Y. H. (2012). The effect of sodium dodecyl sulfate (SDS) and cetyltrimethylammonium bromide (CTAB) on the properties of ZnO synthesized by hydrothermal method. *International Journal of Molecular Sciences*, 13(10), 13275-13293.
- Rani, N. S., Sannappa, J., Demappa, T., & Mahadevaiah (2014). Structural, thermal, and electrical studies of sodium iodide (NaI)-doped hydroxypropyl methylcellulose (HPMC) polymer electrolyte films. *Ionics*, 20(2), 201-207.
- Robinson, R. A., & Stokes, R. H. (2002). *Electrolyte solutions: Second Revised Edition*. Mineola, NY: Dover Publications.
- Rudhziah, S., Ahmad, A., Ahmad, I., & Mohamed, N. S. (2015). Biopolymer electrolytes based on blend of kappa-carrageenan and cellulose derivatives for potential application in dye sensitized solar cell. *Electrochimica Acta*, 175, 162-168.

- Sayyah, S. M., Khaliel, A. B., Abd El-Salam, H. M., & Younis, M. A. (2012). Infrared spectroscopic studies on some thermally degraded poly(methyl methacrylate) doped with *N,N,N',N'*-tetraoxaloyl para sulphanilamide. *Egyptian Journal of Chemistry*, 55(6), 603-623.
- Seidalilir, Z., Malekfar, R., Shiu, J.-W., Wu, H.-P., & Diao, E. W.-G. (2015). High-performance gel-type dye-sensitized solar cells using poly (methyl methacrylate-co-ethylacrylate)-based polymer gel electrolyte with superior enduring stability. *Journal of The Electrochemical Society*, 162(14), H922-H928.
- Shukla, N., Thakur, A. K., Shukla, A., & Marx, D. T. (2014). Ion conduction mechanism in solid polymer electrolyte: An applicability of almond-west formalism. *International Journal of Electrochemical Science*, 9, 7644-7659.
- Silva, M. M., Barros, S. C., Smith, M. J., & MacCallum, J. R. (2004). Characterization of solid polymer electrolytes based on poly (trimethylenecarbonate) and lithium tetrafluoroborate. *Electrochimica Acta*, 49, 1887-1891.
- Singh, M., Singh, V. K., Surana, K., Bhattacharya, B., Singh, P. K., & Rhee, H.-W. (2013). New polymer electrolyte for electrochemical application. *Journal of Industrial and Engineering Chemistry*, 19, 819-822.
- Singh, V. K., Bhattacharya, B., Shukla, S., & Singh, P. K. (2015). New solid-polymer-electrolyte material for dye-sensitized solar cells. *Materials and technology*, 49(1), 123-127.
- Sionkowska, A. (2006). Effects of solar radiation on collagen and chitosan films. *Journal of Photochemistry and Photobiology B: Biology*, 82(1), 9-15.
- Song, D., Cho, W., Lee, J. H., & Kang, Y. S. (2014). Toward higher energy conversion efficiency for solid polymer electrolyte dye-sensitized solar cells: Ionic conductivity and TiO₂ pore-filling. *The Journal of Physical Chemistry Letters*, 5(7), 1249-1258.
- Song, J. Y., Wang, Y. Y., & Wan, C. C. (1999). Review of gel-type polymer electrolytes for lithium-ion batteries. *Journal of Power Sources*, 77(2), 183-197.
- Song, M. Y., Ahn, Y. R., Jo, S. M., Kim, D. Y., & Ahn, J.-P. (2005). TiO₂ single-crystalline nanorod electrode for quasi-solid-state dye-sensitized solar cells. *Applied Physics Letters*, 87(11), 113113.

- Song, M. Y., Kim, D. K., Ihn, K. J., Jo, S. M., & Kim, D. Y. (2004). Electrospun TiO₂ electrodes for dye-sensitized solar cells. *Nanotechnology*, 15(12), 1861-1865.
- Srinivas, K. (1999). *Optical and electrical properties of polymeric materials containing tin based compounds*. Kuala Lumpur, MY: Universiti Malaya.
- Stathatos, E., Lianos, P., & Krontiras, C. (2001). Dye-sensitized photoelectrochemical cell using a nanocomposite SiO₂/poly(ethylene glycol) thin film as electrolyte support. Characterization by time-resolved luminescence and conductivity measurements. *The Journal of Physical Chemistry B*, 105(17), 3486-3492.
- Stephan A. M., & Nahm, K. S. (2006). Review on composite polymer electrolytes for lithium batteries. *Polymer*, 47(16), 5952-5964.
- Stergiopoulos, T., Arabatzis, I. M., Katsaros, G., & Falaras, P. (2002). Binary polyethylene oxide/titania solid-state redox electrolyte for highly efficient nanocrystalline TiO₂ photoelectrochemical cells. *Nano Letters*, 2(11), 1259-1261.
- Stergiopoulos, T., Rozi, E., Karagianni, C.-S., & Falaras, P. (2011). Influence of electrolyte co-additives on the performance of dye-sensitized solar cells. *Nanoscale Research Letters*, 6(1), 307.
- Stolwijk, N. A., & Obeidi, S. (2004). Radiotracer diffusion and ionic conduction in a PEO-NaI polymer electrolyte. *Physical Review Letters*, 93, 125901.
- Subban, R. H. Y., & Arof, A. K. (2003). Experimental investigations on PVC-LiCF₃SO₃-SiO₂ composite polymer electrolytes. *Journal of New Materials for Electrochemical Systems*, 6, 197-203.
- Sun, W., & Xu, H. (2016). Enhanced photovoltaic performances of novel all-ionic liquid integrated poly(acrylic acid/polyethylene glycol) gel electrolytes in quasi-solid-state dye-sensitized solar cells. *RSC Advances*, 6, 68193-68198.
- Suzuki, K., Yamaguchi, M., Hotta, S., Tanabe, N., & Yanagida, S. (2004). A new alkyl-imidazole polymer prepared as an ionic polymer electrolyte by in situ polymerization of dye sensitized solar cells. *Journal of Photochemistry and Photobiology A: Chemistry*, 164, 81-85.

- Tang, Z., Bessho, T., Awai, F., Kinoshita, T., Maitani, M. M., Jono, R., Murakami, T. N., Wang, H., Kubo, T., Uchida, S., & Segawa, H. (2017). Hysteresis-free perovskite solar cells made of potassium-doped organometal halide perovskite. *Scientific Reports*, 7, Article number: 12183.
- Tang, Z., Wu, J., Liu, Q., Zheng, M., Tang, Q., Lan, Z., & Lin, J. (2012). Preparation of poly(acrylic acid)/gelatin/polyaniline gel-electrolyte and its application in quasi-solid-state dye-sensitized solar cells. *Journal of Power Sources*, 203, 282-287.
- Tanio, N., & Nakanishi, T. (2006). Physical aging and refractive index of poly(methyl methacrylate) glass. *Polymer Journal*, 38(8), 814-818.
- Tiwari, P., Srivastava, A. K., Khatak, B. Q., Verma, S., Upadhyay, A., Sinha, A. K., Ganguli, T., Lodha, G. S., & Deb, S. K. (2014). Structural modification of poly methyl methacrylate due to electron irradiation. *Measurement*, 51, 1-8.
- Trukhan, E. M. (1963). Dispersion of the dielectric constant of heterogeneous systems. *Soviet Physics - Solid State*, 4, 2560.
- Vasquez, L. O. (2007). *Fuel cell research trends*. New York, NY: Nova Science Publishers.
- Visjager, F. J. (2001). *Ultra-high molecular weight polymers processing and properties of polyethylene and poly(tetrafluoroethylene)* [doctoral thesis]. Retrieved from <https://www.research-collection.ethz.ch/> on 5th February 2018.
- Vrentas, J. S., & Duda, J. L. (1977). Diffusion in polymer–solvent systems. I. Reexamination of the free-volume theory. *Journal of Polymer Science, Part B: Polymer Physics*, 15, 403-416.
- Wang, G. (2011). Synthesis of poly(*n*-butyl acrylate) homopolymers by activators generated by electron transfer (AGET) ATRP using FeCl₃·6H₂O/succinic acid catalyst. *Iranian Polymer Journal*, 20(11), 931-938.
- Wang, S.-M., Huang, Q.-Z., & Wang, Q.-S. (2005). Study on the synergetic degradation of chitosan with ultraviolet light and hydrogen peroxide. *Carbohydrate Research*, 340(2), 1143-1147.
- Wang, W., & Alexandridis, P. (2016). Composite polymer electrolytes: nanoparticles affect structure and properties. *Polymers*, 8, 387-422.

- Wang, Y., Agapov, A. L., Fan, F., Hong, K., Yu, X., Mays, J., & Sokolov, A. P. (2012). Decoupling of ionic transport from segmental relaxation in polymer electrolytes. *Physical Review Letters*, *108*, 088303.
- Wieczorek, W., Stevens, J. R., & Florjanczyk, Z. (1996). Composite polyether based solid electrolytes. The Lewis acid-base approach. *Solid State Ionics*, *85*(1-4), 67-72.
- Wochnowski, C., Shams Eldin, M. A., & Metev, S. (2005). UV-laser-assisted degradation of poly(methyl methacrylate). *Polymer Degradation and Stability*, *89*(2), 252-264.
- Wu, Y. (2015). *Lithium-ion batteries: Fundamentals and applications*. Boca Raton, FL: CRC Press.
- Yamak, H. B. (2013). *Emulsion polymerization: Effects of polymerization variables on the properties of vinyl acetate based emulsion polymers*. F. Yılmaz (Ed.). Available from: <https://www.intechopen.com/books/polymer-science/emulsion-polymerization-effects-of-polymerization-variables-on-the-properties-of-vinyl-acetate-based>
- Yuan, S., Tang, Q., He, B., & Yang, P. (2014). Efficient quasi-solid-state dye-sensitized solar cells employing polyaniline and polypyrrole incorporated microporous conducting gel electrolytes. *Journal of Power Sources*, *254*, 98-105.
- Yusof, S. M. M., & Yahya, W. Z. N. (2016). Binary ionic liquid electrolyte for dye-sensitized solar cell. *Procedia Engineering*, *148*, 100-105.
- Zhang, C., Xu, T., Bao, Z., & Chen, L. (2017). Synthesis and characterization of fluorinated polyacrylate latex emulsified with novel surfactants. *Designed Monomers and Polymers*, *20*(1), 118-124.
- Zhang, R., Chen, Y., & Montazami, R. (2015). Ionic liquid-doped gel polymer electrolyte for flexible lithium-ion polymer batteries. *Materials*, *8*(5), 2735-2748.
- Zhao, Y., Zhang, Y., Gosselink, D., Doan, T. N. L., Sadhu, M., Cheang, H.-J., & Chen, P. (2012). Polymer electrolytes for lithium/sulfur batteries. *Membranes (Basel)*, *2*(3), 553-564.

Zhou, Y., Xiang, W., Chen, S., Fang, S., Zhou, X., Zhang, J., & Lin, Y. (2009). Improvements of photocurrent by using modified SiO₂ in the poly(ether urethane)/poly(ethylene oxide) polymer electrolyte for all-solid-state dye-sensitized solar cells. *Chemical Communications*, 26, 3895-3897.

University of Malaya

LIST OF PUBLICATIONS AND PAPERS PRESENTED

PATENT

Ramesh S., **Shanti R.**, Ramesh K., Arof A.K., Ezra Morris, & Chee S.Y. (2013). Method of producing a teflon adhesive polymer membrane, PI2013700344, Malaysia.

RESEARCH PUBLICATIONS

Shanti R., Hadi A.N., Salim Y.S., Chee S.Y., Ramesh S., & Ramesh K. (2017). Degradation of ultra-high molecular weight poly(methyl methacrylate-*co*-butyl acrylate-*co*-acrylic acid) under ultra violet irradiation. *RSC Advances*, 7, 112-120.

Shanti R., Bella F., Salim Y.S., Chee S.Y., Ramesh S., & Ramesh K. (2016). Poly(methyl methacrylate-*co*-butyl acrylate-*co*-acrylic acid): Physico-chemical characterization and targeted dye sensitized solar cell application. *Materials & Design*, 108, 560-569.

PAPER PRESENTED

Shanti R., Ramesh S., & Ramesh K. (2014). Development of solid state-dye sensitized solar cell using poly(MMA-*co*-BA-*co*-AA) based electrolyte. 3rd International Conference on Polymer Processing and Characterization (ICPPC 2014), Kerala, India.

Ramesh S., & **Shanti R.** (2014). MMA-*co*-BA-*co*-AA polymer electrolytes for DSSCs. 2nd International Congress on Materials and Renewable Energy, Greece.

Shanti R., Ramesh S., & Ramesh K. (2013). Studies on the properties enhancement of the acrylate-based polymer electrolyte membranes. 7th International Conference on Materials for Advanced Technologies, Suntec Singapore.

Shanti R. (2013). Bio-polymer based electrolytes plasticized with ionic solvents. Physics Colloquium 2013 University Malaya, Kuala Lumpur, Malaysia.

Shanti R., Ramesh S., & Ramesh K. (2013). Utilization of bio-inspired alternative in plasticizing the poly(MMA-*co*-BA-*co*-AA) based electrolytes. 4th International Conference on Functional Materials and Devices, Penang, Malaysia.